



**HAL**  
open science

# Search optimization by symmetric, biased or active random walks

Jean-Francois Rupprecht

► **To cite this version:**

Jean-Francois Rupprecht. Search optimization by symmetric, biased or active random walks. Physics [physics]. Université Pierre et Marie Curie - Paris VI, 2014. English. NNT : 2014PA066488 . tel-01142808

**HAL Id: tel-01142808**

**<https://theses.hal.science/tel-01142808>**

Submitted on 16 Apr 2015

**HAL** is a multi-disciplinary open access archive for the deposit and dissemination of scientific research documents, whether they are published or not. The documents may come from teaching and research institutions in France or abroad, or from public or private research centers.

L'archive ouverte pluridisciplinaire **HAL**, est destinée au dépôt et à la diffusion de documents scientifiques de niveau recherche, publiés ou non, émanant des établissements d'enseignement et de recherche français ou étrangers, des laboratoires publics ou privés.

THÈSE de DOCTORAT  
de l'UNIVERSITÉ PIERRE-ET-MARIE-CURIE PARIS VI

ÉCOLE DOCTORALE 107

Spécialité :

PHYSIQUE

présentée par

M. Jean-François RUPPRECHT

Pour obtenir le grade de

DOCTEUR de l'UNIVERSITÉ PARIS VI

Sujet : Optimisation de processus de recherche  
par des marcheurs aléatoires symétriques, avec biais ou actifs

Title: Search optimization  
by symmetric, biased or active random walks

soutenance prévue le 14 octobre 2014

devant le jury composé de :

Dr. David DEAN .....	Rapporteur
Dr. Athanasios BATAKIS .....	Rapporteur
Dr. Andrea PARMEGGIANI .....	Examineur
Dr. Lydéric BOCQUET .....	Examineur
Dr. Raphael VOITURIEZ .....	Directeur de thèse
Dr. Olivier BÉNICHOU .....	Invité
Dr. Denis GREBENKOV .....	Invité

Laboratoire de Physique Théorique de la Matière Condensée,  
Université Pierre-et-Marie-Curie, UMR 7600,  
4 place Jussieu, 75005 Paris, FRANCE.

This error message was generated  
by an errmessage command,  
so I can't give any explicit help.  
Pretend that you're Hercule Poirot:  
examine all clues, and deduce the truth  
by order and method.

*Journal of Statistical Physics – online article submission form.*



# Contents

<b>Note to the reader</b>	<b>9</b>
<b>Notations</b>	<b>11</b>
<b>1 General introduction</b>	<b>15</b>
1.1 Symmetric, biased and active random walkers . . . . .	17
1.1.1 Pearson walks . . . . .	17
1.1.2 Symmetric and biased Brownian motion . . . . .	19
1.1.3 Symmetric, biased and active particles . . . . .	20
1.2 Random search . . . . .	20
1.2.1 Search without cues . . . . .	20
1.2.2 Search with cues . . . . .	26
1.2.3 Randomized search . . . . .	26
1.3 Framework, objectives, methods . . . . .	27
<b>2 Mathematical introduction: symmetric, biased, active walks</b>	<b>31</b>
2.1 Probability distribution . . . . .	32
2.1.1 Chapman-Kolmogorov equation . . . . .	32
2.1.2 Integro-differential equation on the propagator . . . . .	33
2.1.3 Boundary conditions . . . . .	34
2.2 Survival probability . . . . .	36
2.2.1 Mean-first passage time (MFPT) . . . . .	36
2.2.2 Laplace transform of the survival probability . . . . .	37
2.2.3 Boundary conditions . . . . .	37
2.3 Some exact expressions of the search time . . . . .	39
2.3.1 Symmetric Brownian motion in spherical geometries . . . . .	39
2.3.2 MFPT for an active process: the EPRW random walk in $d = 1$ . . . . .	40
2.4 Perspectives: challenges on the boundary . . . . .	42
<b>I Search for an exit by symmetric or biased Brownian volume diffusion</b>	<b>47</b>
<b>3 FPT in 2D spherically symmetric domains</b>	<b>49</b>
3.1 General formalism and application to angular sectors . . . . .	53
3.1.1 Model and basic equations . . . . .	53
3.1.2 Resolution schemes . . . . .	55
3.1.3 Results for the disk . . . . .	59
3.1.4 Moments and cumulants . . . . .	63
3.2 Extensions and applications . . . . .	68
3.2.1 Annuli . . . . .	68
3.2.2 Advection-diffusion with a radial bias . . . . .	73
3.2.3 Rectangles . . . . .	73
3.2.4 Analogy to microchannel flows . . . . .	74
3.3 Conclusion . . . . .	77
3.4 Perspectives . . . . .	78

<b>II</b>	<b>Search for an exit by surface–mediated diffusion with symmetric or biased Brownian volume diffusion</b>	<b>81</b>
	<b>Introduction</b>	<b>83</b>
<b>4</b>	<b>Surface-mediated diffusion: homogeneous boundary condition</b>	<b>85</b>
4.1	The model . . . . .	86
4.2	General solution . . . . .	87
4.2.1	Basic equations . . . . .	87
4.2.2	General integral equation . . . . .	88
4.2.3	Exact solution . . . . .	90
4.2.4	Are bulk excursions beneficial? . . . . .	92
4.2.5	Perturbative solution (small $\varepsilon$ expansion) . . . . .	92
4.2.6	Approximate solution . . . . .	93
4.3	Particular cases . . . . .	95
4.3.1	Zero bias ( $V = 0$ ) . . . . .	95
4.3.2	Case of a $1/r$ velocity field . . . . .	98
4.3.3	Circular and spherical sectors . . . . .	100
4.4	Conclusion . . . . .	104
<b>5</b>	<b>Surface–mediated diffusion: mixed–boundary condition</b>	<b>107</b>
5.1	The model . . . . .	108
5.2	Exact solution . . . . .	108
5.2.1	Basic equations . . . . .	108
5.2.2	Integral equation . . . . .	109
5.2.3	Exact solution . . . . .	112
5.2.4	Are bulk excursions beneficial? . . . . .	114
5.2.5	Perturbative solution (small $\varepsilon$ expansion) . . . . .	114
5.3	Coarse-grained approach . . . . .	115
5.3.1	Comparison . . . . .	116
5.3.2	Discussion . . . . .	116
5.3.3	Analytical agreement between the coarse-grained and exact solutions . . . . .	118
5.4	Conclusion . . . . .	118
	<b>Conclusion and perspectives</b>	<b>121</b>
<b>III</b>	<b>Search strategy for active processes</b>	<b>123</b>
<b>6</b>	<b>Search strategy for the Pearson random walks</b>	<b>125</b>
6.1	Model and methods . . . . .	126
6.1.1	Model . . . . .	126
6.1.2	Methods and objectives . . . . .	128
6.2	Asymptotic behaviour and optimality . . . . .	130
6.2.1	Diffusive behaviour in the limit $\tau \ll a/v$ . . . . .	130
6.2.2	Asymptotic behaviour in the limit $\tau \gg b/v$ . . . . .	131
6.2.3	Matched asymptotic and optimality . . . . .	134
6.3	Conclusion . . . . .	138
6.4	Perspectives . . . . .	138
6.4.1	Comparison to other distributions of reorientation times . . . . .	138
6.4.2	Chemotactic search . . . . .	141

<b>7</b>	<b>Universal speed–persistence coupling in cells</b>	<b>143</b>
7.1	Introduction . . . . .	144
7.2	Results . . . . .	145
7.2.1	Cell trajectory analysis reveals a universal coupling between cell speed and persistence . . . . .	145
7.2.2	Faster actin retrograde flow lengthens cell persistence time . . . . .	147
7.2.3	Faster actin retrograde flow enhances the asymmetry of polarity cues . . . . .	149
7.2.4	Physical modeling predicts the USPC . . . . .	151
7.2.5	Derivation of the USPC law . . . . .	153
7.2.6	Phase diagram of main cell migration patterns . . . . .	155
7.2.7	Values of the fitting parameters . . . . .	158
7.3	Discussion and conclusion . . . . .	158
7.4	Perspectives . . . . .	161
<b>8</b>	<b>General Conclusion</b>	<b>163</b>
<b>9</b>	<b>Publications</b>	<b>167</b>
<b>IV</b>	<b>Appendix</b>	<b>169</b>
<b>A</b>	<b>FPT in 2D spherically symmetric domains</b>	<b>171</b>
A.1	Simplification of $\alpha_n$ and $M_{nm}$ . . . . .	171
A.1.1	Simplified expressions for $\alpha_0$ . . . . .	171
A.1.2	Simplified expressions for $\alpha_n, n \geq 1$ . . . . .	172
A.1.3	Simplified expression for $M_{nm}$ . . . . .	172
A.1.4	Perturbative expansion of $M_{nm}$ . . . . .	173
A.1.5	Summation identities . . . . .	174
A.2	Spatially averaged variances . . . . .	175
A.3	Convergence to an exponential distribution in the narrow-escape limit . . . . .	175
A.3.1	From the expression for the survival distribution . . . . .	175
A.3.2	From the expression for the moments . . . . .	176
A.4	Computational aspects . . . . .	176
<b>B</b>	<b>Surface–mediated diffusion</b>	<b>177</b>
B.1	Radiative boundary condition on the MFPT . . . . .	177
B.1.1	With an ejection distance ( $a > 0$ ) . . . . .	177
B.1.2	Without an ejection distance ( $a = 0$ ) . . . . .	179
B.2	Quantity $\eta_d/D_2$ is a mean first return time . . . . .	181
B.2.1	Measure of correlations . . . . .	181
B.2.2	Interpretation of $\eta_d/D_2$ as a mean first passage time . . . . .	182
B.3	Detailed calculations . . . . .	183
B.3.1	Matrix elements $I_\varepsilon(n, m)$ in 3D . . . . .	183
B.3.2	Case of a $1/r^2$ velocity field . . . . .	183
B.4	Mixed boundary condition: generalizations . . . . .	184
B.4.1	The disk case (2D) . . . . .	184
B.4.2	Generalization to semi-reflecting targets . . . . .	186



<b>C</b>	<b>Search strategy for the Pearson random walks</b>	<b>189</b>
C.1	Monte–Carlo simulations . . . . .	189
C.1.1	Description of trajectories . . . . .	189
C.1.2	Supplementary figures . . . . .	190
C.2	Exact relations at the boundary conditions . . . . .	191
C.2.1	Condition at $r = a$ . . . . .	191
C.2.2	Condition at $r = b$ . . . . .	192
C.2.3	Solution . . . . .	192
C.2.4	Comparison with simulations . . . . .	194
	<b>Bibliography</b>	<b>197</b>

# Note to the reader

- (1) ► The sentence following a ► symbol is emphasized.
  
- (2) **How to return to the reading page after clicking on a hyperlink** A click on a hyperlink is a jump to the referred equation, definition or citation. To return to the page where the hyperlink was clicked, use the following shortcut command
  - on Adobe Reader, SumatraPDF, PDF XChange Viewer: "Alt + left cursor"
  - on Preview (Mac Os): simultaneously press "Cmd+ Alt + Shift + ( "
  
- (3) I use the following abbreviations:
  - Chap. for a chapter,
  - Sec. for a section,
  - App. for a section within the appendix,
  - Fig. for a figure,
  - Eq. for an equation.

Other abbreviations are defined in the Notation section, p. 11.



# Notations

---

## Mathematical symbols

Definition relation .....	$\equiv$
Norm of the vector $\mathbf{r}$ .....	$ \mathbf{r} $
Average over the angular parameter $\theta$ .....	$\langle \cdot \rangle$
Modified Bessel function of the first kind and of order $n$ .....	$I_n(x)$
Bessel function of the first kind and of order $n$ .....	$J_n(x)$
Legendre polynomial of the order $n$ .....	$P_n(x)$
Kronecker symbol equal to 1 if $m = n$ , 0 otherwise .....	$\delta_{nm}$

## Acronyms

First Passage Time .....	FPT
Mean First Passage Time .....	MFPT
Global MFPT (spatially averaged MFPT) .....	GMFPT
Pearson Random Walk .....	PRW
Exponential Pearson Random Walk .....	EPRW
Universal Coupling between Speed and Persistence .....	UCSP
(mature) Bone Marrow Dendritic Cell .....	(m)BMDC
Retinal pigment epithelium .....	Rpe

## General

Space dimension .....	$d$
Bulk of the confining domain .....	$\Omega \subset \mathbb{R}^d$
Boundary of the confining domain $\Omega$ .....	$\partial\Omega \subset \mathbb{R}^{d-1}$
Target region .....	$\Gamma \subset \partial\Omega$

$(d - 1)$ -sphere of radius $R \geq 0$ .....	$S_R$
Initial position vector .....	$\mathbf{r} \in \Omega$
Uniform measure on $\Omega$ .....	$d\mathbf{r}$
Uniform angular measure on the $(d - 1)$ sphere (Eq. (4.18)) .....	$d\mu_d(\theta)$
Coordinate (e.g. radius) of the boundary containing the target .....	$R$
Half-aperture of a target on the boundary .....	$\varepsilon$
Diffusion coefficient .....	$D$
Radial part of the Laplacian (def. Eq. (2.32)) .....	$\Delta_r$
Laplace–Beltrami operator on the sphere $S_1$ (def. Eq. (2.32)) .....	$\Delta_\theta$
Probability to reach $\mathbf{r}_a$ at time $t_a$ from $\mathbf{r}$ at time $t$ .....	$p(\mathbf{r}_a, t_a   \mathbf{r}, t)$
Probability to reach $\mathbf{r}_a$ at time $t$ from $\mathbf{r}$ at $t = 0$ .....	$p(\mathbf{r}_a, t   \mathbf{r})$
Time needed to reach the target from the initial position $\mathbf{r}$ .....	$\sigma_{\mathbf{r}}$
Time needed to reach the target	
averaged over random uniformly distributed initial positions .....	$\sigma_\Omega$
Survival probability up to time time $t$ , with an initial position at $\mathbf{r}$ .....	$\tilde{S}^{(t)}(\mathbf{r})$
Laplace transform of the survival distribution $\tilde{S}^{(t)}(\mathbf{r})$ .....	$S^{(p)}(\mathbf{r})$
First passage time probability (FPT) density with initial position $\mathbf{r}$ .....	$\tilde{\rho}^{(t)}(\mathbf{r})$
Mean first passage time (MFPT) of the random variable $\tau_{\mathbf{r}}$ .....	$T(\mathbf{r}) = \mathbb{E}[\sigma_{\mathbf{r}}]$
$n$ -th moment averaged over all initial position over $\Omega$ .....	$\overline{\mathbb{E}[\sigma^n]}$
$n$ -th moment averaged over random uniformly distributed positions .....	$\mathbb{E}[\sigma_\Omega^n]$
Fourier coefficients (def. Eq. (3.13a)) .....	$\alpha_0, \alpha_n$
Fourier coefficients of the survival distribution (def. Eq. (3.5)) .....	$a_0^{(p)}, a_n^{(p)}$
Fourier coefficients of the MFPT (def. Eq. (4.10)) .....	$a_n \equiv a_n^{(0)}$
Eigenfunctions of the Laplace–Beltrami operator $\Delta_\theta$ (def. Eq. (3.5)) ...	$V_n(\theta)$
Eigenfunctions of the radial Laplacian operator $\Delta_r$ (def. Eq. (4.10)) .....	$f_n(r)$

## Part I

Long-time decay rate of the survival distribution (def. Eq. (3.45))	$p_1$
Transformation on $p_1$ (def. Eq. (3.46))	$q_1 \equiv i\sqrt{p_1}$
Volume ( $d = 3$ ) or area ( $d = 2$ ) of $\Omega$ (def. Eq. (3.45))	$ \Omega $
Approximate expression for $\mathcal{C}^{(p)}$ (def. Eq. (3.40))	$\mathcal{C}_a^{(p)}$
Deviation to the analytically solvable case (def. Eq. (3.16))	$\gamma^{(p)}$

## Part II

Diffusion coefficient along the surface	$D_1$
Diffusion coefficient within the bulk	$D_2$
Desorption rate	$\lambda$
Adsorption coefficient (def. Eq. (5.7))	$k$
MFPT from the surface coordinate $\theta$ (def. Eq. (5.10))	$t_1(\theta)$
MFPT from the bulk coordinate $(r, \theta)$ (def. Eq. (4.10))	$t_2(r, \theta)$
Fourier coefficients of $t_2$ (def. Eq. (5.10))	$a_n \equiv a_n^{(0)}$
Fourier coefficients related to $t_1$ (def. Eq. (4.31))	$d_n$
Inverse of the bulk GMFPT (def. Eq. (5.3))	$k_b$
Dimensionless radial position after a desorption event	$x \equiv 1 - a/R$
Dimensionless desorption rate	$\omega \equiv R\sqrt{\lambda/D_1}$
Cycle time of a surface exploration & bulk excursion (def. Eq. (5.21))	$T$
Dimensionless function $t_1(\theta)/(\omega^2 T)$	$\psi(\theta)$
Adsorption operator (def. Eq. (4.9))	$(Lf)(r)$
Vector of readsorption (def. Eq. (4.27))	$X_n$
Matrix of readsorption (def. Eq. (5.26))	$X_{nm}$

**Part III**

Run velocity (def. p. 153) .....	$v$
Distribution of reorientation time (def. p. 153) .....	$\pi(t)$
Reorientation rate, i.e. persistence time (def. p. 153) .....	$\tau$
Volume between the sphere $S_a$ and $S_b$ .....	$\Omega_r$
Configuration space: $(\mathbf{r}, \mathbf{v}) \in \Omega$ .....	$\Omega = \Omega_r \times S_v$
Effective diffusion coefficient (def. p. 153) .....	$D = v^2\tau/2$
Radius of the target (def. p. 153) .....	$a$
Radius of reflective boundary .....	$b$
Probability measure coefficient $d\mu(\mathbf{v}') = \omega_d d\theta$ .....	$\omega_d$

**Part 7**

Angular persistence (def. p. 153) .....	$\tau_\phi$
Polarization time (def. p. 153) .....	$\tau_p$
Retrograde flow velocity .....	$V$
Velocity of the cell .....	$v = -V$
Maximal possible velocity of the actin flow (def. p. 152) .....	$\beta$
Unit scale for $\beta_0$ (def. p. 152) .....	$\beta_0$
Concentration of cues above which activation is saturated .....	$C_s$
Averaged velocity at steady state .....	$\bar{V}$
MFPT to $V_f$ from $V_0$ .....	$t(V_f V_0)$
Effective drift coefficient for cues .....	$\tilde{V}$
Diffusion coefficient for cues (p. 151) .....	$D$
Length of the actin filament .....	$L$
Fraction of activated cues (def. p. 152) .....	$c^*(x, t)$
Typical time scale of the actin flow fluctuations (def. p. 152) .....	$\gamma^{-1}$
Angular diffusion coefficient of the actin flow (def. p. 152) .....	$K$
Intensity parameters for fluctuations on the number of cues (def. p. 152) .....	$K_c$
Effective potential (def. p. 153) .....	$W(V)$
In the phase diagram, line separation of the diffusive state .....	$\beta_c(C_s)$
In the phase diagram, line separation of the persistent state .....	$C_s^c(\beta)$







# General introduction

**Abstract** In this introduction, I illustrate the main issues considered in this thesis with examples drawn from various scientific fields. In the context of these examples, I indicate the main results of my thesis by a ► symbol. Technical questions will be discussed in the following chapters. I point out that I will discuss the state of the art of my field of research within the introduction of the following chapters.

## Contents

<b>1.1 Symmetric, biased and active random walkers . . . . .</b>	<b>17</b>
1.1.1 Pearson walks . . . . .	17
1.1.2 Symmetric and biased Brownian motion . . . . .	19
1.1.3 Symmetric, biased and active particles . . . . .	20
<b>1.2 Random search . . . . .</b>	<b>20</b>
1.2.1 Search without cues . . . . .	20
1.2.1.1 Symmetric and biased Brownian motion . . . . .	21
1.2.1.2 Pearson random walks . . . . .	21
Neutron scattering . . . . .	21
Polymer conformation . . . . .	22
Cell motion . . . . .	22
Eye movements . . . . .	23
Animal foraging . . . . .	23
1.2.1.3 Intermittent search: (diffusive/active) or (diffusive/diffusive) . .	23
Porous media . . . . .	24
Biochemical reactions . . . . .	25
Animal foraging . . . . .	26
1.2.2 Search with cues . . . . .	26
Chemotaxis (bacteria) . . . . .	26
Infotaxis (moths) . . . . .	26
1.2.3 Randomized search . . . . .	26
<b>1.3 Framework, objectives, methods . . . . .</b>	<b>27</b>

Consider a gambler – called Sid hereafter – going to a casino with an initial fortune of  $f_0 = 900\text{€}$ . At each successive gamble, Sid wins  $1\text{€}$  with probability  $p$  or loses  $1\text{€}$  with probability  $1 - p$ , independently of past events. Let  $f_n$  denote Sid's fortune after the  $n$ -th gamble. Sid wins if he reaches a total fortune of  $1000\text{€}$  without first getting ruined. Sid keeps gambling until winning or getting ruined, whichever happens first. While the game proceeds, the fortune  $f_n$  after  $n$  gambles is the sum

$$f_n = \Delta_1 + \dots + \Delta_n, \quad f_0 = 900, \quad (1.1)$$

where  $(\Delta_i)$  represents the earnings at the  $i$ -th gamble (we omit the € unit). The set  $\Delta_i$  are  $n$  independent random variables which are identically distributed according to a probability law  $\mathbb{P}(\Delta_i = 1) = p$ ,  $\mathbb{P}(\Delta_i = -1) = 1 - p$ . The set  $f_n$  is called a *discrete random walk*.

The gambler's ruin or win problem provides simple examples of the quantities considered in this manuscript

- The probability that Sid ends winning the game is called a splitting probability. It is a function of the initial fortune  $f_0$  and it is denoted  $\Pi(f_0)$ .
- Sid's winning fortune ( $f = 1000$ ) or the Sid's ruin ( $f = 0$ ) are called the targets. The game ends when Sid's fortune reaches either one of the two targets.
- The duration of the game, whichever its outcome, is a random variable denoted  $\sigma$ .
- The probability that the game is ended at the  $n$ -th step, i.e. that  $\sigma = n$ , is called the first passage time (FPT) probability and is denoted  $\tilde{\rho}^{(n)}(f_0)$ .
- The mean duration of the game is called the mean first passage time (MFPT), denoted  $t(f_0)$ .

Let us make some practical applications and compare the probability for Sid to win the game in the following two situations:

- in the fair (i.e. *symmetric*) coin-flipping game ( $p = 1/2$ ), the winning probability is  $\Pi(900) = \frac{900}{1000} = 90\%$ .
- in the *biased* roulette game ( $p = 18/38 \approx 0,47$ ),  $\Pi(900) = 3.10^{-3}\%$ .

The quantity  $\mu = 1/2 - p$  is called the *bias*. Notice that even a small bias ( $\mu \approx 0.03$ ) leads to a drastic  $10^{-5}$  factor on the winning probability.

► In this thesis, I have computed FPT densities and MFPT to exit a confining domain for *biased* continuous random walks (Parts I, II). I have also computed splitting probabilities in the presence of two targets (see Sec. 3.4).

The concept of a random walk refers to the overall displacement of a point through a sequence of random steps. It was introduced independently by

- Rayleigh to model the addition of sound waves with random phases ([1], 1896),
- Bachelier to model financial speculations ([2], 1900),
- Pearson to model the motion of mosquitoes ([3], 1905).
- Einstein to model the jiggling motion particles in water ([4], 1905).

This history illustrates the versatility of the concept of random walks. I briefly explain the concepts of Pearson and Brownian random walks with a historical perspective in the first Sec. 1.1. The main mathematical tools are introduced in the next Chap. 3.4, p. 78.

In the second section Sec. 1.2, p. 20, I focus on *random searches*. A random search is a random walk which ends at a specific and fixed region of space called the *target*. At the casino, Sid performs a random search for one of the two possible targets at  $f = 1000$  and at  $f = 0$ .

One of the aims of my thesis is to identify optimal search strategies leading to a minimization of the average search time. I illustrate the issues at stakes by simple "preys versus predators" examples. Following the path led by Pearson, a large literature models animal foraging<sup>1</sup> as a first-passage problem [5, 6, 7]. The fact that only the first encounter matters either models that

<sup>1</sup>Foraging is the act of searching for a wild food resources.

the searcher kills the target (e.g. a randomly moving prey steps on an immobile predator) or, conversely, that the searcher is killed at the encounter of the target (e.g. a randomly moving prey finds an immobile predator). Both the minimization and maximization of the search time are relevant for the moving predator and the moving prey, respectively [6]. More generally, the target can represent food, a sexual partner or a shelter, hence search processes are expected to have been optimized to guarantee the survival of the species. Theoretical identification of random search strategies is expected to lead to pattern detection in animal foraging (see the discussion in p. 23).

Random walk modeling of animal foraging generally supposes that (i) the animal has no cue on the whereabouts of the target, and that (ii) the animal has low cognitive skills and is not able to keep memories of its past explorations.

Relatively to point (i), one may argue that the displacement of animals can be correlated to cues indicating the position of the target. For example, these cues can be chemicals emitted by the prey which can be detected by the predator. The presence of cues can first be modeled by a bias in the random walk [8, 9]. However, other search patterns are needed to describe the trajectories of cells (see the chemotaxis algorithm in Sec. 1.2.2, p. 26) or moths (see the infotactic algorithm in Sec. 1.2.2, p. 26).

The second point (ii) illustrates the notion of a memoryless *Markovian* processes, whose mathematical definition is explained in the next Chap. 2. As an example of a non-Markovian search, animals with high cognitive skills (e.g. with a cortex which enables the creation of mental map of the exploration space) have the ability to perform a non-random search. Systematic search have been extensively studied in order to design efficient human operations, such as rescue operations or military tracking of submarines [10, 11]. Though roboticists have undoubtedly high cognitive skills, I explain in Sec. 1.2.3, p. 26 why roboticists use a random search algorithm in the field called randomized planning.

In the last section Sec. 1.3, p. 27, I conclude by giving the specific framework of this thesis and my objectives.

## 1.1 Symmetric, biased and active random walkers

In this section, we first define the two notions of random walk and Brownian motion from a historical perspective. We conclude on the more recent distinction between active and passive particles.

### 1.1.1 Pearson walks

Karl Pearson coined the term "random walk" while posing the following problem to the Editors of the Nature journal [3]:

*"A man starts from a point  $O$  and walks  $l$  yards in a straight line; he then turns through any angle whatever and walks another  $l$  yards in a second straight line. He repeats this process  $n$  times. I require the probability, that after these  $n$  stretches he is at distance between  $r$  and  $r + dr$  from his starting point."*

The length of each straight walks is a deterministic quantity equal to  $l$  yards (see Fig. 1.1). Pearson was interested in the propagation of mosquitoes invading cleared jungle regions . In the next journal edition, Lord Rayleigh gave the following expression for the probability density in the limit of a large number of steps  $n$ :

$$dp(r, n) = \frac{2}{nl^2} \exp\left(-\frac{r^2}{nl^2}\right) r dr, \quad (1.2)$$

which, in the modern mathematical formulation, can be seen as a consequence of the central limit theorem. Rayleigh did not provide the answer for a general value of  $n$ , prompting Pearson's comment that "*from the purely mathematical standpoint, it would still be very interesting to have a solution for  $n$  comparatively small*". Only recently (2011) did Ref. [12] obtain a hypergeometric representation of the density  $p(r, 4)$  for four steps ( $n = 4$ ).

A precise definition of a Pearson random walk relies on the definition of the  $(d - 1)$ -sphere of radius  $v \geq 0$ , denoted  $S_v$ , which is the set of points:

$$S_v \equiv \left\{ \mathbf{v} \in \mathbb{R}^d \mid |\mathbf{v}|^2 = \sum_{i=1}^d v_i^2 = v^2 \right\}. \quad (1.3)$$

**Pearson Random Walks (PRW)** are defined in this thesis as random walks which are composed of straight runs at the constant velocity  $v$  and interspersed by reorientation events:

- (i) The duration  $t$  of each straight random walks are independent and distributed according to a distribution  $\pi(t)$ .
- (ii) At each of all reorientation events, which are instantaneous, the velocity vector  $\mathbf{v}$  is drawn from a uniform distribution on the  $(d - 1)$ -sphere of radius  $v$ . The new velocity vectors  $\mathbf{v}$  are independent of the previous ones.

Mind that Pearson random walks are also called *persistent* random walks [13]. I define the following subcategories for the Pearson random walks:

- the original Pearson random walk: the duration of a run is distributed according to the law  $\pi(t) = \delta(t - \tau)$ , where  $\tau = l/v$  (p. 17).
- the **Exponential Pearson Random Walk (EPRW)**: the duration of a run is exponentially distributed according to the law  $\pi(t) = \exp(-t/\tau)/\tau$ . In the limit of a large number of steps  $n$ , Rayleigh's result Eq. (1.2) applies to the probability distribution  $dp(r, n)$  of the EPRW.
- the **Lévy walks**: the duration of a run is distributed according to a power law  $\pi(t) \sim t^{-\mu}$  for large  $t$ , with  $1 < \mu$ . If  $\mu < 3$ , the variance of the distribution  $\pi(l)$  diverges, the central limit theorem does not apply and Rayleigh's result Eq. (1.2) is not correct in the limit of a large number of steps  $n$ . The overall displacement is mainly due to a few very long runs. The interested reader is referred to [14]. In Part. III, I show that the EPRW search is more efficient to find a single target than any Lévy walk search.

A random walk can also be thought as a displacement in an abstract space. At the casino, Sid playing the fair coin-flipping game undergoes a Pearson random walk along the one dimensional *fortune* space, with a geometric reorientation law  $\pi(t = n\tau) = (1/2)^n$ . In his answer to Rayleigh, Pearson argues that "*one does not expect to find the first stage of a biometric problem provided in a memoir on sound*." However, the problem of the initial Pearson walk with  $n$  random walks of deterministic length  $l$  and turning angle  $(\phi_k)$  is equivalent to the problem that had been considered by Rayleigh [1]: the addition of  $n$  coherent plane waves at the same frequency  $\omega$ , with positive amplitudes  $l$  and phases  $(\phi_k)$ . Waves sum up to contribute to the final amplitude in the complex plane  $X(t) = \sum_{k=1}^n l \exp(i\omega t + \phi_k)$ . The sound intensity is proportional to the norm  $|X|$ , and in the case of a large number of waves  $n$ , the distribution of sound intensity is given by Rayleigh's result in Eq. (1.2). The same argument holds for electromagnetic waves and accounts for the laser speckle effect [15, 16]. In the next Sec. 1.2.1.2, I provide several examples of PRWs in the context of random search.

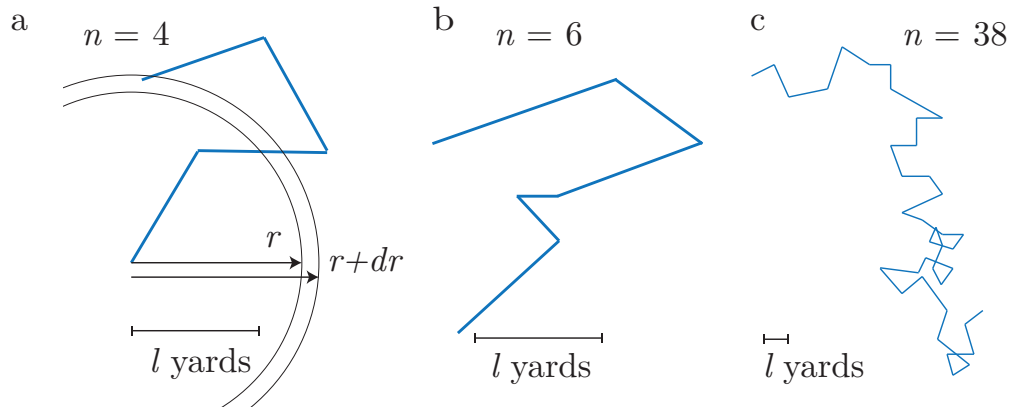


Figure 1.1: (a) The random walk initially described by Pearson, as seen from above, at a low altitude. The distance between two reorientations is constant and is equal to  $l$  yards. (b) The exponential Pearson random walk: the length of each straight walk is random and is exponentially distributed with a mean length  $l$  (yards). (c) The Pearson random walk as seen from above at a high altitude (higher than in (b)): the mean length  $l$  scales smaller, and a larger number of turns  $n$  are visible.

### 1.1.2 Symmetric and biased Brownian motion

In 1853, Robert Brown made the intriguing observation that a small pollen grain keeps jiggling when suspended in water. The riddle of Brownian motion was solved by Einstein in 1905 [4]. Einstein models the pollen grain as a point moving along a 1D line that is displaced at regular time intervals  $\tau$  due to shocks with water molecules.

I consider a simplified version of Einstein's general approach in which the pollen grain is randomly displaced by discrete increments of length  $l$ . The pollen grain is initially at  $f_0 \in l\mathbb{Z}$ . After the  $n$ -th shock with a water molecule, the pollen grain is at the position  $f_n = \Delta_1 + \dots + \Delta_n$ , where the  $(\Delta_i)$  represents the displacement at each shock. The  $(\Delta_i)$  are  $n$  independent random variables which are identically distributed according to a probability law  $\mathbb{P}(\Delta_i = l) = 1/2 - \mu$ ,  $\mathbb{P}(\Delta_i = -l) = 1/2 + \mu$ . Notice that this problem is strictly equivalent to the gambler's problem provided that the length unit  $l$  plays the role of the  $\text{€}$  unit (see p. 15).

The probability  $P(m, n+1) \equiv p(ml, (n+1)\tau|f_0)$  that the pollen grain is at  $f = ml$  after the  $n$ -th shock is given by

$$\begin{aligned} P(m, n+1) &= \mathbb{P}(\Delta_i = l)P(m+1, n) + \mathbb{P}(\Delta_i = -l)P(m-1, n), \\ &= \frac{1}{2} \{P(m+1, n) + P(m-1, n)\} + \mu \{P(m-1, n) - P(m+1, n)\}. \end{aligned} \quad (1.4)$$

The biased Brownian process is obtained in the *continuous limit* of (i) short time intervals  $\tau \rightarrow 0$ , (ii) short displacement lengths  $l \rightarrow 0$ , (iii) short bias  $\mu \rightarrow 0$  and (iv) with fixed ratios:

$$D = \frac{l^2}{2\tau} \quad \text{and} \quad V = \frac{2\mu l}{\tau}. \quad (1.5)$$

The terms  $D$  and  $V$  are called the diffusion coefficient and the drift coefficient respectively. In a symmetric Brownian walk, the drift coefficient is equal to zero (i.e.  $V = 0$ ). In the continuous limit, Eq. (1.4) leads to the following equation on the probability density  $p(f, t|f_0)$ :

$$\frac{\partial p(f, t|f_0)}{\partial t} = -V \frac{\partial p(f, t|f_0)}{\partial f} + D \frac{\partial^2 p(f, t|f_0)}{\partial f^2}. \quad (1.6)$$

where I recall that  $p(f, t|f_0)$  is the probability for the pollen grain to be at the position  $f$  at the time  $t$ , provided that it was initially at  $f_0$ . In the next Chap. 2, p. 31, we recall the method to

recover the latter equation Eq. (1.6) as a special Markovian process. I point out that Brownian motion can be rigorously derived as a limit process of a system of hard-spheres (see the very recent result of Ref. [17]).

### 1.1.3 Symmetric, biased and active particles

In this section we make the distinction between symmetric, biased and active random walks defined over continuous time ( $t \in \mathbb{R}$ ) and space ( $\mathbf{r} \in \mathbb{R}^d$ ).

- (1) In this thesis manuscript, symmetric and biased Brownian particles are said to be *passive*, by opposition to *active* particles defined in the next paragraph. Both symmetric and biased Brownian trajectories are nowhere differentiable and have no well-defined instantaneous velocity [18]. Symmetric Brownian particles do not move on average in a preferred direction, while biased Brownian particles have an overall motion in a preferred direction, characterized by the drift velocity  $V(r)$  defined in Eq. (1.6).
- (2) The term *active* particle refers to the ability for the particle to move at a sustained and well-defined instantaneous velocity  $v$ . With this definition, the position process  $\mathbf{r}(t)$  of an active particle is not Markovian (this point will be further discussed in Sec. 2.1.1, p. 32). Active particles include the classes of
  - (i) active Brownian particles, whose velocity satisfies a Langevin equation (see Eq. (7.7) in Sec. 7, p. 143). In particular, the direction of the velocity vector  $v$  rotates through slow angular diffusion.
  - (ii) PRW particles which move according to straight ballistic motion at a constant speed  $v$  until a random tumble event suddenly decorrelates the orientation (see p. 18),
    - In Part III, we focus on the EPRW and in Sec. 7, p. 143, we construct a model in which cells are described as active Brownian particles. Examples of PRW active particles are discussed in Sec. 1.2.1.2, p. 21. I point out that motile cells [19] and self-propelled Janus particles can be modelled as active Brownian particles [20].

In the next section, I set the general framework of this thesis and I indicate some bounds on my field of research.

## 1.2 Random search

In this section I give an overview of the field of random search processes, with illustrations in various scientific fields. I make the distinction between search processes in the absence or in the presence of cues. I recall that a cue is a piece of information which indicates the direction of the target.

### 1.2.1 Search without cues

The best example of a cueless random search process is the very first step of a diffusion-limited chemical reaction. Most chemical reactions require that a given reactant  $A$  meets a second reactant  $B$ . This first encounter step can be rephrased as a search process involving a searcher  $A$  looking for a target  $B$ . If the search process is the limiting step, the reaction rate is related to the search time of the reactants. The chemical reaction is then said to be diffusion-limited. For example, consider a diffusion-limited catalytic reaction  $A + B \rightarrow B + C$ , such that the

concentration of  $B$  is fixed. Within the Smoluchowski mean-field approximation, the MFPT of  $A$  to  $B$  denoted  $t_{AB}$  provides an estimate of the first-order reaction constant  $k = [B]/t_{AB}$  [21]:

$$\frac{\partial[A]}{\partial t} = -k[A]. \quad (1.7)$$

where  $[A]$  refers to the average concentration of  $A$ . In the rest of this section, I consider situations in which the reactants  $B$  are at a fixed region of space. Three types of dynamics for  $A$  can be distinguished: drifted Brownian processes (Sec. 1.2.1.1), subdiffusive processes (Sec. 1.2.1.1), Pearson random walks (Sec. 1.2.1.2) and intermittent processes (Sec. 1.2.1.3).

### 1.2.1.1 Symmetric and biased Brownian motion

Biochemical reactions which involve only a few reactants are such that the search process is the limiting step [22]. The time needed for an ion to find an open channel is indeed a limiting step in the kinetics of the neurological process of phototransduction [23]. The role of the confining domain on the FPT distribution of a regulation protein to a specific DNA site can account for the bursting dynamics in gene regulation [24].

The trajectories of marked proteins within a cell cytoplasm can be quantitatively described either by:

- (i) unbiased Brownian processes, see Ref. [25] for a complete review.
- (ii) biased Brownian processes, with an effective advection drift which models the effect of active transport [26]. Most proteins can randomly bind and unbind to molecular motors moving along microtubules or along actin filaments [27, 28, 29]. In the regime of a high rate of binding and unbinding, the active transport of these proteins is described as a biased diffusion process [30, 26, 31].
- (iii) subdiffusive processes which model the slowdown of motion due to trapping events in the overcrowded cell [32] (see the recent review of [33] for a first guide to subdiffusion).

Stochastic models for intracellular transport can be found in the reviews [34] and [25].

► In Part. II, I consider the cases of particles confined in a disk which (i) are Brownian and biased by a  $1/r$  radial drift (ii) are subdiffusive due to long waiting times. I show that the subdiffusive case can be deduced from the Brownian case.

### 1.2.1.2 Pearson random walks

The Pearson random walk is defined p. 18 as being composed of straight runs at the constant velocity  $v$  interspersed by reorientation events. In this section, we focus on physical processes which can be modelled as search processes by PRW particles.

**Neutron scattering** The Brownian motion of the pollen grain is due to random shocks with water molecules (see p. 19). A similar description applies for neutrons diffusing in a dense media: neutrons propagate along a straight beam, but can be scattered and reoriented due to local interactions with the constitutive atoms of the media. The trajectories of neutrons are often modelled by EPRWs [35, 36, 37]. In a nuclear reactor, the so-called neutron poisons are fissile atoms that can absorb neutrons and stop the nuclear reaction: in the vocabulary of search processes, these neutron poisons play the role of the target (see [37] p. 177). If the ratio of scatterers to targets is large, then the absorption process of neutrons is well accounted by a Brownian theory. If this ratio is not too large, an EPRW description is required [38].



**Polymer conformation** The backbone of a linear polymer consists in the repetition of an elementary chemical motif called the monomer. Under the assumption that the chemical bounds between monomers can twist in random directions, the resulting polymer configuration is a Pearson walk [39]. As a post-doc in the group, Thomas Guérin quantified the reactivity of a monomer within a polymer chain using first passage time observables [40].

**Cell motion** *E. coli* bacteria have been extensively studied, partly due to their large size. In the absence of chemical gradients, the *E. coli* bacterium swims at random with a succession of runs (approximately straight moves) and tumbles (random changes of direction), as represented in Fig. 1.2. Let me summarize the description by Howard Berg [41] of the trajectories of *E. coli* bacteria in a 3D aqueous solution:

- (i) The durations of successive runs are uncorrelated and are exponentially distributed with mean run time of about 1s. The mean run duration can vary from cell to cell. Run speeds are nearly identical for each cell ( $v \approx 20\mu\text{m}\cdot\text{s}^{-1}$  on average).
- (ii) Following a tumble, the new directions are not exactly chosen according to a uniform law. Indeed, the mean turn angle is equal to 68 degrees which indicates the random walk is slightly correlated.
- (iii) Tumble intervals are distributed exponentially with a mean of about 0.1s. The mean tumble duration does not vary significantly from cell to cell. After a tumble, it takes around 0.1s for the cell to reach its terminal run speed.

► Provided that the turning angle after a tumble is assumed to be uniformly distributed (point (ii)), and that the duration of the phase (iii) is neglected ( $\approx 0.1\text{s}$ ), the motion of a *E. coli* bacterium in the absence of cues is well described by an EPRW.

Similarly to *E. coli* bacteria, the trajectory of bone marrow dendritic cells can be modelled by EPRW processes [42]. These immune cells are involved in the detection of pathogens in mammals. Due to their crucial hunting role, natural selection is expected to have driven dendritic cells to optimize their search strategy [14, 43]. In Sec. 7, p. 143, we construct a model accounting for the experimentally observed relation between the turning rate  $\tau$  of the cell and its velocity  $v$ .

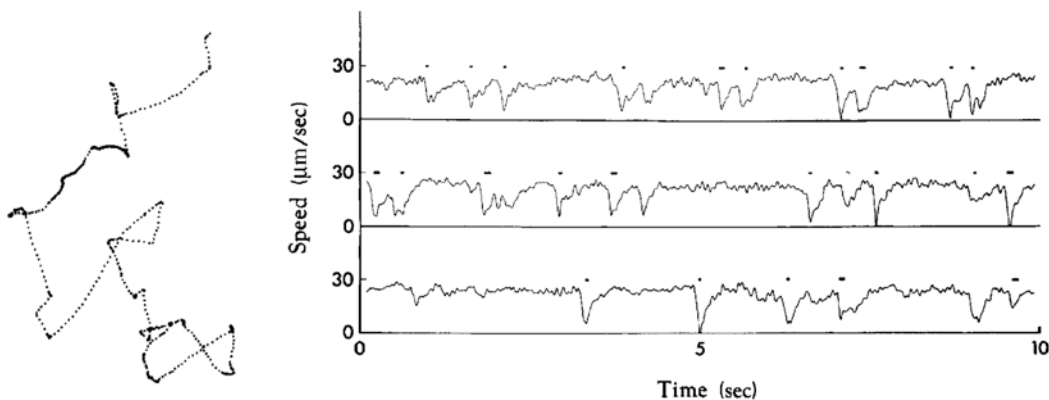


Figure 1.2: Behaviour of a *E. coli* bacterium in a 3D aqueous solution (a) Projected trajectory within a plane. (b) Norm of the velocity (i.e. *speed*) of the *E. coli* whose track is shown in (a). Tumbles occur during the intervals indicated by the horizontal bars. The three tracks of the velocities are stacked on top of each other. Mean speed is  $v \approx 21.2\mu\text{m}\cdot\text{s}^{-1}$ . Notice that the tumble duration is about ten times shorter than the run duration. These figures are excerpts from Ref. [41].

**Eye movements** Eye movements in reading can be modelled as an alternating sequence of fixations, during which the gaze position is stationary, and saccades, during which the gaze moves in a straight direction [44]. This process is well described in Ref. [45] as a stochastic process that I identify as being a PRW.

**Animal foraging** Consider a dog seeking for a ball hidden within the grass of a meadow. The dog is likely to make a straight run, to stop, to sniff the grass for a few seconds before taking a next straight run. In a more general context, animal trajectories often show ballistic phases interspersed with turns which can be interpreted as Lévy walks (defined in p. 17) [46, 5, 6, 7]. Lévy walks are characterized by rare but very long runs, thus Lévy walks are more efficient at exploring space than Brownian motion, which is recurrent (i.e. it returns an infinite number of times to its initial point). The statements of Ref. [5] are that (i) the Lévy walk is an optimal random search strategy, hence (ii) that animals should have naturally evolved search patterns that can be modelled as Lévy walks. Ref. [47] claims that marine predators in the Bay of Biscay perform (i) a Lévy search pattern when the concentration of preys is low and (ii) a Brownian search pattern when the concentration of preys is large.

It is acknowledged in Ref. [5] that in the case of a single target that can be encountered only once (called the non-revisitable case), the optimal search pattern strategy is not of Lévy walk but a straight ballistic walk. Mind that a straight ballistic walk corresponds to an EPRW with  $\tau = \infty$ .

► However, we show in Part. III that the EPRW is an optimizable function of the mean turning rate  $\tau$ , meaning that the optimal EPRW outperforms the straight ballistic walk search pattern. This result contrasts with the predictions of Ref. [5] that we mentioned.

What happens at the stopping phase of an EPRW? I address this question in the next section.

### 1.2.1.3 Intermittent search: (diffusive/active) or (diffusive/diffusive)

Let me consider again the case of a dog in a meadow. In the previous paragraph, I modelled the dog as an EPRW searcher. At the reorientation events, the dog instinctively puts his muzzle into the grass to seek the hidden ball. A reasonable hypothesis is that the dog can find the ball only during these local search phases between two run phases.

During her PhD in the group, Claude Loverdo considered intermittent search strategies combining [14]:

- (1) slow phases (such as symmetric diffusion) that allow the searcher to detect the target,
- (2) fast relocation phases (such as active EPRW) without detection.

► In Part 7, p. 143, I present experimental evidence that some dendritic cells alternate between diffusion phases and active run phases and I build a model that accounts for the intermittent behaviour from minimal microscopic hypothesis (see Fig. 1.3).

I point out that intermittent strategies are shown to outperform Lévy walks strategies in a large class of situations (see Ref. [48] for a complete discussion on this question).

**Surface-mediated diffusion** In the rest of this paragraph, I focus on a specific intermittent process called surface-mediated diffusion which alternates:

- (1) surface (symmetric) diffusion along a boundary of the confining domain, with a diffusion coefficient  $D_1$ ,
- (2) bulk symmetric or bias diffusion within the confining domain, with a diffusion coefficient  $D_2$  and a possible radial bias  $V(r)$ .

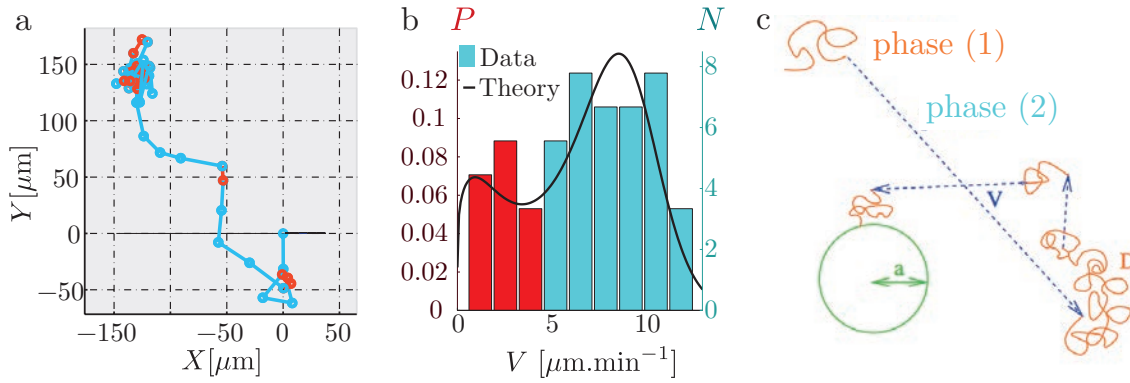
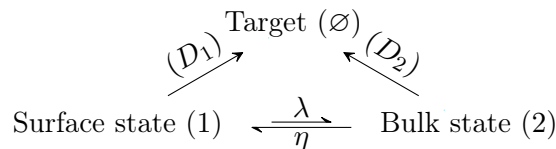


Figure 1.3: Bone marrow dendritic cells (BMDC) exhibit an intermittent behaviour, switching between run phases and diffusive search phases. **(a)** Trajectory of a single cell (141 min) performed by the Institut Curie group, see p. 143. Blue stands for cell speed  $v > 4 \mu\text{m}\cdot\text{min}^{-1}$  and red for  $v < 4 \mu\text{m}\cdot\text{min}^{-1}$ : the cell alternates between blue-colored run phases and red-colored diffusion phases. Circles indicate the confidence interval on the position of the nucleus of the cell ( $3\mu\text{m}$ ). **(b)** Histogram of speeds extracted from the experimental track in Fig. (a) and theoretical distribution of speeds  $P(v)$  (solid black line) from the model (see Sec. 7.2.7, p. 158). **(c)** Model of intermittent search from Ref. [14]: the velocity vector points in a fixed direction during the run phases: the run phases are straight ballistic walks, with exponentially distributed run times. The target, here a disk of radius  $a$ , can only be found during a diffusive phase. This first phenomenological model describe the search of pathogenic agent by an intermittent dendritic cell [14]. The model in Chap. 7, p. 143 goes beyond this first model to predict the observed intermittent behaviour of dendritic cells from microscopic hypothesis.

We consider such a process in Part. II. The term *surface* refers to a subspace of the accessible environment, which may either be one-dimensional or two-dimensional. The particle alternates between the surface and bulk states due to (i) adsorption events to the surface, characterized by the parameter  $\eta^{-1}$  which corresponds to a mean excursion time within the bulk, and to (ii) desorption events from the surface to the bulk at the rate  $\lambda$ .

In a surface-mediated search process, the target is either found through diffusion on the surface or by diffusion within the bulk. The kinetic scheme for a surface-mediated search can be expressed in terms of the parameters  $\lambda, \eta, D_1$  and  $D_2$ :



Mind that the mean return time to the surface  $\eta$  is not a reaction rate as it depends on the initial position of the particle. However, the coarse-grained approximation scheme consists in considering that  $\eta$  is a reaction rate (see p. 83).

The question of the optimality of the search process is to find, if any, the set of parameters  $(\lambda, \eta, D_1, D_2)$  which minimizes the MFPT to the target. This question is all the more interesting since surface-mediated diffusion processes are observed in porous media, intracellular trafficking and ethology.

**Porous media** A porous medium is an assembly of interconnected pores that are filled by a fluid. Aquifers, petroleum rocks, zeolites, bones, cements and ceramics can be modelled as porous media. The pores are generally connected through small openings that restrict inter-pore diffusion. ► If the target represents the opening between two pores, then our results correspond

to the mean time for a reactant to exit from one pore to the next in the absence (Part. I) or presence (Part. II) of surface-mediated diffusion.

The molecular dynamics of a reactant in a porous medium is often modelled as an intermittent interfacial process between the surface of the pore and its volume [49, 50, 51]. Intermittent behaviour of water molecules in porous media was first revealed using Nuclear Magnetic Resonance (NMR) techniques on hydrogen atoms [52, 53]. Due to paramagnetic interactions within the wall surface, the relaxation time of the nuclear spin is significantly shorter for a molecule adsorbed on the surface than for a molecule within the bulk (see the review [54]). Recently, the development of single-particle fluorescence microscopy led to a direct access to the values of the adsorption rate ( $\eta$ ), the desorption rate ( $\lambda$ ) and the local surface diffusion coefficient ( $D_1$ ). These quantities are associated to chemical interactions between the diffusive molecule and the confining surface [55]. In particular, the self-diffusion coefficient of water molecules reaches the unconfined bulk value ( $D_2$ ) beyond 1 nm from the surface (which corresponds to approximately two or three layers of water). This length appears to be independent of the wettability of the surface, while the statistics of relocation ( $\eta$ ) strongly depend on the hydrophilic or hydrophobic nature of the surface [56]. As a side-remark, I have considered the dynamic of fluid with mixed hydrophilic and hydrophobic boundary conditions in Sec. 3.2.4, p. 74.

Surface-mediated reactions are also encountered in the context of heterogeneous catalysis, i.e. chemical reactions induced by catalysts embedded in a surface (see [57, 58, 59]).

**Biochemical reactions** Bacteria rely on restriction enzymes to protect them against viral infection. A restriction enzyme is a protein that cuts DNA at a specific recognition nucleotide sequence. For example, the restriction enzyme EcoRV of *E. coli* bacteria recognizes the sequence GATATC [60]. The efficiency of the search process is of vital (and viral) interest for the bacterium: the restriction enzyme must find its target sequence and cut the virus in two before the virus could take over the bacteria machinery.

In a more general context, the search of a DNA sequence by proteins (such as RNA polymerase) is the first step of gene expression. Proteins find their target recognition site in a remarkably short time: for example, the kinetic rate for the lac repressor is orders of magnitude larger than expected for reactions limited by 3D diffusion [61]. The pioneering studies by Refs. [62, 63] suggested that proteins can bind and diffuse along the surface of the DNA chain due to a weak electrostatic interaction in a process named sliding. Recently, the surge of single-molecule microscopy techniques led to direct observations of switches between sliding phases and three-dimensional excursions [64, 65, 66, 67]. Theoretical investigations showed that the search time for the surface-mediated process is greatly reduced compared to 3D diffusion alone, and that this intermittent process can account for the enhanced reactivity of the lac repressor [68, 69]. However, these models did not consider the spatial correlations between the position at a desorption event and the position of the next readsorption on the surface. ► We explicitly take into account these spatial correlations in our surface-mediated model, Part. II. The spatial correlations play a crucial role as soon as the readsorption rate  $\eta$  is sufficiently large.

Small-scaled biological materials may alternate between bulk diffusion within the cell cytoplasm and lateral diffusion along the cytoplasmic and nuclear membranes. For example, it has been shown in Ref. [70] that viruses in Hela cells can (i) diffuse in the cytoplasm ( $D_2 \approx 0.02 \mu\text{m}\cdot\text{s}^{-1}$ ); (ii) bounce on or bind to the nuclear membrane; (iii) desorb from the nuclear membrane after an exponentially distributed time with a desorption rate  $\lambda \approx 0.1\text{s}$ . However, the value of the surface diffusion coefficients  $D_1$  along the cell membranes is not reported.

**Animal foraging** Mammalian rodent [71] and insects [72] can exhibit wall-following behaviour. The preference of animals to move along the walls of the confining domain is called thigmotaxis. When confined in a disk, cockroaches alternate (i) straight runs along the wall, with an exponential duration of adsorption time within the wall region and (ii) diffusive motion within the bulk of the disk [72]. Thigmotactism could be an advantageous strategy to search for a shelter within cracks in walls [72]. ► In Part. II, I consider the surface-mediated search of a target which is embedded within the confining boundary.

How does a randomly moving animal adapt its search behavior in the presence of olfactory cues that indicate the location of the target? This question is the subject of the next section.

### 1.2.2 Search with cues

**Chemotaxis (bacteria)** In the presence of a gradient of chemo-attractant concentration, *E. coli* bacteria swim up the gradient by adjusting its tumbling rate. Let me briefly quote the paragraph on chemotaxis from the book of Howard Berg [73]:

*"There is no correlation between the change in direction generated by a tumble and the cell's prior course; tumbles have precisely the same effect whether a cell swims in a gradient or not, they just occur with different frequencies. Thus, if life gets better, E. coli swims farther on the current leg of its track and enjoys it more. If life gets worse, it just relaxes back to its normal mode of behavior. E. coli is an optimist."*

The adjustment of the tumbling rate results in a bias towards the most favorable locations of high concentration of chemoattractant, which can be as varied as, for example, salts, glucose, amino acids, or oxygen. Chemotaxis is crucial in the wound healing process, as growth factors diffusing from the wound attract macrophages, which would otherwise move randomly according to an EPRW process [74].

Similar behaviors can be triggered by other kinds of external signal such as: temperature [75], light [76] or magnetic field [77] gradients.

**Infotaxis (moths)** A chemotactic search requires a well-defined gradient of chemoattractants and cannot be used if the concentration of cues is weak. This is, for example, the case of animals sensing odors in air or water: turbulent flows break up the chemical signal into random and disconnected patches of odors. The infotaxis search algorithm [78] is designed to work in this case of sparse and fluctuating cues. This algorithm is based on a maximization of the expected rate of information gain. It produces trajectories such as zigzagging paths which are similar to those observed in the flight of moths [79]. Infotaxis is also used to design olfactory robots [80].

### 1.2.3 Randomized search

Unexpectedly, random search processes are commonly encountered in the field of robotic called randomized motion planning.

A robot is a mechanical device equipped with sensors under the control of a computing system. It is designed to reach a specific goal, starting from a given starting position and moving an unknown environment. The starting point of robot motion planning is to parametrize the full mechanical configuration of the robot through a single point  $\mathbf{r}$  in an abstract configuration space  $\Omega \subset \mathbb{R}^d$ . A human arm, for example, can be described by the vector  $(r_1, r_2)$ , where  $r_1$  represents the angle between the forearm and the upper arm and  $r_2$  the angle between the hand and the forearm. Mind that the mechanical components cannot overlap: this leads to forbidden regions within the configuration space called obstacles.

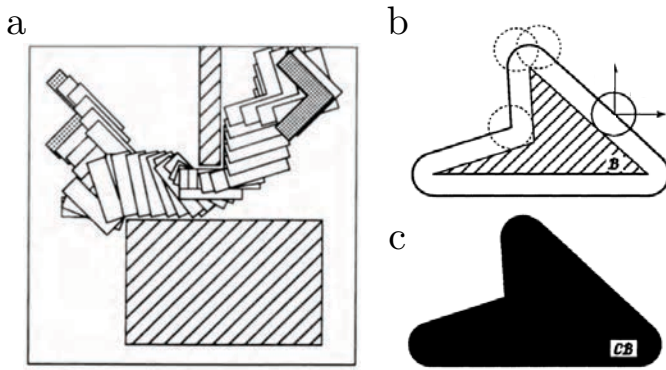


Figure 1.4: (a) A "piano mover problem" consists in moving a  $L$ -shaped object from the left room to the right room. (b) A disk robot (circle) in the presence of a polygon obstacle (hashed region). Dashed circles represent several contact positions. (c) The disk is represented by its center point, the filled-region  $CB$  is the representation of the obstacle in the configuration space [Figs. (a, b, c) excerpted from [81]].

► In the rest of this manuscript, I model the searcher as a single point in a configuration space  $\Omega \subset \mathbb{R}^d$ .

The problem of motion planning is to find a path in the accessible configuration space that brings the robot from its initial configuration point to a given target configuration. A practical example is the problem considered in Fig. 1.4a., which consists in moving a  $L$ -shaped object from the left room to a specific position within the right room.

Generally, the configuration space  $\Omega$  has a large dimension  $d \gg 1$ , so that it is too time consuming to compute the precise shape of the accessible space. A solution consists in moving the robot's representative point according to the Newtonian laws of dynamic in a potential field [82]. The potential field combines attraction to the target region and repulsion from the obstacles. However, the potential field may exhibit local minima that trap the robot away from the target. Adding a random force to the dynamic enables the exit from local minima of the potential [83]. This procedure is called randomized motion planning [84]: the computing system first generates several random trajectories before selecting the trajectory with the minimal target search time.

► The short-time behaviour of the distribution of exit time is particularly relevant for randomized motion planning algorithms. In Part. I, I compute the full distribution of exit time of a biased Brownian particle out of a 2D disk.

### 1.3 Framework, objectives, methods

In this thesis, I focus on random searchers to targets which do not emit cues, which corresponds to searchers with low memory skills. One of my objectives is to identify optimal search strategies. We consider active or passive particles modelling molecules or animals which cannot identify strategies by themselves. In this context, the term strategy refers to the choice of a set of parameters that minimizes the MFPT to the target.

To identify such optimal search strategies, I seek to obtain analytical expressions for first-passage observables, with a particular focus on the MFPT. These observables satisfy linear integro-differential equations (see the next Chap. 2). Challenges in obtaining analytical solutions for these linear equations arise from

- (i) the boundary conditions (Parts. I, II & Sec. 6, p. 125),
- (ii) the coupling between multiple search states (two diffusive states in Part. II, a continuous space of velocities in Part III),
- (iii) the shape of the potential and noise term (Sec. 7, p. 143).

To tackle these challenges, I have developed resolution schemes which are either

- (a) exact and explicit: in Parts I, we compute the exact moments of the exit time out of angular sectors.
- (b) exact but non-explicit: in Part I & II, the exact resolution schemes are formally defined as operators acting on the infinite-dimensional space of Fourier coefficients. In practice, only a finite number  $N$  of Fourier coefficients can be considered and the exact resolution scheme relies on a  $N \times N$  matrix inversion.
- (c) approximate and explicit: in Parts I & II, the approximate expression is obtained by considering that the matrices acting on the Fourier coefficients are diagonal (see Eq. (3.38) & Eq. (4.47)). In Part. III, the challenge (ii) is solved using a decoupling approximation. In Sec. 7, p. 143, Eq. (7.13), we adapt the Kramers approximation scheme to estimate the escape through a potential barrier: our result provides a theoretical explanation for the observed exponential coupling between the cell speed and persistence.

To verify the accuracy of my approximate resolution schemes, I took the initiative to use the *COMSOL Multiphysics* software. This finite element resolution software is shown to be more efficient than random walk sampling techniques (also called Monte-Carlo simulations, see App. A.4, p. 176). For example, the computation of the FPT density of the 3D surface-mediated exit problem takes a few minutes using COMSOL, while Monte-Carlo simulations for this process are lengthy and difficult to implement (see [85]). In Part. 3, our approximate expressions are shown to be in excellent agreement with simulations. In Chaps. 4 & 6, our approximate expressions accurately fit to simulations of the optimal search process.

Before proceeding further, let me conclude this introduction by a popular science overview of my thesis.

## Parenthesis: a popular science overview of my thesis

I presented the following text at the "My 180s Thesis" competition (in French). For the video, click [here](#). I focus on my work on the Pearson random walk (Part. III) and I explain the existence of an optimal turn rate  $\tau$ .

### LE LOUP ET L'AGNEAU, VERSION 2.0

« Un Agneau se désaltérait  
 Dans le courant d'une onde pure,  
 Un loup survient à jeun qui cherchait aventure,  
 Et que la faim en ces lieux attirait. »

Ainsi commence la fable de la Fontaine,  
 Le Loup et l'Agneau, dont l'issue est certaine,  
 Sans autre forme d'hypothèse,  
 Ainsi commence aussi ma thèse.

A quelle heure le Loup mangera-t-il l'Agneau ?  
 A midi ou à minuit ? La réponse dépend de  $\tau$ ,  
 le temps d'une course, dont je parlerai bientôt,

Notez aussi que le Loup ne voit pas l'Agneau,  
 à moins de le trouver sous son museau.

Par un cercle épais je modélise la rivière,  
 L'Agneau, immobile, y sirote un verre,  
 La rivière, le Loup ne peut pas la franchir  
 A sa rencontre il doit donc rebondir.

Le Loup cherche l'Agneau pour lui tenir discours.  
 Tout droit, dans une direction fixe, le Loup court,  
 Pendant un temps noté  $\tau$ . Au temps  $\tau$ , tout court,  
 Il s'arrête, et repart dans une direction aléatoire.  
 Jusqu'à trouver l'Agneau, il en va ainsi de suite.

Si les changements de directions sont rares,  
 Alors  $\tau$  est grand. Droite est la trajectoire  
 Du Loup, quand proche de l'Agneau il transite,  
 Dans sa course folle, il ne peut tourner  
 Si bien que l'Agneau lui file sous le nez  
 Alors aux yeux de l'Agneau le Loup est lent,

Si les changements de direction sont fréquents,  
 Alors  $\tau$  est petit. Le Loup piaffe, se remue,  
 surplace, il reste à la fin comme au début,  
 Alors aux yeux de l'Agneau le Loup est lent,

Dans ma thèse, je crie au Loup l'attitude,  
 qui lui garantit une plus grande promptitude,  
 « Changer de direction, cela n'est pas plus mal ! »  
 Car j'ai montré qu'il existe un  $\tau$  optimal,  
 Qui avance l'heure de la grillade,

Pour notre Loup trêve de jérémiades,  
 Car si ce  $\tau$  optimal il choisit,  
 Alors son repas est à midi,  
 Et non plus à minuit :  
 l'optimum est  
 ici !

Les loups sont-ils donc des théoriciens  
 dont les calculs sont égaux aux miens ?  
 La réponse est non, bien entendu,  
 La sélection naturelle agit à leur insu,  
 Et parmi les loups choisit les plus renards,  
 Qui mangent à midi, l'heure prévue,  
 Par un Physicien sorbonnard.

Il y a-t-il d'autres applications ? Mon modèle  
 Rencontre de l'intérêt à toutes les échelles,  
 Une cellule immunitaire, microscopique,  
 Est un loup en quête d'un microbe passif,  
 Un neutron, à l'échelle atomique,  
 Est un loup en quête d'un noyau radioactif.

La morale de ma fabuleuse thèse,  
 Est qu'il faut, dans une vie, de temps en temps.  
 Savoir changer de direction, mais point trop souvent.  
 Merci de m'avoir suivi le temps d'une parenthèse.





# Mathematical introduction: symmetric, biased and active walks

---

## Contents

---

<b>2.1 Probability distribution . . . . .</b>	<b>32</b>
2.1.1 Chapman-Kolmogorov equation . . . . .	32
2.1.2 Integro-differential equation on the propagator . . . . .	33
2.1.3 Boundary conditions . . . . .	34
2.1.3.1 Absorbing-Dirichlet condition . . . . .	34
2.1.3.2 Reflective-Neumann condition . . . . .	34
2.1.3.3 Semi-reflective condition . . . . .	34
<b>2.2 Survival probability . . . . .</b>	<b>36</b>
2.2.1 Mean-first passage time (MFPT) . . . . .	36
2.2.2 Laplace transform of the survival probability . . . . .	37
2.2.3 Boundary conditions . . . . .	37
<b>2.3 Some exact expressions of the search time . . . . .</b>	<b>39</b>
2.3.1 Symmetric Brownian motion in spherical geometries . . . . .	39
2.3.1.1 Probability density of FPT to a confining $(d - 1)$ -sphere . . . . .	39
2.3.1.2 MFPT to reach a centered $(d - 1)$ -sphere . . . . .	39
2.3.1.3 MFPT to a spherical cap over the $(d - 1)$ -sphere . . . . .	40
2.3.2 MFPT for an active process: the EPRW random walk in $d = 1$ . . . . .	40
<b>2.4 Perspectives: challenges on the boundary . . . . .</b>	<b>42</b>

---

Einstein's interpretation of Brownian motion is that of a pollen grain randomly hopping along the  $lZ$  line due to shocks with water molecules at regular time intervals (see p. 19). Steps are independent of the previous ones, hence the process is said to be *memoryless* or *Markovian*. The probability distribution of the pollen grain is given by Eq. (1.4). In the continuous limit defined in Eq. (1.5), the probability distribution is given by the differential equation (1.6). Mind that Eqs. (1.4) and (1.6) are deterministic equations: the random motion of the particle is taken into account by the diffusion coefficient.

In the present chapter, I define the notion of a Markovian process. Under certain conditions on the Markovian process, integro-differential equations are satisfied by the following path-averaged observables: (i) probability distribution, (ii) FPT density, (iii) MFPT. The resolution of these integro-differential equations in specific confining geometries  $\Omega \subset \mathbb{R}^d$  is the cornerstone of this thesis.

In Sec. 1.1.1, p. 17, I consider active random walks called Pearson walks, that are composed of straight runs interspersed by *instantaneous* reorientation events. Reorientations are discontinuous jumps in the velocity space. In Sec. 2.3, I give the mathematical definition of the jump rate for a continuous Markovian process.

In Sec. 2.3, I recall some known results on the FPT and MFPT in simple geometries, for both the symmetric Brownian processes (see Sec. (2.3.1)) and for a simple active process, the EPRW in  $d = 1$  (see Sec. 2.3.2). The results of Tables. 2.1, 2.2 and 2.3.1.3 are benchmarks for the rest of this thesis manuscript.

## 2.1 Probability distribution

### 2.1.1 Chapman-Kolmogorov equation

A stochastic process satisfies the Markov property if the conditional probability distribution at the times  $t_1 > \dots > t_n$  is fully characterized by the conditional probability distribution at the latest condition  $t_1$ :

$$p(\mathbf{r}, s | \mathbf{r}_1, t_1; \dots; \mathbf{r}_n, t_n) = p(\mathbf{r}, s | \mathbf{r}_1, t_1). \quad (2.1)$$

A stochastic process that satisfies the Markov property is also referred to as memoryless.

Note that a stochastic process which (i) depends only on the time variable and (ii) is time invariant satisfies the Markov property if and only if it is exponentially distributed, i.e. there are  $A > 0$  and  $\lambda > 0$  such that  $p(t|t') = A \exp(-\lambda|t - t'|)$ .

Important examples of **Markovian** processes are:

- the position  $\mathbf{r}(t)$  of a Brownian particle,
- the joint process  $\mathbf{x}(t) = (\mathbf{r}(t), \mathbf{v}(t))$  for an EPRW (defined p. 18).

Important examples of **non-Markovian** continuous processes are:

- the process  $\mathbf{r}(t)$  for an EPRW. One needs to know both the velocity  $\mathbf{v}(t)$  and the position  $\mathbf{r}(t)$  of the searcher at the time  $t$  to deduce the position  $\mathbf{r}(t + dt)$  at the time  $t + dt$ .
- the joint process  $\mathbf{x}(t) = (\mathbf{r}(t), \mathbf{v}(t))$ , with continuous time  $t \in \mathbb{R}^+$ , for any PRW which is not a EPRW. One needs to know the time  $t_r$  of the previous reorientation event to deduce  $\mathbf{x}(t + dt)$  from  $\mathbf{x}(t)$ . The joint process  $\mathbf{x}(t) = (\mathbf{r}(t), \mathbf{v}(t), t_r(t))$  is Markovian – however a diffusion equation cannot be found for this process as it does not satisfy the required uniform convergence properties (see Sec. 2.1.2, p. 33 and Ref. [18]).

Hence position processes for active random walks fall (generally) in the class of **non-Markovian** continuous processes.

Consider a stochastic process that satisfies the Markov property. For  $t' < s < t$ , its conditional probability  $p(\mathbf{r}, t | \mathbf{r}', t')$  can be expressed as [18]

$$p(\mathbf{x}, t | \mathbf{x}', t') = \int_{\Omega} d\mathbf{y} p(\mathbf{x}, t | \mathbf{y}, s) p(\mathbf{y}, s | \mathbf{x}', t'). \quad (2.2)$$

The latter integral equation Eq. (2.2) is called the Chapman-Kolmogorov equation. Equation (2.2) is our starting point in the derivation of the semi-reflective boundary condition on the MFPT of a surface-mediated process (see Sec. B.1, p. 177).

In the next section, I remind the reader about the conditions on the Markov process which lead to integro-differential equations on the conditional probabilities, the FPT density, and the MFPT.

### 2.1.2 Integro–differential equation on the propagator

The solution of the Chapman-Kolmogorov equation can be written as the solution of the two equivalent integro–differential Eqs. (2.4) and (2.5) under three hypothesis of uniform convergence on the conditional probability [18, 86]. The uniform convergence of the quantity

$$\forall(\mathbf{x}, \mathbf{y}) \in \Omega^2, \quad \lim_{\Delta t \rightarrow 0} \frac{1}{\Delta t} p(\mathbf{x}, t + \Delta t | \mathbf{y}, t) \equiv W(\mathbf{x} | \mathbf{y}, t), \quad (2.3)$$

defines the jump rate  $W(\mathbf{x} | \mathbf{y}, t)$ . The two other uniform convergence conditions define the drift coefficient  $V$  and the diffusion matrix  $D$  (see [18]).

► The notion of jump process is encountered: (i) in Part. II, when a diffusive particle adsorbed on the surface is ejected into the bulk, and (ii) in Part. III, as reorientation events for a PRW are jumps in the velocity space (see Sec. 2.3.2, p. 41, for a detailed example).

The first differential equation is called a forward equation and reads, for all  $s > t'$ ,

$$\begin{aligned} \frac{\partial p(\mathbf{y}, s | \mathbf{x}', t')}{\partial s} = & - \sum_{i \in [1, d]} \frac{\partial}{\partial y_i} [V_i(\mathbf{y}, s) p(\mathbf{y}, s | \mathbf{x}', t')] + \frac{1}{2} \sum_{(i, j) \in [1, d]^2} \frac{\partial^2}{\partial y_i \partial y_j} [D_{i, j}(\mathbf{y}, s) p(\mathbf{y}, s | \mathbf{x}', t')] \\ & + \int_{\Omega} d\tilde{\mathbf{x}} \{W(\mathbf{y} | \tilde{\mathbf{x}}, s) p(\tilde{\mathbf{x}}, t | \mathbf{x}', t') - W(\tilde{\mathbf{x}} | \mathbf{y}, s) p(\mathbf{y}, s | \mathbf{x}', t')\}, \end{aligned} \quad (2.4)$$

where  $(y_i)_{i \in [1, d]}$  are the cartesian coordinates of  $\mathbf{y}$ . In the absence of jump terms  $W$ , the Eq. (2.4) is called a Fokker-Planck equation.

The second differential equation is called a backward equation and reads, for all  $t > s$

$$\begin{aligned} \frac{\partial p(\mathbf{x}, t | \mathbf{y}, s)}{\partial s} = & - \sum_{i \in [1, d]} V_i(\mathbf{y}, s) \frac{\partial}{\partial y_i} [p(\mathbf{x}, t | \mathbf{y}, s)] - \frac{1}{2} \sum_{(i, j) \in [1, d]^2} D_{i, j}(\mathbf{y}, s) \frac{\partial^2}{\partial y_i \partial y_j} [p(\mathbf{x}, t | \mathbf{y}, s)] \\ & + \int_{\Omega} d\tilde{\mathbf{x}} W(\tilde{\mathbf{x}} | \mathbf{y}, s) \{p(\mathbf{x}, t | \mathbf{y}, s) - p(\mathbf{x}, t | \tilde{\mathbf{x}}, s)\}. \end{aligned} \quad (2.5)$$

Mind that in the backward equation, the derivatives operator acts on the past variables  $(\mathbf{y}, t')$  and that the drift and diffusion coefficients are not differentiated.

The initial condition for both Eqs. (2.4) and (2.5) is given by a Dirac distribution

$$p(\mathbf{x}, t | \mathbf{y}, t) = \delta(\mathbf{x} - \mathbf{y}). \quad (2.6)$$

The spatial boundary conditions at the frontier of the confining domain  $\partial\Omega$  are specified in Sec. 2.1.3, p. 34. Solutions of the forward and backward Eqs. (2.4) and (2.5) satisfy the Chapman-Kolmogorov integral equations Eq. (2.2) provided that these solutions satisfy the appropriate spatial boundary conditions at  $\partial\Omega$  and the initial condition Eq. (2.6) (see [18]).

In the rest of this thesis, I consider time–invariant systems:  $p(\mathbf{x}, t | \mathbf{y}, s) = p(\mathbf{x}, t - s | \mathbf{y}, 0)$ . The latter identity leads to

$$\forall t > s, \quad \frac{\partial p(\mathbf{x}, t | \mathbf{y}, s)}{\partial s} = \frac{\partial p(\mathbf{x}, t - s | \mathbf{y}, 0)}{\partial s} = - \frac{\partial p(\mathbf{x}, s | \mathbf{y}, 0)}{\partial s}. \quad (2.7)$$

► For an unbiased Brownian process, the diffusion matrix is constant and isotropic (i.e.  $D_{ij}(\mathbf{y}, 0) = D\delta_{ij} > 0$ ) and  $V$  and  $W$  are both equal to zero, hence Eq. (2.5) takes the form of a heat equation:

$$\forall t > s, \quad \frac{\partial p(\mathbf{x}, s | \mathbf{y}, 0)}{\partial s} = D \Delta_{\mathbf{y}} p(\mathbf{x}, s | \mathbf{y}, 0), \quad (2.8)$$

where  $\Delta_{\mathbf{y}}$  is the Laplacian operator acting on the  $\mathbf{y}$  coordinate.

### 2.1.3 Boundary conditions

In the previous section, the probability distribution was shown to satisfy integro–differential equations. The unique solution of these equations is determined through the boundary conditions (see the textbook [87]).

In this section I specify the three classes of boundary conditions encountered in this thesis: the absorbing, reflective and semi–reflective boundary conditions. Mind that if the target is located on the boundary of the confining domain (i.e.  $\Gamma \subset \partial\Omega$ ), the target is also said to be an *exit*. The exit geometry is illustrated in Fig. 2.1.3.

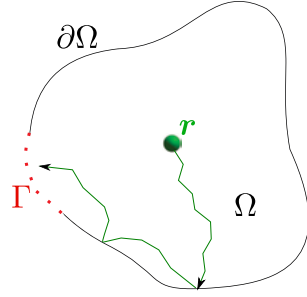


Figure 2.1: Scheme of a Brownian motion in a confined domain  $\Omega$ , with initial position at  $\mathbf{r}$ . The region  $\Gamma$  is absorbing, while the rest of the frontier  $\partial\Omega \setminus \Gamma$  is reflective.

#### 2.1.3.1 Absorbing–Dirichlet condition

I recall that I only consider time–invariant systems, as previously mentioned p. 33. The absorbing boundary condition is specific to the target region, denoted  $\Gamma$ , and reads:

$$p(\mathbf{r}_a, t | \mathbf{r}) = 0, \quad (2.9)$$

and this boundary condition completes both

- (f) the forward differential Eq. (2.4), if  $\mathbf{r}_a \in \Gamma$  and  $\mathbf{r} \in \Omega$ . The particle is removed as soon as it hits the target and there cannot be any particle at the surface of the target.
- (b) the backward differential Eq. (2.5), if  $\mathbf{r} \in \Gamma$  and  $\mathbf{r}_a \in \Omega$ . Once a particle has hit the surface of the target, it cannot return into the bulk.

#### 2.1.3.2 Reflective–Neumann condition

The forward reflective boundary condition is defined by the equation

$$\partial_n p(\mathbf{r}_a, t | \mathbf{r}) = 0, \quad (2.10)$$

where  $\partial_n$  stands for the normal derivative acting on the coordinate  $\mathbf{r}_a$  at  $\mathbf{r}_a \in \partial\Omega \setminus \Gamma$ . Equation (2.10) completes the forward Eq. (2.4).

I define the backward reflective boundary condition by the same expression Eq. (2.10), the difference being that  $\partial_n$  now acts on the past variable  $\mathbf{r}$ . Provided that  $\partial_n$  acts on  $\mathbf{r}$ , Eq. (2.10) completes the backward Eq. (2.4). For stochastic processes with no jump terms, the forward and backward reflective boundary conditions are equivalent. However, the equivalence does not hold in general (see [18] and App. B, p. 177).

#### 2.1.3.3 Semi-reflective condition

The semi-reflective boundary condition is also referred to as the Fourier, Robin, radiative, or partially adsorbing condition. It can be regarded as being intermediate between the adsorbing and the reflecting conditions. In terms of a random walker over a discrete lattice, a partially

adsorbing site is such that there is a probability for adsorption  $q$  and a probability for reflection  $1 - q$  (see Pub. 4). In terms of a random walker in a continuous space, the semi-reflective boundary condition reads:

$$\partial_n p(\mathbf{r}_a, t | \mathbf{r}) = k p(\mathbf{r}_a, t | \mathbf{r}), \quad (2.11)$$

where

- (i)  $\partial_n$  stands for the normal derivative, acting either on the coordinate  $\mathbf{r}_a$  (boundary condition for the forward equation Eq. (2.4)) or on the coordinate  $\mathbf{r}$  (boundary condition for the backward equation Eq. (2.5)),
- (ii)  $k$  is called the adsorption coefficient. The case  $k = 0$  leads to the reflective boundary condition Eq. (2.10); while  $k = \infty$  leads to the adsorbing boundary condition Eq. (2.9).

The reflective boundary condition is related to the mathematical notion of *local time* spent by the random process along the boundary (see [88, 89, 90]).

► Semi-reflective boundary conditions are shown to play a crucial role in the statistics of readsorption on the surface in Part. II. The major difference between Chap. 4 and Chap. 5 lies in the value of the adsorption coefficient  $k_t$  on the surface of the target:

- in Chap. 4,  $k_t = k$ , the target adsorption coefficient is equal to the adsorption coefficient on the rest of the confining domain. The adsorption property is homogeneous within  $\partial\Omega$
- in Chap. 5,  $k_t = \infty$ , which means that the target is perfectly adsorbing.

As soon as the desorption rate is large enough, this difference on the adsorption coefficient  $k_t$  leads to a drastic difference in the value of the search time.

## 2.2 Survival probability

In this section, I consider that the accessible domain  $\Omega$  of the walk contains an absorbing region  $\Gamma$ , which is called the target.

The survival probability quantifies the proportion of searchers which have not encountered the target at the time  $t$ . I explain why Eq. (2.5) on the probability distribution leads to integro-differential equations on the survival probability.

The time needed for the searcher initially at  $\mathbf{r}$  to reach the target for the first time is a random variable, which is denoted  $\sigma_{\mathbf{r}}$ . The survival probability up to time  $t$ , denoted by  $\tilde{S}^{(t)}(\mathbf{r})$ , is the probability that the exit time  $\sigma_{\mathbf{r}}$  is larger than  $t$ :  $\tilde{S}^{(t)}(\mathbf{r}) \equiv \mathbb{P}\{\sigma_{\mathbf{r}} \geq t\}$ . Since the arrival position on the target does not matter for the survival probability,  $\tilde{S}^{(t)}(\mathbf{r})$  is simply obtained by integrating the diffusive propagator over the arrival positions  $\mathbf{r}_a$ :

$$\tilde{S}^{(t)}(\mathbf{r}) = \int_{\Omega} d\mathbf{r}_a p(\mathbf{r}_a, t | \mathbf{r}, 0). \quad (2.12)$$

The quantity  $1 - \tilde{S}^{(t)}(\mathbf{r})$  is the repartition function of a probability measure  $\tilde{\rho}^{(t)}(r, \theta)$ , called the first passage time (FPT) probability density, which satisfies the relation:

$$\tilde{\rho}^{(t)}(\mathbf{r}) = -\frac{\partial \tilde{S}^{(t)}(\mathbf{r})}{\partial t}. \quad (2.13)$$

### 2.2.1 Mean-first passage time (MFPT)

The MFPT, denoted  $\mathbb{E}[\sigma_{\mathbf{r}}]$ , is the averaged survival time weighted by the density  $\tilde{\rho}^{(t)}(\mathbf{r})$ :

$$\mathbb{E}[\sigma_{\mathbf{r}}] \equiv \int_0^{\infty} dt t \tilde{\rho}^{(t)}(\mathbf{r}). \quad (2.14)$$

► For convenience, I use the shorthand notation  $t(\mathbf{r}) \equiv \mathbb{E}[\sigma_{\mathbf{r}}]$ .

Using the relation of Eq. (2.13) and after an integration by parts, one obtains

$$t(\mathbf{r}) = \int_0^{\infty} dt \tilde{S}^{(t)}(\mathbf{r}). \quad (2.15)$$

The definition of Eq. (2.12) implies that

$$t(\mathbf{r}) = \int_0^{\infty} dt \int_{\Omega} d\mathbf{r}_a p(\mathbf{r}_a, t | \mathbf{r}, 0). \quad (2.16)$$

I integrate according to Eq. (2.16) the backward equation (2.5) to obtain the following equation:

$$\sum_{i \in [1, d]} V_i(\mathbf{r}, 0) \frac{\partial t(\mathbf{r})}{\partial r_i} + \frac{1}{2} \sum_{(i, j) \in [1, d]^2} D_{i, j}(\mathbf{r}, 0) \frac{\partial^2 t(\mathbf{y})}{\partial r_i \partial r_j} - \int_{\Omega} d\tilde{\mathbf{x}} W(\tilde{\mathbf{x}} | \mathbf{r}, 0) \{t(\mathbf{r}) - t(\tilde{\mathbf{x}})\} = -1, \quad (2.17)$$

where  $\mathbf{r} = (r_i)$  in cartesian coordinates. For a Brownian process, Eq. (2.17) takes the form of a Poisson equation:

$$D \Delta t(\mathbf{r}) = -1. \quad (2.18)$$

► In Parts II and III we extensively study Eq. (2.17) on the MFPT.

I define the global MFPT (GMFPT), denoted  $\overline{\mathbb{E}[\sigma]}$ , as the MFPT averaged over all starting positions  $\mathbf{r} \in \Omega$ :

$$\overline{\mathbb{E}[\sigma]} \equiv \frac{1}{|\Omega|} \int_{\Omega} d\mathbf{r} \mathbb{E}[\sigma_{\mathbf{r}}], \quad (2.19)$$

where  $d\mathbf{r}$  is the uniform measure over  $\Omega$ .

► The optimizability of the GMFPT is a central question in my thesis.

In the next paragraph, I derive a differential equation on the Laplace transform of the survival probability.

## 2.2.2 Laplace transform of the survival probability

The Laplace transform of the survival probability  $\tilde{S}^{(t)}(r, \theta)$  is defined for all  $p \geq 0$  as

$$S^{(p)}(\mathbf{r}) \equiv \int_0^\infty dt \exp(-pt) \tilde{S}^{(t)}(\mathbf{r}), \quad (2.20)$$

$$= \int_0^\infty dt \exp(-pt) \int_\Omega d\mathbf{r}_a p(\mathbf{r}_a, t | \mathbf{r}, 0). \quad (2.21)$$

Note that one recovers the MFPT by setting  $p = 0$  in Eq. (2.21):  $\mathbb{E}[\sigma_{\mathbf{r}}] = S^{(0)}(\mathbf{r})$ . Due to Eq. (2.13), the Laplace transform of the FPT density  $\tilde{\rho}^{(t)}(r, \theta)$  can be deduced from  $S^{(p)}(\mathbf{r})$  through the relation:

$$\rho^{(p)}(r, \theta) = 1 - p S^{(p)}(r, \theta). \quad (2.22)$$

I integrate the backward equation (2.5) according to Eq. (2.21) to obtain the equation

$$\sum_{i \in \llbracket 1, d \rrbracket} V_i(\mathbf{y}, 0) \frac{\partial S^{(p)}(\mathbf{y})}{\partial y_i} + \frac{1}{2} \sum_{(i,j) \in \llbracket 1, d \rrbracket^2} D_{i,j}(\mathbf{y}, 0) \frac{\partial^2 S^{(p)}(\mathbf{y})}{\partial y_i \partial y_j} - \int_\Omega d\tilde{\mathbf{x}} W(\tilde{\mathbf{x}} | \mathbf{y}, 0) \left\{ S^{(p)}(\mathbf{y}) - S^{(p)}(\tilde{\mathbf{x}}) \right\} = p S^{(p)}(\mathbf{y}) - 1. \quad (2.23)$$

For a Brownian process, Eq. (2.23) takes the form of a Helmholtz equation:

$$D \Delta S^{(p)}(\mathbf{y}) = p S^{(p)}(\mathbf{y}) - 1. \quad (2.24)$$

Why care about  $S^{(p)}(\mathbf{r})$ ? The series expansion of  $\exp(-pt)$  in Eq. (2.20) yields

$$S^{(p)}(\mathbf{r}) = \sum_{n=1}^{\infty} \frac{(-p)^{n-1}}{n!} \mathbb{E}[\sigma_{\mathbf{r}}^n], \quad (2.25)$$

hence  $S^{(p)}(\mathbf{r})$  is a generating function of the moments [91]. The  $n$ -th moment of the exit time reads

$$\mathbb{E}[\sigma_{\mathbf{r}}^n] = (-1)^{n-1} n! \left( \frac{\partial^{n-1} S^{(p)}(\mathbf{r})}{\partial p^{n-1}} \right)_{p=0}, \quad n \geq 1. \quad (2.26)$$

The variance of the exit time is defined as:

$$\text{Var}[\sigma_{\mathbf{r}}] = \mathbb{E}[\sigma_{\mathbf{r}}^2] - \mathbb{E}[\sigma_{\mathbf{r}}]^2. \quad (2.27)$$

► In Part I, I consider the exit problem of a Brownian particle out of an aperture in the boundary of a disk. I solve Eq. (2.24), the Helmholtz equation on the Laplace transform of the survival probability, and I obtain the moments of the exit time through Eq. (2.26).

## 2.2.3 Boundary conditions

In this section, I show that the boundary conditions on the backward probability distribution apply to both the survival probability and the MFPT. I consider the geometry represented in Fig. 2.1.3.

At the absorbing target  $\Gamma$ , integration of Eq. (2.9) according to Eqs. (2.21) and (2.16) leads to the absorbing boundary conditions on the survival probability and on the MFPT:

$$\forall \mathbf{r} \in \Gamma, \quad S^{(p)}(\mathbf{r}) = 0, \quad \text{and} \quad t(\mathbf{r}) = 0, \quad (2.28)$$

with a straightforward interpretation in terms of the search time of the target.



At the reflective boundary  $\partial\Omega \setminus \Gamma$ , integration of Eq. (2.9) according to Eqs. (2.21) and to (2.16) leads to the reflective boundary conditions on the survival probability and on the MFPT:

$$\forall \mathbf{r} \in \partial\Omega \setminus \Gamma, \quad \partial_n S^{(p)}(\mathbf{r}) = 0, \quad \text{and} \quad \partial_n t(\mathbf{r}) = 0. \quad (2.29)$$

I now consider a subset  $\Gamma_k \subset \Omega$  that is semi-reflective, according to the definition Eq. (2.11). After integration over the variables  $\mathbf{r}_a$  and  $t$  according to Eq. (2.16), I obtain the following boundary condition for the MFPT:

$$\forall \mathbf{r} \in \Gamma_k, \quad \partial_n t(\mathbf{r}) = k t(\mathbf{r}). \quad (2.30)$$

► In App. B, p. 177, I generalize Eq. (2.30) to the surface-mediated processes considered in Part. II.

In the next section, I present exact solutions on the exit time statistics for simple processes in spherical geometries.

## 2.3 Some exact expressions of the search time

In this section, I recall some known results about the FPT probability and MFPT in simple geometries, for both Brownian processes (Sec. (2.3.1)) and for a simple jump process (see Sec. (2.3.2)). The results of Table 2.1, 2.2, 2.3.1.3, serve as benchmark for the rest of this thesis manuscript.

We defined the  $(d-1)$ -sphere in the introduction, Eq. (1.3), p. 18. In  $\mathbb{R}^2$  and in cylindrical coordinates  $\mathbf{r} = (r, \theta)$ . In  $\mathbb{R}^3$  and in spherical coordinates  $\mathbf{r} = (r, \theta, \varphi)$  where  $\theta$  is the zenith angle measured from the  $z$ -axis (see Table 2.3.1.3, p. 41).

► The Laplace operator on a function  $f$  of the two spherical coordinates  $(r, \theta)$  of  $\mathbb{R}^d$  is decomposed into two operators:

$$\Delta f = \Delta_r f + \frac{\Delta_\theta f}{r^2}. \quad (2.31)$$

The radial Laplacian  $\Delta_r$  and the Laplace-Beltrami operator  $\Delta_\theta$  read:

$$\Delta_r f = \frac{\partial^2 f}{\partial r^2} + \frac{d-1}{r} \frac{\partial f}{\partial r}, \quad \Delta_\theta f = \frac{1}{\sin^{d-2} \theta} \frac{\partial}{\partial \theta} \left( \sin^{d-2} \theta \frac{\partial f}{\partial \theta} \right). \quad (2.32)$$

### 2.3.1 Symmetric Brownian motion in spherical geometries

For an unbiased Brownian process, the diffusion matrix is constant and isotropic (i.e.  $D_{ij}(\mathbf{y}, 0) = D\delta_{ij} > 0$ ) and  $V$  and  $W$  are zero. The MFPT is the solution of the Poisson Eq. (2.18) and the Laplace transform of the survival probability is the solution of a Helmholtz Eq. (2.24).

#### 2.3.1.1 Probability density of FPT to a confining $(d-1)$ -sphere

A Brownian particle is released at  $t = 0$  within the volume enclosed in a  $(d-1)$ -sphere  $S_R$ . When will the particle cross the sphere  $S_R$  for the first time?

The confining geometry is rotational invariant and the search time only depends on the norm  $|r| = r$ . The general solutions of Eq. (2.17) depend on the dimension  $d$  and read

$$t(r) = \frac{1}{D} \hat{f}(r) + a_0, \quad \text{where} \quad \hat{f}(r) = -\frac{r^2}{2d}. \quad (2.33)$$

where the constant  $a_0$  is to be determined through the boundary condition  $t(R) = 0$  and  $[\partial_r t(r)]_{r=0} = 0$ . The solutions of Eqs. (2.24) with boundary conditions  $S^{(p)}(R) = 0$  and  $[\partial_r S^{(p)}(r)]_{r=0} = 0$  are summarized in Table 2.1, p. 40.

#### 2.3.1.2 MFPT to reach a centered $(d-1)$ -sphere

A Brownian particle is released at  $t = 0$  within the volume enclosed between  $S_R$  and  $S_{R_c}$ , the  $(d-1)$ -spheres of radii  $R$  and  $R_c$ . What is the MFPT to reach the sphere  $S_R$ ?

Rotation invariant solutions of Eq. (2.18) are

$$t(r) = \frac{1}{D} \hat{f}(r) + b_0 g\left(\frac{r}{a}\right) + a_0, \quad (2.34)$$

where  $\hat{f}(r) = -\frac{r^2}{2d}$  and

- (i) the function  $g(r)$ , which satisfies  $g(1) = 0$ , depends on the space dimension  $d$  and is given in Table 2.2.
- (ii) the constants  $b_0$  and  $a_0$  are to be determined by boundary conditions on  $S^{(p)}(R) = 0$  and  $[\partial_r S^{(p)}(r)]_{r=R_c} = 0$ .

The expressions of the MFPT in  $d = 2$  and  $d = 3$  are summarized in Table 2.2.

	$d = 1$	$d = 2$	$d = 3$
$S^{(p)}(r)$	$\frac{1}{p} \left\{ 1 - \frac{\cosh(\sqrt{p}r)}{\cosh(\sqrt{p}R)} \right\}$	$\frac{1}{p} \left\{ 1 - \frac{I_0(\sqrt{p}r)}{I_0(\sqrt{p}R)} \right\}$	$\frac{1}{p} \left\{ 1 - \frac{R \sinh(\sqrt{p}r)}{r \sinh(\sqrt{p}R)} \right\}$
$\mathbb{E}[\sigma(r)] \equiv t(r)$	$\frac{1}{D} \frac{R^2 - r^2}{2}$	$\frac{1}{D} \frac{R^2 - r^2}{4}$	$\frac{1}{D} \frac{R^2 - r^2}{6}$
$\overline{\mathbb{E}[\sigma]} \equiv \overline{t(r)}$	$\frac{R^2}{3D}$	$\frac{R^2}{8D}$	$\frac{R^2}{15D}$
$\text{Var}[\sigma(r)]$	$\frac{1}{D} \frac{R^4 - r^4}{6}$	$\frac{1}{D} \frac{R^2 - r^2}{32}$	$\frac{1}{D} \frac{R^2 - r^2}{90}$

Table 2.1: Statistics on the first-passage time to a  $(d - 1)$ -sphere of radius  $R$  for a Brownian particle initially at the radius  $r \in [0, R]$ : (i)  $S^{(p)}(r)$  is defined in Eq. (2.20), (ii)  $t(r)$  is the MFPT defined in Eq. (2.14) and (iii)  $\text{Var}[\sigma_r]$  is the variance defined in Eq. (2.27). The width of the angular sector  $\phi$  does not affect the kinetic of exit.

### 2.3.1.3 MFPT to a spherical cap over the $(d - 1)$ -sphere

A Brownian particle is released at  $t = 0$  on the surface of  $S_1$ , the  $(d - 1)$ -sphere of radius 1. The region  $\theta = \varepsilon$  is absorbing while the region  $\theta = \phi$  is reflective. What is the MFPT to the absorbing line, denoted  $\mathbb{E}[\sigma_\theta] \equiv g_\varepsilon(\theta)$ ?

The answer is given by the solution of Eq. (2.24) – in which the diffusion operator  $\Delta$  amounts to the sole Laplace-Beltrami operator  $\Delta_\theta$  – completed by boundary condition  $\mathbb{E}[\sigma_\theta] = 0$  and  $[\partial_\theta \mathbb{E}[\sigma_\theta](\theta)]_{\theta=\phi} = 0$ . The expressions of the MFPT in  $d = 2$  and  $d = 3$  are summarized in Table 2.3.1.3, p. 41.

► The expressions of  $g_\varepsilon(\theta)$  given in Table 2.3.1.3 correspond to the limit of zero desorption rate  $\lambda = 0$  for the general surface-mediated process studied in Part. II.

### 2.3.2 MFPT for an active process: the EPRW random walk in $d = 1$

In this section, I consider a jump process in a simple geometry: the particle is released at the position  $\mathbf{r}$  along a  $d = 1$  segment  $[R, R_c]$ . The particle performs an EPRW (see definition p. 18), i.e. ballistic runs with reorientation events at exponentially distributed random time with mean  $\tau$ . I define the angle  $\theta = \widehat{(\mathbf{r}, \mathbf{v})}$ . If the initial velocity of the searcher  $\mathbf{v} = v > 0$  (resp.  $\mathbf{v} = -v < 0$ ), the initial angle is  $\theta = 0$  (resp.  $\theta = \pi$ ). The configuration space is  $\Omega = ([R, R_c]; \theta)$  (see Table 2.4, p. 43).

Reorientation events correspond to the jump term in configuration space  $\Omega$

$$W((r_a, \theta_a) | (r, \theta)) = \frac{1}{\tau} \delta(r_a - r) \delta(|\theta_a - \theta| - \pi). \quad (2.35)$$

where  $\tau$  is the mean run time, and the condition  $\delta(|\theta_a - \theta| - \pi)$  imposes a turn in the direction

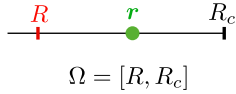
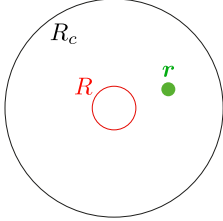
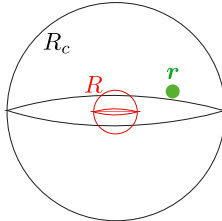
	$d = 1$	$d = 2$	$d = 3$
	 $\Omega = [R, R_c]$		
$g(r/a)$	$\frac{r}{a} - 1$	$\ln\left(\frac{r}{a}\right)$	$\frac{1}{r} - \frac{1}{a}$
$t(r)$	$\frac{(r-R)(2R_c-r-R)}{2D}$	$\frac{R^2-r^2+2R_c^2\ln\left(\frac{r}{R}\right)}{4D}$	$\frac{-r^3R+r(R^3+2R_c^3)-2RR_c^3}{6rRD}$
$\overline{t(r)}$	$\frac{1}{3D}(R-R_c)^2$	$\frac{R^4-4R^2R_c^2+4R_c^4\ln\left(\frac{R}{R_c}\right)+3R_c^4}{8D(R^2-R_c^2)}$	$\frac{(R-R_c)^2(R^3+3R^2R_c+6RR_c^2+5R_c^3)}{15DR(R^2+RR_c+R_c^2)}$

Table 2.2: Mean first passage time  $\mathbb{E}[\sigma_r]$  to reach the  $(d-1)$ -sphere at  $r = R$  for a Brownian particle initially at the radius  $r$  and confined by a reflective boundary at  $r = R_c$ .

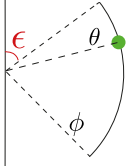
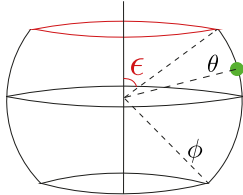
	$d = 1$	$d = 2$
		
$\Delta_\theta f$	$\frac{\partial^2 f}{\partial \theta^2}$	$\frac{1}{\sin \theta} \frac{\partial}{\partial \theta} \left( \sin \theta \frac{\partial f}{\partial \theta} \right)$
$\mathbb{E}[\sigma_\theta] \equiv g_\varepsilon(\theta)$	$\frac{(\theta-\varepsilon)(2\phi-\varepsilon-\theta)}{2D}$	$\frac{1-\cos \phi}{2D} \ln\left(\frac{1-\cos \theta}{1-\cos \varepsilon}\right) + \frac{1+\cos \phi}{2D} \ln\left(\frac{1+\cos \theta}{1+\cos \varepsilon}\right)$
$\overline{\mathbb{E}[\sigma]} \equiv \langle g_\varepsilon   1 \rangle_\varepsilon$	$\frac{(\phi-\varepsilon)^3}{3D\phi}$	$\frac{(1-\cos \phi)^2}{2D} \ln\left(\frac{\sin \phi}{\sin \varepsilon}\right) + \frac{1+\cos(\phi)^2}{2D} \ln\left(\frac{1+\cos \varepsilon}{1+\cos \phi}\right) + \frac{\cos \phi - \cos \varepsilon}{2D_s}$

Table 2.3: Mean first passage time  $\mathbb{E}[\sigma_\theta]$  to a  $(d-1)$ -spherical cap (red color) for a Brownian particle (green dot) diffusing over a portion of a  $(d-1)$ -sphere, where  $\theta$  is the zenith angle:  $\theta \in [\varepsilon, \phi]$ .

of the velocity. The Eq. (2.17) on the MFPT reads in this specific case:

$$v \frac{\partial t(r, 0)}{\partial r} + \frac{1}{\tau} \{t(r, \pi) - t(r, 0)\} = -1, \quad (2.36)$$

$$-v \frac{\partial t(r, \pi)}{\partial r} + \frac{1}{\tau} \{t(r, 0) - t(r, \pi)\} = -1. \quad (2.37)$$

The MFPT satisfies the absorbing boundary condition  $t(R, \theta = \pi) = 0$  and the reflective boundary condition  $[\partial_r t(r, \pi)]_{r=R_c} = [\partial_r t(r, 0)]_{r=R_c} = 0$ .

I propose a resolution method closely related to the method used in Part. III. I introduce

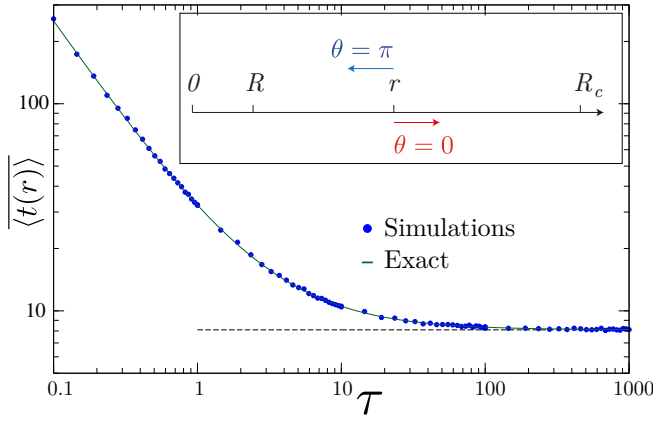


Figure 2.2: EPRW in a 1D geometry. (inset) Scheme of the geometry:  $R = 1$ ,  $R_c = 10$  and  $v = 1$ . (graph) The mean search time averaged over the starting directions and positions (i.e. GMFPT  $\langle t(r) \rangle$  defined in Eq. (2.42)) as a function of the reorientation rate  $\tau$ : (solid line) exact result, (blue dots) Monte-Carlo sampling over  $10^4$  random walks. Notice that the minimum of  $\bar{\Sigma}$  is for a purely ballistic walk ( $\tau \rightarrow \infty$ , dashed line).

two auxiliary functions

$$\langle t(r) \rangle = \frac{1}{2} \{t(r, 0) + t(r, \pi)\} \quad \text{and} \quad Z(r) = \frac{1}{2} \{t(r, 0) - t(r, \pi)\} \quad (2.38)$$

The quantity  $\langle t(r) \rangle$  is the MFPT averaged over the initial velocity  $\theta \in \{0, \pi\}$ . Eqs (2.36) and (2.37) lead to

$$D \frac{\partial^2 \langle t(r) \rangle}{\partial r^2} = -1 \quad \text{and} \quad v \frac{\partial \langle t(r) \rangle}{\partial r} - \frac{2}{\tau} Z(r) = 0, \quad (2.39)$$

where  $D = v^2 \tau / 2$  is an effective diffusion constant. The solution of the diffusion equation on the left hand side of Eq. (2.39) is

$$\langle t(r) \rangle = -\frac{r^2 - R^2}{2D} + b_0 r + a_0. \quad (2.40)$$

The two boundary conditions  $\langle t(R) \rangle = 0$  and  $[\partial_r \langle t(r) \rangle]_{r=0} = 0$  lead to a system of two equations on the two unknown constants  $b_0$  and  $a_0$ . The MFPT averaged over the initial direction of the velocity is finally:

$$\langle t(r) \rangle = -\frac{1}{2D} (r^2 - R^2) + \frac{R_c}{D} (r - R) + \frac{1}{v} (R_c - R). \quad (2.41)$$

In Fig. 2.2, I plot the GMFPT, defined as:

$$\overline{\langle t(r) \rangle} = \frac{1}{|R_c - R|} \int_{\min(R, R_c)}^{\max(R, R_c)} dr \langle t(r) \rangle = \frac{(R - R_c)^2 (3D - (R - R_c)v)}{3R_c D v}. \quad (2.42)$$

Note that the GMFPT is not an optimizable function of  $\tau$  in this  $d = 1$  geometry.

► This  $d = 1$  model of persistent Pearson searcher exemplifies the resolution scheme developed in Part. III.

## 2.4 Perspectives: challenges on the boundary

In the present Chap. 2, p. 31, I define the notion of Markovian processes and I present the general set of integro-differential equations satisfied by first passage observables. In Table 2.4, I summarize the cases that are considered in this thesis manuscript, in terms of the considered geometries and values taken by the diffusion, drift and jump coefficients.

In spite of the linearity of the equations on the first passage observables, obtaining analytical solutions is in general very challenging:

	$\mathbf{r}$	$D_{ij}(\mathbf{r})$	$V_i(\mathbf{r})$	$W(\mathbf{r}_a \mathbf{r}, 0)$
Part I Sec. 3.2.2	$(r, \theta)$	$D\delta_{ij}$	radial	0
Part II Sec. 3.2.2	$(r, \theta; i)$  $i = 1$ : surface  $i = 2$ : bulk		radial	$\lambda \delta(r_a - R - a) \delta(\theta_a - \theta_d) \delta(i_d - 1) \delta(i_a - 2)$  (Jump from the surface state $i_a - 2$  to the bulk state $i_d - 1$ )
Part III Sec. 6	$(\mathbf{r}; \mathbf{v})$  $\theta = \widehat{(\mathbf{r}, \mathbf{v})}$	0	radial	$\frac{1}{\tau} \delta(r_a - r_d)$
Sec. 7	$\mathbf{v}$ : velocity	$(D_r(\mathbf{v}), D_\theta(\mathbf{v}))$	radial	0

Table 2.4: Summary of the cases considered in this thesis manuscript.

- (i) In Parts. I and II the challenges arise from the mixed Dirichlet–Neumann boundary condition. Let me anticipate on the next Chap. 3 and consider the exit problem out of a disk, which is illustrated on Fig. 3.1a, p. 51. For simplicity, I set the radius of the confining disk and the diffusion coefficient to 1:  $R = 1$  and  $D = 1$ . The target  $\Gamma$  is the angular sector  $[\pi - \varepsilon, \pi]$ . The rest of the boundary  $\partial\Omega \setminus \Gamma = [0, \pi - \varepsilon)$  is reflective. In the cylindrical set of coordinates  $\mathbf{r} = (r, \theta)$ , this geometry is  $2\pi$ –symmetric, hence the general solution of Eq. (2.18) reads:

$$t(r, \theta) = \frac{1 - r^2}{4} + \frac{a_0}{2} + \sum_{n=1}^{\infty} a_n r^n \cos(n\theta), \quad (r, \theta) \in [0, 1) \times [0, \pi]. \quad (2.43)$$

The Fourier coefficients  $a_n$ ,  $n \geq 0$  are fixed by the boundary conditions. In Sec. 2.3.1.1, p. 39, I consider the case of a homogeneous Dirichlet boundary condition (e.g.  $\varepsilon = \pi$ ), in which case  $a_n = 0$ , for all  $n \geq 1$ . There is no finite solution in the limit of full Neumann boundary condition ( $\varepsilon = 0$ ) [87]. In terms of the Fourier expansion Eq. (2.43), the mixed Dirichlet–Neumann boundary condition, which corresponds to  $\varepsilon \in ]0, \pi[$ , reads

$$\frac{a_0}{2} + \sum_{n=1}^{\infty} a_n \cos(n\theta) = 0, \quad \theta \in [\pi - \varepsilon, \pi], \quad (2.44a)$$

$$\sum_{n=1}^{\infty} n a_n \cos(n\theta) = \frac{1}{2}, \quad \theta \in [0, \pi - \varepsilon). \quad (2.44b)$$

The problem is to find the Fourier coefficients  $a_n^{(0)}$ ,  $n \geq 0$  given these two Eqs. (2.44a) and (2.44b). This problem is at the core of the Chap. 3.

- (ii) In Part. III, challenges also arise from the boundary conditions. Let me take the example considered in Sec. 2.3.2, p. 40 of the EPRW in  $d = 1$ . Note that the MFPT  $t(R, \pi)$  does not satisfy the Dirichlet condition at the target  $r = R$ , i.e.  $t(R, \pi)$  is not equal to 0. Then, if not zero, what is the value of  $t(R, \pi)$ ? The stumbling block in higher dimensions is the determination of rigorous boundary conditions for the EPRW. In Parts. III, I tackle this problem and determine an approximate expression for the MFPT in  $d = 2$  and  $d = 3$ . Interestingly and in contrast to the  $d = 1$  case, in higher dimensions the MFPT is found to be an optimizable function of the turn rate.







## Part I

# Search for an exit by symmetric or biased Brownian volume diffusion



# First Passage Time distribution in 2D spherically symmetric domains by symmetric or biased Brownian motion

**Abstract** The distribution of exit times is computed for a Brownian particle in spherically symmetric two-dimensional domains (disks, angular sectors, annuli) and in rectangles that contain an exit on their boundary. We propose both an exact solution relying on a matrix inversion, and an approximate explicit solution. The approximate solution is shown to be exact for an exit of vanishing size and to be accurate even for large exits. For angular sectors, we also derive exact explicit formulas for the moments of the exit time. For annuli and rectangles, the approximate expression of the mean exit time is shown to be very accurate even for large exits. The analysis is extended to biased diffusion and is applied to a microfluidic system.

## Contents

<b>3.1</b>	<b>General formalism and application to angular sectors</b>	<b>53</b>
3.1.1	Model and basic equations	53
3.1.2	Resolution schemes	55
3.1.2.1	Exact explicit expression for the MFPT in angular sector	55
3.1.2.2	Exact resolution scheme for the survival probability	56
3.1.2.3	Approximate resolution scheme	59
3.1.3	Results for the disk	59
3.1.3.1	Short-time and long-time behaviour of the FPT density	60
3.1.3.2	Beyond the narrow-escape limit: a simplified expression for the long-time decay rate	62
3.1.4	Moments and cumulants	63
3.1.4.1	Recurrence relation on the Fourier coefficients	64
3.1.4.2	Diffusion in angular sector: explicit exact moments	65
3.1.4.3	Moments in the narrow-escape limit: the case of the disk	67
<b>3.2</b>	<b>Extensions and applications</b>	<b>68</b>
3.2.1	Annuli	68
3.2.1.1	Distribution of the first passage time	68
3.2.1.2	Approximate expression for the MFPT	70
3.2.1.3	Optimization of the GMFPT	72
3.2.2	Advection-diffusion with a radial bias	73
3.2.3	Rectangles	73
3.2.4	Analogy to microchannel flows	74

<b>3.3 Conclusion</b> . . . . .	<b>77</b>
<b>3.4 Perspectives</b> . . . . .	<b>78</b>

---

 This project led to Publication 3.

A particle confined within a pore of a porous medium is often modelled as a Brownian particle confined in a spherical domain  $\Omega$  (see Sec. 1.2.1.3, p. 24). In this chapter, we are interested in the statistics of the exit times, i.e. the first passage times to a target located at the boundary of the confining domain  $\partial\Omega$  by a Brownian particle.

Hitherto most studies focused on the mean first passage time (MFPT) of a Brownian particle to a small exit, which is called the narrow escape problem [92, 93, 94, 95]. For a starting position which is far enough from the boundary, the FPT distribution was shown to be dominated by its exponential tail in the limit of a large confining volume: hence the MFPT was sufficient to characterize the whole FPT distribution, except for the very short-times region [96, 97]. The short-time behavior of this distribution is approximately accounted for by a Dirac distribution whose contribution vanishes in the small exit limit. A generic multi-exponential representation of the FPT distribution in domains with heterogeneous distribution of targets was proposed in [98]. Some progress to precisely describe the short-time behavior of the FPT distribution has been recently achieved by Isaacson and Newby, who proposed a uniform asymptotic approximation of the FPT distribution in the small exit limit for 3D confining domains [95]. However, the exit size is not always small, e.g. in porous media with large interpore channels.

► In this chapter, we address the following question: what is the distribution of the first passage time of confined Brownian particles to an arbitrarily large exit?

To answer this question, we consider a particle diffusing in a confined spherically symmetric two-dimensional domain  $\Omega \subset \mathbb{R}^2$  which is periodic along the angular coordinate  $\theta$  and bounded in the radial coordinate  $r$ . Examples of spherically symmetric two-dimensional domains are disks, angular sectors, and annuli. The analysis is also applicable to rectangles. The boundary of  $\Omega$  is reflecting except for an absorbing patch on the surface through which the particle can escape. In spherically symmetric 2D domains, a Fourier expansion of the survival probability along the periodic coordinate  $\theta$  can be performed. I adapt the resolution schemes described in [99] to solve the Helmholtz equation with mixed boundary conditions satisfied by the survival probability. Our approach leads to both exact and approximate expressions for the FPT distribution and for the moments of the exit time (Sec. 3.1.2). As a result, we managed to describe the whole distribution of first passage times and their moments for the escape problem with arbitrary exit sizes. The approximate solution, which is exact only in the limit of an exit of vanishing width, is shown to be accurate over the whole range of time scales even for large exit sizes.

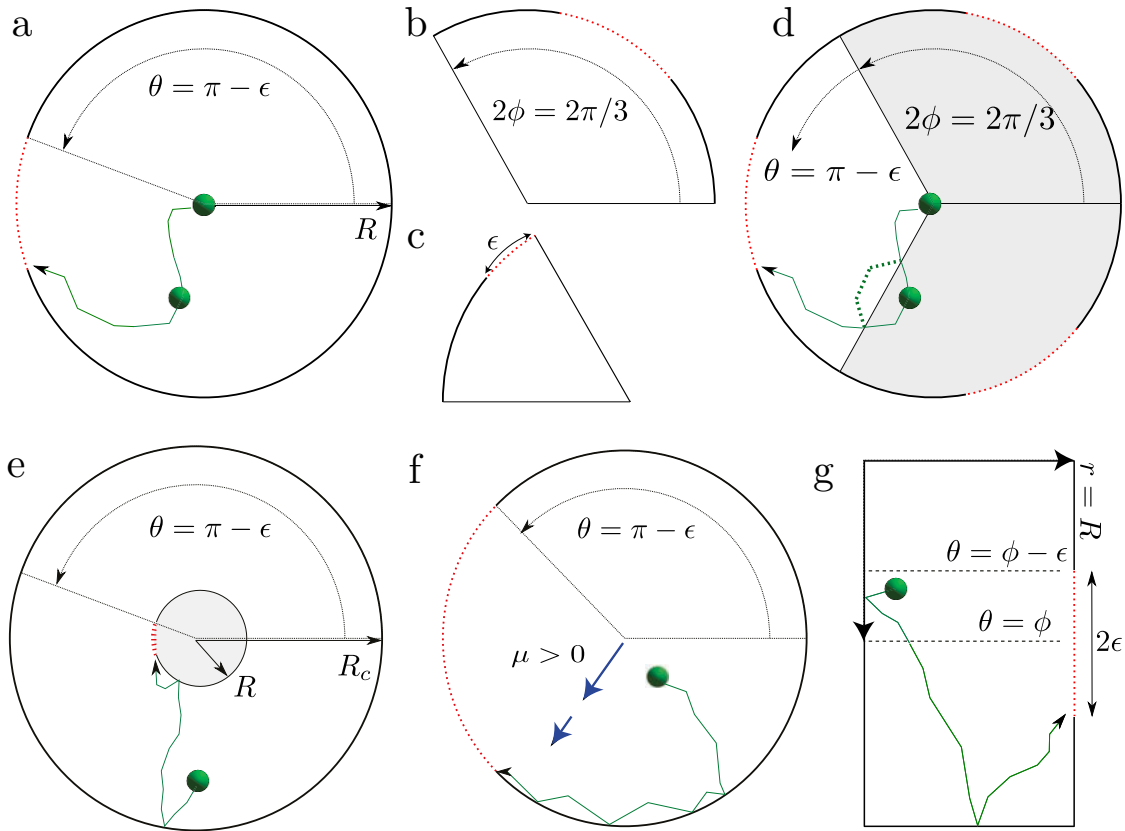


Figure 3.1: (Color Online) A Brownian particle (green circle) diffuses in a domain  $\Omega$  whose boundary is reflecting (solid line) except for an absorbing exit (dashed red line). **(a)**  $\Omega$  is a disk of radius  $R$  and the exit arclength is  $2R\varepsilon$ ; **(b)**  $\Omega$  is an angular sector of half-aperture  $\phi = \pi/3$ , with reflecting rays at  $\theta = 0$  and  $\theta = 2\phi$ ; **(c)**  $\Omega$  is an angular sector of total aperture  $\phi = \pi/3$ , with reflecting rays at  $\theta = 0$  and  $\theta = \phi$  (the exit arclength is  $R\varepsilon$ ); **(d)**  $\Omega$  is a disk with 3 regularly spaced exits of arclength  $2R\varepsilon$  on the boundary. The distribution of exit times through any of the three regularly spaced exits (case **d**) is identical to the distribution of exit times through a single centered exit within an angular sector of half-aperture  $\phi = \pi/3$  (case **b**). I sketch the reflection principle by representing the trajectory of the particle inside the disk with three exits by solid green line, while its image trajectory inside one of the angular sector of half-aperture  $\phi = \pi/3$  is shown by dashed green line; **(e)**  $\Omega$  is an annulus of radii  $R$  and  $R_c$  with an exit of half-width  $\varepsilon$  located on the inner radius  $R$ ; **(f)**  $\Omega$  is a disk and the Brownian particle is advected by a radial flow field  $\vec{v}(r) = \mu D \mathbf{r}/r^2$ , with  $\mu > 0$ , corresponding to an outward drift (blue arrows); **(g)**  $\Omega$  is a rectangle of total width  $R$  and height  $2\phi$ .

	Previous results		Our new results	
	Moments	FPT density	Moments	FPT density
Disk (Fig. 3.1)	$t$ : [92, 100] $\overline{\text{Var}}[\sigma]$ [100]	$\varepsilon \ll 1$ , $\mathbf{r}_0$ away from walls [101]	Exact explicit: $t$ , variance skewness kurtosis	Exact (non-explicit) Approx. (explicit)
Angular Sector (Fig. 3.1)		$\varepsilon \ll 1$ , $\mathbf{r}_0$ away from walls [101]	Exact explicit: $t$ , variance skewness kurtosis	Exact (non-explicit) Approx. (explicit)
Annulus (Fig. 3.8)	$t$ : $(\varepsilon, R/R_c) \ll 1$ [102]	$\varepsilon \ll 1$ , $\mathbf{r}_0$ away from walls [101]	Approx. $t$ for all $R_c$	Exact (non-explicit) Approx. (explicit)
Rectangle (Fig. 3.10)	$t$ : $(\varepsilon, \phi/R) \ll 1$ [102] $t$ : non-explicit [23]	$\varepsilon \ll 1$ , $\mathbf{r}_0$ away from walls [101]	Approx. $t$ for all $R$	Exact (non-explicit) Approx. (explicit)
Drift (Fig. 3.9)	$t$ : $\varepsilon \ll 1$ [103] drift towards the exit		Approx. $t$ for all $\mu$	Exact (non-explicit) Approx. (explicit)

Table 3.1: Summary of the results presented in this chapter and comparison to previous publications. The quantities  $t$  and  $\overline{\text{Var}}[\sigma]$  refer to the MFPT and to the averaged variance, respectively, of the FPT distribution to an exit of width  $\varepsilon$  from an arbitrary starting position  $\mathbf{r}_0 \in \Omega$ . The considered geometries are described in Fig. 3.1.

I apply this approach to the following domains: disks, angular sectors, annuli and rectangles (see Fig. 3.1). Table 3.1 summarizes the new results in this chapter. For Brownian particles confined in an angular sector, I provide the exact explicit expression for the MFPT and for the variance of the exit time (Sec. 3.1.4.2). In the case of a disk, I obtain an expression for the Fourier coefficients of the MFPT which is much simpler than the earlier expression from Ref. [92]. I point out that the variance of the exit time for an arbitrary starting point was previously known only through its leading order term in the small exit limit [101]. I also compute the exact skewness and excess kurtosis of the exit time for a Brownian particle started from an arbitrary point within an angular sector. Away from a boundary layer near the exit, I show that the ratio of the standard deviation to the MFPT is close to 1, the skewness to 2, and the excess kurtosis to 6, indicating that the FPT distribution can be well approximated by an exponential distribution, in contrast to the statement of Ref. [104].

I exhibit the following non-intuitive result on the MFPT of Brownian particles confined to an annulus of radii  $R$  and  $R_c$  (Sec. 3.2.1): under an analytically determined criteria, the MFPT is an optimizable function of the radius  $R_c$ . This result is based on an approximate expression for the MFPT which is in quantitative agreement with numerical simulations even for a large exit size and for arbitrary radius  $R_c$ . In contrast to the classical narrow-escape formulas for the MFPT in 2D domains of Ref. [105] which are not valid for degenerate domains (in which one of dimensions is much smaller than the others), our approximate expression of the MFPT is accurate even in the extreme case  $R_c = R$  which corresponds to a circle. Our approximate expressions are also accurate for rectangular confinements (Sec. 3.2.3).

In Sec. 3.2.2, p. 73, I consider Brownian particles biased by a  $1/r$  radial drift and confined in a disk. This situation is encountered in the biological modelling literature: the trajectories of marked proteins or tracers within the cytoplasm can be quantitatively described by an advection drift which models the effect of the intermittent active transport due to molecular motors stochastically binding and unbinding to microtubules [26].

The Helmholtz equation with mixed boundary conditions is also encountered in microfluidics. In Sec. 3.2.4, p. 74, I explain how the flow rate in a microchannel with ultra-hydrophobic walls [106, 107, 108] can be deduced from our explicit expressions for the MFPT to the exit.

## 3.1 General formalism and application to angular sectors

### 3.1.1 Model and basic equations

We consider a Brownian particle confined in bounded planar domains  $\Omega = \{(r, \theta) \in \mathbb{R}^2 : R_c < r < R, 0 < \theta < 2\phi\}$  which, in polar coordinates  $(r, \theta)$ , are  $2\phi$ -periodic along the angular coordinate  $\theta$  and bounded in the radial coordinate  $r$  by  $R_c$  and  $R$  (e.g., disk ( $\phi = \pi$ ) and angular sector shown in Fig. 3.1 for  $R_c = 0$ ).

► The exit  $\Gamma$  is an arc  $\theta \in [\phi - \varepsilon, \phi + \varepsilon]$  within an otherwise reflecting boundary  $\partial\Omega \setminus \Gamma$  at  $r = R$ . The boundary condition  $r = R_c$  is reflecting. Note that the exit can also be located on the inner circle, in which case one writes  $R < r < R_c$  instead of  $R_c < r < R$ . The angular sector geometry also accounts for the case of multiple regularly spaced exits within a disk. As illustrated on Fig. 3.1(c) for the case  $n = 3$ , the exit through any of  $n$  regularly spaced exits of width  $2\varepsilon$  within a disk can be equivalently represented as the exit through (i) a single opening of width  $2\varepsilon$  at the center of an angular sector of width  $2\pi/n$ , or (ii) through a single opening of width  $\varepsilon$  in the corner of an angular sector of width  $\pi/n$ .

We study the exit time statistics through the Laplace transform of the survival probability  $\tilde{S}^{(t)}(r, \theta)$ , denoted  $S^{(p)}(r, \theta)$  and defined in Eq. (2.20). The differential equation and boundary



conditions on  $\tilde{S}^{(p)}(r, \theta)$  are:

$$D \Delta S^{(p)}(r, \theta) = p S^{(p)}(r, \theta) - 1, \quad (r, \theta) \in \Omega, \quad (3.1a)$$

$$S^{(p)}(r, \theta) = 0, \quad r = R, \quad \theta \in [\phi - \varepsilon, \phi + \varepsilon], \quad (3.1b)$$

$$\partial_r S^{(p)}(r, \theta) = 0, \quad r = R, \quad \theta \in [0, \phi - \varepsilon] \cup (\phi + \varepsilon, 2\phi]. \quad (3.1c)$$

$$\partial_r S^{(p)}(r, \theta) = 0 \quad r = R_c, \quad \theta \in [0, 2\phi), \quad (3.1d)$$

$$\partial_\theta S^{(p)}(r, \theta) = 0 \quad r \in [R_c, R], \quad \theta \in \{0, 2\phi\}. \quad (3.1e)$$

where (i)  $\Delta$  is the Laplacian in cylindrical coordinates ( $d = 2$  in Eq. 2.32) and (ii) the last Eq. (3.1e) incorporates the reflecting boundary condition at the rays  $\theta = 0$  and  $\theta = 2\phi$  or, equivalently, the  $2\phi$ -periodicity of the domain.

In the rest of this section I introduce dimensionless quantities  $r \leftarrow r/R$ ,  $S^{(p)} \leftarrow DS^{(p)}/R^2$ , and  $p \leftarrow R^2 p/D$ , and define the following auxiliary function:

$$u^{(p)}(r, \theta) \equiv S^{(p)}(r, \theta) - S_\pi^{(p)}(r), \quad (3.2)$$

where  $S_\pi^{(p)}(r)$  is the rotation invariant solution of Eq. (3.1a) satisfying  $S_\pi^{(p)}(1) = 0$  and  $\partial_r S_\pi^{(p)}(r) = 0$  at  $r = R_c$ . In the case of diffusion inside an angular sector (with  $R_c = 0$ ),  $S_\pi^{(p)}(r)$  can be written in terms of the zeroth-order modified Bessel function  $I_0(z)$  of the first kind as

$$S_\pi^{(p)}(r) = \frac{1}{p} \left( 1 - \frac{I_0(\sqrt{p}r)}{I_0(\sqrt{p})} \right) \quad (3.3)$$

(expression for the case  $R_c > 0$  is provided in Table 3.2). Note that if the entire boundary at  $r = 1$  is absorbing (i.e.,  $\varepsilon = \phi$ ), the solution of Eq. (3.1a) is  $S^{(p)}(r, \theta) = S_\pi^{(p)}(r)$  [109].

In terms of the auxiliary function  $u^{(p)}(r, \theta)$ , Eqs. (3.1a – 3.1e) become

$$\Delta u^{(p)}(r, \theta) = p u^{(p)}(r, \theta), \quad (r, \theta) \in \Omega \quad (3.4a)$$

$$u^{(p)}(r, \theta) = 0, \quad r = 1, \quad \theta \in [\phi - \varepsilon, \phi + \varepsilon], \quad (3.4b)$$

$$\partial_r u^{(p)}(r, \theta) = -\partial_r S_\pi^{(p)}(r), \quad r = 1, \quad \theta \in [0, \phi - \varepsilon] \cup (\phi + \varepsilon, 2\phi], \quad (3.4c)$$

$$\partial_r u^{(p)}(r, \theta) = 0 \quad r = R_c, \quad \theta \in [0, 2\phi). \quad (3.4d)$$

$$\partial_\theta u^{(p)}(r, \theta) = 0 \quad r \in [R_c, 1], \quad \theta \in \{0, 2\phi\}, \quad (3.4e)$$

Using the separation of variables method, I express a general solution of Eq. (3.4a) which satisfies the periodicity  $\theta \rightarrow \theta + 2\phi$  as

$$u^{(p)}(r, \theta) = \frac{a_0^{(p)}}{2} f_0^{(p)}(r) + \sum_{n=1}^{\infty} a_n^{(p)} f_n^{(p)}(r) \cos\left(\frac{n\pi\theta}{\phi}\right), \quad (r, \theta) \in [0, 1) \times [0, \phi]. \quad (3.5)$$

where the functions  $f_n^{(p)}$  depend on the considered geometry. Since the unknown Fourier coefficients  $a_n^{(p)}$  stand in front of  $f_n^{(p)}$ , one can choose an appropriate normalization of the functions  $f_n^{(p)}$ . I choose the normalization condition  $f_n^{(p)}(1) = \phi/\pi$  ( $n \geq 0$ ). In the case of Brownian particles inside an angular sector ( $R_c = 0$ ),  $f_n^{(p)}$  are expressed in terms of modified Bessel functions  $I_n(z)$  of the first kind:

$$f_n^{(p)}(r) = \frac{\phi}{\pi} \frac{I_{n\pi/\phi}(\sqrt{p}r)}{I_{n\pi/\phi}(\sqrt{p})}, \quad n \geq 0. \quad (3.6)$$

The function  $S_\pi^{(p)}(r)$  defined in Eq. (3.2) is

$$S_\pi^{(p)}(r) = \frac{1 - \frac{\pi}{\phi} f_0^{(p)}(r)}{p}. \quad (3.7)$$

The Fourier coefficients  $a_n^{(p)}$  will be uniquely determined through the boundary conditions (3.4b) and (3.4c). Substituting Eq. (3.5) into Eqs. (3.4b) and (3.4c) leads to the system of equations

$$\frac{a_0^{(p)}}{2} + \sum_{n=1}^{\infty} a_n^{(p)} \cos\left(\frac{n\pi\theta}{\phi}\right) = 0, \quad \theta \in [\phi - \varepsilon, \phi], \quad (3.8a)$$

$$\left[\partial_r f_0^{(p)}\right]_{|r=1} \frac{a_0^{(p)}}{2} + \sum_{n=1}^{\infty} a_n^{(p)} \left[\partial_r f_n^{(p)}\right]_{|r=1} \cos\left(\frac{n\pi\theta}{\phi}\right) = - \left[\partial_r S_\pi^{(p)}\right]_{|r=1}, \quad \theta \in [0, \phi - \varepsilon], \quad (3.8b)$$

where the angular coordinate  $\theta$  is limited to the half-range  $[0, \phi]$  (instead of  $[0, 2\phi]$ ) due to the symmetry of these equations with respect to the change  $\theta \rightarrow 2\phi - \theta$  (this symmetry is also related to the reflection symmetry of the domain with respect to the ray  $\theta = \phi$ ).

In the next section, we propose two schemes (exact and approximate) to solve Eqs. (3.8a) and (3.8b).

### 3.1.2 Resolution schemes

#### 3.1.2.1 Exact explicit expression for the MFPT in angular sector

Let us first simplify previously known results in the case of the MFPT in a disk ( $\phi = \pi$ ) and extend these results to angular sectors. Using the  $p \ll 1$  asymptotic expansion,

$$\frac{I_n(\sqrt{p}r)}{I_n(\sqrt{p})} = r^n \left\{ 1 + \frac{(r^2 - 1)p}{4(1+n)} \right\} + \mathcal{O}(p^2), \quad n \geq 0, \quad (3.9)$$

In the particular case of the MFPT ( $p = 0$ ), Eqs. (3.8a) and (3.8b) read

$$\frac{a_0^{(0)}}{2} + \sum_{n=1}^{\infty} a_n^{(0)} \cos(n\theta) = 0, \quad \theta \in [\pi - \varepsilon, \pi], \quad (3.10a)$$

$$\sum_{n=1}^{\infty} n a_n^{(0)} \cos(n\theta) = \frac{1}{2}, \quad \theta \in [0, \pi - \varepsilon]. \quad (3.10b)$$

In Ref. [92], the solution of these equations was provided in the form:

$$a_0^{(0)} = \frac{\sqrt{2}}{\pi} \int_0^{\pi-\varepsilon} dx \frac{x \sin(x/2)}{\sqrt{\cos x + \cos \varepsilon}}, \quad (3.11a)$$

$$a_n^{(0)} = \frac{1}{\sqrt{2}\pi} \int_0^{\pi-\varepsilon} dt \left( \frac{\partial}{\partial t} \int_0^t dx \frac{x \sin(x/2)}{\sqrt{\cos x - \cos t}} \right) [P_n(\cos t) + P_{n-1}(\cos t)], \quad n \geq 1, \quad (3.11b)$$

where  $P_n(x)$  are Legendre polynomials.

In fact, I show in Appendix A.1 that these equations can be simplified into

$$a_0^{(0)} = -2 \ln \left[ \sin\left(\frac{\varepsilon}{2}\right) \right], \quad (3.12a)$$

$$a_n^{(0)} = \frac{(-1)^{n-1}}{2n} [P_n(\cos \varepsilon) + P_{n-1}(\cos \varepsilon)], \quad n \geq 1. \quad (3.12b)$$

I also extend these results to the calculation of the MFPT in an angular sector of half-aperture  $\phi$  and radius  $r = 1$ :  $\Omega = \{(r, \theta) \in \mathbb{R}^2 : 0 \leq r < 1, 0 < \theta < 2\phi\}$ . Under the change of

variables  $\hat{\theta} = \theta\pi/\phi$  and  $\hat{\varepsilon} = \varepsilon\pi/\phi$ , Eqs. (3.8a) and (3.8b) are reduced to Eqs. (3.10a), (3.10b) in the limit  $p = 0$ , from which

$$a_0^{(0)} = \alpha_0 \equiv -2 \ln \left[ \sin \left( \frac{\varepsilon\pi}{2\phi} \right) \right], \quad (3.13a)$$

$$a_n^{(0)} = \alpha_n \equiv \frac{(-1)^{n-1}}{2n} \left[ P_n \left( \cos \frac{\varepsilon\pi}{\phi} \right) + P_{n-1} \left( \cos \frac{\varepsilon\pi}{\phi} \right) \right], \quad n \geq 1. \quad (3.13b)$$

I conclude that the MFPT from the angular sector for a particle started at position  $(r, \theta)$  is

$$t(r, \theta) = \frac{1-r^2}{4} + \frac{\alpha_0 \phi}{2\pi} + \frac{\phi}{\pi} \sum_{n=1}^{\infty} \alpha_n r^{n\pi/\phi} \cos \left( \frac{n\pi\theta}{\phi} \right), \quad (3.14)$$

where  $\phi$  is the half-aperture of the angular sector, and  $\varepsilon$  is the half-width of the centered exit (see Fig. 3.1(b)). The GMFPT defined in Eq. (2.19) reads

$$\overline{\mathbb{E}[\sigma]} \equiv \frac{2}{\phi} \int_0^\phi \int_0^1 r \, dr \, d\theta \, \mathbb{E} \left[ \tau_{(r,\theta)}^n \right] = \frac{1}{8} + \frac{\alpha_0 \phi}{2\pi}. \quad (3.15)$$

To our knowledge, the results in Eqs. (3.13a), (3.13b), (3.14) and (3.15) are new.

Last, as described in Fig. 3.1(d), I recall that the exit through a window of width  $\varepsilon$  at the corner of the sector of angle  $\pi/m$  can be equivalently represented as the exit through any of  $m$  regularly spaced openings of width  $2\varepsilon$  within a disk. In the limit an infinite number of exits  $m \rightarrow \infty$ , ( $\phi = \pi/m \rightarrow 0$ ) at a fixed ratio  $\varepsilon/\phi$ , the MFPT of Eq. (3.14) tends to the MFPT to the fully absorbing boundary at  $r = 1$ , as expected from Refs. [98, 110].

### 3.1.2.2 Exact resolution scheme for the survival probability

Now I solve the system of equations on the Fourier coefficients  $a_n^{(p)}$  for an arbitrary value of  $p$ . I first introduce

$$\gamma_n^{(p)} \equiv 1 - \frac{[\partial_r f_n^{(p)}]_{r=1}}{n}, \quad n \geq 1, \quad (3.16)$$

which I use to define the following function

$$F^{(p)}(\hat{\theta}) \equiv - \left[ \partial_r S_\pi^{(p)} \right]_{|r=1} - \left[ \partial_r f_0^{(p)} \right]_{|r=1} \frac{a_0^{(p)}}{2} + \sum_{n=1}^{\infty} a_n^{(p)} \gamma_n^{(p)} n \cos(n\hat{\theta}), \quad \theta \in [0, \pi - \hat{\varepsilon}]. \quad (3.17)$$

For diffusion inside an angular sector, the explicit expression for  $\gamma_n^{(p)}$  is

$$\gamma_n^{(p)} \equiv 1 - \frac{\sqrt{p} I_{n\pi/\phi-1}(\sqrt{p}) + I_{n\pi/\phi+1}(\sqrt{p})}{2n I_{n\pi/\phi}(\sqrt{p})}, \quad n \geq 1, \quad (3.18)$$

where we have used the definition (3.6).

Under the change of variables  $\hat{\theta} = \theta\pi/\phi$  and  $\hat{\varepsilon} \equiv \varepsilon\pi/\phi$ , Eqs. (3.8a) and (3.8b) read

$$\frac{a_0^{(p)}}{2} + \sum_{n=1}^{\infty} a_n^{(p)} \cos(n\hat{\theta}) = 0, \quad \hat{\theta} \in [\pi - \hat{\varepsilon}, \pi], \quad (3.19a)$$

$$\sum_{n=1}^{\infty} n a_n^{(p)} \cos(n\hat{\theta}) = F^{(p)}(\hat{\theta}), \quad \hat{\theta} \in [0, \pi - \hat{\varepsilon}], \quad (3.19b)$$

The problem of determining the Fourier coefficients  $a_n^{(p)}$  from Eqs. (3.19a) and (3.19b) is closely related to the problem considered in Ref. [99] for a given function  $F^{(p)}(\hat{\theta})$  which was independent of  $a_n^{(p)}$ . The crucial difference between the present case and the case considered in Ref. [99]

is that the function  $F^{(p)}(\hat{\theta})$  defined in Eq. (3.17) depends on the unknown Fourier coefficients  $a_n^{(p)}$ . In the rest of this section, I adapt the method of Ref. [99] to reduce Eqs. (3.19a) and (3.19b) to a linear system of equations for the Fourier coefficients.

Due to the invertibility of Abel's integral operator, we can define the unique function  $h_1^{(p)}(t), t \in [0, \pi - \hat{\varepsilon}]$  such that

$$\frac{a_0^{(p)}}{2} + \sum_{n=1}^{\infty} a_n^{(p)} \cos(n\hat{\theta}) = \cos(\hat{\theta}/2) \int_{\hat{\theta}}^{\pi - \hat{\varepsilon}} \frac{h_1^{(p)}(t) dt}{\sqrt{\cos \hat{\theta} - \cos t}}. \quad (3.20)$$

Using Mehler's integral representation of Legendre polynomials,

$$P_n(\cos t) = \frac{\sqrt{2}}{\pi} \int_0^t \frac{\cos[(n + \frac{1}{2})x]}{\sqrt{\cos x - \cos t}} dx, \quad (3.21)$$

and using the absorbing condition (3.4b), I show that the Fourier coefficients can be expressed in terms of  $h_1^{(p)}(t)$ :

$$a_0^{(p)} = \sqrt{2} \int_0^{\pi - \hat{\varepsilon}} h_1^{(p)}(t) dt, \quad (3.22a)$$

$$a_n^{(p)} = \frac{1}{\sqrt{2}} \int_0^{\pi - \hat{\varepsilon}} h_1^{(p)}(t) [P_n(\cos t) + P_{n-1}(\cos t)] dt, \quad n \geq 1. \quad (3.22b)$$

After integration of Eq. (3.19b) from 0 to  $x$ ,

$$\sum_{n=1}^{\infty} a_n^{(p)} \sin(nx) = \int_0^x F^{(p)}(u) du, \quad x \in [0, \pi - \hat{\varepsilon}], \quad (3.23)$$

I find that  $h_1^{(p)}(t)$  satisfies the relation

$$\int_0^{\pi - \hat{\varepsilon}} dt h_1^{(p)}(t) \frac{1}{\sqrt{2}} \sum_{n=1}^{\infty} [P_n(\cos t) + P_{n-1}(\cos t)] \sin(nx) = \int_0^x F^{(p)}(u) du. \quad (3.24)$$

Using the identity [see Eq. (2. 6. 31) from Ref. [99]]

$$\frac{1}{\sqrt{2}} \sum_{n=1}^{\infty} [P_n(\cos t) + P_{n-1}(\cos t)] \sin(nx) = \frac{\cos(\frac{x}{2}) H(x-t)}{\sqrt{\cos t - \cos x}}, \quad (3.25)$$

where  $H(t)$  is the Heaviside distribution, I sum up the left-hand side of Eq. (3.24) and get

$$\int_0^x \frac{h_1^{(p)}(t) dt}{\sqrt{\cos t - \cos x}} = \frac{1}{\cos(\frac{x}{2})} \int_0^x F^{(p)}(u) du. \quad (3.26)$$

The function  $h_1^{(p)}(t)$  is determined as the solution of the Abel-type integral equation (3.26) and reads

$$h_1^{(p)}(t) = \frac{2}{\pi} \frac{d}{dt} \int_0^t \frac{\sin(\frac{x}{2}) dx}{\sqrt{\cos x - \cos t}} \left[ \int_0^x F^{(p)}(u) du \right], \quad t \in [0, \pi - \hat{\varepsilon}]. \quad (3.27)$$

Substitution of Eq. (3.27) into Eqs. (3.22a) and (3.22b) leads to the set of equations

$$a_0^{(p)} = \frac{2\sqrt{2}}{\pi} \int_0^{\pi - \hat{\varepsilon}} dx \frac{\sin(x/2)}{\sqrt{\cos x + \cos \hat{\varepsilon}}} \left[ \int_0^x F^{(p)}(u) du \right], \quad (3.28a)$$

$$a_n^{(p)} = \frac{\sqrt{2}}{\pi} \int_0^{\pi - \hat{\varepsilon}} dt \left\{ \frac{\partial}{\partial t} \int_0^t dx \frac{\sin(x/2)}{\sqrt{\cos x - \cos t}} \left[ \int_0^x F^{(p)}(u) du \right] \right\} [P_n(\cos t) + P_{n-1}(\cos t)], \quad n \geq 1. \quad (3.28b)$$

From Eq. (3.17), we see that  $F^{(p)}(u)$  is a linear combination of the unknown Fourier coefficients  $a_m^{(p)}$ , thus Eqs. (3.28a) and (3.28b) define a linear system of equations.

I proceed by simplifying Eqs. (3.28a) and (3.28b) in order to provide explicit relations between the Fourier coefficients.

(i) First, I simplify the identity (3.28a) using the relation

$$2m\alpha_m = \frac{2\sqrt{2}}{\pi} \int_0^{\pi-\hat{\varepsilon}} dx \frac{\sin\left(\frac{x}{2}\right) \sin(mx)}{\sqrt{\cos x + \cos \hat{\varepsilon}}}, \quad m \geq 1. \quad (3.29)$$

To prove Eq. (3.29), I express the terms  $P_m(\cos \hat{\varepsilon})$  and  $P_{m-1}(\cos \hat{\varepsilon})$  in the definition (3.13b) of  $\alpha_m$  through the Mehler's identity (3.21).

I substitute the explicit expression for  $F^{(p)}(u)$  from Eq. (3.17) into Eq. (3.28a). Using the integral representation of  $\alpha_0$  from Eqs. (3.11a) and (3.29), I obtain

$$a_0^{(p)} = -2\alpha_0 \left( \left[ \partial_r S_\pi^{(p)} \right]_{|r=1} + \frac{1}{2} \left[ \partial_r f_0^{(p)} \right]_{|r=1} a_0^{(p)} \right) + \sum_{m=1}^{\infty} 2m\gamma_m^{(p)} \alpha_m a_m^{(p)}. \quad (3.30)$$

(ii) I now simplify the relation (3.28b) for  $a_n^{(p)}$ . Substituting the explicit expression (3.17) for  $F^{(p)}(u)$  into Eq. (3.28b) leads to the following system of equations

$$a_n^{(p)} = -2\alpha_n \left( \left[ \partial_r S_\pi^{(p)} \right]_{|r=1} + \frac{1}{2} \left[ \partial_r f_0^{(p)} \right]_{|r=1} a_0^{(p)} \right) + \sum_{m=1}^{\infty} M_{nm} \gamma_m^{(p)} a_m^{(p)}, \quad n \geq 1, \quad (3.31)$$

where the matrix  $M_{nm}, n \geq 1, m \geq 1$ , is

$$M_{nm} = \frac{\sqrt{2}}{\pi} \int_0^{\pi-\hat{\varepsilon}} \left[ \frac{\partial}{\partial t} \int_0^t dx \frac{\sin(x/2) \sin(mx)}{\sqrt{\cos x - \cos t}} \right] [P_n(\cos t) + P_{n-1}(\cos t)]. \quad (3.32)$$

I show in Appendix A.1.3 that the expression for  $M_{nm}$  can be simplified into

$$M_{nm} = \frac{m}{2} \int_{-\cos(\hat{\varepsilon})}^1 \frac{1}{1+x} [P_m(x) + P_{m-1}(x)] [P_n(x) + P_{n-1}(x)] dx. \quad (3.33)$$

Interestingly, the set of coefficients  $\alpha_n$  is invariant under the action of  $M$ :  $M \cdot \alpha = \alpha$  (see Appendix A.1.3).

(iii) I now write explicitly the system of equations on  $a_n^{(p)}$ . I first define the set of coefficients  $(\tilde{a}_n^{(p)})$  defined through the following matrix inversion:

$$\tilde{a}_n^{(p)} \equiv \left[ \left( I - M\gamma^{(p)} \right)^{-1} \alpha \right]_n, \quad n \geq 1, \quad (3.34)$$

where  $I$  stands for the identity matrix, and  $\gamma^{(p)}$  is a diagonal matrix formed by  $\gamma_n^{(p)}$ . For an angular sector and  $p = 0$ , one has  $\gamma^{(0)} = 0$  and retrieves the expected identity  $\tilde{a}_n^{(0)} = \alpha_n$ . From Eq. (3.31), I have

$$a_n^{(p)} = -2\tilde{a}_n^{(p)} \left( \left[ \partial_r S_\pi^{(p)} \right]_{|r=1} + \frac{1}{2} \left[ \partial_r f_0^{(p)} \right]_{|r=1} a_0^{(p)} \right), \quad n \geq 1. \quad (3.35)$$

Substituting Eq. (3.35) into Eq. (3.31) I obtain a closed system of linear equations for  $a_0^{(p)}$ . Introducing

$$\mathcal{C}^{(p)} \equiv \alpha_0 + \sum_{m=1}^{\infty} 2m\alpha_m \tilde{a}_m^{(p)} \gamma_m^{(p)}, \quad (3.36)$$

the Fourier coefficients of the Laplace transform of the survival probability take the compact exact form:

$$a_0^{(p)} = \mathcal{C}^{(p)} \left\{ \frac{-2 \left[ \partial_r S_\pi^{(p)} \right]_{|r=1}}{1 + \mathcal{C}^{(p)}} \left[ \partial_r f_0^{(p)} \right]_{|r=1} \right\}, \quad (3.37a)$$

$$a_n^{(p)} = \frac{\alpha_n}{(1 - \gamma_n^{(p)})} \left\{ \frac{-2 \left[ \partial_r S_\pi^{(p)} \right]_{|r=1}}{1 + \mathcal{C}^{(p)} \left[ \partial_r f_0^{(p)} \right]_{|r=1}} \right\}, \quad n \geq 1. \quad (3.37b)$$

This solution depends on the coefficients  $\tilde{a}_n^{(p)}$  given by Eq. (3.34). The numerical implementation of the solution from Eqs. (3.37a) and (3.37b) requires the truncation of the matrix  $M$  involved in Eq. (3.34) to a finite size  $N \times N$ . In spite of the truncation, we will refer to the results obtained by this numerical procedure as exact solutions, as their accuracy can be arbitrarily improved by increasing the truncation size  $N$  (I checked numerically that the truncation errors decay very rapidly with  $N$ ). In practice, I set  $N = 100$ .

In the next section, I propose an approximate expression for the Fourier coefficients  $a_n^{(p)}$  which does not rely on a matrix inversion.

### 3.1.2.3 Approximate resolution scheme

► The idea of the approximate solution is to substitute the matrix  $M$  by the identity matrix in Eq. (3.34). I emphasize that the obtention of an approximate solution, which provides a concise and explicit expression for the FPT, is one of the main result of this chapter.

In Refs. [85, 111] and [112], such a substitution was shown to be efficient to compute the MFPT of a particle alternating phases of surface diffusion and phases of bulk diffusions. The substitution of the matrix  $M$  by the identity matrix is exact for  $\hat{\varepsilon} = 0$  as the asymptotic expansion of  $M_{nm}$  in the limit  $\hat{\varepsilon} \ll 1$  reads (see Appendix A.1.4)

$$M_{nm} = \delta_{nm} + \frac{nm^2(-1)^{n+m}}{8} \hat{\varepsilon}^4 + \mathcal{O}(\hat{\varepsilon}^5), \quad n \geq 1, \quad m \geq 1, \quad (3.38)$$

where  $\delta_{nm}$  is the Kronecker symbol. The approximation  $M_{nm} = \delta_{nm}$  allows one to invert the matrix in Eq. (3.34), yielding the following approximate solution:

$$\tilde{a}_n^{(p)} \approx \frac{\alpha_n}{1 - \gamma_n^{(p)}}. \quad (3.39)$$

Within the approximate scheme, I define

$$\mathcal{C}_a^{(p)} \equiv \alpha_0 + \sum_{m=1}^{\infty} \frac{2m\alpha_m^2\gamma_m^{(p)}}{1 - \gamma_m^{(p)}}, \quad (3.40)$$

and then substitute  $\mathcal{C}^{(p)}$  by  $\mathcal{C}_a^{(p)}$  in Eqs. (3.37a) and (3.37b). Note that the approximate solution is also exact in the limit  $\hat{\varepsilon} = \pi$ , as it predicts  $\alpha_n = 0$  for all  $n \geq 0$ .

In the next section, I test the accuracy of the approximate expression for the FPT distribution in the disk. I show that the approximate expression describes accurately the exact FPT distribution for any value of  $\hat{\varepsilon}$  between 0 and  $\pi$ .

### 3.1.3 Results for the disk

In this section, we focus on the FPT distribution for a Brownian particle confined in the disk (Fig. 3.1(a)).

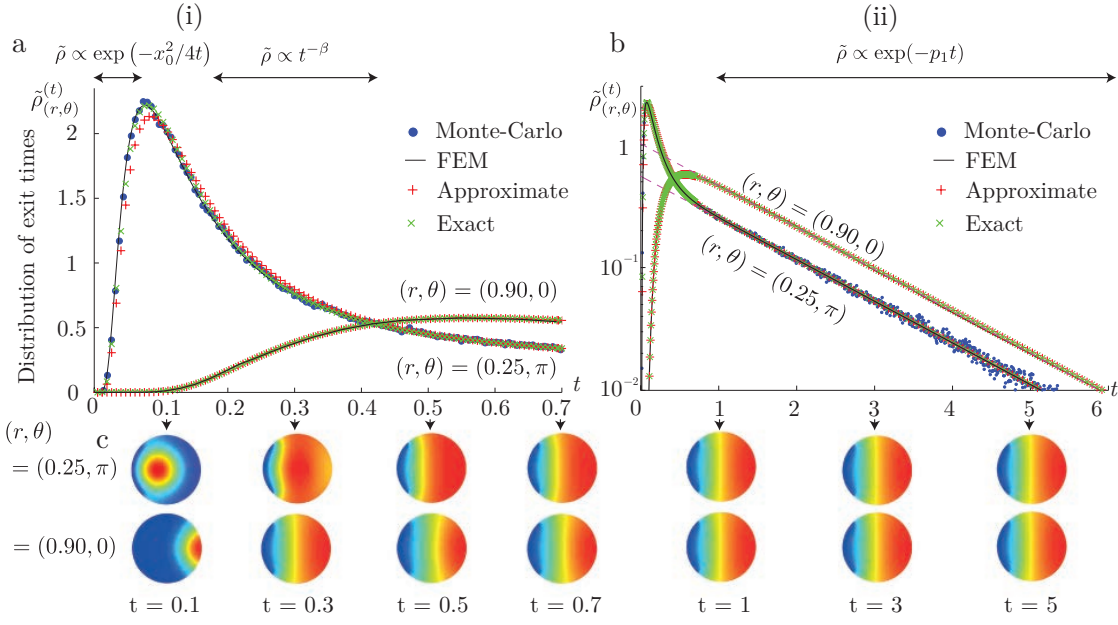


Figure 3.2: **Upper panel:** The probability density of the FPT to exit the unit disk through an aperture of half-width  $\varepsilon = \pi/4$  (Fig. 3.1) for Brownian particles started at  $(r, \theta) = (0.25, \pi)$  and  $(r, \theta) = (0.90, 0)$ . The probability density is plotted on (a) linear scale for  $t \in [0, 0.7]$  and (b) log-linear scale for  $t \in [0, 6]$ . The exact solution from Eqs. (3.37a) and (3.37b) (green crosses) is compared to the approximate solution from Sec. 3.1.2.3 (red pluses), finite element method (solid black line), and Monte Carlo simulations (blue circles) (see Appendix A.4). **Lower panel:** (c) Diffusive propagator  $\tilde{G}^{(t)}(\mathbf{r}_0, \mathbf{r})$  computed by a FEM at times  $t = 0.1, 0.3, 0.5, 0.7, 1, 3, 5$  for the initial positions  $(r, \theta) = (0.25, \pi)$  (top row) and  $(r, \theta) = (0.90, 0)$  (bottom row). Color changes from dark red to dark blue correspond to changes of the diffusive propagator from large to small values. The FPT probability density remains close to zero during the time needed for the diffusive propagator to spread to the exit. After a time  $t > R^2/D = 1$ , (i) the diffusive propagator reaches a steady state profile, and (ii) the FPT is close to an exponential distribution with the decay rate constant  $p_1$  predicted by Eq. (3.43) and shown by magenta dashed lines in (b).

### 3.1.3.1 Short-time and long-time behaviour of the FPT density

Figures 3.2 and 3.3 show the exact and approximate FPT probability densities that are computed through the inverse Laplace transform of  $\rho^{(p)}(r, \theta)$  from Eqs. (3.37a) and (3.37b). The exact and approximate solutions agree well with the numerical results which are obtained by two independent techniques:

- (FEM) a finite element method resolution in the time domain by COMSOL,
- (MC) Monte Carlo simulations of a large sample of random walks (see Appendix A.4 for further information on these computational techniques).

In both numerical solutions, the problem is solved in the time domain, i.e., without Laplace transform inversion. Even for a large exit size  $\varepsilon = \pi/4$ , the approximate solution from Sec. 3.1.2.3 agrees well with both the exact solution and the numerical results (see Fig. 3.2). The agreement is improved uniformly in time for smaller values of  $\varepsilon$  (Fig. 3.3).

The time scale  $R^2/D$  separates the short-time and the long-time behavior of the FPT distribution, as illustrated on Figs. 3.2(a–b). In addition, Fig. 3.2(c) shows the diffusive propagator  $p(\mathbf{r}_a, t|\mathbf{r})$  as a function of the arrival position  $\mathbf{r}_a$  (computed by a finite element

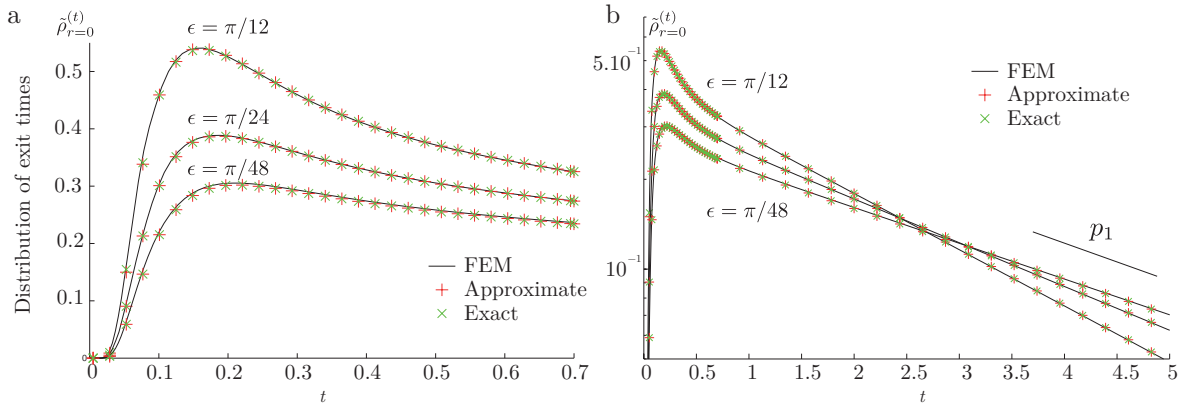


Figure 3.3: The FPT probability density for a disk with an exit of half-width  $\varepsilon = \pi/12, \pi/24, \pi/48$  for Brownian particles started at  $r = 0$ , in (a) linear scale for  $t \in [0, 0.7]$ , and (b) log-linear scale for  $t \in [0, 5]$ . The exact solution from Eqs. (3.37a – 3.37b) (green crosses) is compared to its analytical approximation from Sec. 3.1.2.3 (red pluses), and a finite element method resolution (black solid line), showing an excellent agreement (units:  $R^2/D = 1$ ).

method in COMSOL). The spatial distribution of the diffusive propagator provides the following physical insight on the evolution of the FPT in the short-time (i) and long-time regimes (ii):

(i) For  $t \ll R^2/D$ , most particles do not have enough time to reach the confining boundary (*a fortiori* the exit) and the confining domain appears to be almost infinite. This can be seen on the profile of the diffusive propagator for  $t < 1$  in Fig. 3.2(c). If the distance  $x_0$  from the initial position  $(r, \theta)$  to the center of the exit  $(1, \pi)$ ,  $x_0(r, \theta) = \sqrt{1 + r^2 - 2r \cos(\theta)}$ , is sufficiently small (e.g., for  $(r, \theta) = (0.25, \pi)$  in Fig. 3.2), the short-time behavior of the FPT probability density is approximatively

$$\tilde{\rho}^{(t)}(r, \theta) \approx \frac{x_0(r, \theta)}{\sqrt{4\pi Dt^3}} \exp\left(-\frac{x_0^2(r, \theta)}{4Dt}\right), \quad (3.41)$$

which describes the FPT for a particle started at distance  $x_0$  from the absorbing endpoint of a semi-infinite segment [113]. The exponential factor strongly dominates at short times when  $\sqrt{4Dt} \ll x_0(r, \theta)$ . At the intermediate times, when  $x_0(r, \theta) \ll \sqrt{4Dt} \ll R$ , the FPT probability density exhibits a power law decay,  $\tilde{\rho} \propto t^{-\beta}$ , with  $\beta = 3/2$ . This regime is clearly seen on Fig. 3.2 for a starting position  $(r, \theta) = (0.90, \pi)$ , in which case the fit of the FPT probability density at the intermediate times  $t \in [0.1, 0.7]$  by a power law  $t^{-\beta}$  yields  $\beta = 1.49 \pm 0.02$ , a value which is close to the corresponding value of  $\beta$  in a semi-infinite system ( $\beta = 1.50$ , see Eq. (3.41)).

(ii) For  $t \gg R^2/D$ , the FPT probability density exhibits an exponential tail. The terms in braces in Eqs. (3.37a) and (3.37b) determine the decay rate of the exponential tail. Note that in Fig. 3.2 the rescaled profile of the diffusive propagator appears stationary for all  $t > R^2/D = 1$ , as expected.

The survival probability  $\tilde{S}^{(t)}$  (resp. the FPT probability density  $\tilde{\rho}^{(t)}$ ) can be expressed as the sum over the residues of the Laplace transform  $S^{(p)}$  (resp.  $\rho^{(p)}$ ). For example, if the boundary is fully absorbing (i.e.,  $\varepsilon = \pi$ ), the survival probability of a particle started at  $(r, \theta)$  can be written from Eq. (3.3) [109]

$$\tilde{S}^{(t)}(r, \theta) = \sum_{k=1}^{\infty} \frac{2}{\xi_{0k}} \frac{J_0(\xi_{0k}r)}{J_1(\xi_{0k})} \exp(-\xi_{0k}^2 t), \quad (3.42)$$



where the coefficients  $\xi_{0k}$  are the poles of  $S_\pi^{(p)}(r)$  (as a function of  $p$ ), which turn out to be the zeros of the zeroth order Bessel function:  $J_0(\xi_{0k}) = 0$  for all  $k \geq 1$ . Note that the functions  $S^{(p)}$  and  $\rho^{(p)}$  are related through Eq. (2.22) and therefore have the same poles. In the general case  $\varepsilon < \pi$ , the long-time behavior of the FPT probability density is governed by the smallest decay rate  $p_1$ :  $\tilde{\rho}_\pi^{(t)}(r)$  asymptotically decays as  $\exp(-p_1 t)$  for  $t \gg R^2/D$ . The decay rate  $p_1$  can be expressed in terms of the smallest positive root of the equation

$$1 + \mathcal{C}^{(p_1)} \left[ \partial_r f_0^{(p_1)} \right]_{|r=1} = 0. \quad (3.43)$$

This equation, which uniquely determines  $p_1$ , can be solved numerically (see Fig. 3.4). Note that Eq. (3.43) is independent of the starting position of the particle: in the long-time limit, particles have lost memory of their starting positions. In the next section, I provide explicit estimates of  $p_1$ , which yield the long time asymptotics of the FPT distribution in the narrow-escape limit  $\varepsilon \ll 1$  and beyond.

### 3.1.3.2 Beyond the narrow-escape limit: a simplified expression for the long-time decay rate

The determination of the FPT distribution for arbitrary  $\varepsilon$  presented above is the main result of the present thesis chapter. In this paragraph we first compare our result to the previously known results on the FPT distribution in the narrow-escape limit from Ref. [101]. We then propose a simplified expression for  $p_1$  which does not depend on the specific shape of the domain  $\Omega$ . This simplified expression is asymptotically exact in the limit  $\varepsilon \ll 1$  and is in fact in good agreement with the exact expression for  $p_1$  (computed through Eq. (3.43)) over the whole range of value of  $\varepsilon$  (see Fig. 3.4).

I first point out that at the first order in  $\varepsilon \ll 1$ , Eqs. (3.13a) and (3.13b) read

$$\alpha_0 = 2 \ln \left( \frac{2\phi}{\pi\varepsilon} \right) + \mathcal{O} \left( \left( \frac{\varepsilon\pi}{\phi} \right)^2 \right), \quad (3.44a)$$

$$\alpha_n = \frac{(-1)^{n-1}}{n} + \mathcal{O} \left( \left( \frac{\varepsilon\pi}{\phi} \right)^2 \right), \quad n \geq 1. \quad (3.44b)$$

The logarithmic singularity of Eq. (3.44a) is a well-known result discussed in Ref. [92] for  $\phi = \pi$  and in Ref. [93] for  $\phi < \pi$ .

In this limit  $\varepsilon \ll 1$  and if the starting position  $\mathbf{r}$  is located away from the frontier of the confining domain  $\Omega$ , it has been shown in Ref. [101] that the FPT converges to an exponential distribution with mean the GMFPT  $\overline{\mathbb{E}[\sigma]}$ , defined in Eq. (2.19). Hence Ref. [101] implies the asymptotic identity:  $p_1 = 1/\overline{\mathbb{E}[\sigma]}$ , for  $\varepsilon \ll 1$ . Due to the divergence of  $\alpha_0$  from Eq. (3.44a), the latter identity is equivalent to:

$$p_1 = \frac{|\Omega|}{\pi} \frac{2}{\alpha_0}, \quad \forall \varepsilon \ll 1. \quad (3.45)$$

where  $|\Omega|$  stands for the volume of  $\Omega$ . I stress that the latter expression in Eq. (3.45) depends on  $|\Omega|$ , but not on the precise shape of the domain  $\Omega$ . This statement holds however only in the limit  $\varepsilon \ll 1$ , since the exact result of Eq. (3.43), which is valid for any  $\varepsilon$ , depends a priori on the specific geometry of the domain through the set  $(\gamma_m^{(p)})$  in the expression of  $C^{(p)}$  (see Eq. (3.36)).

► In fact one can propose a simple approximate expression for  $p_1$  with larger range of validity in  $\varepsilon$  than the asymptotic relation from Eq. (3.45). Let us first notice that at the

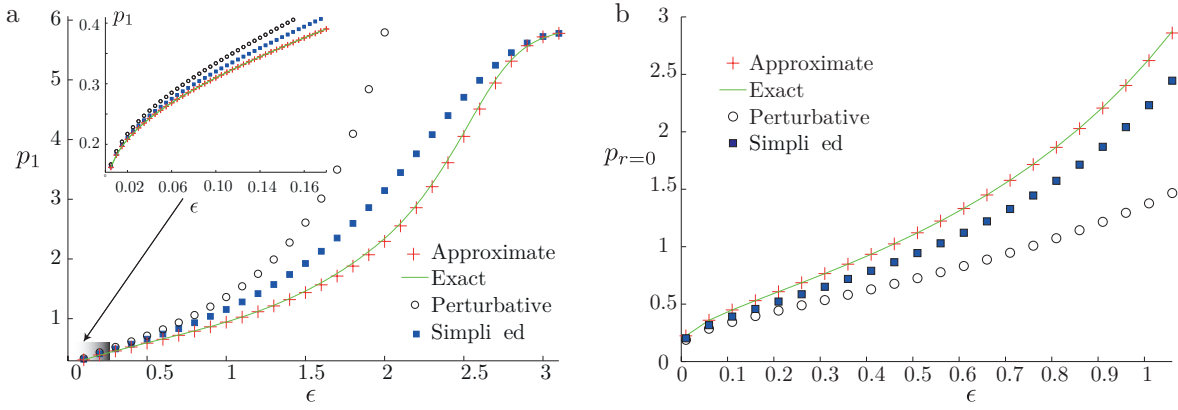


Figure 3.4: Comparison of three approximate schemes describing the long-time behavior of the survival probability for a Brownian particle started at  $r = 0$  which exits a confining disk through an exit of half-width  $\epsilon$ . The quantities  $p_{r=0}$  and  $p_1$  are defined from the asymptotic expansion:  $\log(\tilde{\rho}^{(t)}(r = 0)) \simeq \log(p_{r=0}) - p_1 t$  according to Eq. (3.48). **(a)** Decay rate  $p_1$  of the long-time limit of the survival probability as a function of the exit half-width  $\epsilon$ . The rate  $p_1$  is obtained through: an exponential interpolation of the exact distribution from Eqs. (3.37a) and (3.37b) (solid green line), an exponential interpolation of the approximate distribution from Sec. 3.1.2.3 (red pluses), the asymptotic expression  $p_1 = 2/\alpha_0$  in the limit  $\epsilon \ll 1$  [101] (black circles), and simplified Eq. (3.46) (blue squares). Note that Eq. (3.46) provides accurate results in both limits  $\epsilon = 0$  and  $\epsilon = \pi$ , and is more accurate than the perturbative expansion. **(b)** The prefactor  $p_{r=0}$  to the exponential distribution defined in Eq. (3.48) as a function of the exit half-width  $\epsilon$ .

leading order in  $\epsilon \ll 1$ ,  $\mathcal{C}^{(p)} \approx \alpha_0$ . The latter identity leads us to substitution  $\mathcal{C}^{(p)}$  for  $\alpha_0$  in Eq. (3.43). Setting  $q_1 = i\sqrt{p_1}$ , the simplified expression of Eq. (3.43) is reduced to:

$$\left[ \partial_r f_0^{(q_1)} \right]_{|r=1} \approx \frac{|\Omega|}{\pi} \frac{1}{q_1 \alpha_0}. \quad (3.46)$$

In the limit  $\epsilon \ll 1$ , the simplified expression of Eq. (3.46) leads to the perturbative result of Eq. (3.45). Note that the simplified expression of Eq. (3.46) is also exact for  $\epsilon = \pi$ , in which case  $\alpha_0$  tends to zero and  $p_1$  tends to  $\xi_{01}^2$ , in agreement with Eq. (3.42).

Finally, for a given value of the decay rate  $p_1$ , the residue theorem leads to the following long-time exponential decay of the survival probability:

$$\tilde{S}^{(t)}(r, \theta) \approx \left( -2 \left[ \partial_r S_\pi^{(p_1)} \right]_{|r=1} \right) \left[ \frac{J_0(\sqrt{p_1}r)}{J_0(\sqrt{p_1})} \frac{\alpha_0}{2} + \sum_{m=1}^{\infty} \frac{J_m(\sqrt{p_1}r)}{J_m(\sqrt{p_1})} \alpha_m \cos\left(\frac{m\theta\phi}{\pi}\right) \right] \exp(-p_1 t) \quad (3.47)$$

$$\approx p_{(r,\theta)} \exp(-p_1 t), \quad (3.48)$$

where  $p_{(r,\theta)}$  is the prefactor of the exponential distribution, which depends on the starting position  $X(0) = (r, \theta)$ . In Fig. 3.4, I show that the simplified solution of Eq. (3.46) provides a good approximation over the whole range of values for  $\epsilon$  of  $p_1$ .

### 3.1.4 Moments and cumulants

► In this section I derive exact expressions for the moments of the exit times for a general set of functions  $f_n^{(p)}$ ,  $n \geq 0$ . I emphasize that these expressions are fully explicit in the case of Brownian particles confined in an angular sector.

I use the notations  $a_n^{[k]}$  for the  $k$ -th coefficient in the small  $p \ll 1$  expansion of  $a_n^{(p)}$ :

$$a_n^{(p)} \equiv \sum_{k=0}^{\infty} p^k a_n^{[k]}, \quad n \geq 0. \quad (3.49)$$

By definition  $a_n^{(0)} = a_n^{[0]}$ . Similarly I define for all  $k \geq 0$  the set of coefficients  $S^{[k]}(r, \theta)$ ,  $[\partial_r S_\pi^{[k]}]_{|r=1}$ ,  $[\partial_r f_0^{[k]}]_{|r=1}$ ,  $f_n^{[k]}$ , and  $\gamma_n^{[k]}$  for all  $n \geq 0$ . From Eqs. (3.2) and (3.5), the coefficient  $S^{[j]}(r, \theta)$  is given in terms of  $a_0^{[j]}$ ,  $j \geq 0$ :

$$S^{[j]}(r, \theta) = S_\pi^{[j]}(r) + \sum_{k=0}^j \frac{a_0^{[k]}}{2} f_0^{[j-k]}(r) + \sum_{n=1}^{\infty} \left( \sum_{k=0}^j a_n^{[k]} f_n^{[j-k]}(r) \right) \cos\left(\frac{n\pi\theta}{\phi}\right). \quad (3.50)$$

In the next section, I explain how the coefficients  $a_n^{[j]}$  can be expressed through the lower-order terms  $a_n^{[k]}$ ,  $0 \leq k \leq j-1$ .

### 3.1.4.1 Recurrence relation on the Fourier coefficients

I show that the Fourier coefficients satisfy a hierarchical set of equations, i.e., it is possible to express  $a_n^{[j]}$  in terms of the lower-order coefficients  $a_n^{[k]}$ ,  $n \geq 0$ , with  $k = 0, 1, \dots, j-1$ . The Fourier coefficients of the MFPT are obtained by setting  $p = 0$  in Eqs. (3.37a) and (3.37b):

$$t(r, \theta) = S_\pi^{(0)}(r) + \frac{a_0^{(0)}}{2} f_0^{(0)}(r) + \sum_{n=1}^{\infty} a_n^{(0)} f_n^{(0)}(r) \cos\left(\frac{n\pi\theta}{\phi}\right), \quad (r, \theta) \in \Omega. \quad (3.51)$$

For instance, one retrieves the exact explicit expression (3.14) for the MFPT of Brownian particles confined in an angular sector. In other geometries considered in Sec. 3.2, the exact resolution scheme requires a numerical solution of linear Eqs. (3.34) at  $p = 0$ .

According to Eq. (3.31), the unknown coefficients  $a_n^{[j]}$  are related to the unknown coefficients  $a_0^{[j]}$  and to the known lower-order coefficients  $a_n^{[k]}$ ,  $k = 1, 2, \dots, j-1$ ,

$$\sum_{m=1}^{\infty} (\delta_{nm} - M_{nm} \gamma_m^{[0]}) a_m^{[j]} = -2\alpha_n \left( [\partial_r S_\pi^{[j]}]_{|r=1} + \frac{1}{2} \sum_{k=0}^j a_0^{[j-k]} [\partial_r f_0^{[k]}]_{|r=1} \right) + \sum_{m=1}^{\infty} M_{nm} \left( \sum_{k=1}^j \gamma_m^{[k]} a_m^{[j-k]} \right). \quad (3.52)$$

In terms of the vector  $\tilde{\alpha}_n^{(0)}$  defined by Eq. (3.34) with  $p = 0$ , the matrix  $\tilde{M}$  is defined as

$$\tilde{M} \equiv (I - M \cdot \gamma^{(0)})^{-1} \cdot M. \quad (3.53)$$

where  $I$  stands for the identity matrix, and  $\gamma^{(0)}$  is a diagonal matrix formed by  $\gamma_n^{(0)}$ . In terms of the matrix  $\tilde{M}$ , Eq. (3.52) takes the form

$$a_n^{[j]} = -2\tilde{\alpha}_n^{(0)} \left( [\partial_r S_\pi^{[j]}]_{|r=1} + \frac{1}{2} \sum_{k=0}^j a_0^{[j-k]} [\partial_r f_0^{[k]}]_{|r=1} \right) + \sum_{m=1}^{\infty} \tilde{M}_{nm} \left( \sum_{k=1}^j \gamma_m^{[k]} a_m^{[j-k]} \right). \quad (3.54)$$

Substituting this expression into Eq. (3.30) leads to

$$a_0^{[j]} = \frac{-2\alpha_0 \left( [\partial_r S_\pi^{[j]}]_{|r=1} + \frac{1}{2} \sum_{k=1}^j a_0^{[j-k]} [\partial_r f_0^{[k]}]_{|r=1} \right) + \sum_{m=1}^{\infty} 2m\alpha_m T_m^{[j]}}{1 + [\partial_r f_0^{[0]}]_{|r=1} \left( \alpha_0 + \sum_{m=1}^{\infty} 2m\alpha_m \tilde{\alpha}_m^{(0)} \gamma_m^{[0]} \right)}, \quad (3.55)$$

where

$$T_m^{[j]} = \sum_{k=1}^j \gamma_m^{[k]} a_m^{[j-k]} + \gamma_m^{(0)} \left[ -2\tilde{\alpha}_m^{(0)} \left( \left[ \partial_r S_\pi^{[j]} \right]_{|r=1} + \frac{1}{2} \sum_{k=0}^j a_0^{[j-k]} \left[ \partial_r f_0^{[k]} \right]_{|r=1} \right) + \sum_{l=1}^{\infty} \tilde{M}_{ml} \left( \sum_{k=1}^j \gamma_l^{[k]} a_l^{[j-k]} \right) \right]. \quad (3.56)$$

Equation (3.55) expresses  $a_0^{[j]}$  in terms of the known coefficients  $a_n^{[k]}$ ,  $k = 1, 2, \dots, j-1$ . The coefficients  $a_n^{[j]}$  ( $n \geq 1$ ) are then determined through Eq. (3.54).

Following the idea of Sec. 3.1.2, I define an approximate scheme in which the matrix  $M$  is replaced by the identity matrix in Eqs. (3.37a), (3.37b) and (3.53). This approximation leads to Eq. (3.39) and solves Eq. (3.53) as

$$\tilde{M}_{nm} \approx \frac{M_{nm}}{1 - \gamma_n^{(0)}}. \quad (3.57)$$

I recall that the approximation  $M_{mn} = \delta_{mn}$  is exact in the limit  $\varepsilon = 0$  (see Eq. (3.38)).

In the next section, we focus on Brownian particles confined in an angular sector, in which case the recursive method of Eq. (3.55) provides an exact explicit expression for the variance and an exact computation scheme of the third and fourth moments.

### 3.1.4.2 Diffusion in angular sector: explicit exact moments

For Brownian particles confined in an angular sector, the coefficients  $\gamma_n^{(0)}$  are equal to zero. The recursive scheme provides thus an exact explicit expression for the moments of the exit time as the resolution of Eqs. (3.34) and (3.53) is straightforward. Following the method of Sec. 3.1.4.1, I obtain the second moment of the exit time by combining Eqs. (3.14) and (3.55):

$$\begin{aligned} \mathbb{E} \left[ \sigma_{(r,\theta)}^2 \right] &= \left[ \frac{1}{2} \left( \frac{\alpha_0 \pi}{\phi} \right)^2 + \frac{1}{8} \left( \frac{\alpha_0 \pi}{\phi} \right) (3 - 2r^2) + \frac{3 + r^4 - 4r^2}{32} + \sum_{m=1}^{\infty} \frac{\phi}{m\pi + \phi} \left( \frac{\alpha_m \pi}{\phi} \right)^2 \right] \\ &+ \sum_{n=1}^{\infty} \left[ \alpha_n \left( \frac{1}{4} + \alpha_0 \frac{\phi}{\pi} + \frac{\phi(1-r^2)}{2(n\pi + \phi)} \right) + \sum_{m=1}^{\infty} \frac{M_{nm} \phi^2}{m\pi(m\pi + \phi)} \alpha_m \right] \frac{\phi r^{n\pi/\phi}}{\pi} \cos \left( \frac{n\pi\theta}{\phi} \right). \end{aligned} \quad (3.58)$$

Subtracting the square of the MFPT defined in Eq. (3.14), I obtain the variance of the exit time for any starting position within the angular sector. I point out that the variance was previously known only in the narrow-escape limit  $\varepsilon \ll 1$  through its leading order term  $\alpha_0^2/4$  [101]. Figures 3.5 and 3.6 show the standard deviation, defined as the square root of the variance, as a function of the starting position  $(r, \theta)$  within the disk ( $\phi = \pi$ ) and an angular sector ( $\phi = \pi/3$ ), respectively.

The average of Eq. (3.58) over all starting positions within the angular sector (defined in Eq. (3.15)) leads to

$$\overline{\mathbb{E}[\sigma^2]} = \frac{1}{2} \left( \frac{\alpha_0 \pi}{\phi} \right)^2 + \frac{1}{4} \left( \frac{\alpha_0 \pi}{\phi} \right) + \frac{1}{24} + \sum_{m=1}^{\infty} \frac{1}{m\pi/\phi + 1} \left( \frac{\alpha_m \pi}{\phi} \right)^2. \quad (3.59)$$

On the other hand, the spatial average of Eq. (3.14) turns out to be

$$\overline{\mathbb{E}[\sigma]^2} = \frac{1}{2} \overline{\mathbb{E}[\sigma^2]}. \quad (3.60)$$

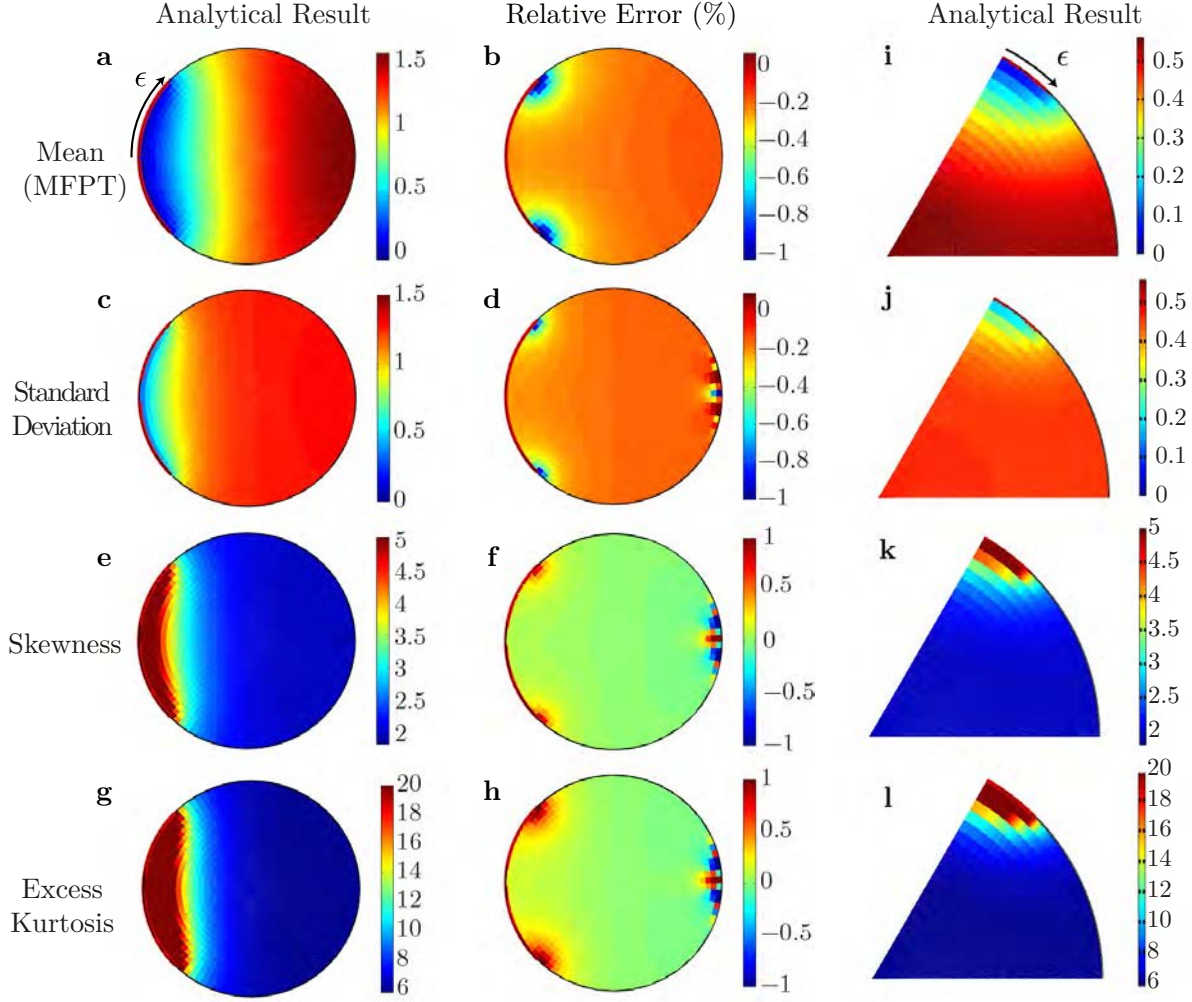


Figure 3.5: Mean, variance, skewness and excess kurtosis of the FPT for a Brownian particle confined in: a disk ( $\phi = \pi$ ) with the exit width  $2\epsilon = \pi/2$  shown by red line (**left column**), and an angular sector ( $\phi = \pi/3$ ) with an exit at the corner of the width  $\epsilon = \phi/4$  shown by red line (**right column**). The middle column (**b-d-f-h**) shows the relative error  $(X_n - X_a)/X_n$  between the analytical result  $X_a$  and a finite element method resolution  $X_n$ . The exit of half-width  $\epsilon = \pi/4$  is shown by red line. The relative error for the cumulants is the largest near the edges of the exit. Outside a boundary layer near to the exit, the first four moments are very close to those of an exponential distribution (for which the standard deviation is equal to the mean, while the skewness and excess kurtosis are equal to 2 and 6 respectively).

Combining these two results, one gets the following expression of the spatial average of the variance:

$$\overline{\text{Var}[\sigma]} = \overline{\mathbb{E}[\sigma]^2} = \frac{1}{4} \left( \frac{\alpha_0 \pi}{\phi} \right)^2 + \frac{1}{8} \left( \frac{\alpha_0 \pi}{\phi} \right) + \frac{1}{48} + \frac{1}{2} \sum_{m=1}^{\infty} \frac{1}{m\pi/\phi + 1} \left( \frac{\alpha_m \pi}{\phi} \right)^2. \quad (3.61)$$

The equality between the averaged variance and the averaged second moment,  $\overline{\text{Var}[\sigma]} = \overline{\mathbb{E}[\sigma]^2}$ , was previously obtained from general arguments [100].

I now consider the random variable  $\sigma_{\Omega}$ , defined as the exit time of a particle started at a random starting position, with uniform distribution within  $\Omega$ . Although the averaged moments

are identical,  $\overline{\mathbb{E}[\sigma^n]} = \mathbb{E}[\sigma_\Omega^n]$  (see Appendix A.2), the variance of  $\sigma_\Omega$ ,

$$\text{Var}[\sigma_\Omega] = \frac{1}{4} \left( \frac{\alpha_0 \pi}{\phi} \right)^2 + \frac{1}{8} \left( \frac{\alpha_0 \pi}{\phi} \right) + \frac{5}{192} + \sum_{m=1}^{\infty} \frac{1}{m\pi/\phi + 1} \left( \frac{\alpha_m \pi}{\phi} \right)^2. \quad (3.62)$$

is different from the spatially averaged variance of Eq. (3.61).

Following the method of Sec. 3.1.4.1, I compute the Fourier coefficient of the third moment from the Fourier coefficients of the two first moments. Similarly, I compute the fourth moment from the three first moments. I define the skewness  $\text{Ske}[\sigma_{(r,\theta)}]$  and the excess kurtosis  $\text{Kur}[\sigma_{(r,\theta)}]$  as

$$\text{Ske}[\sigma_{(r,\theta)}] = \mathbb{E} \left[ \left( \frac{\sigma - \mathbb{E}[\sigma]}{\sqrt{\mathbb{E}[\sigma^2] - \mathbb{E}[\sigma]^2}} \right)^3 \right]; \quad \text{Kur}[\sigma_{(r,\theta)}] = \mathbb{E} \left[ \left( \frac{\sigma - \mathbb{E}[\sigma]}{\sqrt{\mathbb{E}[\sigma^2] - \mathbb{E}[\sigma]^2}} \right)^4 \right] - 3. \quad (3.63)$$

Figures 3.5 and 3.6 show the skewness and the excess kurtosis for a Brownian particle confined in a disk and an angular sector, respectively. The lower bounds for the skewness and kurtosis are respectively 2 and 6, e.g. the values of the skewness and excess kurtosis of an exponential distribution. A positive skewness indicates that the distribution of exit times is always skewed to the right of the MFPT. The distribution is also leptokurtic, meaning that the excess kurtosis is positive: very long residence times occur more frequently than predicted by a Gaussian distribution.

The ratio of the standard deviation to the mean, the skewness, and the excess kurtosis diverge when the distance between the starting position and the center of the exit tends to zero. This is consistent with the short-time behavior of the FPT distribution.

### 3.1.4.3 Moments in the narrow-escape limit: the case of the disk

The argument of Ref. [101] holds in the narrow-escape limit  $\varepsilon \ll 1$  and for an starting position  $\mathbf{r}$  away from the frontier of the confining domain  $\Omega$ . Under these two assumptions, one expects the set  $(\mathbb{E}[\sigma_{(r,\theta)}^n])$ ,  $n \geq 1$  to converge to the set  $(n! \mathbb{E}[\sigma_{(r,\theta)}])$ ,  $n \geq 1$  which are the set of moments of an exponential distribution of mean  $\mathbb{E}[\sigma_{(r,\theta)}]$ .

Figure 3.6 shows the first four cumulants of the exit time in the case  $\varepsilon = \pi/60$  in the boundary of an unit disk. Following the argument of Ref. [92], I introduce

$$\delta = -\varepsilon \ln \left( \frac{\varepsilon}{2} \right), \quad (3.64)$$

and define the boundary layer  $\mathcal{B}[(1, \pi), \delta]$  as the intersection of  $\Omega$  with the disk of radius  $2\delta$  centered on the exit  $(r, \theta) = (1, \pi)$  (i.e. the area enclosed by the dashed line in Fig. 3.6). For a starting position  $(r, \theta) \in \Omega \setminus \mathcal{B}[(1, \pi), \delta]$  outside the boundary layer, the ratio of the standard deviation to the MFPT is close to 1, while the skewness and excess kurtosis are respectively close to 2 and 6, as for an exponential distribution. As a consequence, for a sufficiently small exit and for a starting position  $(r, \theta) \in \Omega \setminus \mathcal{B}[(1, \pi), \delta]$  outside the boundary layer, the exit time follows approximately an exponential distribution whose mean is the MFPT defined by Eq. (3.14). This observation extends the predictions of Ref. [101].

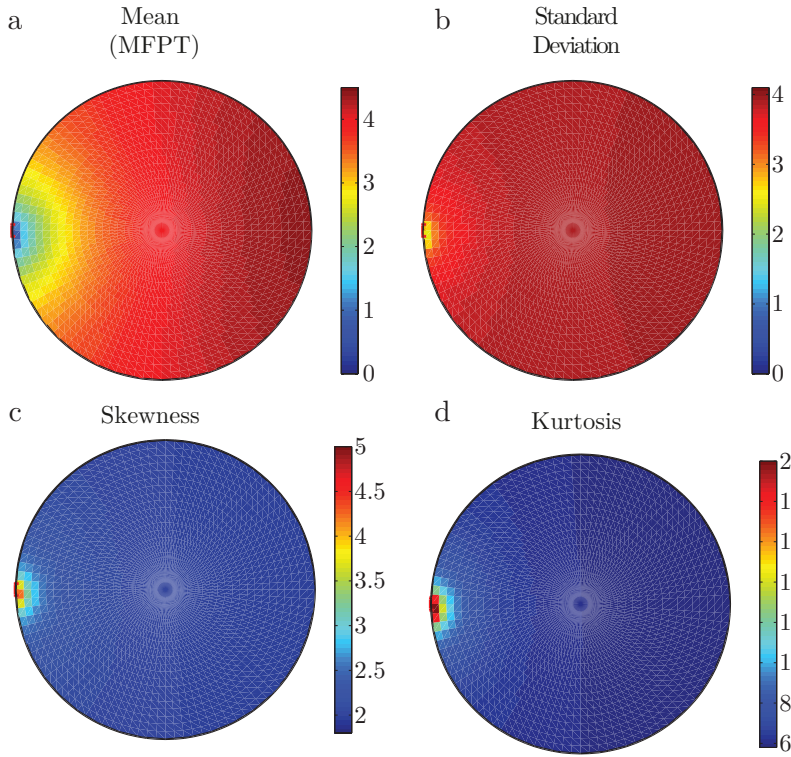


Figure 3.6: First four cumulants of the exit time from a disk for  $\varepsilon = \pi/60$ : (a) MFPT; (b) standard deviation; (c) skewness; (d) excess kurtosis. The dashed line shows the boundary layer, i.e. the region enclosed within the disk of radius  $2\varepsilon \ln(\varepsilon/2)$ . Note that outside the boundary layer, (i) the standard deviation is approximately equal to the MFPT, and (ii) the skewness and excess kurtosis are approximately equal to 2 and 6 that correspond to an exponential distribution.

## 3.2 Extensions and applications

In this section, I discuss various applications of our approach. First, I apply the general framework of Sec. 3.1 to consider the exit time for a Brownian particle from annuli (Sec. 3.2.1). Second, I extend the method of Sec. 3.1 to obtain the FPT distribution for particles moving according to radial advection-diffusion (Sec. 3.2.2). I also show the applicability of this method to the FPT problems in rectangles (3.2.3). Finally, I briefly discuss the analogies of the FPT problem to microchannel flows (Sec. 3.2.4). Table 3.2 summarizes explicit expressions of the functions  $S_\pi^{(p)}(r)$  and  $f_n^{(p)}$  for each considered domain. Using Table 3.2 to compute the Fourier coefficients in Eqs. (3.37a) and (3.37b), one gets the FPT distribution for each considered geometry. In addition, the recursive scheme in Eq. (3.55) provides all the moments of the exit time.

► Our approximate expressions for the MFPT are summarized in Table 3.3.

### 3.2.1 Annuli

I consider the confining domain  $\Omega$  to be an annulus with concentric circular boundaries at  $r = R = 1$  and  $r = R_c$ :  $\Omega = \{(r, \theta) \in \mathbb{R}^2 : R_c < r < 1, 0 \leq \theta < 2\pi\}$  for  $R_c < 1$  (the exit is located on the outer boundary) or  $\Omega = \{(r, \theta) \in \mathbb{R}^2 : 1 < r < R_c, 0 \leq \theta < 2\pi\}$  for  $R_c > 1$  (the exit is located on the inner boundary). The boundary at  $r = R_c$  is fully reflecting, while the boundary at  $r = 1$  is reflecting except for an absorbing arc of length  $2\varepsilon$ , as illustrated in Fig. 3.8(b).

#### 3.2.1.1 Distribution of the first passage time

In Fig. 3.7 we represent the FPT probability density  $\tilde{\rho}^{(t)}(r, \theta)$  for an annulus with  $R_c = 0.70$  and an exit of half-size  $\varepsilon = \pi/24$ , with three starting positions:  $(r, \theta) = (0.90, \pi)$ ,  $(0.90, \pi/2)$ , and  $(0.90, 0)$ . The exact, approximate and numerical schemes agree well in the whole range of times.

Case	Quantity	Series expansion in $p \ll 1$
Full disk (no bias) Sec. 3.1	$S_\pi^{(p)}(r) = \frac{1}{p} \left( 1 - \frac{I_0[\sqrt{pr}]}{I_0[\sqrt{p}]} \right)$ $f_n^{(p)}(r) = \frac{I_n(\sqrt{pr})}{I_n(\sqrt{p})}$ $\gamma_n^{(p)} = 1 - \frac{\sqrt{p} I_{n-1}(\sqrt{p}) + I_{n+1}(\sqrt{p})}{2n I_n(\sqrt{p})}$	$\frac{1-r^2}{4} + \frac{(-3+4r^2-r^4)}{64}p$ $r^n \left( 1 + \frac{(r^2-1)p}{4(1+n)} \right)$ $-\frac{p}{2n(n+1)}$
Angular Sector half-width $\phi$ Sec. 3.1	$S_\pi^{(p)}(r) = \frac{1}{p} \left( 1 - \frac{I_0[\sqrt{pr}]}{I_0[\sqrt{p}]} \right)$ $f_n^{(p)}(r) = \frac{\phi}{\pi} \frac{I_{n\pi/\phi}(\sqrt{pr})}{I_{n\pi/\phi}(\sqrt{p})}$ $\gamma_n^{(p)} = 1 - \frac{\sqrt{p} I_{n\pi/\phi-1}(\sqrt{p}) + I_{n\pi/\phi+1}(\sqrt{p})}{2n I_{n\pi/\phi}(\sqrt{p})}$	$\frac{1-r^2}{4} + \frac{(-3+4r^2-r^4)}{64}p$ $\frac{\phi r^{\frac{n\pi}{\phi}}}{\pi} \left( 1 + \frac{(r^2-1)\phi p}{4(n\pi+\phi)} \right)$ $-\frac{p\phi}{2n\pi \left( \frac{n\pi}{\phi} + 1 \right)}$
Full Disk with bias: $\vec{v}(r) = \frac{\mu D}{r^2} \mathbf{r}$ Sec. 3.2.2	$S_\pi^{(p)}(r) = \frac{1}{p} - \frac{r^{-\frac{\mu}{2}} I_{\mu/2}(\sqrt{pr})}{p I_{\mu/2}(\sqrt{p})}$ $f_n^{(p)}(r) = r^{-\frac{\mu}{2}} \frac{I_{\mu_n}(\sqrt{pr})}{I_{\mu_n}(\sqrt{p})}$ <p>where <math>\mu_n = \sqrt{n^2 + \left(\frac{\mu}{2}\right)^2}</math></p> $\gamma_n^{(p)} = 1 - \frac{[\partial_r f_n^{(p)}]_{r=1}}{n}$	$(1-r^2) \left( \frac{1}{2(2+\mu)} + p \frac{(-6-\mu+(2+\mu)r^2)}{8(2+\mu)^2(4+\mu)} \right)$ $r^{(\mu_n-\mu)/2} \left( 1 + p \frac{r^2-1}{2(2+\mu_n)} \right)$ $1 + \frac{\mu}{2n} - \frac{\mu_n}{n} - \frac{p}{2n(1+\mu_n)}$
Annuli Sec. 3.2.2	$\rho_n(\sqrt{pr}) \equiv \frac{I_n[\sqrt{pr}]}{I_n[\sqrt{p}]}, \quad \nu_n(\sqrt{pr}) \equiv \frac{K_n[\sqrt{pr}]}{K_n[\sqrt{p}]}$ $S_\pi^{(p)}(r) = \frac{1}{p} - \frac{1}{p} \frac{\rho_0(\sqrt{pr}) - \frac{\rho'_0(\sqrt{pr})}{\nu'_0(\sqrt{p}R_c)} \nu_0(\sqrt{pr})}{1 - \frac{\rho'_0(\sqrt{pr})}{\nu'_0(\sqrt{p}R_c)}}$ $f_n^{(p)}(r) = \frac{\rho_n(\sqrt{pr}) - \frac{\rho'_n(\sqrt{p}R_c)}{\nu'_n(\sqrt{p}R_c)} \nu_n(\sqrt{pr})}{1 - \frac{\rho'_n(\sqrt{p}R_c)}{\nu'_n(\sqrt{p}R_c)}}$ $\gamma_n^{(p)} = 1 - \frac{[\partial_r f_n^{(p)}]_{r=1}}{n}$	$\frac{1}{4} (1 - r^2 + 2R_c^2 \log(r))$ $\frac{r^{2n} + R_c^{2n}}{r^n(1+R_c^{2n})} + \mathcal{O}(p^2)$ $\frac{2R_c^{2n}}{1+R_c^{2n}}$
Rectangle of width $\phi = \pi$ Sec. 3.2.3	$S_\pi^{(p)}(r) = \frac{1}{p} \left( 1 - \frac{\cosh(\sqrt{pr})}{\cosh(\sqrt{p}R)} \right)$ $f_n^{(p)}(r) = \frac{\cosh(\sqrt{p+n^2} r)}{\cosh(\sqrt{p+n^2} R)}$ $\gamma_n^{(p)} = 1 - \frac{\sqrt{p+n^2} \tanh(\sqrt{p}R)}{n}$	$\frac{R^2-r^2}{2} + \frac{1}{24} (-r^4 + 6r^2R^2 - 5R^4) p$ $\frac{\cosh(nr)}{\cosh(nR)}$ $(1 - \tanh(nR)) - \frac{\left( \frac{nR}{\cosh(nR)^2} + \tanh(nR) \right) p}{2n^2}$

3. FPT in 2D spherically symmetric domains

Table 3.2: Summary of the quantities involved in the computation of the Laplace transform of the survival probability in five studied geometries. The functions  $f_n$  are defined for all  $n \geq 0$  while the functions  $\gamma_n$  are defined for all  $n \geq 1$ .

The short-time behavior of the FPT distribution strongly depends on the initial position of the particle. If the starting position is far from the exit [e.g.  $(r, \theta) = (0.90, 0)$ ], the FPT probability density is negligible up to time  $t \approx R^2/D = 1$ . For a starting position that is within the boundary layer defined in Sec. 3.1.4.2 [e.g.  $(r, \theta) = (0.90, \pi)$ ], the FPT probability



Case	MFPT
Angular Sector of half-width $\phi$ Sec. 3.1 Fig. 3.1	$a_0^{(0)} = \alpha_0 \equiv -2 \ln \left[ \sin \left( \frac{\varepsilon\pi}{2\phi} \right) \right],$ $a_n^{(0)} = \alpha_n \equiv \frac{(-1)^{n-1}}{2n} \left[ P_n \left( \cos \frac{\varepsilon\pi}{\phi} \right) + P_{n-1} \left( \cos \frac{\varepsilon\pi}{\phi} \right) \right],$ $t(r, \theta) \equiv \mathbb{E} [\sigma_{(r, \theta)}] = \frac{1-r^2}{4} + \frac{\alpha_0}{2} \frac{\phi}{\pi} + \frac{\phi}{\pi} \sum_{n=1}^{\infty} \alpha_n r^{n\pi/\phi} \cos \left( \frac{n\pi\theta}{\phi} \right),$ $\overline{\mathbb{E} [\sigma]} = \frac{1}{8} + \frac{\alpha_0}{2} \frac{\phi}{\pi}.$
Disk with bias Sec. 3.2.2 Fig. 3.9	$a_0^{(0)} \approx \frac{2}{2+\mu} \left\{ \alpha_0 + \sum_{k=1}^{\infty} 2k \left[ -1 + \frac{\mu}{2k} + \sqrt{1 + \left( \frac{\mu}{2k} \right)^2} \right] \alpha_k^2 \right\}$ $a_n^{(0)} \approx \frac{2}{2+\mu} \frac{\alpha_n}{\sqrt{1 + \left( \frac{\mu}{2n} \right)^2 - \frac{\mu}{2n}}}$ $\overline{\mathbb{E} [\sigma]} \approx \frac{1}{2+\mu} \left\{ \alpha_0 + \sum_{k=1}^{\infty} 2k \left[ -1 + \frac{\mu}{2k} + \sqrt{1 + \left( \frac{\mu}{2k} \right)^2} \right] \alpha_k^2 \right\} + \frac{1}{4(2+\mu)}$
Annuli Sec. 3.2.2 Fig. 3.8	$a_0^{(0)} \approx (1 - R_c^2) \left[ \alpha_0 + \sum_{k=1}^{\infty} \left( \frac{2R_c^{2k}}{R_c^{2k}-1} \right) 2k \alpha_k^2 \right]$ $a_n^{(0)} \approx (1 + R_c^{2n}) \frac{1-R_c^2}{1-R_c^{2n}} \alpha_n$ $\overline{\mathbb{E} [\sigma]} \approx \frac{1-R_c^2}{2} \left[ \alpha_0 + \sum_{k=1}^{\infty} \left( \frac{R_c^{2k}}{R_c^{2k}-1} \right) 4k \alpha_k^2 \right] + \frac{1}{8} (1 - 3R_c^2) + \frac{1}{2} \frac{R_c^4 \ln(R_c)}{R_c^2-1}.$
Rectangle of width $\phi = \pi$ Sec. 3.10	$a_0^{(0)} \approx 2R \left\{ \alpha_0 + \sum_{k=1}^{\infty} [-1 + \coth(kR)] 4k \alpha_k^2 \right\}$ $a_n^{(0)} \approx \frac{2R}{\coth(nR)} \alpha_n$ $\overline{\mathbb{E} [\sigma]} \approx R \left\{ \alpha_0 + \sum_{k=1}^{\infty} [-1 + \coth(kR)] 4k \alpha_k^2 \right\} + \frac{R^2}{3}$

Table 3.3: Summary of the result on the MFPT in five studied geometries.

density is sharply picked at  $t \approx x_0^2/D = 1$ , where  $x_0$  is the distance to the center of the exit. In contrast, the long-time behavior ( $t \gg R^2/D$ ) of the FPT probability density is independent of the initial position.

In the next section, we obtain an explicit approximate expression for the MFPT. Using this approximate expression we find that the MFPT is an optimizable function of  $R_c$  under analytically determined criteria.

### 3.2.1.2 Approximate expression for the MFPT

We substitute  $\mathcal{C}^{(0)}$  by  $\mathcal{C}_a^{(0)}$  from Eq. (3.40) into Eqs. (3.37a) and (3.37b) and use the expressions of Table 3.2 to get the approximate expression for the MFPT given in table. 3.3.

Notice that for  $R_c = 0$ , we retrieve the exact Eqs. (3.14) and (3.15). Let us now compare the approximate solution to previously known results in two limits  $R_c \rightarrow 1$  and  $R_c \gg 1$ . This comparison provides an error estimate of the approximate solution in the limit  $\varepsilon \ll 1$ .

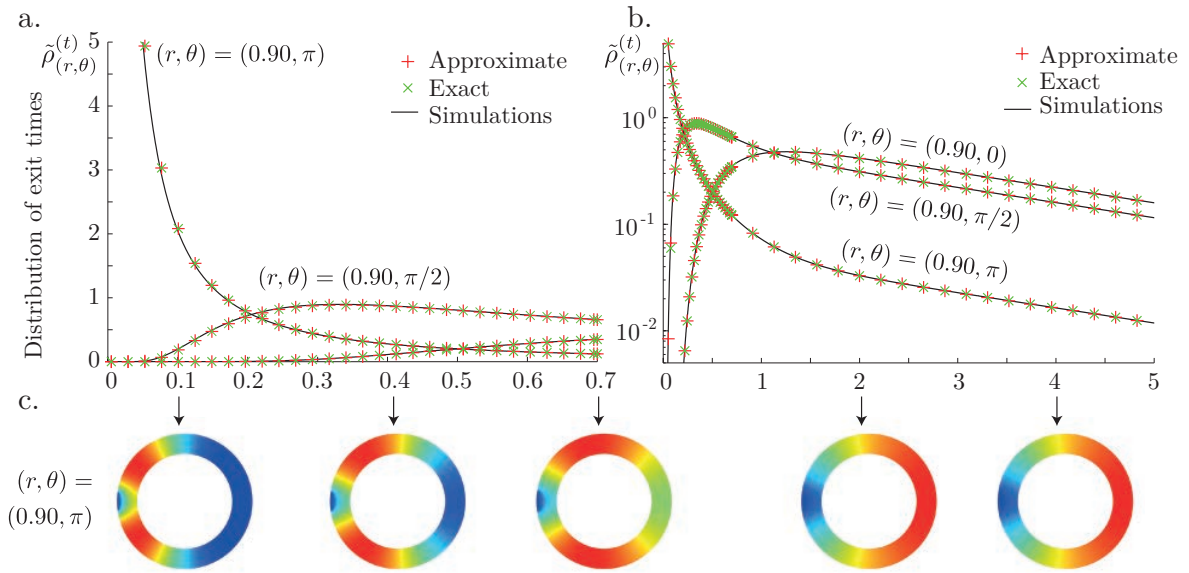


Figure 3.7: **Upper panel:** The probability density of the FPT to exit an annulus between two circles of radii  $R_c = 0.7$  and  $R = 1$  through an exit of half-width  $\varepsilon = \pi/24 \approx 0.13$  within the outer radius  $R$ , for a Brownian particle started at  $(r, \theta) = (0.90, \pi)$ ,  $(0.90, \pi/2)$ ,  $(0.90, 0)$ . The FPT probability density is shown in (a) linear scale for  $t \in [0, 0.7]$ , and (b) log-linear scale for  $t \in [0, 6]$ . The exact solution from Eqs. (3.37a) and (3.37b) (green crosses) is compared to its analytical approximation from Sec. 3.1.2.3 (red pluses) and a finite element method numerical solution (black solid line). **Lower panel:** Diffusive propagator  $\tilde{G}^{(t)}(\mathbf{r}_0, \mathbf{r})$  computed by a FEM at times  $t = 0.1, 0.4, 0.7, 2, 4$  for the initial position  $(r, \theta) = (0.90, \pi)$ . Color changes from dark red to dark blue correspond to changes of the diffusive propagator from large to small values. After a time  $t > R^2/D = 1$ , the diffusive propagator reaches a steady state profile, and the FPT distribution agrees well with an exponential distribution with the decay rate constant  $p_1$ .

(i) In the limit  $R_c \rightarrow 1$ , using the identity

$$\sum_{m=1}^{\infty} 2m\alpha_m^2 = \alpha_0, \quad (3.65)$$

which is valid for any value of  $\varepsilon$  (and proved in Appendix A.1.5), we show that the approximate expression for the MFPT (defined in Eq. (3.51)) is

$$\mathbb{E}[\sigma_{(r,\theta)}] = \frac{1}{2}(\pi - \theta)(\pi + \theta) + \mathcal{O}(1 - R_c), \quad \theta \in [0, \pi - \varepsilon]. \quad (3.66)$$

The approximate expression is equal to the MFPT of a purely one-dimensional process up to  $\mathcal{O}(\varepsilon)$  terms. The average of Eq. (3.66) over all angles  $\theta \in [0, \pi]$  is equal to  $\pi^3/(3\pi)$ , which is close to the exact result  $(\pi - \varepsilon)^3/(3\pi)$ . Note that asymptotic formulas of Ref. [92] on the MFPT in 2D domains are not valid in the limit  $R_c \rightarrow 1$ .

(ii) In the large volume limit  $R_c \gg 1$ , we use Eq. (3.65) to show that the first Fourier coefficient of the MFPT reads

$$a_0^{(0)} \approx (R_c^2 - 1)(\alpha_0 + 4R_c^{-2}) + \mathcal{O}(1/R_c^4). \quad (3.67)$$

In the limit  $\varepsilon \ll 1$ , the latter expansion can be identified with the result of Ref. [105] (p. 503) which is shown to be exact up to a  $\mathcal{O}(\varepsilon)$  term.

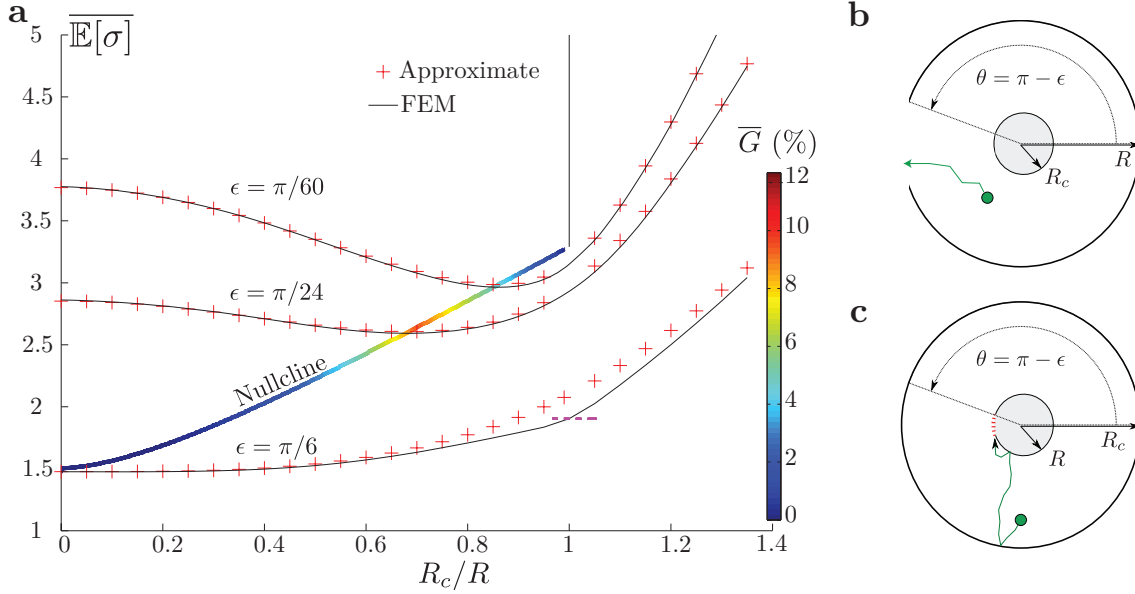


Figure 3.8: (a) GMFPT to an exit of half-width  $\epsilon$  for a Brownian particle confined in an annulus  $\Omega$  of radii  $R_c$  and  $R = 1$  (illustrated by (b) for  $R_c > R$  and (c) for  $R_c < R$ ). The approximate solution (red pluses), defined in Table 3.3, is compared to finite element method simulations (black solid line). The 1D GMFPT from Eq. (3.66),  $(\pi - \epsilon)^3/(3\pi)$ , is shown by magenta dotted line for  $\epsilon = \pi/6$ . The colored solid line indicates the loci of the minima of the GMFPT, with the color code being a function of the gain  $\overline{G}$ , defined by Eq. (3.70). The gain has a sharp maximum  $G \approx 10\%$  for  $R_c^{(c)} = 0.70$  and  $\epsilon = 0.13 \ll 1$ . (b,c) Two annuli with  $R_c < 1$  (b) and  $R_c > 1$  (c). The Brownian particle shown by green circle diffuses in the annulus before crossing the exit of half-width  $\epsilon$ .

### 3.2.1.3 Optimization of the GMFPT

Now we focus on the GMFPT  $\overline{\mathbb{E}[\sigma]}$  defined in Eq. (2.19). In Fig. 3.8, we present the GMFPT as a function of  $R_c$  for different exit sizes  $\epsilon$ . Interestingly, for small enough exit sizes  $\epsilon < \epsilon_c$ , the GMFPT is minimized for a specific value of the reflecting boundary radius  $R_c^{(c)} < 1$ .

In the narrow-escape limit  $\epsilon \ll 1$ ,  $R_c^{(c)} = 1$  is a global minimum of the GMFPT: the GMFPT at  $R_c = 1$  converges to  $\pi^2/3$  while the GMFPT diverges logarithmically with  $\epsilon \ll 1$  for any other value of  $R_c \neq 1$ . For increasing values of  $\epsilon$ , the global minimum of the GMFPT is reached at smaller values  $R_c^{(c)} < 1$ . Eventually, the minimum  $R_c^{(c)} = 0$  emerges for exit sizes larger than a threshold:  $\epsilon_c \simeq 0.51$ .

We determine an approximate value for the threshold  $\epsilon_c$  based on the approximate expression for the GMFPT in Table 3.3, p. 70. We first notice that for all  $R_c \geq 1$ , the GMFPT is a monotonically increasing function of  $R_c$ , hence  $R_c^{(c)} \leq 1$ . We define  $\epsilon_c$  as the largest value of  $\epsilon$  such that the GMFPT is a locally decreasing function at  $R_c = 0$ . This local condition is fulfilled if and only if the second derivative of the GMFPT  $\overline{\mathbb{E}[\sigma]}$  is negative at  $R_c = 0$ , leading to the following criterion on  $\epsilon_c$ :

$$\alpha_0(\epsilon_c) = 4\alpha_1(\epsilon_c) - \frac{3}{4}, \quad (3.68)$$

where  $\alpha_0$  and  $\alpha_1$  are given in Eqs. (3.12a) and (3.12b). Assuming  $\epsilon_c \ll 1$ , Eq. (3.68) can be solved explicitly to get

$$\epsilon_c \approx \exp\left(\frac{8 \ln(2) - 13}{16}\right) \approx 0.60, \quad (3.69)$$

In turn, the numerical solution of Eq. (3.68) yields  $\varepsilon_c \simeq 0.51$  which is close to the above estimate.

One may ask how much time can be gained by setting  $R_c$  to the optimal  $R_c^{(c)}$ ? We define the gain  $\bar{G}$  as

$$\bar{G} = \frac{\min\left(\overline{\mathbb{E}[\sigma]}_{R_c=0}, \overline{\mathbb{E}[\sigma]}_{R_c=1}\right) - \overline{\mathbb{E}[\sigma]}_{R_c^{(c)}}}{\min\left(\overline{\mathbb{E}[\sigma]}_{R_c=0}, \overline{\mathbb{E}[\sigma]}_{R_c=1}\right)}, \quad (3.70)$$

so that  $\bar{G}$  lies between 0 and 1. The loci of the minima of the GMFPT are the set of points  $(R_c^{(c)}, \overline{\mathbb{E}[\sigma]}_{R_c^{(c)}})$  which are shown in Fig. 3.8 and colored according to the gain  $\bar{G}$ .

The gain has a sharp maximum  $G \approx 10\%$  for  $R_c^{(c)} \simeq 0.70$  and  $\varepsilon \simeq 0.13 \ll 1$ . Notice that the optimal gain is obtained for a value of  $\varepsilon$  such that the GMFPT at  $R_c = 0$  is approximately equal to the GMFPT at  $R_c = 1$ . The optimal  $R_c^{(c)}$  results from a trade-off between two competing geometrical effects: (i) increasing  $R_c \ll R$  reduces the accessibility to the exit for remote particles which have to circumvent the reflecting boundary at  $r = R_c$ ; and (ii) once a particle is close to the exit, increasing  $R_c$  increases the probability for the particle to cross the exit.

### 3.2.2 Advection-diffusion with a radial bias

We consider a diffusive particle confined in a disk of radius  $R$  whose motion is biased by a  $1/r$  velocity field  $\vec{v}(r)$ . The velocity field  $\vec{v}(r)$  is characterized by a dimensionless parameter  $\mu$ :

$$\vec{v}(r) = \frac{\mu D}{r^2} \mathbf{r}. \quad (3.71)$$

Note that  $\mu > 0$  corresponds to an outward drift. Setting units by  $R = 1$  and  $D = 1$ , the backward diffusion Eq. (3.1a) on the survival probability reads

$$\left(\Delta + \frac{\mu}{r} \partial_r\right) S^{(p)}(r, \theta) = p S^{(p)}(r, \theta) - 1, \quad r \in [0, 1), \quad \theta \in [0, 2\pi). \quad (3.72)$$

A separation of variables method provides the set  $f_n^{(p)} \cos(n\theta)$  of solutions for Eq. (3.72), see Table 3.2.

The approximate for the MFPT defined Sec. 3.1.2.3 is given in table. 3.3. In Fig. 3.9, we compare the approximate MFPT  $\mathbb{E}[\sigma_0]$  (for a particle started at  $r = 0$ ) to the result obtained by a finite element method. The MFPT diverges for all  $\mu \leq -2$ : the inward drift strongly confines particles at  $r = 0$ . In the limit  $\mu \gg 1$ , the MFPT converges to the MFPT of a 1D process given by Eq. (3.66), up to a small  $\mathcal{O}(\varepsilon)$  correction. The MFPT is a monotonically decreasing functions of  $\mu$ , as illustrated in Fig. 3.9(a), and there is no optimal drift which minimizes the MFPT.

### 3.2.3 Rectangles

We consider the confining domain  $\Omega$  to be a rectangle  $\Omega = [0, R] \times [0, \phi]$  with reflecting edges at  $r = 0$ ,  $\theta = 0$  and  $\theta = \phi$ . The boundary at  $r = R$  is reflecting except for an absorbing segment of length  $\varepsilon$  at the corner, as illustrated in Fig. 3.10(b). Setting units by  $\phi = \pi$  and  $D = 1$ , the Helmholtz equation on the survival probability reads [113, 18]

$$\left(\frac{\partial^2}{\partial r^2} + \frac{\partial^2}{\partial \theta^2}\right) S^{(p)}(r, \theta) = p S^{(p)}(r, \theta) - 1 \quad (r, \theta) \in \Omega. \quad (3.73)$$

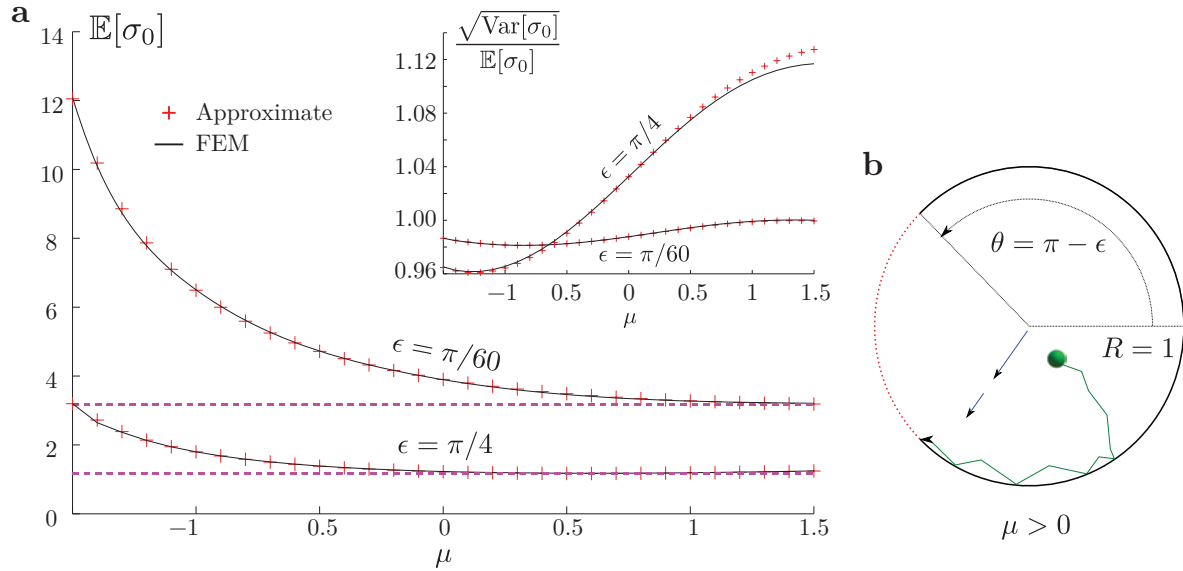


Figure 3.9: (a) The MFPT  $\mathbb{E}[\sigma_0]$  to an exit of half-width  $\epsilon = \pi/4$  for Brownian particles whose diffusive motion is biased by a  $1/r$  velocity field  $\vec{v}(r) = \mu D \mathbf{r}/r^2$ . Particles are started at  $r = 0$  inside the unit disk [as sketched in (b)]. The analytical approximation (red pluses), defined in Table 3.3, p. 70, is compared to a finite element method (denoted FEM, black solid line). The 1D GMFPT from Eq. (3.66), i.e.,  $(\pi - \epsilon)^3/(3\pi)$ , is shown by horizontal magenta dashed lines. The ratio of the standard deviation to the MFPT is represented in the inset. Note that the smaller the  $\epsilon$ , the closer this ratio is to 1. (b) A Brownian particle (shown by green circle) is advected by a radial flow field  $\vec{v}(r) = \mu D \mathbf{r}/r^2$ , with  $\mu > 0$  corresponding to an outward drift (blue arrows). The particle is reflected by the boundary at  $r = 1$  before crossing the exit (shown by red dashed line) of half width  $\epsilon = \pi/4$ .

The approximate for the MFPT defined Sec. 3.1.2.3 is given in Table. 3.3. Notice that in the limit  $R \ll \phi = \pi$ , the GMFPT converges to the GMFPT of a 1D process given by Eq. (3.66), up to small  $\mathcal{O}(\epsilon)$  correction. In the opposite limit  $R \gg 1$ , the relation

$$-1 + \coth(kR) = -1 + \frac{1 + \exp(-2kR)}{1 - \exp(-2kR)} = 2\beta^2 + \mathcal{O}(\beta^4) \quad (3.74)$$

with  $\beta = \exp(-R)$ , leads to

$$a_0^{(0)} \approx 4R \left[ \ln \left( \frac{2}{\epsilon} \right) + 2\beta^2 \right] + \mathcal{O}(\beta^4) \quad (3.75)$$

in the small  $\epsilon \ll 1$  limit. The latter expression can be identified with the result presented in [105] (p. 496), which is shown to be exact up to a  $\mathcal{O}(\epsilon)$  term.

### 3.2.4 Analogy to microchannel flows

Large pressure drops are necessary to cause liquid flow in microchannels due to viscous dissipation at the boundary (no-slip condition). In order to increase the flow rate (at a given pressure drop), one can introduce ultra-hydrophobic grooves so that the layer of gas trapped within the grooves would act as an air-cushion for the fluid flow [107, 108]. We consider an array of ultra-hydrophobic grooves aligned in the direction of the pressure drop  $z$  obtained by a periodic repetition of a fundamental cell of width  $\theta = 2\phi$ . The floor of the microchannel is at the depth  $r = R$  (see Fig. 3.11). The top surface at  $r = 0$  can be assumed to be either (i) a free surface such that the shear stress is equal to zero, or (ii) a no-slip surface (as considered in Ref. [106]).

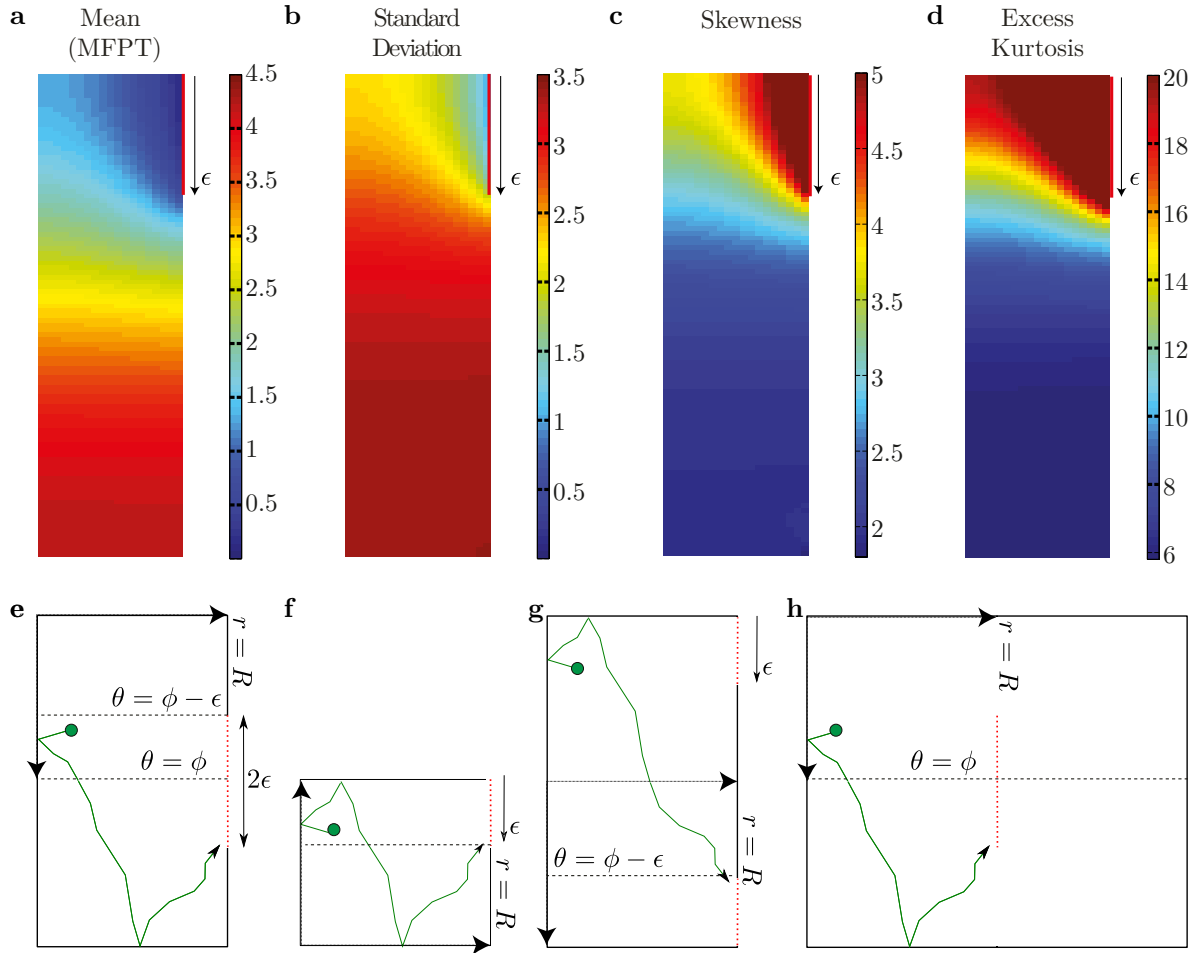


Figure 3.10: **Upper panel:** The cumulants of the exit time as functions of the starting position of the Brownian particle within the rectangle  $\Omega = [0, R] \times [0, \phi]$  with  $R = 1$  and  $\phi = \pi$ . The exit (shown by red line and an arrow) is a linear segment of total width  $\epsilon = \pi/4$  on the edge of length  $\pi$ . The cumulants computed through the approximate resolution (defined in Table 3.3, p. 70): (a) MFPT; (b) standard deviation; (c) skewness; and (d) excess kurtosis. **Lower panel:** The distribution of the FPT is identical for the four cases: (e) rectangle  $\Omega = [0, R] \times [0, 2\phi]$  with reflecting walls, pierced by a centered opening of width  $2\epsilon$ ; (f) rectangle  $\Omega = [0, R] \times [0, \phi]$  with reflecting walls, pierced by an opening of width  $\epsilon$  located in a corner; (g) rectangle  $\Omega = [0, R] \times [0, 2\phi]$  with reflecting walls, pierced by two cornered openings, each of width  $\epsilon$ ; and (h) rectangle  $\Omega = [0, 2R] \times [0, 2\phi]$  with reflecting walls and a centered linear absorbing region (vertical red dashed line) of total width  $2\epsilon$ . Green circle represents the position of a particle in these rectangles.

In the case of a no-slip condition at  $r = R$  (case (ii)) and in the limit  $R \gg \phi$ , an exact solution of the stationary flow was found in terms of the set  $(\alpha_n)$  defined in Eqs. (3.12a) and (3.12b) [106]. In this section we show how our method can be adapted to provide: (i) an approximate solution for the flow which is accurate for any value of  $R$ , and (ii) an exact resolution scheme as well as an approximate explicit expression for a time-dependent problem, i.e., the evolution of the flow from a given radial profile at  $t = 0$  to the steady state profile at  $t = \infty$ .

The flow is assumed to be (i) Newtonian and incompressible, (ii) at zero Reynolds number, (iii) in the absence of external force (e.g. gravitational force), and (iv) under a constant pressure gradient  $\frac{\partial p}{\partial z} = q$ . Under these assumptions the Navier-Stokes equation on the velocity profile

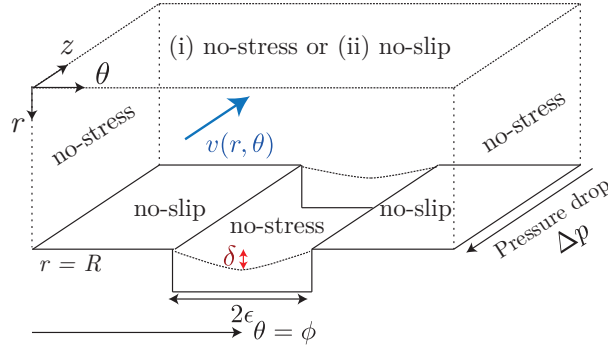


Figure 3.11: Scheme of the microchannel flow problem, in which the floor of a channel of depth  $R$  contains a large number of regularly spaced grooves of width  $2\epsilon$  parallel to the flow direction ( $0z$ ). This structure can be modeled by the periodic repetition of a fundamental cell of width  $2\phi$ , resulting in a no-shear condition  $\theta = 0$  and  $\theta = 2\phi$ . The shear stress is assumed to be zero along the free surfaces within the groove at  $r = R$  (the free surface lies above trapped gas phase). In turn, non-slip boundary condition is imposed on the remaining part of the groove. The top surface at  $r = 0$  can be assumed to be: (i) a free surface along which the shear stress is assumed to be zero (ii) a no-slip surface (i.e. the case considered in Ref. [106]). The problem consists in determining the stationary velocity profile  $v^{(\infty)}(r, \theta)$  for an incompressible Newtonian fluid at low Reynolds numbers and under constant pressure drop.

$\tilde{v}^{(t)}(r, \theta)$  reads as

$$\rho \frac{\partial \tilde{v}^{(t)}(r, \theta)}{\partial t} = \mu \Delta \tilde{v}^{(t)}(r, \theta) + q, \quad (r, \theta) \in [0, R] \times [0, 2\phi], \quad (3.76)$$

where  $\rho$  is the mass density of the fluid and  $\mu$  its viscosity. In dimensionless variables  $\theta \leftarrow \pi\theta/\phi$ ,  $R \leftarrow \pi R/\phi$ ,  $\tilde{v}^{(t)} \leftarrow (\pi/\phi)^2 (\mu/q) \tilde{v}^{(t)}$  and  $t \leftarrow (\mu\phi^2 t)/(\rho\pi^2)$ , Eq. (3.76) becomes

$$\frac{\partial \tilde{v}^{(t)}(r, \theta)}{\partial t} = \Delta \tilde{v}^{(t)}(r, \theta) + 1, \quad (r, \theta) \in [0, R] \times [0, 2\pi] \quad (3.77)$$

In the stationary regime ( $t = \infty$ ), Eq. (3.77) reads

$$\Delta \tilde{v}^{(\infty)}(r, \theta) = -1, \quad (r, \theta) \in [0, R] \times [0, 2\pi]. \quad (3.78)$$

The latter equation on the stationary flow  $\tilde{v}^{(\infty)}(r, \theta)$  can be identified with the equation on the MFPT (e.g. Eq. (3.1a) at  $p = 0$ ). The Laplace transform of Eq. (3.77) is

$$\Delta v^{(p)}(r, \theta) = p v^{(p)}(r, \theta) - \tilde{v}^{(0)}(r) - \frac{1}{p}, \quad (3.79)$$

where  $\tilde{v}^{(0)}(r)$  is the initial velocity profile at  $t = 0$ , which is assumed to be independent of  $\theta$ . Note that the long-time flow profile  $\tilde{v}^{(\infty)}(r, \theta)$  can be deduced from  $v^{(p)}(r, \theta)$  through the relation:

$$\lim_{p \rightarrow 0} p v^{(p)}(r, \theta) = \tilde{v}^{(\infty)}(r, \theta). \quad (3.80)$$

Eq. (3.79) is completed by the following boundary conditions. The shear stress is assumed to be zero along the free surfaces, i.e., at  $\theta = 0$ ,  $\theta = 2\pi$ ,  $r = 0$ , and within the groove at  $r = R$  (the free surface lies above the gas trapped within the groove). We consider the case  $\delta = 0$ , where  $\delta$  is the maximum penetration of the free surface into the groove. This approximation is justified because the surface of the groove is hydrophobic. At the bottom surface  $r = R$ , the velocity field satisfies the mixed boundary conditions:

- (i) non-slip conditions along the hydrophobic surface:  $v^{(p)}(r, \theta) = 0$  for all  $\theta \in [\pi - \varepsilon, \pi + \varepsilon]$  (similar to Eq. (3.4b)),
- (ii) no-shear conditions along the free surface:  $[\partial_r v^{(p)}(r, \theta)]_{r=R} = 0$  for all  $\theta \in [0, \pi - \varepsilon] \cup (\pi + \varepsilon, 2\pi]$  (similar to Eq. (3.4c)).

Similarly to Eq. (3.2), we define the auxiliary function

$$u^{(p)}(r, \theta) \equiv v^{(p)}(r, \theta) - v_{\pi}^{(p)}(r), \quad (3.81)$$

where  $v_{\pi}^{(p)}(r)$  is the rotation invariant solution of Eq. (3.79) satisfying  $v_{\pi}^{(p)}(1) = 0$ , and either  $\partial_r S_{\pi}^{(p)}(r) = 0$  at  $r = 0$  for a free surface (i), or  $v_{\pi}^{(p)}(1) = 0$  at  $r = 0$  for a no-slip surface (ii).

The Fourier expansion of the function  $u^{(p)}(r, \theta)$  according to Eq. (3.5) defines the Fourier coefficients  $a_n^{(p)}$ . In the case of free surface, functions  $f_n^{(p)}$  are given in Table 3.2. In the case of a no-slip surface, functions  $f_n^{(p)}$  read

$$f_n^{(p)}(r) = \frac{\sinh(\sqrt{p + n^2} r)}{\sinh(\sqrt{p + n^2} R)}, \quad n \geq 0. \quad (3.82)$$

The Fourier coefficients  $a_n^{(p)}$  are shown to satisfy Eqs. (3.19a) and (3.19b). One can therefore apply the resolution scheme presented in Sec. 3.1.2 to derive both an exact and an approximate expression for the Laplace transform  $v^{(p)}(r, \theta)$  of the flow velocity. An approximate expression for stationary velocity profile  $\tilde{v}^{(\infty)}(r, \theta)$  is then deduced from Eq. (3.80).

### 3.3 Conclusion

We studied the Helmholtz equation with mixed boundary conditions on spherically symmetric two-dimensional domains (disks, angular sectors, annuli). This classical boundary value problem describes how diffusive particles exit from a domain through an opening on the reflecting boundary. The Dirichlet boundary condition on the opening is mixed with the Neumann boundary condition on the remaining part of the boundary that presents the major challenge in the resolution of this problem. For this reason, most previous studies were focused on the asymptotic analysis for small exits.

In order to overcome this limitation, we developed a new approach, in which the problem is reduced to a set of linear equations on the Fourier coefficients of the survival probability. We provide then two resolution schemes which are applicable for arbitrary exit sizes. The first scheme is exact but it relies on a numerical solution of linear equations and requires thus a matrix inversion. In turn, the second scheme is explicit (without matrix inversion) but approximate. As a result, we managed to derive the whole distribution of first passage times and their moments for the escape problem with arbitrary exit sizes. The approximate solution was shown to be accurate over the whole range of times. These analytical solutions have been successfully verified by extensive numerical simulations, through both a finite element method resolution of the original boundary value problem and by Monte-Carlo simulations.

Using this method, we analyzed the behavior of the FPT probability density for various initial positions. When the initial position is far from the exit, the FPT probability density was shown to be accurately approximated by an exponential distribution. In this situation, the whole distribution of FPTs is essentially determined by the MFPT for which we derived exact explicit relations. The developed method is also applied to rectangular domains and to biased diffusion with a radial drift within a disk.

Since the Helmholtz equation with mixed boundary conditions is also encountered in microfluidics [106], heat propagation [114], quantum billiards [115], and acoustics [116], the developed method can find numerous applications beyond first passage processes.



## Summary

For Brownian particles confined in spherically symmetric 2D domains, we obtained

- (1) exact resolution schemes for the FPT density and moments.
- (2) concise yet precise approximate expressions for the FPT density and moments.

## 3.4 Perspectives

As extensions of this work, I have

- (a) computed the MFPT in the limit of small perturbations to the disk geometry (see Fig. 3.12(a)). I consider:

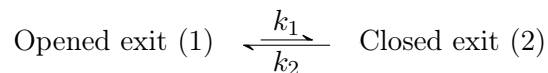
- small perturbations in the geometry of the target, while the rest of the confining domain is unperturbed and kept as portion of a circle. The radius of the target is at  $r = R + \eta(\theta)$  for all  $\theta \in [\pi - \varepsilon, \pi]$ . I have shown that the identity on the boundary condition for the MFPT at the target in (i) the limit of a small deformation  $\eta(\theta) \ll 1$  and (ii) in the limit of a semi-reflective target with a high adsorption rate  $k_t \gg R^{-1}$ , with the relation:

$$k_t(\theta) = \frac{1}{R^2} \frac{\partial \eta(\theta)}{\partial \theta} \quad (3.83)$$

- small perturbations in the geometry of the reflective confining geometry, while the exit is unperturbed and kept as a portion of a circle.
- small perturbations in the overall circle geometry: both the exit and the confining are deformed.

The relation of Eq. (3.83) appears to be previous unreported, although the semi-reflective condition at the target has been shown to model *entropic barriers*. An example of entropic barrier is the escape of a disk through a connected narrow rectangular tunnel [89, 34, 117, 118]. This geometry models dendritic spines along neurons, which consists of a bulbous head connected to the parent dendrite by a narrow neck. Spines are used to focus high concentrations of signals, which should be kept long enough to initiate signaling cascades. The escape of diffusing neurotransmitter out of the spine is a limiting step in some neural processes [119].

- (b) computed the MFPT to a gated exit in the boundary of a disk (see Fig. 3.12(b)), using the method developed the present Chap. 3. The exit switch between a close and a opened state, following a first order kinetic



I focused on the  $k_{12} = k_{21} = k$  case. Asymptotics results in the limit of a small target aperture  $\varepsilon$  are presented in Refs. [120, 121], but only in the  $d = 1$  and  $d = 3$  geometries. Our resolution scheme provides an expression in the  $d = 2$  geometry. Our main result is that the gated target emphasizes the non-exponential behaviour at short times. The gated exit problem is relevant for cell-trafficking studies, as most membrane proteins switch between opened and closed states [122].

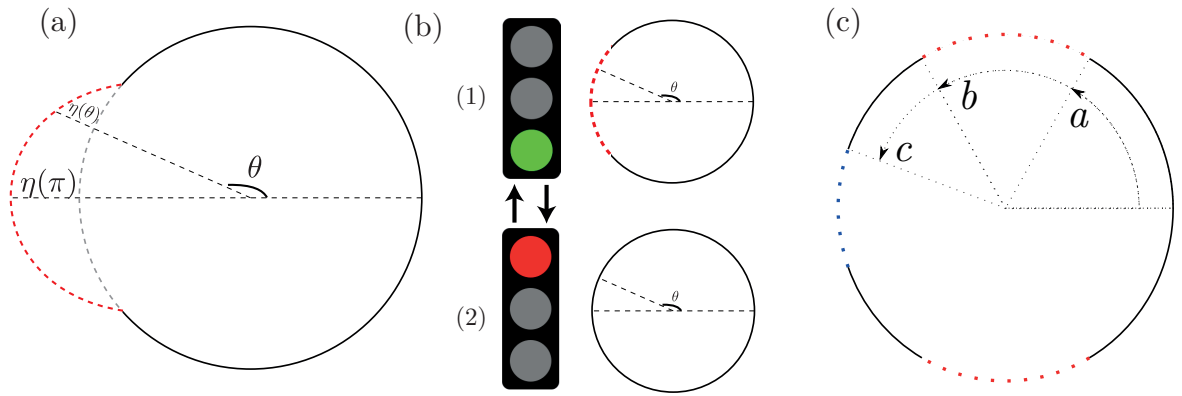


Figure 3.12: Sketches of the considered geometries.

- (c) obtained exact expressions for the unconditional MFPT and splitting probability in the presence of two exits, the first in the region  $\theta \in [a, b]$  and the second in the region  $\theta \in [\pi, c]$  (see Fig. 3.12(c)). In particular, the probability to reach the exit  $[b, a]$  for a particle starting from boundary  $r = R$  at the angle  $\theta \in [b, c]$  takes the concise expression:

$$\Pi(\theta) = \frac{F \left[ \sin^{-1} \left( \frac{\sqrt{\tan^2(\frac{c}{2}) - \tan^2(\frac{\theta}{2})}}{\sqrt{\tan^2(\frac{c}{2}) - \tan^2(\frac{b}{2})}} \right), \alpha \right]}{F \left[ \frac{\pi}{2}, \alpha \right]}, \quad (3.84)$$

where the function  $F$  denotes the elliptic integral of the first kind and

$$\alpha = \frac{\sqrt{\tan^2(\frac{c}{2}) - \tan^2(\frac{b}{2})}}{\sqrt{\tan^2(\frac{c}{2}) - \tan^2(\frac{a}{2})}}. \quad (3.85)$$



## Part II

Exit time with surface-mediated  
diffusion  
with symmetric or biased Brownian  
volume diffusion



# Introduction: Surface-Mediated Diffusion

**Abstract** In the previous chapter, we quantified the exit time kinetic through bulk 2D diffusion. Here, in addition to the bulk diffusion process, we consider that diffusive particles can randomly bind, unbind and diffuse along the boundary: this process is called surface-mediated diffusion. The question is the following: can surface-mediated diffusion speed up the exit process compared to both the surface and the bulk diffusion processes?

Surface-mediated processes, in which a particle randomly alternates between surface and bulk diffusions, are relevant for various chemical and biochemical processes such as reactions in porous media or trafficking in living cells (see Sec. 1.2.1.3, p. 23). When the target is located on the boundary of the confining domain, e.g. in the case of interfacial reactions, the target is said to be an *exit* [123, 124].

Several papers showed that intermittent dynamics between two diffusive phases – a slow phase allowing the searcher to detect the target and a fast phase without detection – can lead to fast kinetics (see Sec. 1.2.1.3). The time spent in each phase was assumed in Refs. [125, 126] to be controlled by an internal clock which is independent of any geometrical parameter.

In the particular case of interfacial reactions (defined in Sec. 1.2.1.3, p. 23), the time spent in a bulk excursion is controlled by the statistics of return to the surface and therefore by the geometry of the confining domain [127, 125, 128]. While the desorption rate from the surface is independent of any geometrical parameter, the switching dynamics from the bulk to the surface is determined by the statistics of returns to the surface. The statistics of returns to the surface depend (i) on the dynamics of the diffusing particle and (ii) on the adsorption property of the surface.

In order to explicitly take into account the coupling of the intermittent dynamics to the geometry of the confinement, several authors focused either on the disk or on the sphere geometry:

- Refs. [129, 130] are coarse-grained (i.e. mean-field) approaches which conclude on the absence of an optimal desorption rate for the surface-mediated process on the sphere ( $d = 3$ ).
- Refs. [101, 111] present calculations of the MFPT for the surface-mediated process and conclude on the existence of an optimal desorption rate in both the disk ( $d = 2$ ) and sphere ( $d = 3$ ) geometries.
- Refs. [131, 132] consider a discrete surface-mediated process in  $d = 2$  and conclude on the existence of an optimal desorption rate.

The first calculations of the MFPT in spherical geometries showed that obtaining exact analytical expressions is technically difficult ([101, 111]). The technicality of the problem naturally triggers the following question: could simple mean-field arguments predict most of the interesting physics?

The coarse-grained approach from [130] provides a concise resolution scheme for the surface-mediated problem. Following Ref. [130], I briefly focus on the exit out of a sphere ( $d = 3$ ) through a spherical cap. The bulk of sphere, the target within the sphere and the rest of the sphere surface are considered as effective states, denoted by  $b$ ,  $s$  and  $\emptyset$  respectively, with no inner spatial degrees of freedom. The effective set of kinetic equations:

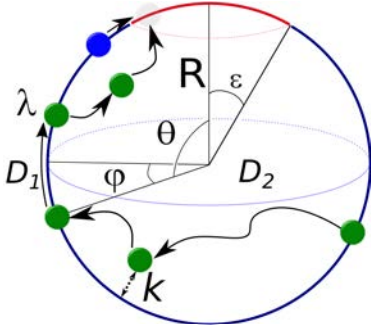
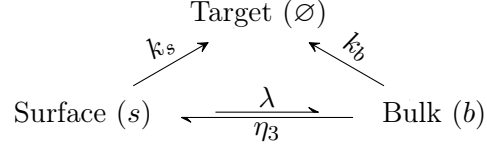


Figure 3.13: Model of surface-mediated diffusion in a sphere of radius  $R$  containing a perfectly adsorbing cap (a target). For finite values of  $k$ , particles (represented as small spheres) diffusing in the bulk randomly bind to or bounce from the remaining (non-adsorbing) part of the sphere surface (outside the target cap). The target is reached either from the bulk (shown by the green particle), or from the surface (shown by the blue particle).



combines the four first-order reaction rates

- (i)  $\lambda$  (denoted as  $\beta$  in [130]) is the desorption rate ( $s \rightarrow b$ );
- (ii)  $\eta_3$  defined in Eq. (5.22) as the inverse of the mean re-adsorption time on the sphere, which is associated with the effective adsorption ( $b \rightarrow s$ );
- (iii)  $k_s$  defined as the inverse of the surface GMFPT for the surface search alone ( $s \rightarrow \emptyset$ );
- (iv)  $k_b$  defined as the inverse of the bulk GMFPT for the bulk search alone ( $b \rightarrow \emptyset$ );

This reaction scheme predicts a monotonic behavior for the surface GMFPT as a function of the desorption rate  $\lambda$ : the surface GMFPT is minimal for either a pure surface search ( $\lambda = 0$ ) or a pure bulk search ( $\lambda = \infty$ ). This striking difference with Ref. [111] was attributed in [130] to the non-locality of the desorption process, in which the instantaneous ejection at a non-zero distance  $a$  implied a violation of the detailed balance condition. In contrast, our interpretation for the minimum is that bulk excursions reduce the time loss due to the recurrence of surface Brownian motion by bringing the particle, through the bulk, to unvisited regions of the surface. In Sec. 5.2.2, we explain why mean-field approach necessarily elude the existence of a finite desorption rate.

► In the following two Chaps. 4 and 5, we develop a unified theoretical framework to compute the MFPT to a target on the surface of a 2D or 3D spherical domain which encompasses

- (i) an imperfect adsorption step, and a local desorption rate ( $a = 0$ , see Sec. 4.3.1.2, p. 95),
- (ii) a biased diffusion process within the bulk (see Sec. 4.3.2, p. 98),
- (iii) a second purely reflecting boundary (see Sec. 4.3.1.3, p. 96),
- (iv) a target of arbitrary reactivity for incoming particle from the bulk (see Sec. B, p. 177).
- (v) an arbitrary number of regularly spaced targets on the surface (see Sec. 4.3.3, p. 100).

Biased diffusion mimics the effect of active transport [31, 26], thus this surface-mediated process provides a minimal transport model for intracellular trafficking.

# Surface-mediated diffusion: homogeneous boundary condition

## Contents

<b>4.1</b>	<b>The model</b> . . . . .	<b>86</b>
<b>4.2</b>	<b>General solution</b> . . . . .	<b>87</b>
4.2.1	Basic equations . . . . .	87
4.2.2	General integral equation . . . . .	88
4.2.3	Exact solution . . . . .	90
4.2.4	Are bulk excursions beneficial? . . . . .	92
4.2.5	Perturbative solution (small $\varepsilon$ expansion) . . . . .	92
4.2.6	Approximate solution . . . . .	93
<b>4.3</b>	<b>Particular cases</b> . . . . .	<b>95</b>
4.3.1	Zero bias ( $V = 0$ ) . . . . .	95
4.3.1.1	Exit problem for a perfect adsorption . . . . .	95
4.3.1.2	Exit time for a partial adsorption . . . . .	95
4.3.1.3	Reflecting boundary and entrance time . . . . .	96
4.3.2	Case of a $1/r$ velocity field . . . . .	98
4.3.3	Circular and spherical sectors . . . . .	100
4.3.3.1	Circular sector . . . . .	101
4.3.3.2	Spherical sector . . . . .	103
4.3.3.3	Multiple targets on the circle . . . . .	103
<b>4.4</b>	<b>Conclusion</b> . . . . .	<b>104</b>

In this chapter, I present an exact calculation of the mean first-passage time (MFPT) to a target on the surface of a 2D or 3D spherical domain, for a molecule alternating phases of surface diffusion on the domain boundary and phases of bulk diffusion. I generalize the results of Ref. [111] in the following four directions:

- (i) we consider the general case of an *imperfect adsorption step*, so that the molecule can bounce several times before being adsorbed to the confining surface [37, 133, 90, 89];
- (ii) the geometry adopted is a *general annulus*, whose either interior, or exterior boundary is purely reflecting;
- (iii) we take into account the effect of an *exterior radial force field* which, for instance, can schematically mimic the effect of active transport;
- (iv) we take into account an *arbitrary number of regularly spaced targets* on the surface.



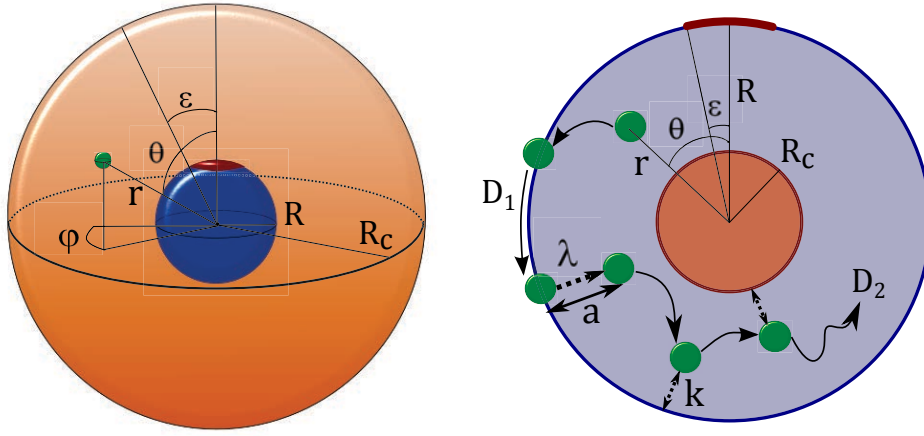



Figure 4.1: Model - *Left*: Static picture of the entrance problem in 3D - *Right*: Dynamic picture of the exit problem in 2D. The green sphere stands for the diffusing molecule and the red sector stands for the target.

This chapter is organized as follows. In Sec. 4.1, p. 86, we define the model under study; in Sec. 4.2, p. 87, we show that the MFPT can be determined by solving coupled partial differential equations that can actually be converted into a single integral equation. We then provide an exact solution of this integral equation, as well as an approximate, more tractable, solution. In Sec. 4.3, p. 95, we give fully explicit expressions of the MFPT by applying this general formalism to particular cases, representative of the four aforementioned extensions.

 This project led to Publication 4.

## 4.1 The model

The surface-mediated process under study is illustrated in Fig. 4.1. We consider a molecule diffusing in the volume  $\Omega$  between two concentric spheres of radii  $R$  and  $R_c$ . The molecule alternates phases of bulk diffusion (with diffusion coefficient  $D_2$ ) and phases of surface diffusion on the boundary of the sphere of radius  $R$  (with diffusion coefficient  $D_1$ ) which contains a target. The target is defined in 2D by the arc  $\theta \in [-\varepsilon, \varepsilon]$ , and in 3D by the region of the sphere such that  $\theta \in [0, \varepsilon]$  where  $\theta$  is in this case the elevation angle in spherical coordinates. Note that as soon as  $\varepsilon \neq 0$ , the target can be reached both by surface and bulk diffusion.

In this model, a molecule hitting the sphere of radius  $R_c$  is immediately reflected. In contrast, when the molecule reaches the sphere of radius  $R$ , which contains the target, it is imperfectly adsorbed: the molecule hitting the boundary at  $\mathbf{r} = (R, \theta)$ ,  $\theta \in [0, \pi]$  is at random either adsorbed to the sphere of radius  $R$  or reflected back in the bulk. The quantity  $k$  which describes the rate of adsorption is more precisely defined through the radiative boundary condition Eq. (4.5) (for a discrete model approach, see Appendix A in [112]). In particular,  $k = \infty$  corresponds to a perfectly adsorbing boundary and  $k = 0$  to a perfectly reflecting boundary. Notice that for finite  $k$ , molecules hitting the target from the bulk can be reflected.

The time spent during each surface exploration on the sphere of radius  $R$  is assumed to follow an exponential law with desorption rate  $\lambda$ . At each desorption event, the molecule is assumed to be ejected from the surface point  $\mathbf{r} = (R, \theta)$  to the bulk point  $\mathbf{r} = (R - a, \theta)$ . In what follows,  $a$  can be positive or negative:  $a > 0$  for the exit problem ( $R > R_c$ ), and  $a < 0$  for the entrance problem ( $R < R_c$ ). Although formulated for any value of the parameter  $a$  such that  $|a| \leq |R - R_c|$  (to ensure that the particle remains inside the domain after reflection), in most physical situations of interest  $|a|$  is much smaller than  $R$ . Note finally that a non zero ejection distance  $a$  is required in the limit of perfect adsorption  $k = \infty$ , otherwise the diffusing

molecule would be instantaneously re-adsorbed on the surface.

In 3D, the entrance problem ( $R_c > R$ ) can account for the time needed for a virus initially in the cell (the sphere of radius  $R_c$ ) to get into the nucleus (the sphere of radius  $R$ ) through a single nuclear pore (the target) in the presence of diffusion on the nuclear membrane. In turn, the exit problem ( $R > R_c$ ) in 3D may describe macromolecules searching an exit from the cell through a channel (or channels) in the cellular membrane. In that case, the surface of the nucleus is considered as purely reflecting. The 2D geometry could correspond to cells that are confined, as realized in vitro for example in [134].

## 4.2 General solution

### 4.2.1 Basic equations

We define  $t_1(\theta)$  as the MFPT for particles started on the surface at the angle  $\theta$ , and  $t_2(r, \theta)$  stands for the MFPT for particles started at the bulk point  $(r, \theta)$ . For the process defined above, the jump rate  $W(\mathbf{r}_a|\mathbf{r}_d, 0)$  between the state  $\mathbf{r}_d = (r_d, \theta_d; i_d)$  and  $\mathbf{r}_a = (r_a, \theta_a; i_a)$  is

$$W(\mathbf{r}_a|\mathbf{r}_d, 0) = \lambda \delta(r_a - R - a) \delta(\theta_a - \theta_d) \delta(i_d - 1) \delta(i_a - 2). \quad (4.1)$$

where  $i_d = 1$  (resp.  $i_d = 2$ ) if the particle is initially on the surface (resp. in bulk). From Eq. (2.17), we deduce that the MFPT satisfies the equations

$$\frac{D_1}{R^2} \Delta_\theta t_1(\theta) + \lambda (t_2(R - a, \theta) - t_1(\theta)) = -1 \quad (\varepsilon < \theta < \pi), \quad (4.2)$$

$$D_2 \left( \Delta_r + \frac{v(r)}{D_2} \partial_r + \frac{\Delta_\theta}{r^2} \right) t_2(r, \theta) = -1 \quad ((r, \theta) \in \Omega), \quad (4.3)$$

where:

- (i)  $t_1(\theta)$  stands for the MFPT for a molecule initially on the sphere of radius  $R$  at angle  $\theta$ , and  $t_2(r, \theta)$  stands for the MFPT for a molecule initially at a bulk point  $(r, \theta)$  within the annulus  $\Omega = (R_c, R) \times [0, \pi]$ ; note that, due to the symmetry  $t_i(\theta) = t_i(-\theta)$ , in 2D  $\theta$  can be restricted to  $[0, \pi]$ ;
- (ii)  $\Delta_r$ , the radial Laplacian and  $\Delta_\theta$ , the angular Laplacian (i.e. the Laplace–Beltrami operator) are defined in Eq. (2.32).
- (iii)  $v(r)$  is the radial velocity of the molecule resulting from an external force.

In Eqs. (4.2, 4.3), the first terms of the left hand side account for diffusion respectively on the surface and in the bulk, while the second term of Eq. (4.2) describes desorption events. These equations have to be completed by boundary conditions:

- (i) reflecting boundary condition on the sphere of radius  $R_c \geq 0$

$$\frac{\partial t_2}{\partial r} \Big|_{\mathbf{r}=(R_c, \theta)} = 0 \quad (0 \leq \theta \leq \pi) \quad (4.4)$$

(note that this condition holds even in the presence of the velocity field  $v(r)$ , see e.g. [135]);

- (ii) radiative boundary condition

$$\frac{\partial t_2}{\partial r} \Big|_{\mathbf{r}=(R, \theta)} = k \{t_1(\theta) - t_2(R, \theta)\} \quad (0 \leq \theta \leq \pi), \quad (4.5)$$

which describes the partial adsorption events on the sphere of radius  $R$  (see App. B.1, p. 177 for a justification of this boundary condition). For the exit problem ( $R > R_c$ ), the radial axis points towards the surface and  $k > 0$ , while for the entrance problem ( $R < R_c$ ), the radial axis points outwards the surface and  $k < 0$ . Finally, the limit  $k = \pm\infty$  describes the perfect adsorption for which the above condition reads as  $t_1(\theta) = t_2(R, \theta)$ .

(iii) Dirichlet boundary condition

$$t_1(\theta) = 0 \quad (0 \leq \theta \leq \varepsilon), \quad (4.6)$$

which expresses that the target is an absorbing zone (the search process is stopped on the target).

In what follows we will use two dimensionless quantities

$$x \equiv 1 - a/R, \quad (4.7)$$

$$\omega \equiv R\sqrt{\lambda/D_1}, \quad (4.8)$$

and the operator  $L$  acting on a function  $f$  as

$$(Lf)(r) \equiv f(r-a) - f(r) - \frac{1}{k} \partial_r f(r). \quad (4.9)$$

#### 4.2.2 General integral equation

► We show that the coupled Eqs. (4.2, 4.3) with the boundary conditions (4.4-4.6) lead to the integral equation (4.24) for  $t_1$  only.

The starting point is a Fourier decomposition of  $t_2$ :

$$t_2(r, \theta) = a_0 + \frac{1}{D_2} \hat{f}(r) + b_0 f_0(r) + \sum_{n=1}^{\infty} a_n f_n(r) V_n(\theta) + \sum_{n=1}^{\infty} a_{-n} f_{-n}(r) V_n(\theta), \quad (4.10)$$

with coefficients  $a_n$  to be determined, and

- (i)  $\hat{f}(r)$  is a rotation-invariant solution of Eq. (4.3) regular at  $r = 0$ , previously defined in Eq. (2.3.1.1).
- (ii)  $f_0(r)$  is a non-constant solution of the homogeneous equation

$$\left( \Delta_r + \frac{v(r)}{D_2} \partial_r \right) f_0(r) = 0, \quad (4.11)$$

the choice of  $f_0(r)$  being up to an additive constant and a multiplicative prefactor. It can be shown that  $f_0(r)$  necessarily diverges at  $r = 0$  in our cases of interest;

- (iii) the set of functions  $\{f_n(r), V_n(\theta)\}_{n \in \mathbb{Z}}$  is an eigenbasis of the homogeneous equation associated to Eq. (4.3):

$$-\Delta_\theta V_n(\theta) = \rho_n V_n(\theta) \quad (n \geq 0), \quad (4.12)$$

$$r^2 \left( \Delta_r + \frac{v(r)}{D_2} \partial_r \right) f_n(r) = \rho_{|n|} f_n(r) \quad (n \in \mathbb{Z}), \quad (4.13)$$

with  $V_{-n}(\theta) = V_n(\theta)$  due to the reflection symmetry, and

$$\rho_n = \begin{cases} n^2 & (d = 2), \\ n(n+1) & (d = 3). \end{cases} \quad (4.14)$$

We set

$$V_n(\theta) = \begin{cases} \begin{cases} 1 & (n = 0) \\ \sqrt{2} \cos(n\theta) & (n > 0) \end{cases} & (d = 2), \\ \sqrt{2n+1} P_n(\cos \theta) & (n \geq 0) \quad (d = 3), \end{cases} \quad (4.15)$$

where  $P_n(z)$  are Legendre polynomials. In turn, the functions  $f_n(r)$  which depend on the velocity field  $v(r)$ , will be determined individually case by case (see Sec. 4.3).

In the following, we will use two inner products:

$$(f, g) \rightarrow \langle f|g \rangle \equiv \int_0^\pi f(\theta)g(\theta)d\mu_d(\theta), \quad (4.16)$$

$$(f, g) \rightarrow \langle f|g \rangle_\varepsilon \equiv \int_\varepsilon^\pi f(\theta)g(\theta)d\mu_d(\theta), \quad (4.17)$$

where  $d\mu_d(\theta)$  are the measures in polar ( $d = 2$ ) and spherical coordinates ( $d = 3$ ):

$$d\mu_2(\theta) = \frac{d\theta}{\pi}, \quad d\mu_3(\theta) = \frac{\sin \theta}{2}d\theta. \quad (4.18)$$

With these definitions, the eigenvectors  $V_n(\theta)$  are orthonormal

$$\langle V_n|V_m \rangle = \delta_{nm}. \quad (4.19)$$

We now use the boundary conditions (4.4-4.6) to determine the coefficients  $\{a_n\}_n$  defining  $t_2(r, \theta)$  in Eq. (4.10).

(i) The reflecting boundary condition (4.4) reads

$$b_0 \partial_r f_0(r)|_{R_c} + \frac{1}{D_2} \partial_r \hat{f}(r)|_{R_c} + \sum_{n=1}^{\infty} (a_n \partial_r f_n + a_{-n} \partial_r f_{-n})|_{R_c} V_n(\theta) = 0, \quad (4.20)$$

which, using the orthogonality in Eq. (4.19), leads to the following relations

$$b_0 = -\frac{1}{D_2} \left( \frac{\partial_r \hat{f}(r)}{\partial_r f_0(r)} \right)_{|r=R_c}, \quad a_n \partial_r f_n(r)|_{r=R_c} = -a_{-n} \partial_r f_{-n}(r)|_{r=R_c}. \quad (4.21)$$

Note that, in the case  $R_c = 0$ , the first condition reads  $b_0 = 0$ .

(ii) Substituting Eq. (4.10) into the radiative boundary condition Eq. (4.5), projecting it onto the basis  $V_n(\theta)$  and using Eq. (4.21), we obtain two supplementary conditions:

$$a_0 - \frac{1}{D_2} \left( \frac{\partial_r \hat{f}(r)}{\partial_r f_0(r)} \right)_{|r=R_c} \left( f_0(R) + \frac{1}{k} \partial_r f_0(R) \right) + \frac{1}{D_2} \left( \hat{f}(R) + \frac{1}{k} \partial_r \hat{f}(R) \right) = \langle t_1|1 \rangle, \quad (4.22)$$

$$a_n \left[ f_n(R) + \frac{1}{k} \partial_r f_n(R) - \left( \frac{\partial_r f_n(r)}{\partial_r f_{-n}(r)} \right)_{|r=R_c} \left( f_{-n}(R) + \frac{1}{k} \partial_r f_{-n}(R) \right) \right] = \langle t_1|V_n \rangle. \quad (4.23)$$

On the other hand, the radiative boundary condition in Eq. (4.5) and the operator  $L$  defined in Eq. (4.9) allow one to rewrite Eq. (4.2) as

$$-\Delta_\theta t_1(\theta) = \frac{\omega^2}{\lambda} + \omega^2 (L t_2)(R) \quad (\varepsilon < \theta < \pi),$$

which becomes, using Eqs. (4.10, 4.21, 4.22, 4.23),

$$-\Delta_\theta t_1(\theta) = \omega^2 T + \omega^2 \sum_{n=1}^{\infty} X_n \langle t_1|V_n \rangle V_n(\theta) \quad (\varepsilon < \theta < \pi), \quad (4.24)$$

where

$$T \equiv \frac{1}{\lambda} + \frac{\eta_d}{D_2}, \quad (4.25)$$

$$\eta_d \equiv - \left( \frac{\partial_r \hat{f}(r)}{\partial_r f_0(r)} \right)_{|r=R_c} Lf_0(R) + L\hat{f}(R), \quad (4.26)$$

$$X_n \equiv \frac{Lf_n(R) - \left( \frac{\partial_r f_n(r)}{\partial_r f_{-n}(r)} \right)_{|r=R_c} Lf_{-n}(R)}{f_n(R) + \frac{1}{k} \partial_r f_n(R) - \left( \frac{\partial_r f_n(r)}{\partial_r f_{-n}(r)} \right)_{|r=R_c} (f_{-n}(R) + \frac{1}{k} \partial_r f_{-n}(R))} \quad (n \geq 1). \quad (4.27)$$

In Appendix B.2 we identify the quantity  $\eta_d/D_2$  as the mean first passage time on the sphere of radius  $R$  for a molecule initially at  $r = R - a$ . Thus the time  $T$  is the sum of a mean exploration time  $\eta_d/D_2$  and a mean ‘‘exploitation’’ time  $1/\lambda$ .

(iii) The absorbing boundary condition (4.6) and the relation  $t'_1(\pi) = 0$  which comes from the invariance of  $t_1$  under the symmetry  $\theta \rightarrow 2\pi - \theta$ , lead after integration of Eq. (4.24) to

$$t_1(\theta) = \begin{cases} \omega^2 T g_\varepsilon(\theta) + \omega^2 \sum_{n=1}^{\infty} \frac{X_n}{\rho_n} \langle V_n | t_1 \rangle_\varepsilon \{V_n(\theta) - V_n(\varepsilon)\} & (\varepsilon < \theta < \pi), \\ 0 & (0 \leq \theta \leq \varepsilon), \end{cases} \quad (4.28)$$

where  $\rho_n$  is defined in Eq. (4.14) and  $g_\varepsilon(\theta)$  is the solution of the problem:

$$\Delta_\theta g_\varepsilon(\theta) = -1, \quad \text{with } g_\varepsilon(\varepsilon) = 0 \quad \text{and} \quad g'_\varepsilon(\pi) = 0. \quad (4.29)$$

Note that  $R^2 g_\varepsilon(\theta)/D_1$  represents the MFPT to the target when  $\lambda = 0$ , i.e. the MFPT to a spherical cap over the  $(d-1)$ -sphere which are recalled in Table 2.3.1.3.

Equivalently, Eq.(4.28) reads

$$\psi(\theta) = \begin{cases} g_\varepsilon(\theta) + \omega^2 \sum_{n=1}^{\infty} \frac{X_n}{\rho_n} \langle V_n | \psi \rangle_\varepsilon \{V_n(\theta) - V_n(\varepsilon)\} & (\varepsilon < \theta < \pi), \\ 0 & (0 \leq \theta \leq \varepsilon), \end{cases} \quad (4.30)$$

where  $\psi(\theta) \equiv t_1(\theta)/(\omega^2 T)$  is a dimensionless function.

### 4.2.3 Exact solution

► The function  $\psi(\theta)$  can be developed on the basis of functions  $\{V_n(\theta) - V_n(\varepsilon)\}_n$ ,

$$\psi(\theta) = g_\varepsilon(\theta) + \sum_{n=1}^{\infty} d_n \{V_n(\theta) - V_n(\varepsilon)\} \quad (\varepsilon < \theta < \pi), \quad (4.31)$$

with coefficients  $\{d_n\}_{n \geq 1}$  to be determined. Due to Eq. (4.28), the vector  $\mathbf{d} = \{d_n\}_{n \geq 1}$  is a solution of the equation

$$\sum_{n=1}^{\infty} d_n \{V_n(\theta) - V_n(\varepsilon)\} = \omega^2 \sum_{n=1}^{\infty} \left( U_n + \sum_{m=1}^{\infty} Q_{n,m} d_m \right) \{V_n(\theta) - V_n(\varepsilon)\}, \quad (4.32)$$

where we have defined the vectors  $\mathbf{U}$  and  $\boldsymbol{\xi}$  by their  $n$ -th coordinates:

$$U_n \equiv \frac{X_n}{\rho_n^2} \xi_n, \quad \xi_n \equiv \rho_n \langle g_\varepsilon(\theta) | V_n(\theta) \rangle_\varepsilon \quad (n \geq 1), \quad (4.33)$$

and the matrices  $Q$  and  $I_\varepsilon$  by their elements:

$$Q_{n,m} \equiv \frac{X_n}{\rho_n} I_\varepsilon(n, m), \quad I_\varepsilon(n, m) \equiv \langle V_n(\theta) | V_m(\theta) - V_m(\varepsilon) \rangle_\varepsilon \quad (m \geq 1, n \geq 1) \quad (4.34)$$

As Eq. (4.32) is satisfied for all  $\theta \in (\varepsilon, \pi)$ , the coefficients  $d_n$  can be found by inverting the underlying matrix equation as

$$d_n = \left[ \omega^2 (I - \omega^2 Q)^{-1} U \right]_n. \quad (4.35)$$

The MFPT  $t_1(\theta)$  can be explicitly rewritten as

$$t_1(\theta) = \begin{cases} \omega^2 T \left[ g_\varepsilon(\theta) + \sum_{n=1}^{\infty} d_n \{V_n(\theta) - V_n(\varepsilon)\} \right] & (\varepsilon < \theta < \pi), \\ 0 & (0 \leq \theta \leq \varepsilon). \end{cases} \quad (4.36)$$

The averaged MFPT  $\langle t_1 \rangle$  which is defined by averaging over a uniform distribution of the starting point, is then easily obtained as

$$\langle t_1 \rangle \equiv \int_0^\pi t_1(\theta) d\mu_d(\theta) = \omega^2 T \left( \langle g_\varepsilon | 1 \rangle_\varepsilon + \sum_{n=1}^{\infty} d_n \xi_n \right), \quad (4.37)$$

where we have used the following relation

$$\langle V_n(\theta) - V_n(\varepsilon) | 1 \rangle_\varepsilon = -\langle V_n(\theta) - V_n(\varepsilon) | \Delta_\theta g_\varepsilon(\theta) \rangle_\varepsilon = \rho_n \langle V_n(\theta) | g_\varepsilon(\theta) \rangle_\varepsilon = \xi_n.$$

Finally, the MFPT  $t_2(r, \theta)$  is given by Eq. (4.10), in which the coefficients  $\beta_0$  and  $a_n$  are obtained from Eqs. (4.21, 4.22, 4.23):

$$t_2(r, \theta) = \langle t_1 \rangle + \frac{\eta_d}{D_2} + \frac{1}{D_2} \left( \hat{f}(r) - \hat{f}(R-a) \right) - \frac{1}{D_2} \left( \frac{\partial_r \hat{f}}{\partial_r f_0} \right)_{r=R_c} \left( f_0(r) - f_0(R-a) \right) \\ + \sum_{n=1}^{\infty} a_n V_n(\theta) \left\{ f_n(r) - \left( \frac{\partial_r f_n}{\partial_r f_{-n}} \right)_{r=R_c} f_{-n}(r) \right\}, \quad (4.38)$$

with

$$a_n = \frac{T \rho_n d_n}{L f_n(R) - \left( \frac{\partial_r f_n}{\partial_r f_{-n}} \right)_{r=R_c} L f_{-n}(R)} \quad (n \geq 1). \quad (4.39)$$

Table 4.2 summarizes the quantities which are involved in Eqs. (4.36, 4.37, 4.38) and independent of the detail of the radial bulk dynamics. In turn, the quantities  $T$ ,  $\eta_d$  and  $X_n$  are expressed by Eqs. (4.25, 4.26, 4.27) through the functions  $\hat{f}$ ,  $f_0$  and  $f_n$  and thus depend on the specific dynamics in the bulk phase and will be discussed in Sec. 4.3 for several particular examples.

A numerical implementation of the exact solutions in Eqs. (4.36, 4.37, 4.38) requires a truncation of the infinite-dimensional matrix  $Q$  to a finite size  $N \times N$ . After a direct numerical inversion of the truncated matrix  $(I - \omega^2 Q)$  in Eq. (4.35), the MFPTs from Eqs. (4.36, 4.37, 4.38) are approximated by truncated series (with  $N$  terms). We checked numerically that the truncation errors decay very rapidly with  $N$ . In a typical case of moderate  $\omega < 100$ , the results with  $N = 100$  and  $N = 200$  are barely distinguishable. In turn, larger values of  $\omega$  (or  $\lambda$ ) may require larger truncation sizes. In the following examples, we used  $N = 200$ . In spite of the truncation, we will refer to the results obtained by this numerical procedure as *exact solutions*, as their accuracy can be arbitrarily improved by increasing the truncation size  $N$ . These exact solutions will be confronted to approximate and perturbative solutions described in the next subsections.

#### 4.2.4 Are bulk excursions beneficial?

Before considering these perturbative and approximate solutions, we address the important issue of determining whether bulk excursions are beneficial for the search. This question can be answered by studying the sign of the derivative of  $\langle t_1 \rangle$  with respect to  $\lambda$  at  $\lambda = 0$ . In terms of  $\tilde{Q} = -QR^2/D_1$ , the MFPT from Eq. (4.37) reads

$$\langle t_1 \rangle = \frac{R^4}{D_1^2} (1 + \lambda \eta_d / D_2) \left[ \frac{D_1}{R^2} \langle g_\varepsilon | 1 \rangle_\varepsilon + \left( \boldsymbol{\xi} \cdot \lambda (I + \lambda \tilde{Q})^{-1} \mathbf{U} \right) \right]. \quad (4.40)$$

The derivative of  $\langle t_1 \rangle$  with respect to  $\lambda$  is

$$\frac{\partial \langle t_1 \rangle}{\partial \lambda} = \frac{R^4 \eta_d}{D_1^2} \left[ \frac{D_1}{D_2 R^2} \langle g_\varepsilon | 1 \rangle_\varepsilon + \left( \boldsymbol{\xi} \cdot \frac{(\eta_d^{-1} + 2\lambda)I + \lambda^2 \tilde{Q}}{(I + \lambda \tilde{Q})^2} \mathbf{U} \right) \right]. \quad (4.41)$$

If the derivative is negative at  $\lambda = 0$ , i.e.

$$\frac{D_1}{D_2} \leq - \frac{R^2}{\langle g_\varepsilon | 1 \rangle_\varepsilon} \frac{(\boldsymbol{\xi} \cdot \mathbf{U})}{\eta_d}, \quad (4.42)$$

bulk excursions are beneficial for the search. Explicitly, the critical ratio of the bulk-to-surface diffusion coefficients, below which bulk excursions are beneficial, is

$$\frac{D_{2c}}{D_1} = - \frac{\eta_d \langle g_\varepsilon | 1 \rangle_\varepsilon}{R^2} \left[ \sum_{n=1}^{\infty} X_n \langle g_\varepsilon | V_n \rangle_\varepsilon^2 \right]^{-1}. \quad (4.43)$$

#### 4.2.5 Perturbative solution (small $\varepsilon$ expansion)

While Eq. (4.36) for  $t_1$  is exact, it is not fully explicit since it requires either the inversion of the (infinite-dimensional) matrix  $I - \omega^2 Q$ , or the calculation of all the powers of  $Q$ . In this section, we give the first terms of a small  $\varepsilon$  expansion of the MFPT, while in the next one we provide an approximate solution that improves in practice the range of validity of this perturbative solution. Both solutions rely on the orthogonality of functions  $V_n$  in the small target size limit  $\varepsilon \rightarrow 0$ , which implies that the matrix  $Q$  is diagonal in this limit.

More precisely, as  $V_n(\theta) = V_n(-\theta)$ , necessarily  $\partial_\theta V_n(0) = 0$ , so that for  $\varepsilon$  close to zero and for all  $\theta \in [0, \varepsilon]$ , one has:  $V_n(\theta) = V_n(0) + O(\theta^2)$ . As a consequence, the function  $I_\varepsilon(n, m)$  introduced in Eq. (4.34), reads for all  $m, n \geq 1$  (see also Appendix B.3.1)

$$I_\varepsilon(n, m) \equiv \langle V_n(\theta) | V_m(\theta) - V_m(\varepsilon) \rangle_\varepsilon = \langle V_n(\theta) | V_m(\theta) \rangle - V_m(\varepsilon) \langle V_n(\theta) | 1 \rangle + O(\varepsilon^3) = \delta_{nm} + O(\varepsilon^3). \quad (4.44)$$

The first terms of a small  $\varepsilon$  expansion of the MFPT can then be exactly calculated. Relying on the expansion Eq. (4.44), one can replace  $I_\varepsilon(n, n)$  by 1 to get in 2D

$$\frac{\langle t_1 \rangle}{\omega^2 T} = \left( \frac{\pi^2}{3} + 2\omega^2 \sum_{n=1}^{\infty} \frac{X_n}{n^2(n^2 - \omega^2 X_n)} \right) - \pi\varepsilon + \left( 1 - 2\omega^2 \sum_{n=1}^{\infty} \frac{X_n}{n^2 - \omega^2 X_n} \right) \varepsilon^2 + O(\varepsilon^3), \quad (4.45)$$

and in 3D

$$\frac{\langle t_1 \rangle}{\omega^2 T} = -2 \ln(\varepsilon/2) - \left( 1 + \omega^2 \sum_{n=1}^{\infty} \frac{(2n+1)X_n}{n(n+1)(\omega^2 X_n - n(n+1))} \right) + O(\varepsilon^2). \quad (4.46)$$

The comparison of the perturbative solutions to the exact and approximate ones is presented in Figs. 4.2, 4.3, 4.5, 4.7 and it is discussed below.

## 4.2.6 Approximate solution

As mentioned above, we now provide an approximate solution that improves in practice the range of validity of the perturbative solution. This approximation relies on the fact that, due to Eq. (4.44), the matrix  $Q$  defined in Eq. (4.34) reads

$$Q_{nm} = \delta_{mn}Q_{nn} + O(\varepsilon^3). \quad (4.47)$$

Keeping only the leading term of this expansion, one gets

$$d_n \approx \frac{\omega^2 U_n}{1 - \omega^2 Q_{nn}} \quad (n \geq 1). \quad (4.48)$$

From Eqs. (4.33, 4.37, 4.48) we then obtain the following approximation for the search time:

$$\langle t_1 \rangle \approx \omega^2 T \left[ \langle g_\varepsilon | 1 \rangle_\varepsilon + \omega^2 \sum_{n=1}^{\infty} \frac{X_n \langle g_\varepsilon | V_n \rangle_\varepsilon^2}{1 - \omega^2 \frac{X_n}{\rho_n} I_\varepsilon(n, n)} \right]. \quad (4.49)$$

Note that this expression is fully explicit as soon as the functions  $\hat{f}$ ,  $f_0$  and  $f_n$  defined in Eqs (4.11) and (4.13) are determined. In Section 4.3, we will consider particular examples and write these functions explicitly. As we will show numerically, this approximation of  $t_1$ , which was derived for small  $\varepsilon$ , is in an excellent quantitative agreement with the exact expression for a wide range of parameters and even for large targets (see Figs. 4.2, 4.3, 4.5, 4.7).



Table 4.1: Summary of formulas for computing the vector  $\xi$  and the matrix  $Q$  in Eqs. (4.33, 4.34) that determine the coefficients  $d_n$  according to Eq. (4.35).

Expressions	2D	3D
$V_n(\theta)$	$\begin{cases} 1 & (n = 0) \\ \sqrt{2} \cos(n\theta) & (n > 0) \end{cases}$	$\sqrt{2n+1} P_n(\cos \theta)$
$\rho_n$	$n^2$	$n(n+1)$
$d\mu_d(\theta)$	$d\theta/\pi$	$\sin \theta d\theta/2$
$g_\varepsilon(\theta)$	$\frac{1}{2}(\theta - \varepsilon)(2\pi - \varepsilon - \theta)$	$\ln \left( \frac{1 - \cos(\theta)}{1 - \cos(\varepsilon)} \right)$
$\langle g_\varepsilon   1 \rangle_\varepsilon$	$\frac{1}{3\pi}(\pi - \varepsilon)^3$	$\ln \left( \frac{2}{1 - \cos \varepsilon} \right) - \frac{1 + \cos \varepsilon}{2}$
$\langle g_\varepsilon   V_n \rangle_\varepsilon$	$-\frac{\sqrt{2}}{\pi n^2} \{(\pi - \varepsilon) \cos(n\varepsilon) + \sin(n\varepsilon)/n\}$	$-\frac{\sqrt{2n+1}}{2} \frac{1}{n(n+1)} \left\{ \left( 1 + \frac{n \cos \varepsilon}{n+1} \right) P_n(\cos \varepsilon) + \frac{P_{n-1}(\cos \varepsilon)}{n+1} \right\}$
$I_\varepsilon(n, n)$	$\frac{1}{\pi} \left( \pi - \varepsilon + \frac{\sin 2n\varepsilon}{2n} \right)$	$\frac{2n+1}{2} \left( -P_n(u) \frac{u P_n(u) - P_{n-1}(u)}{n+1} + \frac{F_n(u)+1}{2n+1} \right)$
$I_\varepsilon(n, m)$	$\frac{2}{\pi} \frac{\cos(n\varepsilon) \frac{\sin(m\varepsilon)}{m} - \cos(m\varepsilon) \frac{\sin(n\varepsilon)}{n}}{n^2 - m^2} m^2$	(see Appendix B.3.1)

Table 4.2: Functions  $\hat{f}$ ,  $f_0$  and  $f_n$  for several particular cases (see also App. B.3.2, p. 183).

Case	Quantity	2D	3D
No bias ( $V = 0$ )	$\hat{f}$	$-r^2/4$	$-r^2/6$
	$f_0$	$\ln r$	$R/r$
	$f_n$	$r^n$	$r^n$
	$f_{-n}$	$r^{-n}$	$r^{-n-1}$
Velocity field: $\vec{v}(r) = -\frac{\mu D_2}{r^2} \vec{r}$	$\hat{f}$	$-r^2/(2(2 - \mu))$	$-r^2/(2(3 - \mu))$
	$f_0$	$[(r/R)^\mu - 1]/\mu$	$(r/R)^{\mu-1}/(1 - \mu)$
	$f_n$	$r^{\mu/2+\gamma_n}$	$r^{(\mu-1)/2+\gamma_n}$
	$f_{-n}$	$r^{\mu/2-\gamma_n}$	$r^{(\mu-1)/2-\gamma_n}$
		$(\gamma_n \equiv \sqrt{n^2 + \mu^2/4})$	$(\gamma_n \equiv \sqrt{n(n+1) + (\mu-1)^2/4})$
Sector of angle $\phi$ (no bias, $V = 0$ )	$\hat{f}$	$-r^2/4$	$-r^2/6$
	$f_0$	$\ln r$	$R/r$
	$f_n$	$r^{n\pi/\phi}$	$r^{-(1/2)+\gamma_n}$
	$f_{-n}$	$r^{-n\pi/\phi}$	$r^{-(1/2)-\gamma_n}$
			$(\gamma_n \equiv \sqrt{n(n+1)(\pi/\phi)^2 + 1/4})$

## 4.3 Particular cases

We apply the above theoretical approach to various examples. The only quantities needed to obtain fully explicit expressions of Eqs. (4.37, 4.49, 4.45, 4.46) are the functions  $\hat{f}$ ,  $f_0$  and  $f_n$  defined in Eqs. (4.11, 4.13) which are involved in the definitions of the quantities  $T$  and  $X_n$  according to Eqs. (4.25, 4.27). These quantities are listed in Table 4.2 for the representative cases discussed in this section. Throughout this section, all the quantities ( $R$ ,  $R_c$ ,  $a$ ,  $\varepsilon$ ,  $\lambda$ ,  $D_1$ ,  $D_2$ ,  $k$ ,  $\langle t_1 \rangle$ ) are written in dimensionless units. The physical units can be easily retrieved from the definitions of these quantities.

### 4.3.1 Zero bias ( $V = 0$ )

#### 4.3.1.1 Exit problem for a perfect adsorption

In the case of the exit problem with  $R_c = 0$ , perfect adsorption ( $k = \infty$ ) and no bias, the formula (4.49) reproduces the results of [111]. The coefficient  $\eta_d/D_2$  is the mean first passage time to the  $(d-1)$ -sphere of radius  $R$ , starting from  $r = R - a$ ,

$$\frac{\eta_d}{D_2} = \frac{a(2R - a)}{2d}. \quad (4.50)$$

From the expressions for the quantities  $T$  and  $X_n$ ,

$$T = \frac{1}{\lambda} + \frac{R^2}{2dD_2}(1 - x^2), \quad X_n = x^n - 1,$$

we retrieve the approximate expressions for the MFPT in 2D

$$\langle t_1 \rangle \approx \frac{\omega^2 T}{\pi} \left[ \frac{1}{3}(\pi - \varepsilon)^3 + \frac{2\omega^2}{\pi} \sum_{n=1}^{\infty} \frac{x^n - 1}{n^4} \frac{((\pi - \varepsilon) \cos(n\varepsilon) + \sin(n\varepsilon)/n)^2}{1 - \frac{\omega^2}{\pi} \frac{x^n - 1}{n^2} (\pi - \varepsilon + \frac{\sin 2n\varepsilon}{2n})} \right],$$

and in 3D:

$$\langle t_1 \rangle \approx \omega^2 T \left[ \ln \left( \frac{2}{1 - \cos \varepsilon} \right) - \frac{1 + \cos \varepsilon}{2} + \frac{\omega^2}{4} \sum_{n=1}^{\infty} \frac{(x^n - 1)(2n + 1)}{n^2(n + 1)^2} \frac{\left( \left( 1 + \frac{n \cos \varepsilon}{n + 1} \right) P_n(\cos \varepsilon) + \frac{P_{n-1}(\cos \varepsilon)}{n + 1} \right)^2}{1 - \frac{\omega^2}{2} \frac{(x^n - 1)(2n + 1)}{n(n + 1)} I_\varepsilon(n, n)} \right]. \quad (4.51)$$

► We emphasize that bulk excursions can be beneficial for the MFPT even for the bulk diffusion coefficient  $D_2$  smaller than the surface diffusion coefficient  $D_1$  [111]. This can be understood qualitatively by the fact that bulk diffusion induces flights towards remote and unvisited regions of the sphere  $r = R$ . These long-range hops can diminish the time for target encounter (provided that the time spent in the bulk phase is not too large).

#### 4.3.1.2 Exit time for a partial adsorption

We now give an explicit expression of the results (4.49) and (4.43) for a 2D exit problem with  $R_c = 0$  and with an imperfect adsorption on the sphere of radius  $R$ . Using the expressions from Table 4.2, the coefficients  $\eta_d$  and  $X_n$  are

$$\eta_d = \frac{R^2}{2d} \left( 1 - x^2 + \frac{2}{kR} \right), \quad X_n = \frac{x^n - 1 - \frac{n}{kR}}{1 + \frac{n}{kR}}. \quad (4.52)$$

Thus the approximate MFPT in 2D reads

$$\langle t_1 \rangle \approx \frac{\omega^2 T}{\pi} \left[ \frac{1}{3}(\pi - \varepsilon)^3 - \frac{2\omega^2}{\pi} \sum_{n=1}^{\infty} \frac{1 - x^n + \frac{n}{kR}}{n^4 \left(1 + \frac{n}{kR}\right)} \frac{((\pi - \varepsilon) \cos(n\varepsilon) + \sin(n\varepsilon)/n)^2}{1 - \frac{\omega^2}{\pi} \frac{x^n - 1 - \frac{n}{kR}}{n^2 \left(1 + \frac{n}{kR}\right)} (\pi - \varepsilon + \frac{\sin 2n\varepsilon}{2n})} \right], \quad (4.53)$$

and the critical ratio of the bulk-to-surface diffusion coefficients in Eq. (4.43), below which bulk excursions are beneficial, takes the form

$$\frac{D_{2c}}{D_1} = \left(1 - x^2 + \frac{2}{kR}\right) \frac{\pi(\pi - \varepsilon)^3}{24} \left[ \sum_{n=1}^{\infty} \frac{1 - x^n + \frac{n}{kR}}{n^4 \left(1 + \frac{n}{kR}\right)} ((\pi - \varepsilon) \cos(n\varepsilon) + \sin(n\varepsilon)/n)^2 \right]^{-1}. \quad (4.54)$$

Similarly, one can write explicit formulas in 3D.

The MFPT as a function of the desorption rate  $\lambda$  is shown on Fig. 4.2 for different values of the bulk diffusion coefficient  $D_2$  and the target sizes  $\varepsilon = 0.01$  and  $\varepsilon = 0.1$ , both in two and three dimensions. One can see that the approximate solution (4.53) (shown by circles) accurately follows the exact solution (shown by lines) for a wide range of parameters. In turn, the perturbative solutions in Eqs. (4.45, 4.46) (shown by pluses) are accurate for small  $\varepsilon = 0.01$  but they deviate from the exact ones for larger  $\varepsilon = 0.1$ .

The quality of the approximate and perturbative solutions can also be analyzed on Fig. 4.3 which shows the MFPT as a function of the target size  $\varepsilon$  (with a moderate value  $\lambda = 10$ ). Once again, the approximate solution is very accurate for the whole range of  $\varepsilon$ , with a notable deviation only at  $\varepsilon$  close to 1. The perturbative solution starts to deviate for  $\varepsilon \geq 0.1$  (as the desorption rate  $\lambda$  appears in the coefficients of the perturbative series, the validity range would of course depend on  $\lambda$  used).

The situation of quasi-perfect adsorption ( $kR \gg 1$ ) is shown to be asymptotically equivalent with the case of short ejection distance ( $a/R \ll 1$ ), as illustrated on Fig. 4.4.

#### 4.3.1.3 Reflecting boundary and entrance time

Now we provide an explicit form for Eqs. (4.49, 4.43) in the presence of a perfectly reflecting sphere of radius  $R_c$ . We recall that the case  $R_c > R$  (resp.  $R_c < R$ ) is called an entrance (resp. exit) problem.

Using the expressions from Table 4.2, the coefficients  $\eta_d$  and  $X_n$  can be written as

$$\eta_2 = \frac{R^2}{4} \left(1 - x^2 + \frac{2}{kR}\right) + \frac{R_c^2}{2} \left(\ln(x) - \frac{1}{kR}\right), \quad (4.55)$$

$$\eta_3 = \frac{R^2}{6} \left(1 - x^2 + \frac{2}{kR}\right) + \frac{R_c^3}{3R} \left(1 - \frac{1}{x} - \frac{1}{kR}\right), \quad (4.56)$$

and

$$X_n = \frac{x^n - 1 - \frac{n}{kR} + \left(\frac{R_c}{R}\right)^{2n} \left[x^{-n} - 1 + \frac{n}{kR}\right]}{1 + \frac{n}{kR} + \left(\frac{R_c}{R}\right)^{2n} \left[1 - \frac{n}{kR}\right]} \quad (d = 2), \quad (4.57)$$

$$X_n = \frac{x^n - 1 - \frac{n}{kR} + \frac{n}{n+1} \left(\frac{R_c}{R}\right)^{2n+1} \left[x^{-n-1} - 1 + \frac{n+1}{kR}\right]}{1 + \frac{n}{kR} + \frac{n}{n+1} \left(\frac{R_c}{R}\right)^{2n+1} \left[1 - \frac{n+1}{kR}\right]} \quad (d = 3). \quad (4.58)$$

It is worth noting an interesting dependence of  $\langle t_1 \rangle$  on the radius  $R_c$  when  $R_c$  and  $a$  are both small. One finds in 2D

$$\frac{\partial \langle t_1 \rangle}{\partial R_c} \Big|_{R_c=0} = 0, \quad \frac{\partial^2 \langle t_1 \rangle}{\partial R_c^2} \Big|_{R_c=0} = \left(\frac{D_2}{D_1} - \frac{\pi^2}{24}\right) \frac{4\lambda a R}{D_1 D_2}, \quad (4.59)$$

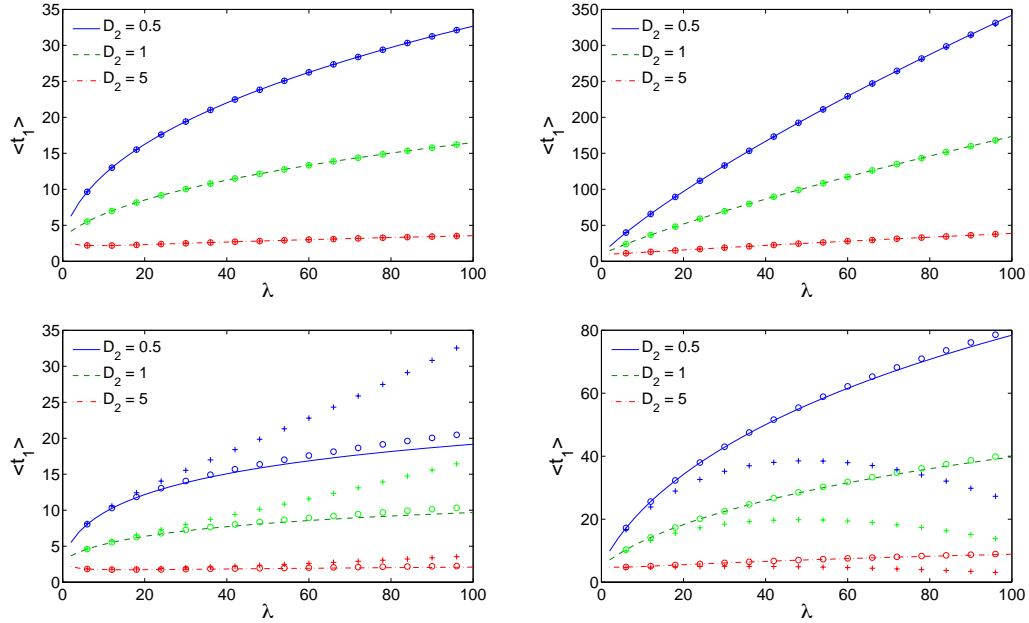


Figure 4.2: MFPT  $\langle t_1 \rangle$  as a function of the desorption rate  $\lambda$  for domains with partial adsorption  $k = 1$ : comparison between the exact solution (lines), approximate solution (circles) and perturbative solution (pluses) for 2D (left) and 3D (right), with  $\varepsilon = 0.01$  (top) and  $\varepsilon = 0.1$  (bottom). The other parameters are:  $R = 1$ ,  $D_1 = 1$ ,  $a = 0.01$ , no bias ( $V = 0$ ), and  $D_2$  takes three values 0.5, 1 and 5 (the truncation size is  $N = 200$ ).

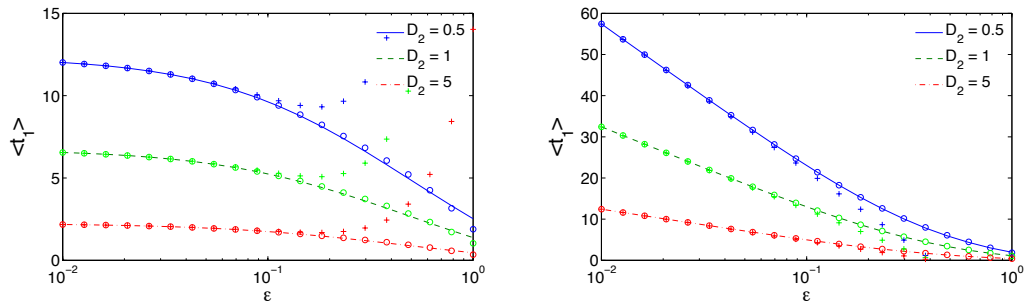


Figure 4.3: Global mean first passage time  $\langle t_1 \rangle$  (averaged over the sphere surface) as a function of the target size  $\varepsilon$  for domains with partial adsorption  $k = 1$ : Comparison between the exact solution (lines), approximate solution (circles) and perturbative solution (pluses) for 2D (left) and 3D (right). The other parameters are:  $R = 1$ ,  $D_1 = 1$ ,  $a = 0.01$ ,  $\lambda = 10$ , no bias ( $V = 0$ ), and  $D_2$  takes three values 0.5, 1 and 5 (the truncation size is  $N = 200$ ).

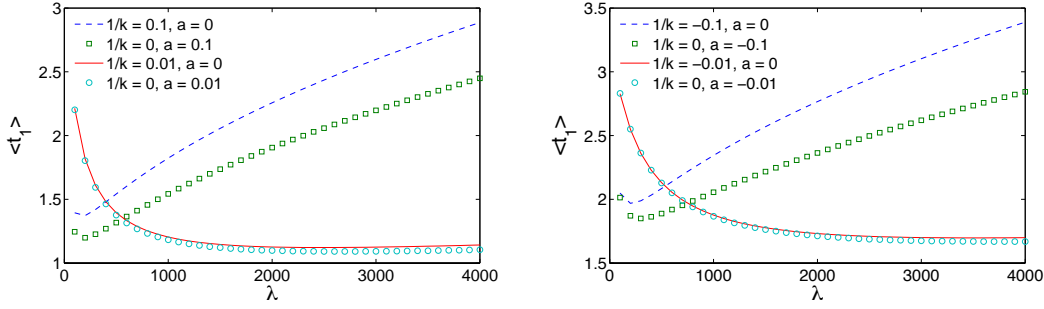


Figure 4.4: Global mean first passage time  $\langle t_1 \rangle$  (averaged over the surface) computed through Eq. (4.37) as a function of the desorption rate  $\lambda$  for several combinations of the parameters  $k$  and  $a$ , with  $R_c = 0$  (left) and  $R_c = \sqrt{2} > R = 1$  (right). The relation between  $1/k$  and  $a$  is asymptotically valid for small  $a$ . If both values of  $a$  and  $1/k$  are close to zero, the MFPT (green line) tends to be a constant which is equal to the MFPT on a segment of length  $2\pi$ . Here  $d = 2$ ,  $R = 1$ ,  $D_1 = 1$ ,  $D_2 = 5$ ,  $\varepsilon = 0$ , no bias ( $V = 0$ ) (the truncation size is  $N = 200$ ).

and in 3D,

$$\frac{\partial \langle t_1 \rangle}{\partial R_c} \Big|_{R_c=0} = \frac{\partial^2 \langle t_1 \rangle}{\partial R_c^2} \Big|_{R_c=0} = 0, \quad \frac{\partial^3 \langle t_1 \rangle}{\partial R_c^3} \Big|_{R_c=0} = \left( \frac{D_2}{D_1} - \frac{8}{27} [2 \ln(2/\varepsilon) - 1] \right) \frac{9\lambda a R}{8D_1 D_2}. \quad (4.60)$$

In 2D, as long as  $D_2/D_1 > \pi^2/24 \approx 0.411$  introducing a reflecting sphere of small radius  $R_c$  increases the search time. This can be understood as follow: increasing  $R_c \ll R$  increases the duration of flights between remote and unvisited regions of the sphere  $r = R$ , as these flights have to circumvent an obstacle at  $r = R_c$ . These long-range flights can reduce the search time only if they are not too time costly, hence the condition on  $D_2 > D_{2c}$ . The critical diffusion coefficient  $D_{2c}$  increases with  $R_c < R$  (Fig. 4.6).

### 4.3.2 Case of a $1/r$ velocity field

We now examine the case of a radial  $1/r$  velocity field  $\vec{v}(r)$  characterized by a dimensionless parameter  $\mu$ :

$$\vec{v}(r) = -\frac{\mu D_2}{r^2} \vec{r}. \quad (4.61)$$

Substituting the functions  $\hat{f}$ ,  $f_0$  and  $f_n$  from Table 4.2 into Eq. (4.25), we can write the coefficients  $\eta_d$  and  $X_n$  as

$$\eta_2 = \frac{R^2}{2(2-\mu)} \left[ \left( 1 - x^2 + \frac{2}{kR} \right) + \frac{2}{\mu} \left( \frac{R_c}{R} \right)^{2-\mu} \left( x^\mu - 1 - \frac{\mu}{kR} \right) \right], \quad (4.62)$$

$$\eta_3 = \frac{R^2}{2(3-\mu)} \left[ \left( 1 - x^2 + \frac{2}{kR} \right) + \frac{2}{\mu-1} \left( \frac{R_c}{R} \right)^{3-\mu} \left( x^{\mu-1} - 1 - \frac{\mu-1}{kR} \right) \right], \quad (4.63)$$

$$X_n = \frac{x^{\gamma_0+\gamma_n} - 1 - \frac{\gamma_n + \gamma_0}{kR} + \frac{\gamma_n + \gamma_0}{\gamma_n - \gamma_0} \left( \frac{R_c}{R} \right)^{2\gamma_n} \left[ x^{\gamma_0-\gamma_n} - 1 + \frac{\gamma_n - \gamma_0}{kR} \right]}{1 + \frac{\gamma_n + \gamma_0}{kR} + \frac{\gamma_n + \gamma_0}{\gamma_n - \gamma_0} \left( \frac{R_c}{R} \right)^{2\gamma_n} \left[ 1 - \frac{\gamma_n - \gamma_0}{kR} \right]}, \quad (4.64)$$

where

$$\gamma_n = \begin{cases} \sqrt{n^2 + \mu^2/4} & (d=2) \\ \sqrt{n(n+1) + (\mu-1)^2/4} & (d=3) \end{cases} \quad (n \geq 1), \quad (4.65)$$

and  $\gamma_0 = \mu/2$  in 2D and  $\gamma_0 = (\mu-1)/2$  in 3D. Note that in the limit  $\mu = 0$ , one gets  $\gamma_n = n$  ( $n \geq 0$ ) in 2D, and  $\gamma_0 = -1/2$  and  $\gamma_n = n + 1/2$  in 3D, so that the above results are reduced to

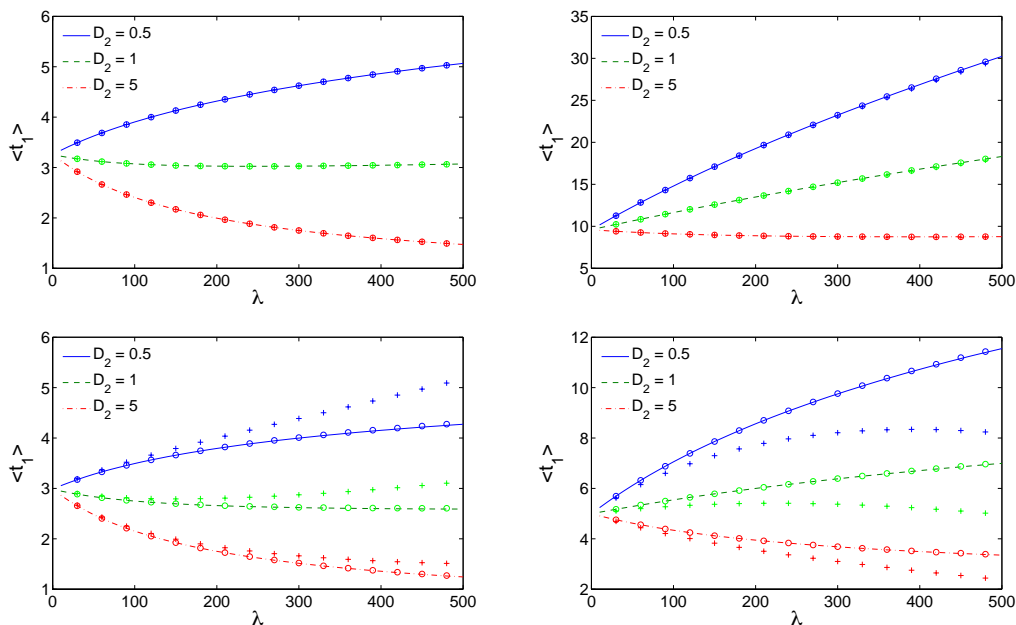


Figure 4.5: Global mean first passage time  $\langle t_1 \rangle$  (averaged over the surface) as a function of the desorption rate  $\lambda$  for an annulus with the inner radius  $R_c = 0.5$  and the outer radius  $R = 1$ : comparison between the exact solution (lines), approximate solution (circles) and perturbative solution (pluses) for 2D (left) and 3D (right), with  $\varepsilon = 0.01$  (top) and  $\varepsilon = 0.1$  (bottom). The other parameters are:  $D_1 = 1$ ,  $a = 0.01$ ,  $k = \infty$ , no bias ( $V = 0$ ), and  $D_2$  takes three values 0.5, 1 and 5 (the truncation size is  $N = 200$ ).

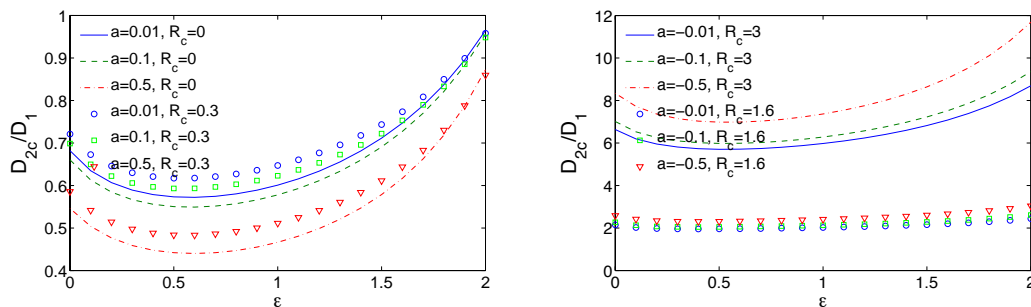


Figure 4.6: Critical ratio of the bulk-to-surface diffusion coefficients  $D_{2c}/D_1$  in 2D, with perfect adsorption and no bias ( $k = \infty$ ,  $V = 0$ ) computed through Eq. (4.43) as a function of the target size  $\varepsilon$  for different values of  $a$  and  $R_c$ : the exit problem ( $R_c < 1$ ) on the left and the entrance problem ( $R_c > 1$ ) on the right (the truncation size is  $N = 200$ ).

the previous case. The case  $\mu = d$  has to be considered separately because  $\hat{f}(r) = \frac{r^2}{4}(1 - 2 \ln r)$  in both 2D and 3D.

The same expression for  $\eta_d$  stands in the cases  $\mu = 0$  in 2D and  $\mu = 1$  in 3D:

$$\eta_d = \frac{R^2}{4} \left( 1 - x^2 + \frac{2}{kR} \right) + \frac{R_c^2}{2} \left( \ln x - \frac{1}{kR} \right).$$

When  $R_c = 0$  and  $\mu \geq d$ , the MFPT to the sphere  $\eta_d/D_2$  diverges, which causes the critical bulk diffusion coefficient  $D_{2c}$  to diverge.

Figure 4.7 shows the MFPT  $\langle t_1 \rangle$  as a function of the desorption rate  $\lambda$  in the presence of a  $1/r$  velocity field. As earlier, the exact, approximate and perturbative solutions are in an excellent agreement for a wide range of parameters. Figure 4.8 shows a similar dependence for different field intensities  $\mu$  (if  $\mu > 0$ , the velocity field points towards the origin, while  $\mu < 0$  means that the velocity field points towards the exterior). For  $R_c < R$  (resp.  $R_c > R$ ), for a fixed  $\lambda$  the search is on average faster as  $\mu$  is more negative (resp. positive). Finally, in Fig. 4.9, the critical ratio of the bulk-to-surface diffusion coefficients is shown as a function of the target size, both in two and three dimensions. The dependence on the field intensity  $\mu$  is stronger in 2D than in 3D.

For  $R < R_c$ , large absolute values of the drift coefficient increase  $\langle t_1 \rangle$  and  $D_{2c}$  as (i) a strong outward drift ( $|\mu| \gg |\mu_c|$ ) diminishes the probability for fast relocation through the central region; (ii) a strong inward drift ( $\mu \gg |\mu_c|$ ) traps the diffusing molecule in the central region and increases  $\eta_d/D_2$ , the MFPT to the surface  $r = R$  after ejection.

Although we derived the formulas for both 2D and 3D cases, the  $1/r$  velocity field is mainly relevant in two dimensions as being a potential field. In three dimensions, the potential field exhibits  $1/r^2$  dependence. This case, as well as many others, can be treated by our theoretical approach after solving Eqs. (4.11) and (4.13) for the functions  $f_0(r)$  and  $f_n(r)$ . This is a classical problem in mathematical physics. For instance, the aforementioned velocity field  $1/r^2$  in three dimensions involves hypergeometric functions, as shown in Appendix B.3.2.

### 4.3.3 Circular and spherical sectors

The above approach can also be applied for investigating the MFPTs in circular and spherical sectors of a given angle  $\phi$  (Fig. 4.10). In most biological situation such as viral trafficking,  $\phi \ll \pi$  but the arguments presented here stand for arbitrary  $\phi$ . For this purpose, the angular basis functions  $V_n(\theta)$  can be rescaled by the factor  $\phi/\pi$ :

$$V_n(\theta) = \begin{cases} \begin{cases} 1 & (n = 0), \\ \sqrt{2} \cos(n\theta\pi/\phi) & (n > 0) \end{cases} & (d = 2), \\ \sqrt{2n+1} P_n(\cos(\theta\pi/\phi)) & (n \geq 0) \quad (d = 3), \end{cases} \quad (4.66)$$

and  $V_{-n}(\theta) = V_n(\theta)$ . These basis functions satisfy

$$-\Delta_\theta V_n(\theta) = (\pi/\phi)^2 \rho_n V_n(\theta) \quad (0 \leq \theta \leq \phi, n \geq 0), \quad (4.67)$$

$$r^2 \left( \Delta_r + \frac{v(r)}{D_2} \partial_r \right) f_n(r) = (\pi/\phi)^2 \rho_{|n|} f_n(r) \quad (n \in \mathbb{Z}). \quad (4.68)$$

As previously, we define two scalar products

$$(f, g) \rightarrow \langle f|g \rangle = \int_0^\phi f(\theta)g(\theta)d\mu_d(\theta),$$

$$(f, g) \rightarrow \langle f|g \rangle_\varepsilon = \int_\varepsilon^\phi f(\theta)g(\theta)d\mu_d(\theta),$$

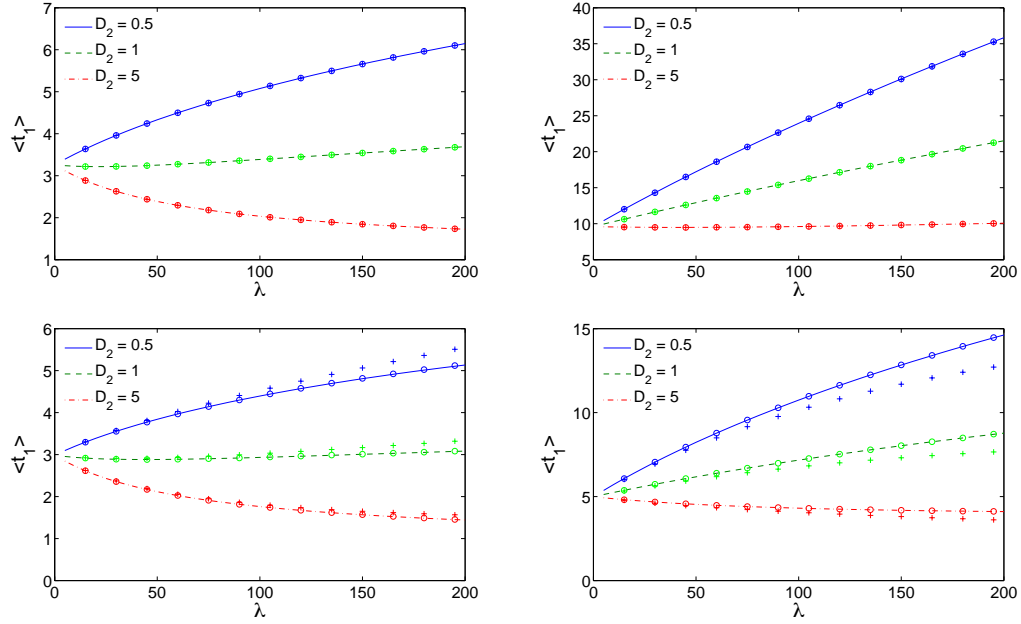


Figure 4.7: MFPT  $\langle t_1 \rangle$  as a function of the desorption rate  $\lambda$  in the presence of a  $1/r$  velocity field: comparison between the exact solution (lines), approximate solution (circles) and perturbative solution (pluses) for 2D with  $\mu = 1$  (left) and 3D with  $\mu = 2$  (right), with  $\varepsilon = 0.01$  (top) and  $\varepsilon = 0.1$  (bottom). The other parameters are:  $D_1 = 1$ ,  $a = 0.01$ ,  $k = \infty$ , and  $D_2$  takes three values 0.5, 1 and 5 (the truncation size is  $N = 200$ ).

where  $d\mu_d(\theta)$  is the measure in polar ( $d = 2$ ) or spherical ( $d = 3$ ) coordinates for all  $\theta \in [0, \phi]$ :

$$d\mu_2(\theta) = \frac{d\theta}{\phi} \quad \text{and} \quad d\mu_3(\theta) = \frac{\pi \sin \theta}{\phi} d\theta.$$

This modified measure is such that the eigenvectors  $V_n(\theta)$  are orthonormal:  $\langle V_n(\theta) | V_{n'}(\theta) \rangle = \delta_{nn'}$ .

#### 4.3.3.1 Circular sector

One can easily extend the function  $g_\varepsilon(\theta)$  for a sector of angle  $\phi$ :

$$g_\varepsilon(\theta) = \frac{1}{2}(\theta - \varepsilon)(2\phi - \varepsilon - \theta). \quad (4.69)$$

The direct computation yields

$$\begin{aligned} \langle g_\varepsilon | 1 \rangle_\varepsilon &= \frac{(\phi - \varepsilon)^3}{3\phi}, \\ \langle g_\varepsilon | V_n \rangle_\varepsilon &= -\frac{\phi\sqrt{2}}{\pi^2 n^2} \left( (\phi - \varepsilon) \cos(\pi n \varepsilon / \phi) + \frac{\phi}{\pi} \frac{\sin(\pi n \varepsilon / \phi)}{n} \right), \end{aligned}$$

and

$$\begin{aligned} I_{nn} &= 1 - \frac{\varepsilon}{\phi} + \frac{\sin(2\pi n \varepsilon / \phi)}{2\pi n} \quad (n \geq 1), \\ I_{nm} &= \frac{2m^2}{\pi(m^2 - n^2)} \left( \cos(\pi m \varepsilon / \phi) \frac{\sin(\pi n \varepsilon / \phi)}{n} - \cos(\pi n \varepsilon / \phi) \frac{\sin(\pi m \varepsilon / \phi)}{m} \right) \quad (m \neq n, m, n \geq 1) \end{aligned}$$

that generalize formulas from Table 4.2.



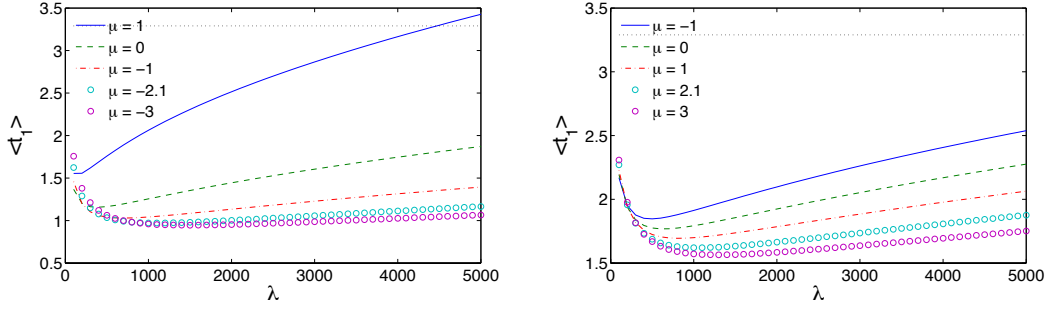


Figure 4.8: MFPT  $\langle t_1 \rangle$  computed through Eq. (4.49) as a function of the desorption rate  $\lambda$  for several values of the drift coefficient for  $R_c = 0$  (left) and  $R_c = \sqrt{2} > R = 1$  (right), in 2D. When  $\mu > 0$ , the velocity field points towards the origin, while  $\mu < 0$  means that the velocity field points towards the exterior. For  $R_c < R$  (resp.  $R_c > R$ ), for a fixed  $\lambda$  the search is on average faster as  $\mu$  is more negative (resp. positive). Here  $d = 2$ ,  $R = 1$ ,  $D_1 = 1$ ,  $D_2 = 5$ ,  $\varepsilon = 0$ ,  $k = \infty$  and  $a = 0.05$  for  $R_c = 0$  and  $a = -0.05$  for  $R_c = \sqrt{2}$  (the truncation size is  $N = 200$ ).

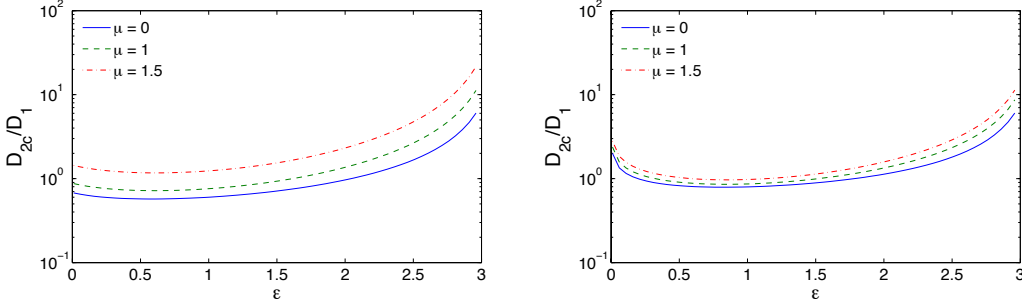


Figure 4.9: The critical ratio  $D_{2c}/D_1$  as a function of the target size  $\varepsilon$  in 2D (left) and 3D (right) in the presence of a  $1/r$  velocity field with three force intensities:  $\mu = 0$  (solid line),  $\mu = 1$  (dashed line) and  $\mu = 1.5$  (dash-dotted line). The other parameters are:  $R = 1$ ,  $a = 0.01$ ,  $R_c = 0$  and  $k = \infty$  (the truncation size is  $N = 200$ ).

In order to complete the formulas for search times, one needs to compute the coefficient  $\eta_d$  in Eq. (4.26) and the coefficients  $X_n$  in Eq. (4.27) that incorporate the radial dependences (e.g., the velocity field  $v(r)$  or the partial adsorption on the boundary). Since the functions  $\hat{f}(r)$  and  $f_0(r)$  remain unchanged (see Table 4.2), the coefficient  $\eta_d$  is given by previous explicit formulas: Eqs. (4.55, 4.56) with no bias ( $V = 0$ ) and Eqs. (4.62, 4.63) for the velocity field  $1/r$ . In turn, the functions  $f_n(r)$  are modified for the sector because of the prefactor  $(\pi/\phi)^2$  in Eq. (4.68). For instance, if there is no bias,  $f_n(r) = r^{n\pi/\phi}$ , from which

$$X_n = \frac{\left(x^{n\pi/\phi} - 1 - \frac{n\pi/\phi}{kR}\right) + (R_c/R)^{2n\pi/\phi} \left(x^{-n\pi/\phi} - 1 + \frac{n\pi/\phi}{kR}\right)}{1 + \frac{n\pi/\phi}{kR} + (R_c/R)^{2n\pi/\phi} \left(1 - \frac{n\pi/\phi}{kR}\right)}$$

that extends Eq. (4.57) in 2D. The case of the velocity field  $1/r$  can be studied in a similar way.

Note that the small  $\varepsilon$  expansion in Eq. (4.45) is modified as

$$\frac{\langle t_1 \rangle}{\omega^2 T} = \left( \frac{\phi^2}{3} + 2\omega^2 (\phi/\pi)^4 \sum_{n=1}^{\infty} \frac{X_n}{n^2(n^2 - \omega^2 X_n)} \right) - \phi\varepsilon + \left( 1 - 2\omega^2 (\phi/\pi)^2 \sum_{n=1}^{\infty} \frac{X_n}{n^2 - \omega^2 X_n} \right) \varepsilon^2 + O(\varepsilon^3). \quad (4.70)$$

### 4.3.3.2 Spherical sector

One can also compute the MFPT for a spherical sector of angle  $\phi$ . The angular basis functions  $V_n(\theta)$  were given in Eq. (4.66), while the function  $g_\varepsilon(\theta)$  satisfying Eq. (4.29) with  $g'_\varepsilon(\phi) = 0$  is

$$g_\varepsilon(\theta) = \frac{1 - \cos \phi}{2} \ln\left(\frac{1 - \cos \theta}{1 - \cos \varepsilon}\right) + \frac{1 + \cos \phi}{2} \ln\left(\frac{1 + \cos \theta}{1 + \cos \varepsilon}\right). \quad (4.71)$$

The integration yields

$$\langle g_\varepsilon | 1 \rangle_\varepsilon = \frac{(1 - \cos \phi)^2}{2} \ln\left(\frac{\sin \phi}{\sin \varepsilon}\right) + \frac{1 + \cos(\phi)^2}{2} \ln\left(\frac{1 + \cos \varepsilon}{1 + \cos \phi}\right) + \frac{\cos \phi - \cos \varepsilon}{2}. \quad (4.72)$$

One also needs to compute the projections

$$\langle g_\varepsilon | V_n \rangle_\varepsilon = \sqrt{2n + 1} \frac{\pi}{2\phi} \int_\varepsilon^\phi d\theta \sin \theta g_\varepsilon(\theta) P_n(\cos(\theta\pi/\phi)). \quad (4.73)$$

When  $m = \pi/\phi$  is an integer,  $\cos(m\theta)$  can be expressed in powers of  $\cos \theta$ ,

$$\cos(m\theta) = 2^{m-1} [\cos \theta]^m + m \sum_{j=1}^{[m/2]} (-1)^j \binom{m-2-j}{j-1} \frac{2^{m-2j-1}}{j} [\cos \theta]^{m-2j}, \quad (4.74)$$

(here  $[m/2]$  is the integer part of  $m/2$ , and we used the convention for binomial coefficients that  $\binom{n}{0} = 1$  for any  $n$ ) so that the computation is reduced to the integrals

$$\begin{aligned} J_k &\equiv 2k \int_\varepsilon^\phi d\theta \sin \theta g_\varepsilon(\theta) [\cos(\theta)]^{k-1} \\ &= (1 - \cos \phi) ([\cos \phi]^k - 1) \ln\left(\frac{1 - \cos \varepsilon}{1 - \cos \phi}\right) - (1 - \cos \phi) \sum_{j=1}^k \frac{[\cos \varepsilon]^j - [\cos \phi]^j}{j} \\ &\quad + (1 + \cos \phi) ([\cos \phi]^k - (-1)^k) \ln\left(\frac{1 + \cos \varepsilon}{1 + \cos \phi}\right) - (1 + \cos \phi) \sum_{j=1}^k (-1)^{k-j} \frac{[\cos \varepsilon]^j - [\cos \phi]^j}{j}. \end{aligned}$$

Using this formula, the projections  $\langle g_\varepsilon | V_n \rangle_\varepsilon$  can be easily and rapidly computed. Similarly, one can proceed with the computation of the matrix elements  $I_\varepsilon(n, n')$ ,

$$I_\varepsilon(n, n') = \sqrt{2n + 1} \sqrt{2n' + 1} \frac{\pi}{2\phi} \int_\varepsilon^\phi d\theta \sin \theta P_n(\cos(m\theta)) [P_{n'}(\cos(m\theta)) - P_{n'}(\cos(m\varepsilon))],$$

which are reduced to integrals of polynomials. When  $\pi/\phi$  is not integer, the above integrals can be computed numerically.

The radial functions  $\hat{f}(r)$  and  $f_0(r)$  remain unchanged, while  $f_n(r)$  are given in Table 4.2 for the case with no bias. The coefficient  $\eta_d$  remains unchanged (cf. Eq. (4.56)), while the coefficients  $X_n$  are given by Eq. (4.64) with  $\gamma_0 = -1/2$  and  $\gamma_n = \sqrt{n(n+1)(\pi/\phi)^2 + 1/4}$ . The case of the velocity field  $1/r$  can be studied in a similar way.

### 4.3.3.3 Multiple targets on the circle

The MFPT to reach a target of angular extension  $2\varepsilon$  in a circular sector of half aperture  $\phi = \pi/N_t > \varepsilon$  (with integer  $m$ ) (see Fig. 4.10) can actually be rephrased as the unconditional mean search time of  $N_t$  equally spaced targets of the same size  $2\varepsilon$  on the circle of radius  $R$ .

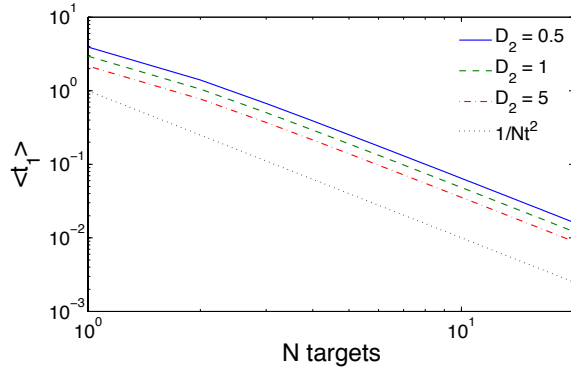
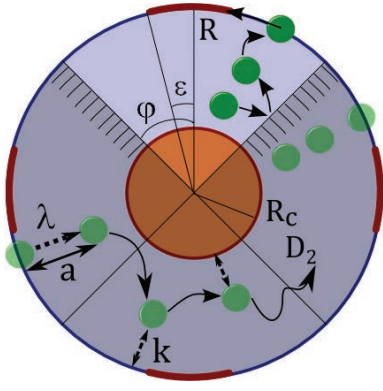


Figure 4.10: *Left* - The search problem of four regularly spaced targets can be represented as a one target search in an angular sector  $2\pi/4$  with reflecting edges. The shadow green sphere represents the real position of the molecule in the disk while the solid green sphere represents its image in the angular sector  $2\pi/4$ . *Right* - MFPT  $\langle t_1 \rangle$  as a function of the number of targets  $N_t$  for  $\lambda = 100$ , with the total target length  $\varepsilon_{\text{tot}} = 0.01$ . This time decreases as  $1/N_t^2$ , as one can expect from the limiting case  $\lambda = 0$ . The other parameters are:  $R = 1$ ,  $D_1 = 1$ ,  $a = 0.01$ ,  $R_c = 0$ ,  $k = \infty$ ,  $R_c = 0$ , no bias ( $V = 0$ ) and  $D_2$  takes three values 0.5, 1 and 5 (the truncation size is  $N = 200$ ).

Indeed in 2D, due to the reflection principle for random walks, the time spent to reach any of the  $m$  equally spaced targets on the circle is equal to the time required to reach a single target within a wedge with reflecting edges at  $\theta = \pm\pi/N_t$ .

Figure 4.10 shows the MFPT  $\langle t_1 \rangle$  in 2D as a function of the number of targets  $N_t$ , with a fixed total target length  $\varepsilon_{\text{tot}} = 0.01$ . This time decreases as  $1/N_t^2$ , as one can expect from the limiting case  $\lambda = 0$ .

The same procedure in 3D would be to match the time spent to reach any of  $m$  equally spaced target caps of size  $2\varepsilon < 2\pi/N_t$  on a sphere with the time required to reach the target cap  $\theta \in [-\varepsilon, \varepsilon]$  of a cone with reflecting edges at  $\theta = \pm\pi/N_t > \varepsilon$  (for all  $\phi \in [0, 2\pi]$ ). Although not exact because the volume of a sphere cannot be filled by cones, this procedure is expected to provide an accurate approximation for the unconditional MFPT as soon as the number of targets is sufficiently high. For instance, in the case of 60 equally spaced targets on the sphere, the total excluded volume (i.e. the volume between cones) represents less than 1% of the total sphere volume. Knowing that the number of membranes or nuclear pores in a cell usually exceeds 100 [26], the results of Sec. 4.3.3 should be relevant for cell trafficking studies.

## 4.4 Conclusion

We have developed a general theoretical approach to investigate searching of targets on the boundary of a confining medium by surface-mediated diffusion when the phases of bulk and surface diffusion are alternating. This is a significant extension of the previous results from [101, 111] in order to take into account imperfect adsorption, the presence of an exterior radial force, multiple regularly spaced targets and general annulus shapes. The coupled differential equations on the MFPTs  $t_1(\theta)$  and  $t_2(r, \theta)$  are reduced to an integral equation for  $t_1(\theta)$  alone whose solution is then found in a form of Fourier series. Linear relations for the Fourier coefficients involve an infinite-dimensional matrix whose inversion yields an exact but formal solution for the MFPTs. A finite-size truncation of this matrix yields a very accurate and rapid numerical solution of the original problem. In addition, we propose a fully explicit approximate solution as well as a perturbative one. Although both solutions are derived under

the assumption of small targets, the approximate solution turned out to be remarkably accurate even for large targets. We illustrate the practical uses of the theoretical approach and the properties of the MFPTs by considering in detail several important examples, for instance diffusion in a velocity  $1/r$  field. The approximate solution from Sec. 4.2.6, p. 93 is reminiscent of the approximate solution from Sec. 3.1.2.3, p. 59. The approximate resolution scheme provides concise expressions for the MFPT which accurately predict its optimizability.

#### SUMMARY OF MAIN RESULTS

- (1) We obtain an exact resolution scheme for the MFPT,
- (2) we show that the MFPT is optimizable under analytical criteria,
- (3) the explicit approximate expression for MFPT predicts the optimum with a remarkable accuracy,
- (4) the optimization holds even in the case of a local desorption event  $a = 0$  (in contrast to Ref. [130]).

Extensions to this project are considered in Sec. 5.4, p. 121.

4. Surface-mediated diffusion:  
homogeneous boundary condition

# Surface-mediated diffusion: mixed-boundary condition

---

## Contents

<b>5.1</b>	<b>The model</b> . . . . .	<b>108</b>
<b>5.2</b>	<b>Exact solution</b> . . . . .	<b>108</b>
5.2.1	Basic equations . . . . .	108
5.2.2	Integral equation . . . . .	109
5.2.3	Exact solution . . . . .	112
5.2.4	Are bulk excursions beneficial? . . . . .	114
5.2.5	Perturbative solution (small $\varepsilon$ expansion) . . . . .	114
<b>5.3</b>	<b>Coarse-grained approach</b> . . . . .	<b>115</b>
5.3.1	Comparison . . . . .	116
5.3.2	Discussion . . . . .	116
5.3.3	Analytical agreement between the coarse-grained and exact solutions . . . . .	118
<b>5.4</b>	<b>Conclusion</b> . . . . .	<b>118</b>

---

In the previous Chap. 4, we considered the case an uniformly semi-reflective surface *including the target*. The MFPT was found to be an optimizable function of the desorption rate even for a distance of ejection after desorption  $a$  set to zero [112]. The favorable effect of desorptions was attributed in [111] to the fact that bulk excursions reduce the time wasted due to the recurrence of surface Brownian motion, by bringing particles through the bulk to unvisited regions of the sphere. Previous mean-field treatments, which ignored spatial correlations, missed this possible optimum [129].

In the meantime, the surface-mediated search for a *perfectly adsorbing target within an otherwise semi-reflecting sphere* was considered in [130]. This model is relevant in numerous real situations in which the particle reactivity with the target is not related to its affinity with the rest of the surface, which is in particular the case for the exit problem.

Relying on the elegant first order kinetic presented in the introduction (p. 83), the coarse-grained approach of Ref. [130] provides approximate expressions for the surface and bulk GMFPTs. We recall that the surface GMFPT is the averaged MFPT for a uniform distribution of starting points over either the sphere surface (see Eq. (2.19)). In contrast to the results of the previous Chap. 4, the coarse-grained approach predicts a monotonic GMFPT as a function of the desorption rate.

In the present chapter, we clarify this puzzling situation and we address the question of the optimality of the GMFPTs as a function of the desorption rate for (i) the mixed boundary condition of [130] and (ii) in the specific case of the sphere ( $d = 3$ ). More precisely,

- (i) we provide an exact solution for the MFPT;
- (ii) we prove that the surface GMFPT is an optimizable function with respect to the desorption rate, under analytically determined criteria;

- (iii) we compare our results with the coarse-grained approach of [130], which is shown to be accurate only in a limited region of the parameter space.

 This project led to publication 5.

## 5.1 The model

The 3D model considered here appears at first to be very similar to the one model considered in 4.1. We consider particles diffusing in a three-dimensional spherical cavity of radius  $R$  (see Fig. 3.13) switching between phases of surface diffusion with diffusion coefficient  $D_1$  and phases of bulk diffusion with diffusion coefficient  $D_2$ . The time spent on the surface is assumed to follow an exponential law with desorption rate  $\lambda$ . The target is a cap defined as the portion of the sphere  $\theta \in [0, \varepsilon]$ , where  $\theta$  is the elevation angle in spherical coordinates.

► The crucial difference with the previous Chap. 4, p. 85 is that the target is now considered as perfectly reactive, i.e. particles react as soon as they encounter the target for the first time.

We will focus on the surface GMFPT  $\langle t_1 \rangle$  to the target, which is defined here as the average of the MFPT over a uniform distribution of the starting points on the sphere surface, *including the target*. In turn, in Ref. [130], the MFPT was averaged over the starting points outside the target; we denote this average as  $\langle t_1 \rangle_{[1]}$ . The two averages are related by  $\langle t_1 \rangle = A \langle t_1 \rangle_{[1]}$ , where  $A$  is a geometrical factor which reads

$$A = \frac{1}{1 + \tan^2(\varepsilon/2)}. \quad (5.1)$$

The non-reactive part of the sphere is considered as semi-reflective: a particle reaching by bulk diffusion the non-reactive part of the sphere surface gets randomly either adsorbed or reflected back in the bulk. The probability for binding to the surface is an increasing function of the adsorption coefficient  $k$ , which will be precisely defined through the radiative boundary condition for the MFPT in Eq. (5.7). In particular,  $k = \infty$  (resp.  $k = 0$ ) corresponds to a perfectly adsorbing (resp. reflecting) boundary (see Sec. 2.1.3, p. 34). Notice that the model that we consider here is exactly the same as in Ref. [130].

As mentioned in Sec. 2.3.1, p. 39, the limits  $\lambda = 0$  and  $\lambda = \infty$  correspond to simple situations. In the case  $\lambda = 0$ , particles are trapped on the surface until they reach the target, and the exact expression for the surface GMFPT is recalled in Sec. 2.3.1.3, p. 40 and reads

$$t_s = \langle t_1 \rangle_{\lambda=0} = \frac{R^2}{D_1} \left\{ \ln \left( \frac{2}{1 - \cos \varepsilon} \right) - \frac{1 + \cos \varepsilon}{2} \right\}. \quad (5.2)$$

The limit  $\lambda = \infty$  is equivalent to a purely reflecting boundary. The asymptotic behavior for the narrow escape limit  $\varepsilon \ll 1$  is given in [92]

$$t_b = \langle t_1 \rangle_{\lambda=\infty} = \frac{\pi R^2}{3D_2\varepsilon} \{1 + \varepsilon \ln(\varepsilon) + O(\varepsilon)\}. \quad (5.3)$$

Notice that the bulk and surface GMFPTs diverge as  $\varepsilon$  tends to zero, as it can be seen in particular in the above limits. Indeed a point-like target ( $\varepsilon = 0$ ) is detectable neither by bulk (3D) excursions nor by surface (2D) diffusion.

## 5.2 Exact solution

### 5.2.1 Basic equations

We define  $t_1(\theta)$  as the MFPT for particles started on the sphere at the angle  $\theta$ , and  $t_2(r, \theta)$  stands for the MFPT for particles started at the bulk point  $(r, \theta)$  (the second angular coordinate

$\phi$  is irrelevant due to the symmetry and thus ignored). We apply Eqs. (4.2) and (4.3) for the process described in Sec. 5.1, with  $a = 0$ ,

$$\frac{D_1}{R^2} \Delta_\theta t_1(\theta) + \lambda (t_2(R, \theta) - t_1(\theta)) = -1 \quad (\varepsilon < \theta < \pi), \quad (5.4)$$

$$D_2 \left( \Delta_r + \frac{\Delta_\theta}{r^2} \right) t_2(r, \theta) = -1 \quad ((r, \theta) \in \Omega). \quad (5.5)$$

where  $\Delta_r$  and  $\Delta_\theta$  are defined in Eq. (2.32). The boundary conditions for the process defined in Sec. 5.1 are

(i) the Dirichlet boundary condition

$$t_1(\theta) = 0 \quad (0 \leq \theta \leq \varepsilon), \quad (5.6)$$

which expresses that the search process is stopped on the target.

(ii) the mixed boundary condition

$$t_2(R, \theta) = \begin{cases} 0 & (0 \leq \theta \leq \varepsilon), \\ t_1(\theta) - \frac{1}{k} \frac{\partial t_2}{\partial r} \Big|_{r=R, \theta} & (\varepsilon < \theta \leq \pi), \end{cases} \quad (5.7)$$

in which the first relation expresses perfect adsorption on the target ( $\theta \in [0, \varepsilon]$ ) while the second relation (radiative B.C.) implements an imperfect adsorption process on the rest of the surface ( $\theta \in [\varepsilon, \pi]$ ).

The mixed boundary condition from Eqs. (5.6) and (5.7) is the major difference of the present model from the case of Chap. 4, p. 85, in which the radiative B.C. was imposed over the whole boundary, including the target. Although this modification may seem minor, the difference on the target reactivity has a drastic effect on the surface GMFPT for short adsorption times ( $\lambda \gg D_1/R^2$ ) or low adsorption rates ( $kR \ll 1$ ), as shown in Fig. B.4 below.

## 5.2.2 Integral equation

► From the set of Eqs. (5.4) – (5.7) we now derive an integral equation on  $t_1$  only.

We first recall that the eigenfunctions of the Laplace-Beltrami operator  $\Delta_\theta$  over the 2-sphere (defined in Eq. (2.32)) are expressed in terms of the Legendre polynomials  $P_n$

$$-\Delta_\theta P_n(\cos \theta) = \rho_n P_n(\cos \theta) \quad (n \geq 0), \quad (5.8)$$

where  $\rho_n = n(n+1)$ . We set  $V_n(\theta) = \sqrt{2n+1} P_n(\cos \theta)$  to get the orthonormality  $\langle V_n | V_m \rangle = \delta_{nm}$ . We define the inner products  $\langle f | g \rangle_\varepsilon$  and  $\langle f | g \rangle_\pi$  as in Eqs. (4.16) and (4.17). We also define

$$K_{mn}^{(\varepsilon)} \equiv \langle V_n | V_m \rangle_\varepsilon \quad (m, n \geq 0), \quad (5.9)$$

with the explicit expressions listed in Table 5.1.

The starting point for solution of the set of equations (5.4 and (5.5) is a Fourier decomposition of  $t_2(r, \theta)$ ,

$$t_2(r, \theta) = a_0 - \frac{r^2}{2dD_2} + \sum_{n=1}^{\infty} a_n \left( \frac{r}{R} \right)^n V_n(\theta), \quad (5.10)$$

where  $d = 3$  for the three-dimensional spherical cavity considered here (in Appendix B.4.1, we show how this approach can be directly translated for two-dimensional problems).



Dimension	$d = 3$
$V_n(\theta)$	$\sqrt{2n+1} P_n(\cos \theta)$
$g_\varepsilon(\theta)$	$\ln \left( \frac{1-\cos(\theta)}{1-\cos(\varepsilon)} \right)$
$\langle g_\varepsilon   1 \rangle_\varepsilon \equiv \langle g_\varepsilon \rangle_\varepsilon$	$\ln \left( \frac{2}{1-\cos \varepsilon} \right) - \frac{1+\cos \varepsilon}{2}$
$u$	$\cos \varepsilon$
$F_n(u), n \geq 1$	$\left\{ \sum_{k=1}^n 2(u-1)P_k^2(u) + [P_k(u) - P_{k-1}(u)]^2 \right\}$ $-(u-1)P_n^2(u) + (u-1)P_0^2(u) + u$
$\xi_n (n \geq 1)$	$-\frac{\sqrt{2n+1}}{2} \left\{ \left( 1 + \frac{nu}{n+1} \right) P_n(u) + \frac{P_{n-1}(u)}{n+1} \right\}$
$K_{00}^{(\varepsilon)}$	$\frac{1+\cos(\varepsilon)}{2}$
$K_{n0}^{(\varepsilon)} (n \geq 1)$	$\frac{P_{n+1}(u)-P_{n-1}(u)}{2\sqrt{2n+1}}$
$K_{nn}^{(\varepsilon)} (n \geq 1)$	$\frac{F_n(u)+1}{2}$
$K_{nm}^{(\varepsilon)} (m \neq n)$ $n, m \geq 1$	$\frac{\sqrt{2n+1}\sqrt{2m+1}}{2(m(m+1)-n(n+1))} ((m-n)uP_m(u)P_n(u) +$ $+nP_{n-1}(u)P_m(u) - mP_{m-1}(u)P_n(u))$
$I_{nn}^{(\varepsilon)} (n \geq 1)$	$\frac{2n+1}{2} \left\{ -P_n(u) \frac{uP_n(u)-P_{n-1}(u)}{n+1} + \frac{F_n(u)+1}{2n+1} \right\}$
$I_{nm}^{(\varepsilon)} (m \neq n)$ $m, n \geq 1$	$\frac{\sqrt{2n+1}\sqrt{2m+1}m}{2(n+1)[m(m+1)-n(n+1)]} ((n-m)uP_m(u)P_n(u)$ $+(m+1)P_m(u)P_{n-1}(u) - (n+1)P_n(u)P_{m-1}(u))$

Table 5.1: Summary of the quantities involved in the computation of the vector  $\xi$  and the matrices  $Q$  and  $P$  in Eqs. (5.29) and (5.31) that determine the Fourier coefficients  $d_n$  of  $t_1(\theta)$  according to Eq. (5.33).

Due to the B.C. (5.7), the projection of  $t_2(R, \theta)$  onto the orthonormal basis  $\{V_n(\theta)\}_{n \geq 0}$ , is

$$\int_0^\pi t_2(R, \theta) V_n(\theta) \sin \theta d\theta = \int_\varepsilon^\pi t_1(\theta) V_n(\theta) \sin \theta d\theta - \int_\varepsilon^\pi \frac{1}{k} \frac{\partial t_2}{\partial r} \Big|_R V_n(\theta) \sin \theta d\theta. \quad (5.11)$$

The Fourier decomposition (5.10) leads to linear equations on the coefficients  $a_0$  and  $a_n$ ,  $n \geq 1$ ,

$$a_0 - \frac{R^2}{2dD_2} \left( 1 + \frac{2K_{00}^{(\varepsilon)}}{kR} \right) = \langle t_1 | 1 \rangle - \sum_{m=1}^{\infty} \frac{mK_{0m}^{(\varepsilon)}}{kR} a_m, \quad (5.12)$$

$$a_n + \sum_{m=1}^{\infty} \frac{mK_{nm}^{(\varepsilon)}}{kR} a_m = \langle t_1 | V_n \rangle + \frac{RK_{n0}^{(\varepsilon)}}{dkD_2}. \quad (5.13)$$

First, one can solve the set of linear equations (5.13), independently of Eq. (5.12), by writing

$$\sum_{m=1}^{\infty} (\delta_{n,m} + M_{nm}) a_m = \hat{U}_n, \quad (5.14)$$

where

$$M_{nm} \equiv \frac{m}{kR} K_{nm}^{(\varepsilon)}, \quad (5.15)$$

$$\hat{U}_n \equiv \langle t_1 | V_n \rangle + \frac{R}{dkD_2} K_{n0}^{(\varepsilon)} \quad (5.16)$$

for all  $n, m \geq 1$ . Formally, the solution of this system of equations is

$$a_n = \left[ (\mathbb{I} + M)^{-1} \hat{U} \right]_n, \quad (5.17)$$

where  $(\mathbb{I})_{n,m} = \delta_{n,m}$  stands for the identity matrix. Note that  $t_1(\theta)$  and thus  $\hat{U}_n$  are still unknown.

Second, substituting the B.C. (5.7) into the diffusion equation (5.4) leads to

$$-\frac{D_1}{R^2} \Delta_\theta t_1(\theta) = -1 + \frac{\lambda}{k} \frac{\partial t_2}{\partial r} \Big|_{\mathbf{r}=(R,\theta)}. \quad (5.18)$$

The substitution of Eq. (5.10) into this relation yields

$$-\Delta_\theta t_1(\theta) = -\omega^2 T + \omega^2 \sum_{n=1}^{\infty} a_n \frac{n}{kR} V_n(\theta), \quad (5.19)$$

where we defined

$$\omega \equiv R\sqrt{\lambda/D_1}, \quad (5.20)$$

$$T \equiv \frac{1}{\lambda} + \frac{1}{\eta_3}, \quad (5.21)$$

$\eta_3$  being the inverse of the mean re-adsorption time on the surface after a desorption event defined in Eq. (4.56):

$$\eta_3 \equiv \frac{dkD_2}{R}. \quad (5.22)$$

The solution of Eq. (5.19) which satisfies the B.C.  $t_1(\varepsilon) = 0$ , is

$$t_1(\theta) = \omega^2 T g_\varepsilon(\theta) - \omega^2 \sum_{n=1}^{\infty} a_n \frac{n}{kR} \frac{V_n(\theta) - V_n(\varepsilon)}{\rho_n} \quad (5.23)$$

for  $\varepsilon < \theta < \pi$ , and  $t_1(\theta) = 0$  otherwise ( $0 \leq \theta \leq \varepsilon$ ). Here,  $R^2 g_\varepsilon(\theta)/D_1$  is the MFPT for a search on the sphere (i.e. when  $\lambda = 0$ ) which is recalled in Table 2.3.1.3. Using the formal expression (5.17) for  $a_n$  and introducing the dimensionless function

$$\psi(\theta) = \frac{t_1(\theta)}{\omega^2 T}, \quad (5.24)$$

one can represent Eq. (5.23) as an integral equation on  $\psi(\theta)$

$$\psi(\theta) = g_\varepsilon(\theta) + \sum_{n,m=1}^{\infty} \frac{V_n(\theta) - V_n(\varepsilon)}{\rho_n} X_{nm} \left( \frac{R}{dkD_2T} K_{0m}^{(\varepsilon)} + \omega^2 \langle \psi | V_m \rangle \right) \quad (5.25)$$

for  $\varepsilon < \theta < \pi$ , and  $\psi(\theta) = 0$  otherwise. Here, we introduced

$$X_{nm} \equiv -\frac{n}{kR} \left[ (\mathbb{I} + M)^{-1} \right]_{nm}. \quad (5.26)$$

### 5.2.3 Exact solution

Expanding the function  $\psi(\theta) - g_\varepsilon(\theta)$  on the complete basis of functions  $\{V_n(\theta) - V_n(\varepsilon)\}_{n \geq 1}$ ,

$$\psi(\theta) = g_\varepsilon(\theta) + \sum_{n=1}^{\infty} d_n \{V_n(\theta) - V_n(\varepsilon)\} \quad (\varepsilon < \theta < \pi), \quad (5.27)$$

one obtains a set of linear equations for the unknown coefficients  $\{d_n\}_{n \geq 1}$

$$\sum_{n=1}^{\infty} d_n \{V_n(\theta) - V_n(\varepsilon)\} = \omega^2 \sum_{n=1}^{\infty} \left( U_n + \sum_{l=1}^{\infty} Q_{nl} d_l \right) \{V_n(\theta) - V_n(\varepsilon)\}, \quad (5.28)$$

where we defined the vectors  $\mathbf{U}$  and  $\boldsymbol{\xi}$  by their  $n$ -th coordinates ( $n \geq 1$ )

$$U_n \equiv \frac{1}{\rho_n} \sum_{m=1}^{\infty} X_{nm} \left( \frac{\xi_m}{\rho_m} + \frac{K_{0m}^{(\varepsilon)} R}{dkD_2\omega^2 T} \right), \quad (5.29)$$

$$\xi_n \equiv \rho_n \langle g_\varepsilon | V_n \rangle_\varepsilon, \quad (5.30)$$

and the matrices  $Q$  and  $I^{(\varepsilon)}$  by their  $n$ -th row and  $l$ -th column ( $n, l \geq 1$ )

$$Q_{nl} \equiv \frac{1}{\rho_n} \sum_{m=1}^{\infty} X_{nm} I_{ml}^{(\varepsilon)}, \quad (5.31)$$

$$I_{ml}^{(\varepsilon)} \equiv \langle V_m(\theta) | V_l(\theta) - V_l(\varepsilon) \rangle_\varepsilon. \quad (5.32)$$

As Eq. (5.28) is satisfied for all  $\theta \in [\varepsilon, \pi]$ , the coefficients  $d_n$  are found as

$$d_n = \left[ \omega^2 (\mathbb{I} - \omega^2 Q)^{-1} U \right]_n. \quad (5.33)$$

Combining this relation with Eqs. (5.24, 5.27), one finally obtains an exact representation for the MFPT

$$t_1(\theta) = \omega^2 T \left( g_\varepsilon(\theta) + \sum_{n=1}^{\infty} d_n \{V_n(\theta) - V_n(\varepsilon)\} \right) \quad (5.34)$$

for  $\varepsilon < \theta \leq \pi$ , and  $t_1(\theta) = 0$  for  $0 \leq \theta \leq \varepsilon$ .

Averaging  $t_1(\theta)$  over the whole surface and using the relation

$$\langle P_n(\cos \theta) - P_n(\cos \varepsilon) | 1 \rangle_\varepsilon = \rho_n \langle P_n(\cos \theta) | g_\varepsilon(\theta) \rangle_\varepsilon = \xi_n,$$

we obtain the exact formula for the surface GMFPT

$$\langle t_1 \rangle = \omega^2 T \left( \langle g_\varepsilon \rangle + \sum_{n=1}^{\infty} d_n \xi_n \right), \quad (5.35)$$

where  $\langle g_\varepsilon \rangle$  is the averaged surface search time, recalled in Table 5.1.

► Equations (5.34) and (5.35) are among the main results of this thesis chapter, and several comments are in order

- (i) As expected, in both limits  $\lambda = 0$  and  $k = \infty$ , we retrieve the limit of the MFPTs for the surface search process alone  $t_1(\theta) \rightarrow \frac{R^2}{D_1} g_\varepsilon(\theta)$ .
- (ii) A physical interpretation of Eq. (5.35) is that the surface GMFPT is the product of the mean time  $T = \lambda^{-1} + \eta_3^{-1}$  for an elementary cycle composed of one surface exploration and one bulk excursion, by the mean number of cycles before reaching the target.
- (iii) A numerical implementation of the exact solutions in Eqs. (5.34) and (5.35) requires a truncation of the infinite-dimensional matrix  $Q$  to a finite size  $N \times N$ . As in the previous Chap. 4, Eq. 4.39, we refer to the results obtained by this numerical procedure as *exact solutions*, as their accuracy can be arbitrarily improved by increasing the truncation size  $N$ . This is also reminiscent of the exact resolution procedure used to compute the FPT density in Part. I.
- (iv) The Eq. (5.35) is valid for arbitrary target size  $\varepsilon$ , provided that the series are truncated at sufficiently high  $N$ .

Substituting Eqs. (5.24) and (5.27) into Eq. (5.16), we deduce the Fourier coefficients  $a_n$  of  $t_2(r, \theta)$  for  $n \geq 1$

$$a_n = \sum_{m=1}^{\infty} \left( (\mathbb{I} + M)^{-1} \right)_{nm} \left( \omega^2 T \left[ \frac{\xi_m}{\rho_m} + (I^{(\varepsilon)} \mathbf{d})_m \right] + \frac{RK_{m0}^{(\varepsilon)}}{dkD_2} \right),$$

while  $a_0$  is found from Eq. (5.12). The coefficients  $a_n$  determine an exact representation (5.10) of the MFPT  $t_2(r, \theta)$ . Therefore one gets a complete exact solution of the problem for any starting point. In particular, the bulk GMFPT  $\langle t_2 \rangle$  averaged over uniformly distributed starting points in the bulk, reads

$$\langle t_2 \rangle \equiv \frac{2\pi}{4\pi R^3/3} \int_0^R dr r^2 \int_0^\pi d\theta \sin \theta t_2(r, \theta) = a_0 - \frac{3R^2}{10dD_2}, \quad (5.36)$$

since the other terms from Eq. (5.10) vanish due to the orthogonality of  $V_n(\theta)$ . Substituting an expression for  $a_0$ , one gets

$$\langle t_2 \rangle = \langle t_1 \rangle + \frac{R^2}{2dD_2} \left( \frac{2}{5} + \frac{2K_{00}^{(\varepsilon)}}{kR} \right) - \sum_{m,n=1}^{\infty} \frac{mK_{0m}^{(\varepsilon)}}{kR} a_m. \quad (5.37)$$

Compared to the relation on  $a_n$  from Eq. (4.39) in the previous chapter, the mixed boundary condition (5.7) results in the more sophisticated Eq. (5.36) for  $a_n$ .

### 5.2.4 Are bulk excursions beneficial?

Despite the prediction of Ref. [130] that the bulk and surface GMFPTs are monotonic functions of  $\lambda$ , the exact solutions prove to admit a minimum, as seen in Fig. 5.2b on the example of the surface GMFPT.

► In this section we focus on the surface GMFPT and we determine sufficient conditions for this GMFPT to be an optimizable function of  $\lambda$ , which are set by two requirements:

- (i) The desorption events should decrease the search time for small enough values of  $\lambda$ . This first condition is fulfilled when the derivative of the surface GMFPT is negative at  $\lambda = 0$ . We first rewrite the coefficients  $U_n$  as

$$U_n = Z_n + \frac{1}{dkR + \lambda \frac{R^2}{D_2}} \frac{D_1}{D_2} W_n, \quad (5.38)$$

where

$$Z_n \equiv \frac{1}{\rho_n} \sum_{m=1}^{\infty} X_{nm} \frac{\xi_m}{\rho_m}, \quad \text{and} \quad W_n \equiv \frac{1}{\rho_n} \sum_{m=1}^{\infty} X_{nm} K_{0m}^{(\varepsilon)}. \quad (5.39)$$

The derivative of the GMFPT at  $\lambda = 0$  is

$$\left( \frac{\partial \langle t_1 \rangle}{\partial \lambda} \right)_{|\lambda=0} = \frac{R^4}{D_1^2} \left[ \frac{D_1}{dkRD_2} \left( \langle g_\varepsilon \rangle + (\boldsymbol{\xi} \cdot \mathbf{W}) \right) + (\boldsymbol{\xi} \cdot \mathbf{Z}) \right]. \quad (5.40)$$

This derivative is negative provided that

$$\frac{D_2}{D_1} \geq \left( \frac{D_2}{D_1} \right)_{\text{low}}, \quad \left( \frac{D_2}{D_1} \right)_{\text{low}} = -\frac{1}{dkR} \frac{\langle g_\varepsilon \rangle + (\boldsymbol{\xi} \cdot \mathbf{W})}{(\boldsymbol{\xi} \cdot \mathbf{Z})}, \quad (5.41)$$

where we used the inequality  $(\boldsymbol{\xi} \cdot \mathbf{Z}) < 0$ .

- (ii) The mean surface search time is lower than the mean bulk search time, i.e.  $t_s < t_b$ . This second bound (ii) is obtained when the surface search time  $R^2 \langle g_\varepsilon \rangle / D_1$  (at zero desorption rate) is lower than the search time at infinite desorption rate. Using the first-order asymptotic expansion of Eqs. (5.2, 5.3), this condition is explicitly given up to the second order in  $\varepsilon \ll 1$  as

$$\frac{D_2}{D_1} \leq \left( \frac{D_2}{D_1} \right)_{\text{up}}, \quad \left( \frac{D_2}{D_1} \right)_{\text{up}} = \frac{\pi}{3\varepsilon(1 - \varepsilon \ln \varepsilon)(2 \ln(2/\varepsilon) - 1)} + O(\varepsilon). \quad (5.42)$$

Combining the above inequalities, one gets a sufficient condition for the surface GMFPT to be optimizable for  $\varepsilon \ll 1$

$$\left( \frac{D_2}{D_1} \right)_{\text{low}} \leq \frac{D_2}{D_1} \leq \left( \frac{D_2}{D_1} \right)_{\text{up}}. \quad (5.43)$$

Figure 5.3 displays the regime of parameters for which the surface GMFPT is optimizable.

### 5.2.5 Perturbative solution (small $\varepsilon$ expansion)

The first terms of a perturbative expansion with respect to  $\varepsilon$  of Eq. (5.35) can easily be obtained. At first order in  $\varepsilon$ , one has

$$U_n = U_n^{(0)} + O(\varepsilon) = \frac{\sqrt{2n+1}}{n^2(n+1)^2} \frac{\frac{n}{kR}}{1 + \frac{n}{kR}} + O(\varepsilon),$$

$$Q_{mn} = Q_{mn}^{(0)} + O(\varepsilon) = \frac{1}{n(n+1)} \frac{\frac{n}{kR}}{1 + \frac{n}{kR}} \delta_{m,n} + O(\varepsilon),$$

from which

$$\begin{aligned} d_n &= \omega^2 [(\mathbb{I} - \omega^2 Q^{(0)})^{-1} U^{(0)}]_n + O(\varepsilon) \\ &= \frac{\omega^2}{n(n+1)} \frac{\left(\frac{n}{kR}\right) (2n+1)}{n(n+1) + \omega^2 \left(\frac{n/kR}{1+n/kR}\right)} + O(\varepsilon). \end{aligned}$$

One finds therefore

$$\psi(\theta) = -2 \ln \varepsilon + 2 \ln (2 \sin(\theta/2)) - \omega^2 \sum_{n=1}^{\infty} \left(\frac{n}{kR}\right) \frac{2n+1}{n(n+1)} \frac{1 - P_n(\cos \theta)}{n(n+1) + \omega^2 \left(\frac{n}{kR}\right)} + O(\varepsilon). \quad (5.44)$$

Averaging the latter relation over  $\theta$  yields (we recall that  $\psi(\theta) = \langle t_1 \rangle / \omega^2 T$ , see Eq. (5.24)),

$$\langle t_1 \rangle = \omega^2 T \left( 2 \ln(2/\varepsilon) - 1 - \omega^2 \sum_{n=1}^{\infty} \frac{2n+1}{n(n+1)} \frac{\frac{n}{kR}}{n(n+1)(1 + \frac{n}{kR}) + \omega^2 \frac{n}{kR}} + O(\varepsilon) \right). \quad (5.45)$$

Notice that this expression is identical to Eq. (4.46), i.e. the perturbative development at  $\varepsilon \ll 1$  for the case of a uniformly semi-reflecting sphere, *including the target*. In the limit of very small  $\varepsilon$ , the target is mainly reached from the adsorbed (surface) state, while its reactivity from the bulk is expected to be negligible. As seen on Fig. 5.2, the smaller the desorption rate  $\lambda$ , the larger the domain of applicability in  $\varepsilon$  of the perturbative development. Note also that in Fig. 5.2b, the first-order expression exhibits a minimum with respect to the desorption rate.

### 5.3 Coarse-grained approach

In the coarse-grained approach of [130], the bulk, the target and the rest of the surface are considered as effective states, denoted by  $b$ ,  $s$  and  $\emptyset$ , with no inner spatial degrees of freedom. The coarse-grained approach has been defined in p. 83. We recall that the rate  $k_s$  is defined as the inverse of the surface GMFPT of Eq. (5.2) for the surface search alone ( $s \rightarrow \emptyset$ , where  $\emptyset$  refers to the target)

$$k_s = \frac{A}{t_s}, \quad (5.46)$$

where the prefactor  $A$  from Eq. (5.1) accounts for the difference between the averages over the initial position mentioned above; (iv) the rate  $k_b$  defined as the inverse of the bulk GMFPT of Eq. (5.3) for the bulk search alone ( $b \rightarrow \emptyset$ ). As in Ref. [130], we define

$$k_b \equiv \frac{dD_2\varepsilon}{\pi R^2}, \quad (5.47)$$

which is the inverse of the first-order asymptotics in the limit  $\varepsilon \ll 1$  of Eq. (5.3).

In the following, we focus on the MFPT averaged over the sphere surface  $\langle t_1 \rangle$  and compare our exact expression Eq. (5.35) to the concise approximate expression derived in [130] for the surface GMFPT

$$\langle t_1 \rangle \simeq A \frac{\eta_3 + \lambda + k_b}{\eta_3 k_s + \lambda k_b + k_b k_s}. \quad (5.48)$$

► The coarse grained expression Eq. (5.48) from Ref. [130] predicts a monotonic behavior for the surface GMFPT as a function of the desorption rate  $\lambda$ . Similar results can be obtained for  $\langle t_2 \rangle$ , i.e. the MFPT averaged over the sphere volume.

### 5.3.1 Comparison

Figure 5.1 shows that the coarse-grained approach and the exact solution are in good agreement for the values of the adsorption parameter  $kR = 6.4 \cdot 10^{-4}$ ,  $6.4 \cdot 10^{-3}$ ,  $6.4 \cdot 10^{-2}$ , which are used for an analogous plot in [130]. However, as soon as  $kR$  is large enough, the exact and approximate curves are significantly different, as illustrated on Fig. 5.2 (for  $kR = 1, 10, 100$ ). Finally, and most importantly, the exact solution for the surface GMFPT  $\langle t_1 \rangle$  can exhibit a minimum with respect to  $\lambda$  (see Fig. 5.2b) as opposed to the coarse-grained approach which always predicts a monotonic behavior. Similarly, the bulk GMFPT  $\langle t_2 \rangle$  from Eq. (5.37) also exhibits a minimum with respect to  $\lambda$  for the parameters used in Fig. 5.2b (not shown).

Note that in all considered cases of Figs. 5.1, 5.2 the coarse-grained approach underestimates the search time at large  $\lambda$ . This discrepancy is due to the approximate expression of  $t_b$  used in [130] to estimate  $k_b$ . As expected, in a similar two-dimensional problem, our solution at large  $\lambda$  coincides with the earlier exact result of [92] for the MFPT when the surface is perfectly reflecting (see Appendix B.4.1).

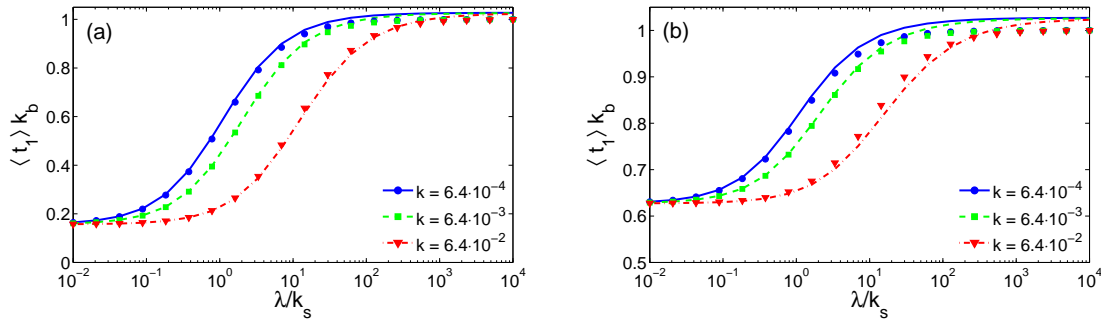


Figure 5.1: Comparison between the coarse-grained (symbols) and exact (lines) surface GMFPT  $\langle t_1 \rangle$  as a function of the desorption rate  $\lambda$ , for  $\varepsilon = 0.02$ ,  $N = 3 \cdot 10^4$  and several values of  $kR = 6.4 \cdot 10^{-4}$ ,  $6.4 \cdot 10^{-3}$ ,  $6.4 \cdot 10^{-2}$  (from [130]), with  $D_2 = D_1 = 1$  (a) and  $D_2 = 4D_1 = 4$  (b) in arbitrary units in which  $R = 1$ .

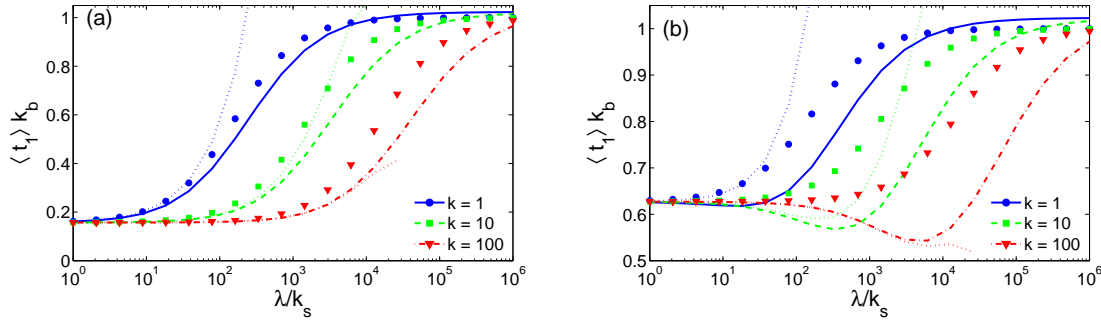


Figure 5.2: Comparison between the coarse-grained (symbols) and exact (lines) surface GMFPT  $\langle t_1 \rangle$  as a function of the desorption rate  $\lambda$ , for  $\varepsilon = 0.02$ ,  $N = 3 \cdot 10^4$  and several values of  $kR = 1, 10, 100$ , with  $D_2 = D_1 = 1$  (a) and  $D_2 = 4D_1 = 4$  (b). The dotted curves illustrate the perturbative solution (5.45) which is accurate for moderate  $\lambda$  but strongly deviates for very large  $\lambda$ .

### 5.3.2 Discussion

► We now discuss quantitatively the validity domain of the coarse-grained approach and explain qualitatively why it fails to reproduce the minimum of the surface GMFPTs with respect to  $\lambda$ .

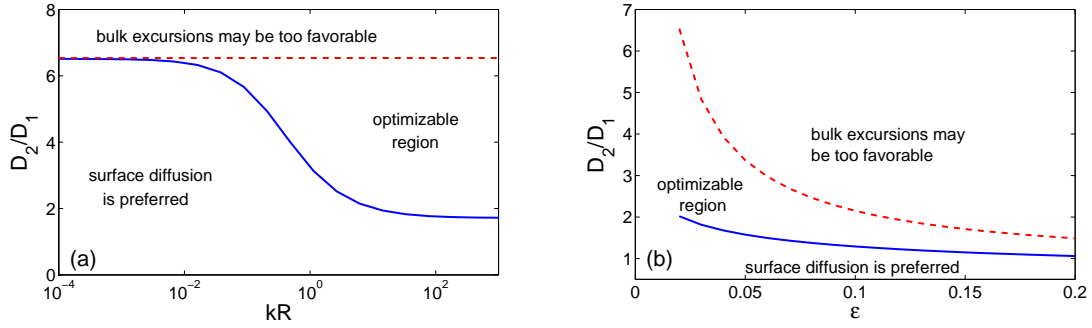


Figure 5.3: The regions of optimality for the surface GMFPT  $\langle t_1 \rangle$ . **(a)** The critical ratio  $D_2/D_1$  as a function of the adsorption coefficient  $k$  for a fixed value of the target half-width  $\varepsilon = 0.02$ ; **(b)** The critical ratio  $D_2/D_1$  as a function of the target size  $\varepsilon$ , for the adsorption coefficient  $kR = 10$ . Below the lower bound (dashed red line), surface diffusion is preferred. Above the upper bound (solid blue line), the GMFPT is smaller in the desorbed state than in the adsorbed state. In between, the surface GMFPT is an optimizable function of  $\lambda$ . Series are truncated at  $N = 10^4$ .

As suggested in [130], the validity of the coarse-grained approach requires the equilibration times for homogenization within each state to be faster than the other time scales of the process. In particular, the equilibration rate should be larger than:

- (i) the target encounter rate, i.e.,

$$\max(k_s, k_b) \ll \min(D_1/R^2, D_2/R^2), \quad (5.49)$$

which implies  $\varepsilon \ll 1$ . The coarse-grained approach can only describe narrow escape situations  $\varepsilon \ll 1$ , as mentioned in [130], whereas the exact solution presented here is valid for arbitrary  $\varepsilon$ .

- (ii) the inverse of the mean time for re-adsorption on the surface after desorption, i.e.,

$$\eta_3 = 3kD_2/R \ll \min(D_1/R^2, D_2/R^2), \quad (5.50)$$

which implies in particular that  $kR \ll 1$ . Indeed, as seen in Appendix B.2.1, in the regime  $kR \ll 1$ , the spatial correlations between the starting and ending points of bulk excursions are negligible. The condition (5.50) is satisfied in the situations displayed in Fig. 5.1.

However, Eq. (5.50) is not longer satisfied in both situations of Fig. 5.2, and one notices that the coarse-grained solution does not match with the exact result. This is particularly visible in Fig. 5.2b, where the surface GMFPT  $\langle t_1 \rangle$  exhibits a minimum with respect to the desorption rate  $\lambda$ .

The condition (5.50) for the applicability of the coarse-grained approach turns out to be incompatible with the existence of the minima of the bulk and surface GMFPTs with respect to  $\lambda$ . Such a minimum can be attributed to the fact that bulk excursions reduce the time loss due to the recurrence of surface Brownian motion by bringing the particle, through the bulk, to unvisited regions of the surface. In the coarse-grained approach, a bulk excursion  $s \rightarrow b \rightarrow s$  “consumes” time but brings the particle back to its initial effective state  $s$ . The assumption that the starting and ending points of bulk excursions belong to the same effective state  $s$  necessarily eludes the optimization property.



More precisely, bulk excursions are expected to be favorable if they are fast (e.g. large adsorption rate  $\eta_3$ ) and long-ranged ( $kR \ll 1$ , see Appendix B.2.1). This is in clear contradiction with the condition (5.50) of applicability of the coarse-grained approach. Due to the relation  $\eta_3 = 3kD_2/R$ , this condition is achieved for a high enough diffusion coefficient  $D_2$ , which sets the lower bound of  $D_2/D_1$  derived above. However, if the ratio  $D_2/D_1$  is too large, bulk excursions can be too favorable so that the optimum would be achieved for  $\lambda = \infty$ . The upper bound  $(D_2/D_1)_{\text{up}}$  in Eq. (5.43) excludes this possibility. The set of conditions on the diffusion coefficients ratio is illustrated on Fig. 5.3.

Understanding by analytical means the agreement between the exact and coarse-grained expressions of Eqs. (5.35) and (5.48) under the assumptions of Eqs. (5.49) and (5.50) is a challenging question. A first step in this direction is presented in the next paragraph 5.3.3, in which the agreement is found within the domain of applicability of the perturbative expansion (introduced in Sec. 5.2.5).

### 5.3.3 Analytical agreement between the coarse-grained and exact solutions

Figure 5.1 shows a good agreement between the exact and coarse-grained expressions (5.35, 5.48). However, finding an explicit analytical relation between these two expressions under the general conditions (5.49, 5.50) seems non-trivial.

We focus here on the following specific successive limits (i) small target extension ( $\varepsilon \ll 1$ ); (ii) low-desorption rate regime ( $\lambda \ll k_s$ ); (iii) and intermediate range for the adsorption rate  $k_b \ll \eta_3 \ll \min(D_2/R^2, D_1/R^2)$ .

On one hand, the coarse-grained expression in these limits reads

$$\langle t_1 \rangle \approx \left(1 + \frac{\lambda}{\eta_3}\right) t_s + O\left(\varepsilon, \frac{\lambda}{k_s}\right), \quad (5.51)$$

where we have used that  $k_b/k_s \ll 1$  and  $k_b/\eta_3 \ll 1$  for a fixed value of  $\eta_3$  at sufficiently small  $\varepsilon \ll 1$ .

On the other hand, in the limit  $\varepsilon \ll 1$  the perturbative expansion of Eq. (5.45) is accurate. In the above-mentioned limits it reads

$$\langle t_1 \rangle \approx \left(1 + \frac{\lambda}{\eta_3}\right) t_s + O\left(\varepsilon, \frac{\lambda}{k_s}, kR\right), \quad (5.52)$$

where we have used that

$$\sum_{n=1}^{\infty} \frac{2n+1}{n(n+1)} \frac{\frac{n}{kR}}{n(n+1)\left(1 + \frac{n}{kR}\right) + \frac{\lambda R^2}{D_1} \frac{n}{kR}} \approx 1 + O(kR, R^2\lambda/D_1), \quad (5.53)$$

and that the condition  $R^2\lambda/D_1 \ll 1$  is guaranteed from the condition  $\lambda/k_s \ll 1$ .

The identification of the first order terms in Eqs. (5.51, 5.52) shows analytically the agreement between the coarse-grained and exact solutions within a range of parameters which necessarily satisfies Eqs. (5.49, 5.50). Notice that the argument presented here relies on the condition  $k_b/\eta_3 \ll 1$  which is not satisfied in the situations represented on Fig. 5.1.

## 5.4 Conclusion

We have obtained an exact expression for the MFPT and their spatial averages, called bulk and surface GMFPTs, for the process studied in [130]. Compared to [111, 101], the introduction of the surface binding rate  $k$  allowed one to avoid using the ejection distance  $a$  (i.e. to set  $a = 0$ ) after each desorption events. In contrast to the statement of [130], we have shown that the bulk

and surface GMFPTs can be optimized even in this situation and that this optimality property is not related to the non-locality of the intermittent process considered in [111, 101].

These exact results can be extended in several directions to include

- (i) the search for a semi-reflecting target, with an adsorption parameter different from the rest of the surface (see Appendix B.4.2);
- (ii) the 2D search for an angular aperture on the boundary of a disk (see Appendix B.4.1);
- (iii) the biased search for an arbitrary number of regularly spaced targets over an otherwise semi-reflecting annulus (2D) or cone (3D), following the method of [112].

Notably, even for a 3D search for a purely reflecting target and for a 2D search with a bulk diffusion coefficient  $D_2$  smaller than the surface diffusion coefficient  $D_1$ , the surface GMFPT can be an optimizable function with respect to the desorption rate (see Figs. B.4 and B.2 below).

#### Summary of main results

- (1) We obtain an exact resolution scheme for the MFPT,
- (2) We can optimize the MFPT under analytical criteria, in contrast to Ref. [130],
- (3) We fixed the range of validity for the coarse-grained approach of Ref. [130],
- (4) The above results hold in the analogous 2D geometry (see Appendix 5.2.2).

Extensions to this project are considered in Sec. 5.4, p. 121.

5. Surface-mediated diffusion:  
mixed-boundary condition

# Conclusion and perspectives

**Conclusion** Let me summarize the results of Part. II concerning exit processes through surface-mediated diffusion:

- In Chap. 4, p. 85, we determined the MFPT to a spherical cap target which is perfectly adsorbing for particles hitting from the bulk, while the rest of the surface was semi-reflective with an adsorption coefficient  $k$ .
- In Chap. 5, p. 107, we considered a spherical cap target which is semi-reflecting for particles hitting from the bulk with an adsorption coefficient  $k_t$ . We recover the case of a homogeneous adsorption by setting  $k_t = k$ , in which case the target has the same adsorption coefficient as the rest of the surface. This assumption  $k_t = k$  drastically simplifies the system of equations on the Fourier coefficients ( $a_n$ ) from Eqs. (B.49) and (B.50). Mind that our exact solution is not explicit, as it relies on a matrix inversion Eq. (5.33) that provides the Fourier coefficients ( $d_n$ ).

The developed approach forms the theoretical ground for a systematic study of surface-mediated processes which are relevant for chemical and biochemical reactions in porous catalysts and living cells.

**Perspectives** As extensions of this work, I have

- (1) quantified numerically both the optimal desorption rate and the gain obtained by the surface-mediated process. In Fig. 5.4, we represent the gain  $G$  computed as:

$$G = \frac{\min(\tau_1(\lambda = \infty), \tau_1(\lambda = 0))}{\langle t_1 \rangle(\lambda_{opt})} \quad (5.54)$$

Interestingly, the gain is maximal along the line  $\tau_1(\lambda = \infty) = \tau_1(\lambda = 0)$  in terms of the set of parameters  $(kR, D_2/D_1)$ . The maximal gain is equal to  $74 \pm 1\%$  for  $\varepsilon = 2.10^{-3}$ , and it is a decreasing function in terms of the width of the target  $\varepsilon$ .

- (2) shown that the mean-field approach from Ref. [136], called mean-field teleportation, cannot predict the optimality of the surface-mediated diffusion process considered in Chaps. 4–5. Instead, I have developed a new mean-field approach called the correlation-less teleportation (CLT), which consists

- in neglecting the correlation spatial correlation during bulk excursions, which is equivalent to setting  $a = R$  for the probability distribution. This leads to  $\Pi(\theta) = 1/(2\pi)$ <sup>1</sup> in the  $d = 2$  case and  $\Pi(\theta) = 1/(4\pi)$  in  $d = 3$ .
- in setting the mean return to sphere time to be equal to  $\eta_d = 1/(dkR)$  (i.e.  $a = 0$ ).

The correlation-less teleportation method leads to the following analytical expression for the surface GMFPT

$$\langle t_{CLT} \rangle = \frac{1}{\omega^2} \left( 1 + \frac{\omega^2 D_1}{2kR D_2} \right) \frac{1 - \frac{\varepsilon}{\pi} - \frac{\tanh(\omega(\pi-\varepsilon))}{\pi\omega}}{\frac{\varepsilon}{\pi} + \frac{\tanh(\omega(\pi-\varepsilon))}{\pi\omega}}, \quad (5.55)$$

The advantage of this mean-field approach are (i) that it does neglect the spatial correlation between desorption and adsorption events and (ii) that correctly predicts the value of the

<sup>1</sup>I recall that  $\Pi(\theta)$  corresponds to the probability density for a particle, initial desorbed at  $\theta = 0$ , first reach the surface  $r = R$  at the angle  $\theta$  in the absence of a target (see Sec. B.2.1).

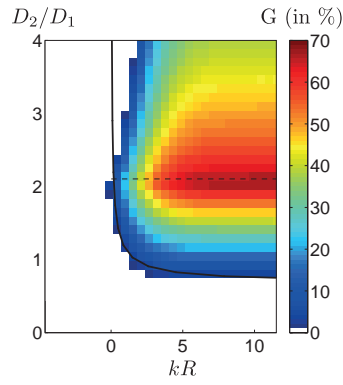


Figure 5.4: Gain in the surface GMFPT  $G$  (defined in Eq. (5.54)) expressed in % in terms of the ratio of the bulk to surface diffusion coefficients  $D_2/D_1$  and adsorption coefficient  $kR$ , for a perfectly adsorbing target of half width  $\varepsilon = 2.10^{-3}$  within the boundary of a  $d = 2$  disk. The gain is maximal along the line  $\tau_1(\lambda = \infty) = \tau_1(\lambda = 0)$ , indicated by a dashed line.

minimum of the GMFPT in the regime  $kR \ll 1$  and leads to analytical formulas for the optimal desorption rate and for its corresponding search time. But the gain in the MFPT is significant only in the region  $kR \gg 1$ , hence the correlation-less teleportation appears to have a limited interest.

- (3) computed the Laplace transform of the FPT distribution to the exit, using the method developed in Chaps. 4–5,
- (4) computed the MFPT for the gated exit problem in the case  $\varepsilon = 0$  (see p. 78 for a definition).

## Part III

# Search strategy for active processes



# Search strategy for the Pearson random walks

In this chapter, we consider a minimal model of an active random search process: the exponential Pearson random walk (EPRW), whose trajectory is composed of straight runs at the constant velocity  $v$  interrupted by instantaneous reorientation events at exponentially distributed random times. We focus on the global mean first-passage time (GMFPT) to a single spherical target located at the center of the spherical confining domain, both in two or three dimensions. Using two approximate resolution schemes, we show that the GMFPT can be minimized in terms of an optimal persistence time for both specular or diffusive confining boundaries.

**This chapter contains work in progress, indicated by a  $\blacktriangle$  symbol.**

## Contents

<b>6.1</b>	<b>Model and methods</b>	<b>126</b>
6.1.1	Model	126
6.1.2	Methods and objectives	128
6.1.2.1	Considered MFPTs quantities	128
6.1.2.2	Position of the problem	128
6.1.2.3	Two resolution schemes	129
6.1.2.4	Questions and objectives	129
<b>6.2</b>	<b>Asymptotic behaviour and optimality</b>	<b>130</b>
6.2.1	Diffusive behaviour in the limit $\tau \ll a/v$	130
	Diffusion equation	130
	Behaviour at the boundary in the limit $\tau \ll a/v$	130
6.2.2	Asymptotic behaviour in the limit $\tau \gg b/v$	131
6.2.2.1	Specular confinement	131
6.2.2.2	Stubborn confinement	132
6.2.2.3	Diffusive boundary	132
	Zeroth order term: ballistic search time is finite	133
	First order term: optimality of search process	133
6.2.3	Matched asymptotic and optimality	134
6.2.3.1	Optimality and plateau with $\tau$ for specular confinement	134
6.2.3.2	Diffusive confinement	135
<b>6.3</b>	<b>Conclusion</b>	<b>138</b>
<b>6.4</b>	<b>Perspectives</b>	<b>138</b>
6.4.1	Comparison to other distributions of reorientation times	138
6.4.1.1	Regular steps: Dirac distribution	138
6.4.1.2	Lévy distribution	140
6.4.2	Chemotactic search	141



Searchers with at least short range memory skills exhibit persistent motion, such as bacteria [137] or larger organisms [138]. These searchers are often modelled as active random walks [139] which are characterized by their well-defined instantaneous velocity  $v$ , in contrast to *passive* Brownian random walks. As explained in Sec. 2.1.1, p. 32, for active random walks the position process  $\mathbf{r}(t)$  is not Markovian and we cannot apply the asymptotic results from Ref. [140] on the mean first-passage time (MFPT) and on the full distribution of the first-passage time.

A minimal model of active random walk is the Pearson random walk (PRW, see also p. 18), whose trajectory is composed of ballistic motions at a constant velocity  $v$  within a space  $\Omega_r \subset \mathbb{R}^d$  which are interrupted by instantaneous and isotropic reorientations. The duration  $t$  between two reorientations is a random variable with a probability density denoted  $\pi(t)$ . The choice

$$\pi(t) = \frac{e^{-t/\tau}}{\tau}, \quad \forall t \geq 0, \quad (6.1)$$

defines the exponential PRW (EPRW) process.

Some exact results have been derived concerning the diffusion properties of PRW in infinite space [141] and the mean return time in confined domains [142, 143]. However, the question of determining first-passage properties of PRW defined over *continuous* time and space has been unanswered so far.

In this chapter, we compute the global MFPT (GMFPT) to reach a centered spherical target within a spherical confining domain. The fact that only the first passage matters corresponds implicitly to the case of a destructive search, since the target can be discovered only once. The GMFPT is shown to admit a minimum as a function of the reorientation rate  $\tau$ . This minimum corresponds to an optimal search strategy which is very different from the simple ballistic motion expected in the case of Poisson distributed targets [14]. The GMFPT is sufficient to characterize the whole FPT distribution: indeed, Monte-Carlo simulations show that the global FPT distribution is very well approximated by an exponential distribution as soon as  $a/b < 0.1$  (see App. Sec. C.1.2, p. 190).

The Ref. [144] considers an EPRW with motion at regular discrete times on a  $\mathbb{N}^d$  lattice whose target is a single site of the lattice. In spite of some similarities between the discrete and continuous models, the process considered in this chapter cannot be obtained from the continuous limit of the discrete process of Ref. [144]. In Ref. [144], the direction of the velocity vector is drawn from a finite set (of cardinal 4 for a  $d = 2$  lattice, of cardinal 6 for a  $d = 3$  lattice), in contrast to present model in which the direction of the velocity vector is drawn over the continuous interval  $[0, 2\pi]$ . Therefore, we cannot apply the results from [144] to the continuous model considered here and we need to develop a new mathematical framework.

## 6.1 Model and methods

### 6.1.1 Model

The position and velocity of the searcher are respectively labelled by  $\mathbf{r}$  and  $\mathbf{v}$ . The velocity vector  $\mathbf{v}$  performs a discrete time random walk within  $S_v$ , the  $(d - 1)$ -sphere of radius  $v \geq 0$  (see p. 18). According to the space dimension  $d$ ,

- (1)  $d = 1$ : the velocity vector  $\mathbf{v}$  equals  $\pm v$ . This geometry is considered in Sec. 2.3.2, p. 40.
- (2)  $d = 2$ : the velocity vector  $\mathbf{v}$  belongs to a circle of radius  $v$ . The vector  $\mathbf{v}$  is parametrized by the angle  $\theta = \widehat{(\mathbf{r}, \mathbf{v})}$  and through the scalar product  $\mathbf{r} \cdot \mathbf{v} = rv \cos \theta$ . Notice that the search

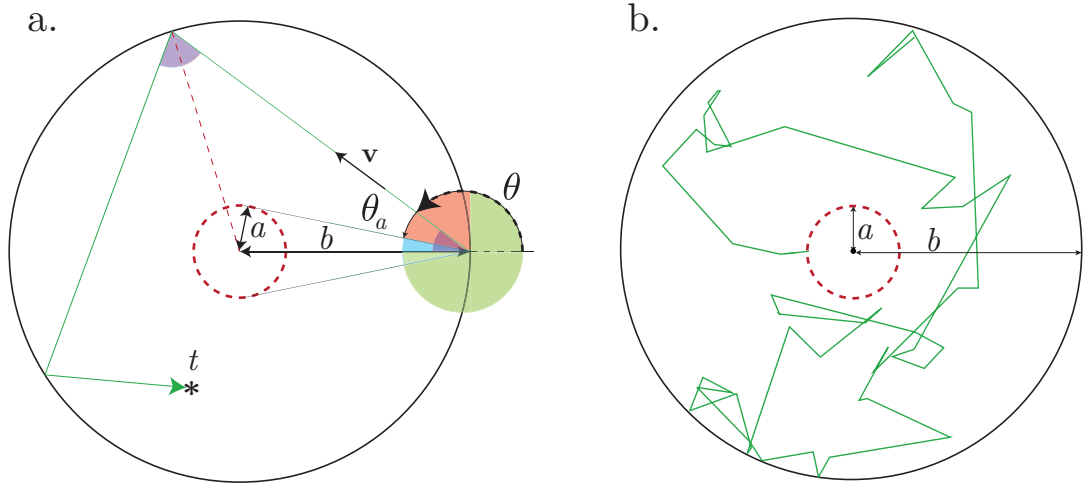


Figure 6.1: Trajectory of a Pearson Random Walk in  $d = 2$  dimensions with a specular confinement at  $r = b$ . (a.) Sketch of the geometry. The length of the run is  $v\tau$ . From the confining boundary, the target is seen under an half-angle  $\theta_a = \arcsin(b/a)$ . For symmetry reasons, the initial direction of the velocity  $\theta$  can be folded within the interval  $[\pi/2, \pi]$  (b.) Simulated trajectory of an exponential PRW (EPRW).

problem is invariant by the transformation  $\mathbf{r} \rightarrow -\mathbf{r}$  and therefore by the transformation  $\theta \rightarrow -\theta$ . In the rest of this section we consider that  $\theta \in [0, \pi]$  (see Fig. 6.1).

- (3)  $d = 3$ : the velocity vector  $\mathbf{v}$  belongs to a sphere of radius  $v$ . The vector  $\mathbf{v}$  is parametrized by the polar angle  $\theta \in [0, \pi]$  (the vector  $\mathbf{r}$  defines the zenith direction such that  $\mathbf{r} \cdot \mathbf{v} = rv \cos \theta$ ) and by the azimuthal angle  $\phi \in [0, \pi]$ . Notice that the search problem is independent of the  $\phi$  coordinate of the velocity vector. After each reorientation event, we can set  $\phi = 0$ , hence after each reorientation event the  $d = 3$  process can be projected within a  $d = 2$  disk.

The latter point (3) gives the hint that we can consider the problem in the more general framework of an arbitrary angular probability distribution  $d\mu(\theta)$  for the reorientation direction, as discussed in the "Perspectives" section Sec. 6.4, p. 138

**Target ( $r = a$ )** The process is stopped as soon as the position  $\mathbf{r}$  of the searcher crosses the target, a  $(d - 1)$ -sphere of radius  $|\mathbf{r}| = a$ :  $T(|\mathbf{r}| = a, \mathbf{v}) = 0$  for all incoming  $\mathbf{v}$ , i.e. for all  $\mathbf{v}$  such that  $\mathbf{v} \cdot \mathbf{n}_a < 0$  where  $\mathbf{n}_a$  is the local outgoing normal vector to  $S_a$ .

**Confinement ( $r = b$ )** We will consider three types of confining boundary at  $r = b$ :

- (a) **specular** boundary, i.e. the incident velocity vector is reflected as a mirror would reflect a ray of light. More precisely, if  $\mathbf{n}_b$  is the outgoing normal vector to the boundary, the relation between the reflected  $\mathbf{v}'$  and the incident  $\mathbf{v}$  vectors reads

$$\mathbf{v}' = \mathbf{v} - 2(\mathbf{v} \cdot \mathbf{n}_b) \mathbf{n}_b. \quad (6.2)$$

- (b) **scattering** boundary, i.e. that the incident velocity vector  $\mathbf{v}$  is scattered into an outgoing vector  $\mathbf{v}'$  with a random direction  $\mathbf{v}' \cdot \mathbf{n}_b < 0$  which is uniformly distributed on the sphere  $S_v$ . We consider the

- **diffusive** condition, i.e. the particle is immediately reoriented when hitting the boundary  $r = b$ ,
- **stubborn** condition, i.e. the particle sticks for the remaining time before the next reorientation.

The diffusive boundary condition seems adapted to the study of living micro-swimmers, which change their direction whenever they encounter a boundary [145]. In the Appendix C.1.1, we explain how to deal with the boundary conditions to generate random trajectories (i.e. Monte-Carlo sampling). The behaviour of the MFPT in the limit  $b/v \ll \tau$  crucially depends on the choice of boundary condition: the MFPT tends to a finite value in the diffusive case, but it diverges with  $\tau$  in the specular and stubborn cases (see Sec. 6.2, p. 130).

## 6.1.2 Methods and objectives

### 6.1.2.1 Considered MFPTs quantities

In the rest of this chapter, we define several MFPTs quantities:

- (i) The MFPT from the position  $\mathbf{r}$  with the initial velocity  $\mathbf{v}$  is denoted  $t(\mathbf{r}, \mathbf{v})$ .
- (ii) The MFPT averaged over all possible starting velocities  $\mathbf{v} \in S_v$  is denoted  $\langle t(\mathbf{r}) \rangle$ :

$$\langle t(\mathbf{r}) \rangle \equiv \int_{\mathbf{v}' \in S_v} t(\mathbf{r}, \mathbf{v}') d\mu(\mathbf{v}'). \quad (6.3)$$

Similarly we define  $\langle \cdot \rangle_\omega$ , which refers to the angular average over a subset  $\omega$  of  $S_v$ .

- (iii) The averaged MFPT over all possible starting positions  $\mathbf{r} \in \Omega_r$  and over all possible starting velocities  $\mathbf{v} \in S_v$  is called the global MFPT (GMFPT) and is denoted  $\overline{\langle t \rangle}$ , i.e.

$$\overline{\langle t \rangle} \equiv \int_{\mathbf{r} \in \Omega_r} \langle t(\mathbf{r}) \rangle d\mu(r), \quad (6.4)$$

where  $d\mu(\mathbf{r})$  is the uniform probability measure on  $\Omega_r$ , defined in Table 6.1.

Quantity	$d = 1$	$d = 2$	$d = 3$
$\omega_d$ (defined by $d\mu(\mathbf{v}') = \omega_d d\theta$ )	$\frac{1}{2}$	$\frac{1}{\pi}$	$\frac{\sin \theta}{2}$
$\theta$	$\{0, \pi\}$	$[0, \pi]$	$[0, \pi]$
$d\mu(r)$	$\frac{dr}{b-a}$	$\frac{2rdr}{(b-a)^2}$	$\frac{3r^2dr}{(b-a)^3}$

Table 6.1: Definition of quantities relative to probability measures.

### 6.1.2.2 Position of the problem

From Eq. (2.17), the MFPT  $t(\mathbf{r}, \mathbf{v})$  is shown to satisfy the following integro-differential equation:

$$\mathbf{v} \cdot \nabla_{\mathbf{r}} t(\mathbf{r}, \mathbf{v}) + \frac{1}{\tau} \int_{\mathbf{v}' \in S_v} \{t(\mathbf{r}, \mathbf{v}') - t(\mathbf{r}, \mathbf{v})\} d\mu(\mathbf{v}') = -1, \quad (6.5)$$

where

- (i)  $\mathbf{r} \in \Omega_r$ , i.e.  $\Omega_r$  is the volume enclosed between the spheres  $S_a$  and  $S_b$ .
- (ii)  $\nabla_{\mathbf{r}}$  is the gradient operator, such that in Cartesian coordinates  $\mathbf{v} \cdot \nabla_{\mathbf{r}} = v_x \partial_x + v_y \partial_y$  if  $d = 2$ . The first term in the left-hand side of Eq. (6.5) corresponds to the phases of ballistic motion.

- (iii)  $d\mu_v(\mathbf{v}') = \omega_d d\theta$  is the uniform probability measure on the  $S_v$  sphere. The second term in the left-hand side of Eq. (6.5) corresponds to the reorientation process.

The Eq. (6.5) is to be completed by boundary conditions. As mentioned in Sec. 2.4, p. 42, determining an exact expression of the MFPT at the boundaries is a difficult problem. To overcome this difficulty, we have developed two resolution schemes that we present in the next paragraph.

### 6.1.2.3 Two resolution schemes

To tackle the difficulty of determining the values of the MFPT at the boundaries, we propose two resolution schemes:

- (1) A first idea is to search for exact expressions for the GMFPT in the two limits  $\tau \rightarrow 0$ , denoted  $t^{(1)}$ , and  $\tau \rightarrow \infty$ , denoted  $t^{(2)}$ . We call *matched asymptotics expansion* the approximation  $\overline{\langle t \rangle} \approx t^{(1)} + t^{(2)}$ , which is shown in Sec. 6.2, p. 130 to accurately predict the optimal reorientation rate.
- (2) A second idea is to establish *exact relations at the boundary conditions* on the averaged search times  $\langle t(a) \rangle$  and  $\langle t(b) \rangle$ . This second method is developed in the Appendix Sec. C.2, p. 191.

In the rest of this thesis chapter, we apply the matched asymptotics expansion method.

### 6.1.2.4 Questions and objectives

Our two resolution schemes aim at answering the following questions concerning the GMFPT:

- (a) What is the asymptotic behaviour of the GMFPT, defined in Eq. (6.4), in the limit  $\tau \ll a/v$ , and in the limit  $\tau \gg b/v$ ? [Answer: see Eq. (6.12) and Eq. (6.18)].
- (b) Is there an optimal reorientation rate minimizing the GMFPT in the case of a diffusive boundary condition? [Answer: yes there is, see Eq. (6.17)]
- (c) What is the scaling law for the optimal reorientation rate minimizing the GMFPT (if any) in terms of the geometric parameters  $a$  and  $b$ ? [Answer: see Eq. (6.31)]
- (d) How does the GMFPT with a specular confining boundary compare to the GMFPT with a diffusive confining boundary? In particular, is the optimal search process for a specular boundary faster or slower than for a diffusive boundary? [Answer: see p. 135]

## 6.2 Asymptotic behaviour and optimality

### 6.2.1 Diffusive behaviour in the limit $\tau \ll a/v$

In the first paragraph, we explain how to derive an approximate diffusion equation on the MFPT from Eq. (6.5) that is exact in the limit  $\tau \rightarrow 0$ .

**Diffusion equation** We use the method first introduced in Ref. [48] and which is inspired by the resolution scheme for the  $d = 1$  problem (see Sec. 2.3.2, p. 40). We define the vector  $\mathbf{Z}(\mathbf{r}) = \langle \mathbf{v}' t(\mathbf{r}, \mathbf{v}') \rangle$ , where the averaging operator  $\langle \cdot \rangle$  is defined in Eq. (6.3). Considering the products of  $\mathbf{v}$  times Eq. (6.5) yields

$$\nabla \cdot \mathbf{Z}(\mathbf{r}) = -1 \quad \text{and} \quad \mathbf{Z}(\mathbf{r}) = \tau \langle \mathbf{v}' \cdot \nabla t(\mathbf{r}, \mathbf{v}') \rangle, \quad (6.6)$$

which in turns provides the following equation in Cartesian coordinates

$$\tau \sum_{i \in \llbracket 1, d \rrbracket} \sum_{j \in \llbracket 1, d \rrbracket} \frac{\partial^2}{\partial x_i \partial x_j} \langle v_i v_j t(\mathbf{r}, \mathbf{v}) \rangle = -1. \quad (6.7)$$

► We now make the assumption that the MFPT and the initial velocities are uncorrelated. This decoupling assumption writes, for all  $\mathbf{r} \in \Omega_r$ ,

$$\langle v_i v_j t(\mathbf{r}, \mathbf{v}) \rangle \approx \langle v_i v_j \rangle \langle t(\mathbf{r}, \mathbf{v}) \rangle = \frac{v^2}{d} \delta_{ij} \langle t(r) \rangle, \quad \forall (i, j) \in \llbracket 1, d \rrbracket \times \llbracket 1, d \rrbracket. \quad (6.8)$$

Notice that the decoupling approximation is exact in the case  $d = 1$  because  $v_i v_i = v^2$  is a constant.

► Combining Eq. (6.7) and the approximation of Eq. (6.8) leads to the following effective diffusion equation

$$D \Delta \langle t(r) \rangle = -1, \quad \forall \mathbf{r} \in \Omega_r. \quad (6.9)$$

where  $D = v^2 \tau / d$  is an effective diffusion coefficient. The decoupling approximation, which relies on the approximation that the MFPT is independent of the direction of the initial velocity  $\mathbf{v}$ , is expected to be valid in the limit  $\tau \rightarrow a/v$ .

The search process of a spherical target  $S_a$  within a spherical confining domain  $S_b$  is invariant under rotation of the position vector  $\mathbf{r}$ . Rotation invariant solutions of Eq. (6.9) are read:

$$\langle t(r) \rangle = \frac{1}{D} \hat{f}(r) + b_0 g\left(\frac{r}{a}\right) + a_0, \quad (6.10)$$

where the quantities  $\hat{f}(r)$  and  $g\left(\frac{r}{a}\right)$  are defined in Sec. 2.3.1.2, p. 39; the constants  $b_0$  and  $a_0$  are to be determined by the boundary conditions on  $\langle t(r) \rangle$  at  $r = a$  and  $r = b$ .

**Behaviour at the boundary in the limit  $\tau \ll a/v$**  In the limit  $\tau \ll a/v$ , the MFPT is solution of the Poisson equation Eq. (6.9) and the process converges to a symmetric Brownian process (see the introduction, Sec. 2.2.1, p. 36). In the limit  $\tau \ll a/v$ , the MFPT does not depend on the direction of the velocity  $\theta$  so that the boundary conditions are

$$\langle t(a) \rangle = 0, \quad \text{and} \quad [\partial_r \langle t(r) \rangle]_{r=b} = 0, \quad (6.11)$$

for the diffusive, specular and stubborn types of boundary conditions. Using the results of Sec. 2.3.1.2, p. 39 with the substitution  $D = v^2 \tau / d$  leads to the following expression of the GMFPT:

$$\overline{\langle t \rangle} \underset{v\tau \ll a}{\sim} \bar{t}^{(1)} \equiv \begin{cases} \frac{1}{v\tau} \left( \frac{b^4 \log(\frac{b}{a})}{b^2 - a^2} + \frac{a^2 - 3b^2}{4} \right) & \underset{a \ll b}{\sim} \frac{b^2}{v\tau} \ln\left(\frac{b}{a}\right) & (d=2), \\ \frac{1}{v\tau} \left( \frac{b^3}{a} - \frac{9b^2}{5} - \frac{9a^3(a+b)}{5(a^2+ab+b^2)} + 2a^2 \right) & \underset{a \ll b}{\sim} \frac{b^3}{av\tau} & (d=3), \end{cases} \quad (6.12)$$

The expressions of Eq. (6.12) are shown to fit to the numerical simulations for  $\tau$  as high as  $a/v$  (see in Fig. 6.2).

$$\overline{\text{Var}[\sigma]} =_{v\tau \ll a} \sim \bar{v}^{(1)} \equiv \begin{cases} \sim_{a \ll b} & (d=2), \\ \sim_{a \ll b} & (d=3), \end{cases} \quad (6.13)$$

In the next two paragraphs, we consider the limit  $\tau \rightarrow \infty$ , which is shown to depend on the diffusive, specular or stubborn nature of the boundary condition.

## 6.2.2 Asymptotic behaviour in the limit $\tau \gg b/v$

We derive a renewal equation Eq. (6.17) that is valid in  $\tau \gg b/v$ , first in the case of a specular confining boundary.

### 6.2.2.1 Specular confinement

We consider a searcher initially at a random position within  $\Omega_r$ . The probability to reach the target in a single run reads

$$p_h = \int_a^b dp_r(r) p_{\text{dir}}(r) p_{\text{reach}}(r), \quad (6.14)$$

where

- (i)  $dp_r(r)$  is the probability distribution of the position of the searcher at reorientation events. Based on the results from Monte-Carlo simulations (see Fig. C.1) in the Appendix Sec. C.1.2, p. 190), we assume that  $p_r$  has relaxed to a steady state which in the limit  $a/b \ll 1$  is the uniform distribution  $dp_r(r) = d\mu(r)$ .
- (ii)  $p_{\text{dir}}(r)$  is the probability of choosing a direction that crosses the target (either directly or after a single reflexion at  $r = b$ ). At first order in  $a/r \ll 1$ , it reads

$$p_{\text{dir}}(r) = \begin{cases} 2 \frac{a}{\pi r} & (d=2), \\ \frac{a^2}{2r^2} & (d=3). \end{cases} \quad (6.15)$$

- (iii)  $p_{\text{reach}}(r) = \exp(-r/\tau)$  is the probability of performing a sufficient long run to reach the target.

Combining the definition of Eq. (6.14) and Eq. (6.15), the average hitting probability after a reorientation reads

$$p_h = \begin{cases} \frac{4a}{\pi b^2} \tau \left(1 - e^{-\frac{b}{\tau}}\right) & (d=2), \\ \frac{3a^2}{2b^3} \tau \left(1 - e^{-\frac{b}{\tau}}\right) & (d=3), \end{cases} \quad (6.16)$$

In the limit  $\tau \gg b/v$  and  $a/b \ll 1$ , the GMFPT is expected to be equal to

$$\bar{t}^{(2)} = \tau_f \left\{ \sum_{n=1}^{\infty} n p_h (1 - p_h)^n \right\} = \tau_f \frac{1 - p_h}{p_h}, \quad (6.17)$$

where

- (i)  $(1 - p_h)/p_h$  the mean number of unsuccessful reorientations before reaching the target (which is the mean of a geometric distribution),
- (ii)  $\tau_f$  is the mean time spent between two reorientations. In the specular and stubborn cases,  $\tau_f = \tau$  but not in the diffusive case (see Eq. (6.23)).

The Eq. (6.17) can be obtained as a renewal equation:  $\bar{t}^{(2)} = p_h \tau_f + (1 - p_h) \bar{t}^{(2)}$  [113]. Combining Eq. (6.17) and Eq. (6.16), we obtain:

$$\bar{t} \underset{a/v \ll b/v \ll \tau}{\sim} \bar{t}^{(2)} = \begin{cases} \frac{\pi b^2}{4a} \frac{1}{(1 - e^{-\frac{b}{\tau v}})} \sim \tau \frac{\pi}{4} \frac{b}{a} & (d = 2), \\ \frac{2b^3}{3a^2} \frac{1}{(1 - e^{-\frac{b}{\tau v}})} \sim \tau \frac{2}{3} \left(\frac{b}{a}\right)^2 & (d = 3). \end{cases} \quad (6.18)$$

which corresponds to the results of Monte–Carlo simulations (see Figs. 6.2 and 6.4).

Similarly, we obtain the variance of the first passage time in the regime  $\tau \gg b/v$ :

$$\overline{\text{Var}[\sigma]} = \tau_f^2 \frac{1 - p_f}{p_f^2} \sim (\bar{t}^{(2)})^2. \quad (6.19)$$

### 6.2.2.2 Stubborn confinement

The method is similar to the one presented for the specular case, and leads to:

$$\bar{t}^{(2)} = \begin{cases} \tau \frac{\pi}{2} \frac{b}{a} e^{\frac{b}{\tau}} & (d = 2), \\ 2\tau \left(\frac{b}{a}\right)^2 e^{\frac{b}{\tau}} & (d = 3). \end{cases} \quad (6.20)$$

The expression Eq. (6.20) diverges in the limit  $\tau \ll a/v$ . Rather than using 6.20, we use the following efficient expression,

$$\bar{t}^{(2)} = \begin{cases} \frac{\pi}{2} \frac{b^2}{a} \frac{1}{(1 - e^{-\frac{b}{\tau}})} & (d = 2), \\ 2\tau \left(\frac{b}{a}\right)^2 \frac{b}{(1 - e^{-\frac{b}{\tau}})} & (d = 3). \end{cases} \quad (6.21)$$

which is also valid in the large range of  $b/v \ll \tau$  and which tends to 0 in the limit  $\tau \ll a/v$ .

► For stubborn or specular confinement at  $r = b$ , the MPFT is an increasing and unbounded function of  $\tau$  in the limit  $\tau \gg b/v$ . In the diffusive limit  $\tau \ll a/v$ , the GMFPT (which does not depend on the specular or scattering nature of the confinement) is a decreasing function with  $\tau$ . Therefore the GMFPT is therefore an optimizable function of  $\tau$  in both cases of specular or stubborn confinement.

### 6.2.2.3 Diffusive boundary

In the following paragraph, we justify that the GMFPT is still an increasing function of  $\tau$  in case of a the diffusive confinement, which implies that the GMFPT is an optimizable function.

We consider the next order terms in  $\tau$  in the probability  $p_h$  to reach the target between two encounters with the confining boundary  $r = b$ :

$$p_h = p_h^{(0)} + \sum_{n=1}^{\infty} \frac{p_h^{(n)}}{\tau^n}. \quad (6.22)$$

The terms  $p_h^{(n)}$  quantifies the probability of events with  $n$  reorientations along the trajectory between the two encounters with the boundary at  $r = b$ .

**Zeroth order term: ballistic search time is finite** We use the same argument with Eq. (6.17), with:

- (i)  $p_h^{(0)} = 2a/(\pi b)$  in  $d = 2$ , and  $p_h^{(0)} = (a/b)^2$  in  $d = 3$ ,
- (ii)  $\tau_f = 4b/(v\pi)$  in  $d = 2$ , and  $\tau_f = b/v$  in  $d = 3$ , is the average time between two reorientations when reaching the boundary at  $r = b$ .

Substitution of these values for  $p_h$  and  $\tau_f$  within Eq. (6.17) leads to

$$\langle \bar{t} \rangle \underset{a/v \ll b/v \ll \tau}{\sim} \bar{t}^{(2)} = \begin{cases} 2 \frac{b^2}{va} & (d = 2), \\ 2 \frac{b^3}{va^2} & (d = 3), \end{cases} \quad (6.23)$$

which corresponds to behavior observed in Monte–Carlo simulations (see Figs. 6.2 and 6.4).

► For a diffusive confinement at  $r = b$ , the MPFT converges to a finite value in the limit  $\tau \rightarrow \infty$ . We consider the next order term  $p_h^{(1)}$  and show that the MFPT converge to this finite value from below, which is sufficient to conclude on the optimizability of the search process.

**First order term: optimality of search process** We now consider the first order term  $p_h^{(1)}$ . The probability density  $dp_h^{(1)}/\tau$  to reach the target through a single reorientation from  $r(t)$  reads

$$\frac{dp_h^{(1)}}{\tau} = \frac{dt}{\tau} \left( \frac{a}{r(t)} \right)^{d-1} \omega_d, \quad (6.24)$$

which is the product of (i) the probability density for reorientations  $dt/\tau$  by (ii) the probability for a reorientation towards the target from the position  $r(t) = \sqrt{v^2 t^2 + b^2 + 2vbt \cos \theta}$ , where  $\theta$  is the initial direction of the velocity. The overall probability  $p_h^{(1)}/\tau$  is the sum over all possible reorientation times  $t$  and over all possible initial velocity directions  $\theta \in [\pi/2, \pi - \arcsin(b/a)]$ :

$$\frac{p_h^{(1)}}{\tau} = 2\omega_d \int_{\pi/2}^{\pi - \arcsin(b/a)} d\mu(\theta) \int_0^{-2b \cos \theta} \frac{dt}{\tau} \left( \frac{a}{\sqrt{v^2 t^2 + 2vbt \cos \theta + b^2}} \right)^{d-1}. \quad (6.25)$$

The integral in Eq. (6.25) can be computed numerically. We derive a simple approximate expression for Eq. (6.25). We expect  $p_h^{(1)}$  to behave as the product of (i) the time  $\tau_f$  of a flight between two reorientations at the boundary  $r = b$ , and (ii) the probability  $\bar{p}_h \approx p_h^{(0)}$  to reach the target through a ballistic run and averaged over the initial positions in the disk:

$$p_h^{(1)} \approx \tau_f p_h^{(0)} = \begin{cases} \frac{8}{\pi^2} \frac{a}{v} & (d = 2), \\ \frac{a^2}{vb} & (d = 3). \end{cases} \quad (6.26)$$

The approximate expressions of Eq. (6.26) are in good agreement with the numerical evaluations of Eq. (6.25). In  $d = 2$ , Eq. (6.26) does not depend on  $b$  and accordingly, the exact evaluation of Eq. (6.25) weakly depends on  $b$ . The interpretation in  $d = 2$  is that, even in the limit of long runs limit, hits after a single reorientation within the bulk of the disk mostly occur within the neighborhood of the target ( $r = a$ ).



We now introduce in Eq. (6.17) the expression of Eq. (6.22) truncated at its first order in  $\tau \gg b/v$  to obtain the asymptotic GMFPT:

$$\overline{\langle t \rangle} \underset{a/v \ll b/v \ll \tau}{\sim} \frac{\tau_f}{p_h^{(0)}} \left( 1 - \frac{1}{\tau} \frac{p_h^{(1)}}{p_h^{(0)}} \right) \approx \begin{cases} \frac{2b^2}{va} - \frac{32}{\pi^3} \frac{b^3}{av^2} \frac{1}{\tau} & (d=2), \\ \frac{2b^3}{va^2} - \frac{b^4}{a^2v^2} \frac{1}{\tau} & (d=3). \end{cases} \quad (6.27)$$

The expression Eq. (6.27) accurately predict the behavior of simulations at large  $b/v \ll \tau$ . Hence, we have justified that the GMFPT converges to  $\tau_f/p_h^{(0)}$  as an increasing function of  $\tau$ .

► The expression Eq. (6.27) leads to an intuitive interpretation for the optimal reorientation rate. In contrast to the ballistic case ( $\tau = \infty$ ), at a finite reorientation rate  $\tau$  the searcher has the opportunity to turn when it is close to the target, with a relatively high probability to encounter the target in a very short time.

### 6.2.3 Matched asymptotic and optimality

We call *matched asymptotics expansion* for the MFPT and variance the quantities

$$\overline{\langle t \rangle} = \bar{t}^{(1)} + \bar{t}^{(2)}, \quad \text{and} \quad \overline{\langle v \rangle} = \bar{v}^{(1)} + \bar{v}^{(2)}, \quad (6.28)$$

where  $\bar{t}^{(1)}$  is given by Eq. (6.12) and  $\bar{t}^{(2)}$  is given by Eq. (6.17), Eq. (6.21) or Eq. (6.23) for specular, stubborn or diffusive confinement, respectively. As  $\bar{t}^{(1)} = 0$  for  $\tau = 0$ , the expression  $\overline{\langle t \rangle}$  has the expected behavior  $\overline{\langle t \rangle} \rightarrow \bar{t}^{(2)}$  in the limit  $b/v \ll \tau$ . Conversely, in the limit  $\tau \ll a/v$ :  $\overline{\langle t \rangle} \rightarrow \bar{t}^{(1)}$ . In the next section, the matched asymptotic expansion is shown to lead to an accurate approximate expression for the optimal reorientation rate.

#### 6.2.3.1 Optimality and plateau with $\tau$ for specular confinement

In this section, we obtain the scaling law of the optimal reorientation time  $\tau_{\text{opt}}$  in the case of a specular confining boundary, which is shown in the next section to hold in the cases of a stubborn or diffusive confinement.

We propose to estimate the optimal reorientation rate  $\tau_{\text{opt}}$  from the matched asymptotic expansion, as the solution of the equation:

$$\frac{\partial \overline{\langle t \rangle}}{\partial \tau} \Big|_{\tau_{\text{opt}}} = \frac{\partial \bar{t}^{(1)}}{\partial \tau} \Big|_{\tau_{\text{opt}}} + \frac{\partial \bar{t}^{(2)}}{\partial \tau} \Big|_{\tau_{\text{opt}}} = 0 \quad (6.29)$$

From Eq. (6.29), the proposed optimal reorientation rate  $\tau_{\text{opt}}$  exhibits a linear scaling with the system size  $b$

$$\tau_{\text{opt}} \underset{a \ll b}{\sim} \zeta \frac{b}{v} \quad (6.30)$$

with a proportionality constant that depend (i) weakly on the space dimension ( $\zeta = 0.08 \pm 0.02$  in  $d = 2$  and  $\zeta = 0.09 \pm 0.02$  in  $d = 3$ ) and (ii) very weakly on the target size  $a$ , as long as the system is large  $b \gg a$ . Notice that for large system sizes the optimal persistence length becomes much larger than the target size. The theoretical optimal reorientation rate Eq. (6.30) is shown to agree with Monte–Carlo simulations (see Fig. 6.4).

These conclusions are similar to those from the discrete lattice model of Ref. [144], in which the proportionality coefficients were found to be:  $\zeta = 0.14$  in  $d = 2$  and  $\zeta = 0.12$  in  $d = 3$ . We

stress that this is not be expected a priori, in the sense that the process considered here is not a continuous limit of the discrete process studied in Ref. [144]. The difference with the scaling  $\tau_{\text{opt}} \sim a \log(b/a)$  from Ref. [146] is explained by a different condition on the target detection: in the "static model" of Ref. [146] the target is detected only if a reorientation event occur within the sphere  $S_a$ .

We expect the GMFPT at the optimal reorientation rate to scale as  $\tau_{\text{opt}}/p_h$ , using similar arguments as in Sec. 6.2.2, p. 131 that  $\bar{t}_{\text{opt}} \approx \tau_{\text{opt}}/p_h$ . Indeed, due to the scaling  $\tau_{\text{opt}} \propto b$  from Eq. (6.30), we expect the value of the search time at optimality to be close to the value of  $\bar{t}^{(2)}$  for a diffusive confining boundary (given in Eq. (6.23)). The intuition is confirmed by Monte-Carlo simulations (see Fig. 6.4), which indicate the following scaling for the optimal search time:

$$\overline{\langle t \rangle}_{\text{opt}} \underset{a \ll b}{\sim} \begin{cases} \xi \frac{2b^2}{av} & (d = 2), \\ \xi \frac{2b^3}{va^2} & (d = 3), \end{cases} \quad (6.31)$$

where the coefficient  $\xi$  is close to 1:  $\xi = (0.85 \pm 0.05)$  in  $d = 2$  and  $\xi = (0.9 \pm 0.05)$  in  $d = 3$ ).

The GMFPT is shown in Fig. 6.4 to exhibit a large plateau around  $\tau = \tau_{\text{opt}}$  in which the GMFPT does not significantly differ from its value at optimality (see Figs. 6.2 and 6.4). The lower bound of the plateau is estimated by the cross-over reorientation rate  $\tau_m$  from the diffusive limit to the optimal regime, i.e.  $\bar{t}^{(1)}(\tau_m) \approx \bar{t}_{\text{opt}}$ ,

$$\tau_m \underset{a \ll b}{\sim} \begin{cases} \frac{a}{2v} \ln\left(\frac{b}{a}\right) & (d = 2), \\ \frac{a}{2v} & (d = 3), \end{cases} \quad (6.32)$$

Conversely, the upper bound of the plateau is estimated by the cross-over reorientation rate  $\tau_p$  from the optimal regime to the ballistic limit, i.e.  $\bar{t}_{\text{opt}} \approx \bar{t}^{(2)}(\tau_p)$ ,

$$\tau_p \underset{a \ll b}{\sim} \begin{cases} \frac{8}{\pi v} b & (d = 2), \\ \frac{3b}{v} & (d = 3), \end{cases} \quad (6.33)$$

Within the range  $\tau \in [\tau_m, \tau_p]$ , the GMFPT varies by less than a factor 2 (see Fig. 6.4).

### 6.2.3.2 Diffusive confinement

▲ As predicted by Sec. 6.2.2.3, p. 132, an optimum is visible in Fig. 6.2. However, the quantity  $\bar{t}^{(1)} + \bar{t}^{(2)}$ , with  $\bar{t}^{(1)}$  given by Eq. (6.12) and  $\bar{t}^{(2)}$  by Eq. (6.23), is a monotonously decreasing function of  $\tau$ , thus the method used for the specular case is not applicable. Nevertheless, the expression from Eq. (6.30) provides an excellent estimate for the optimal reorientation rate  $\tau_{\text{opt}}$  for the diffusive case, with  $\zeta = ?$  in  $d = 2$  and  $\zeta = ?$  in  $d = 3$ . The scaling from Eq. (6.31) on the optimal search time holds, with  $\xi = 0.90 \pm 2$  in  $d = 2$  and  $\xi = ? \pm 2$  in  $d = 3$ .

▲ Remarkably, the optimal search process appears to be faster in the case of a specular confinement than in the case of a diffusive confinement (see Figs. 6.2 and 6.4). The relative gain through a specular confinement compared to a diffusive confinement appears to be constant with  $b$ , within the range 5 to 7%<sup>1</sup>. An interpretation for the favorable effect of the specular

<sup>1</sup>In  $d = 2$  and with  $a = 1$ :  $5.5 \pm 0.1\%$  for  $b = 50$ ;  $7.5 \pm 0.1\%$  for  $b = 100$ ;  $6.5 \pm 0.1\%$  for  $b = 100$ .

boundary is that the probability  $p_{\text{dir}}(r)$  to be reoriented in a direction that leads to the target is lower in the diffusive case than in the specular case. In the diffusive case, in an intermediate region  $a/v \ll \tau \ll b/v$  we can estimate  $p_{\text{dir}}(r)$  as:

$$p_{\text{dir}}(r) = \frac{2a\tau_{\text{opt}} \left( (b + 2\tau_{\text{opt}}) - e^{-\frac{b}{\tau_{\text{opt}}}} (3b + 2\tau_{\text{opt}}) \right)}{\pi b^3} \quad (6.34)$$

which is about 20% lower than the  $p_{\text{dir}}(r)$  for the specular case given in Eq. (6.15).

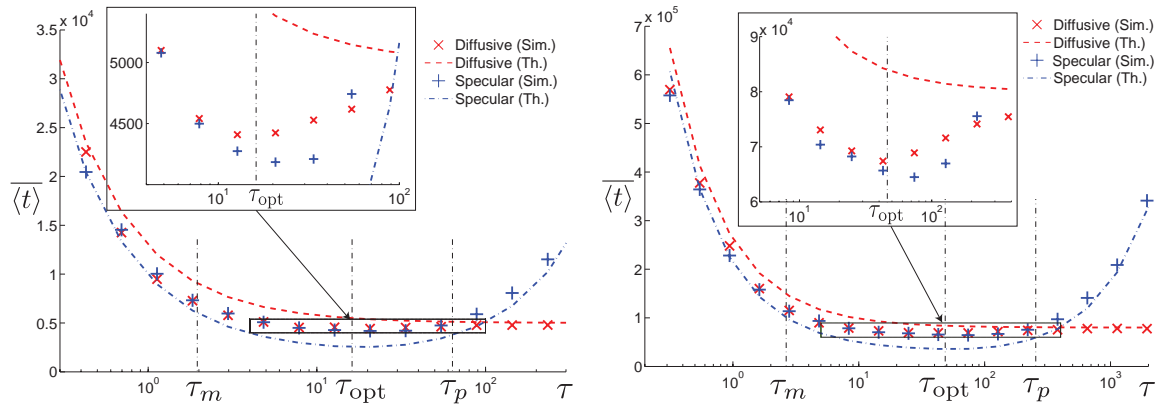


Figure 6.2: Simulations of the global mean first passage time (GMFPT) to a centered unit disk ( $d = 2$ ) as a function of the reorientation rate  $\tau$  in the presence of a spherical confining boundary at (left)  $b = 50$  and (right)  $b = 200$  that is either (red  $\times$  symbols) diffusive confining boundary or (blue  $+$  symbols) specular. The matched asymptotic expression (red and blue dashed lines) fits to the simulations in both limits  $\tau \gg b/v$  and  $\tau \ll a/v$ . The MFPT appears to be flat within the predicted plateau region  $[\tau_m, \tau_p]$  (Insets) Zoom on the optima of the MFPT. The expression for the optimal reorientation rate from Eq. 6.30 (middle vertical dashed line) is in good agreement with the position of the optima. The optimal search time obtained by simulations is (left) 5.5% and (right) 6.5% lower than for a diffusive boundary.

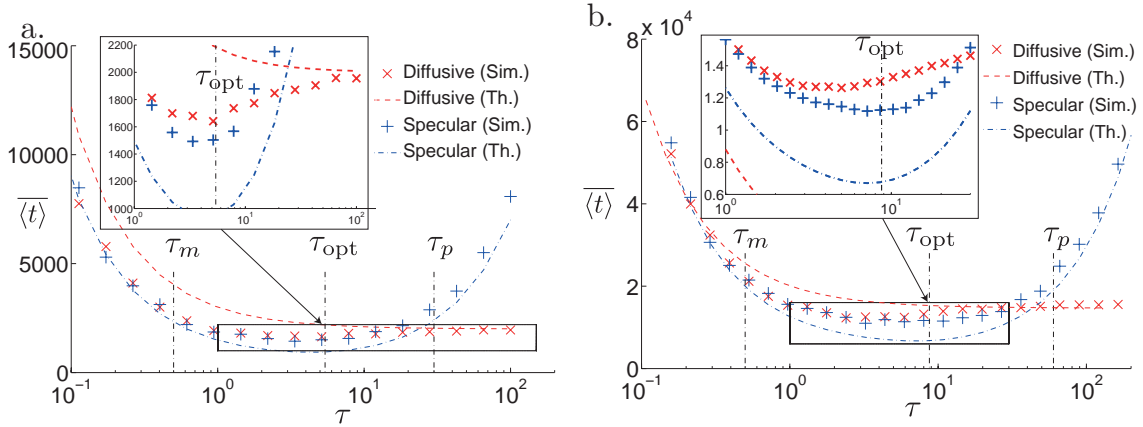


Figure 6.3: Simulations of the global mean first passage time (GMFPT) to a centered unit sphere ( $d = 3$ ) target as a function of the reorientation rate  $\tau$  in the presence of a spherical confining boundary at (a.)  $b = 10$  and (b.)  $b = 20$  that is either (red  $\times$  symbols) diffusive confining boundary or (blue  $+$  symbols) specular. (inset) The asymptotic behavior at  $b/v \ll \tau$  with diffusive confinement from Eq. (6.27) (indicated by red triangles) is in qualitative agreement with simulations up to  $\tau = \tau_{opt}$ .

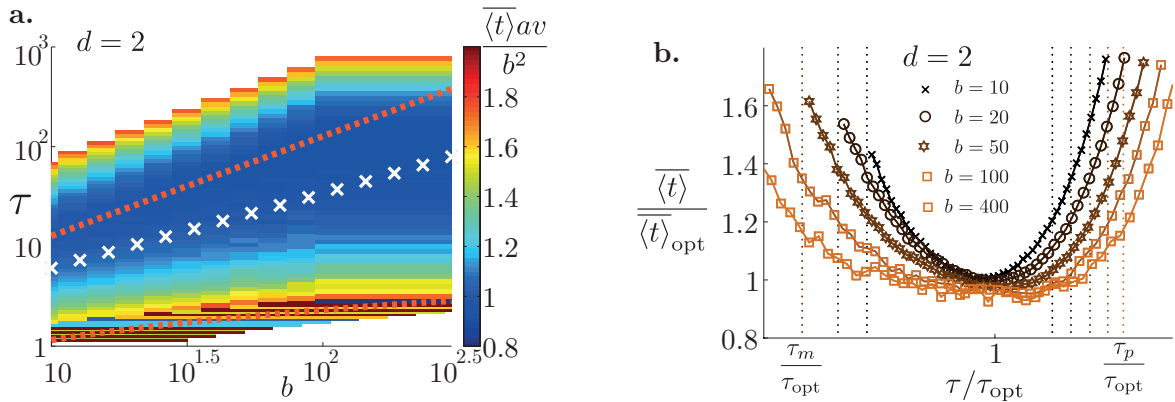


Figure 6.4: **▲ Scaling laws for optimal GMFPT and optimal reorientation rate in  $d = 2$  geometry** Simulations of the GMFPT to a centered unit disk, in terms of the reorientation rate  $\tau$  and of the radius  $b$  of the specular spherical confinement, validate the predicted scaling laws for the optimal GMFPT (Eq. (6.31)) and the optimal reorientation rate. (6.30). (a.) The rescaled GMFPT, expressed as a function of  $b$  and  $\tau$  (log-scales), appears to be flat in the predicted plateau region  $[\tau_m, \tau_p]$  (b.) The rescaled GMFPT, expressed in terms of rescaled reorientation rates  $\tau / \tau_{opt}$ , is close to 1 over the rescaled plateau range  $[\tau_m / \tau_{opt}, \tau_p / \tau_{opt}]$  (indicated by vertical dashed line).

## 6.3 Conclusion

Our interpretation for the optimal strategy is the following: in the regime  $\tau \ll b/v$ , the random walk behaves as a regular diffusion and is therefore recurrent for  $d = 2$ . The exploration of space is therefore redundant and yields a search time that scales in this regime as  $|\Omega_r| \ln |\Omega_r|$ . As soon as  $\tau \approx b/v$ , the search process is less redundant and the search time is expected to scale  $|\Omega_r|$ . In the ballistic regime  $\tau \gg b/v$ , the search time is at least proportional to  $|\Omega_r|$  (e.g. the diffuse confinement) or diverges if the searcher is trapped in extremely long unsuccessful ballistic excursions (e.g. the specular confinement). At the finite optimal reorientation rate  $\tau_{\text{opt}}$ , the searcher has a chance to get reoriented when it is close to the target, with a consequent high probability to encounter the target within the next run. The optimal reorientation rate scales linearly with the system characteristic size  $b$  of the confinement:  $\tau_{\text{opt}} = \zeta b$ . We stress that the proportionality factor  $\zeta$  takes a notably small value  $\zeta \approx 0.1$  that we can predicted analytically.

## 6.4 Perspectives

We consider other distributions  $\pi(t)$  of the reorientation times, with steps either at regular time intervals or and Lévy distributed time intervals. In Sec. 6.4.2, p. 141, we briefly explain how to generalize our result to the chemotactic search process.

### 6.4.1 Comparison to other distributions of reorientation times

#### 6.4.1.1 Regular steps: Dirac distribution

In this section, we consider that reorientations occur at regular time intervals  $\tau$ , which is equivalent to considering a random distribution of reorientation times  $\pi(t) = \delta(t - \tau)$ , where  $\delta$  is the Dirac function.

► In Fig. 6.5, we present Monte-Carlo simulations of the GMFPT with diffusive confinement and in  $d = 2$ . The GMFPT displays local minima at  $\tau = b/v$ ,  $\tau \approx b/(2v)$  and  $\tau \approx b/(3v)$ , as well as an inflexion point for  $\tau \approx b/(4v)$ . The interpretation is that the choice  $\tau = b/(nv)$  maximizes the probability to reach the target after the  $n$ -th reorientation event. In the next paragraph, we obtain an analytical description for the minima at  $\tau = b/v$ .

We consider a searcher initially at the confining boundary  $r = b$  and oriented in a random direction  $\theta$  which is uniformly distributed within  $[0, \pi/2]$ . The final position of the particle is either  $\tilde{r}(\theta) = \sqrt{b^2 + v^2\tau^2 + 2bv\tau \cos(\theta)} \in ]a, b[$ ,  $\tilde{r}(\theta) = a$  or  $\tilde{r}(\theta) = b$ . Indeed, three situations occur depending on the value of the ratio  $(v\tau)/b$ :

- (i) if  $b < v\tau < 2b$ , again three situations may occur depending on the value of the initial direction  $\theta \in [0, \pi/2]$  (see Fig. 6.5).
  - (a) if  $\pi - \theta_a < \theta < \pi$ , where  $\theta_a = \arcsin(a/b)$ , the searcher hits the target in a time  $b/v$  (up to a minor term that scales as  $a/v$ ).
  - (b) if  $\pi - \theta_b < \theta < \pi - \theta_a$ , where  $\theta_b = \arccos[\tau/(2b)]$ , the searcher is reoriented at the position  $\tilde{r}(\theta) \in ]a, b[$ . The final radius of a searcher whose initial direction is  $\theta = \theta_a$  is denoted  $r_b \equiv \tilde{r}(\theta_a)$  and reads:

$$r_b \equiv \sqrt{b^2 - 2\sqrt{b^2 - a^2}v\tau + v^2\tau^2}. \quad (6.35)$$

The distribution of final position  $\tilde{r}$  after a single run is a non-uniformly distributed random variable, with a density probability equal to the Jacobian:

$$\left| \frac{\partial \theta}{\partial \tilde{r}} \right| = \frac{2\tau \tilde{r}}{b\tau \sqrt{4b^2\tau^2 - (b^2 - \tilde{r}^2 + \tau^2)^2}}. \quad (6.36)$$

Notice that the Jacobian defined in Eq. (6.36) diverges for  $b - \tau$  (i.e.  $\theta = 0$ ), which is expected since a small variation of  $\tilde{r}$  around  $b - \tau$  corresponds to an abrupt change in the value of  $\theta$ .

- (c) if  $\pi/2 < \theta < \pi - \theta_b$ , the searcher takes a time  $-2b \cos(\theta)/v$  to reach its final position at  $\tilde{r} = b$ . The mean return time to the boundary  $r = b$ , averaged over the angles  $\theta \in [\theta_b, \pi/2]$ , reads:

$$\int_{\pi/2}^{\pi - \theta_b} \frac{2d\theta}{\pi} \left\{ -2\frac{b}{v} \cos(\theta) \right\} = \frac{2b \left( 2 - \sqrt{4 - \frac{v^2\tau^2}{b^2}} \right)}{\pi v}. \quad (6.37)$$

- (ii) if  $v\tau < (b - a)$ , the final position of the particle is  $\tilde{r}(\theta)$  takes all values between  $b$  and its minimal value  $r_b \equiv b - v\tau$ .
- (iii) if  $2b < v\tau$ , the search time is a constant of  $\tau$  and is strictly equal to the expression of Eq. (6.23). Within a single run from the boundary, the target is either hit or is missed and the final position is  $\tilde{r} = b$ . We set  $\theta_b = \theta_a$  if  $2b < v\tau$ .

We focus on the regime  $b < v\tau < 2b$ . The renewal equation method [113] leads to the following integral equation on the search time:

$$\langle t(b) \rangle = \frac{2a}{\pi b} \frac{b}{v} + \int_{r_b}^b \frac{2d\tilde{r}}{\pi} \left| \frac{\partial \theta}{\partial \tilde{r}} \right| \{ \tau + \langle t(\tilde{r}) \rangle \} + \left[ 1 - \frac{2\theta_b}{\pi} \right] \left[ \frac{2b}{\pi v} \left( 2 - \sqrt{4 - \frac{v^2\tau^2}{b^2}} \right) + \langle t(b) \rangle \right]. \quad (6.38)$$

where (i) the first term in the right hand side of Eq. (6.38) corresponds to the product of the probability to reach the target in a single run by the characteristic time of the run, (ii) the second term corresponds to the reorientation events at a random position  $\tilde{r} \in [r_b, b]$ , and (iii) the last term corresponds to the product of the probability to reach the boundary at  $\tilde{r} = b$  in a single run by the sum of (a) the average time Eq. (6.37) to reach the boundary at  $\tilde{r} = b$  and (b) of the averaged search time from  $\tilde{r} = b$ .

To simplify the expression of Eq. (6.38), we make the assumption that

$$\langle t(\tilde{r}) \rangle \approx \frac{1}{\pi} \frac{a}{\tilde{r}} \frac{\tilde{r}}{v} + \{ \tau + \langle t(b) \rangle \} \left[ 1 - \frac{a}{\pi \tilde{r}} \right], \quad (6.39)$$

which is justified as (i) the first term on the right hand side of Eq. (6.39) corresponds to a success to encounter the target after the reorientation event, and (ii) the second term corresponds to a failure to encounter the target after the reorientation event. With the approximation of Eq. (6.39), the Eq. (6.38) becomes:

$$\langle t(b) \rangle = \frac{\frac{2a}{\pi} \frac{b}{v} + \int_{r_b}^b \frac{2d\tilde{r}}{\pi} \left| \frac{\partial \theta}{\partial \tilde{r}} \right| (2\tau + a/v) + \left[ 1 - \frac{2\theta_b}{\pi} \right] \left[ \frac{2b}{\pi v} \left( 2 - \sqrt{4 - \frac{v^2\tau^2}{b^2}} \right) \right]}{1 - \int_{r_b}^b d\tilde{r} \left| \frac{\partial \theta}{\partial \tilde{r}} \right| \left[ 1 - \frac{a}{\pi \tilde{r}} \right] - \left[ 1 - \frac{2\theta_b}{\pi} \right]}. \quad (6.40)$$

The expression Eq. (6.40) provides a satisfactory description of the minimum at  $\tau = b/v$  (see Fig. 6.5. b.).

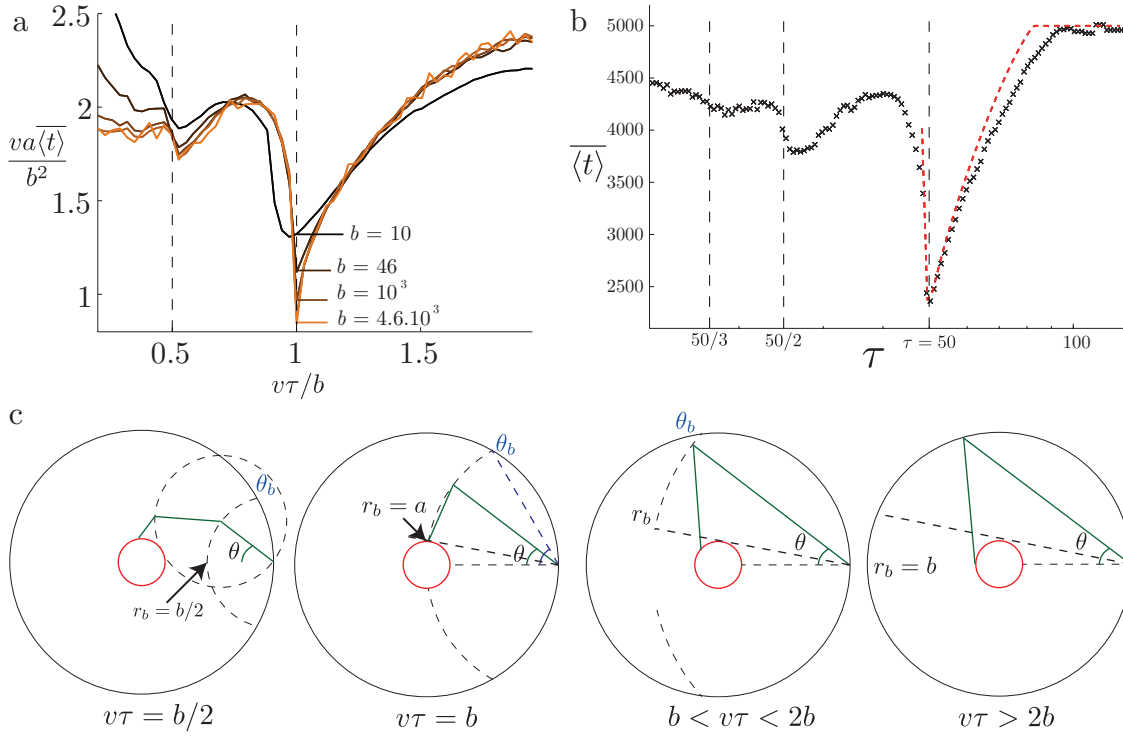


Figure 6.5: The global mean first passage time (GMFPT) to a centered spherical target of radius  $a = 1$  by a Pearson random walk of constant length  $v\tau$ , confined by a diffusive boundary at  $r = b$ , displays several local minima. (a) The GMFPT, rescaled by  $b^2/(av)$ , is expressed in terms of the reorientation rate, rescaled by  $b/v$ , and shows a global minimal at  $v\tau/b = 1$  for several values of  $b$ : 10, 46,  $10^3$ ,  $4.6 \cdot 10^3$  (samples of  $10^5$  events) (b) GMFPT with  $b = 200$ : simulations with  $10^6$  events (black  $\times$  symbols) compared to the theoretical expression from Eq. (6.40) (dashed red line). (c) Sketch of the search process. The choice  $\tau = b/(nv)$  maximizes the probability to reach the target after the  $n$ -th reorientation event.

### 6.4.1.2 Lévy distribution

In this section, we consider a reorientation distribution that is a symmetric Lévy law (restricted to positive values) of index  $\mu$  and scale parameter  $\tau$ . This distribution is defined by the Fourier transform  $\hat{P}(k) = \exp(-\tau k^\mu)$  so that  $P(t) \underset{b/v \ll t}{\sim} t^{-\mu-1}$ . For  $0 < \mu < 1$ , the mean reorientation time is infinite, yielding in turn an infinite search time. We focus on the regime  $1 < \mu \leq 2$  and we evaluate the search time by numerical simulations, with random reorientation times generated according to the Chambers-Mallow-Stuck method [147]. The search time for the Lévy strategy is minimized when  $\mu = 2$ , i.e. when the reorientation time has a finite second moment (in which case the walk is no longer of Lévy type).

It is still unclear which of the EPRW or the Lévy walks with  $1.8 < \mu \leq 2$  leads to the fastest search process (see Fig. 6.6). However, the optimal EPRW performs better than any Lévy walk as soon as  $1 < \mu < 1.8$ .

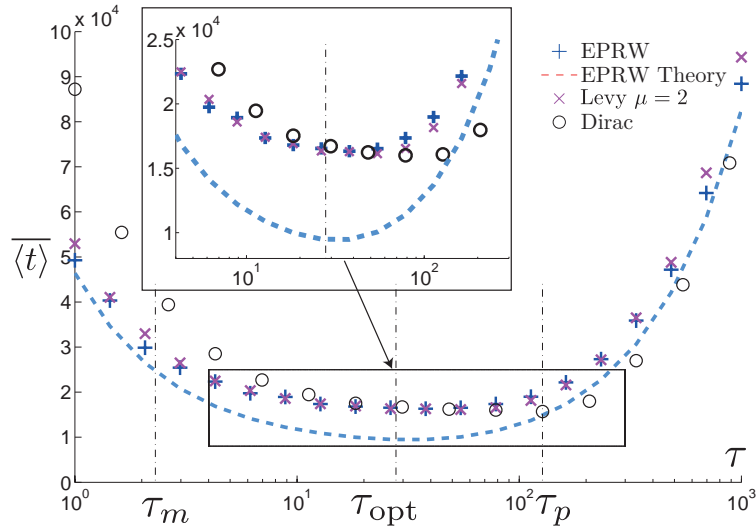


Figure 6.6: Global mean first passage time to a centered target of radius (top row)  $a = 1$  in the presence of a specular spherical confining boundary at  $b = 100$  for several distributions of the run time: (blue + symbols) exponential ; (magenta  $\times$  symbols) Lévy distribution with  $\mu = 2$  ; (black o symbols) regular run times (i.e. Dirac distribution).

### 6.4.2 Chemotactic search

It is possible to generalize the arguments concerning both the diffusive limit  $\tau \ll a/v$  (Sec. 6.2.1, p. 130) and the ballistic limit  $\tau \gg b/v$  (Sec. 6.2.2, p. 131) to account for:

- (i) a reorientation rate  $\tau(r)$  which depends on the position of the particle  $r$ . This corresponds to the chemotactic random walk, defined in Sec. 1.2.2, p. 26,
- (ii) a varying velocity field  $v(r)$  which depends on the position of the particle  $r$ .
- (iii) an anisotropic reorientation distribution  $d\mu(\theta)$ .

In the diffusive limit  $\tau \ll a/v$ , the three corresponding processes can be described as a biased Brownian process.

#### SUMMARY OF MAIN RESULTS

- (1) The limit  $\tau \ll a/v$  leads to a symmetric Brownian process with a vanishing effective diffusion coefficient  $D = d/(v^2\tau)$  and to a diverging GMFPT,
- (2) The optimal reorientation rate  $\tau_{opt} = \zeta b$  scales linearly with the system size, with a remarkably small proportionality coefficient ( $\zeta \approx 0.10$ ).
- (3) The optimization property holds
  - (i) for different types of confinement (specular or diffusive),
  - (ii) different distributions of step lengths (exponential, Lévy, regular).



6. Search strategy for the Pearson  
random walks


# Universal speed–persistence coupling in cells

"Tracking is fun"

Howard Berg, *E. Coli in Motion* [137].

In this thesis chapter, I will present a recent joint experimental and theoretical work that revealed an universal coupling between the cell speed and the cell persistence. On the basis of extensive experimental data *in vitro* and *in vivo*, cell persistence, which quantifies the straightness of trajectories, is shown to be robustly coupled to migration speed. This universal speed persistence coupling (USPC) is found to be a generic law of cell migration. We suggest that the USPC originates in the advection of polarity cues by a dynamic actin cytoskeleton undergoing flows at the cellular scale. The analysis relies on a theoretical model that is validated by measures of the directional persistence of dendritic cells upon modulation of actin flow speeds.

Beyond the quantitative prediction of the observed exponential correlation between speed and persistence that characterizes the USPC, the model provides an explicit construction of single cell dynamics as an active Brownian particle from simple microscopic hypothesis, and yields a generic phase diagram of cellular trajectories that reproduces the migration patterns of most cell types.

 This work led to Publication 2 and is a joint project of

- the Institute of Science and Technology group in Vienna. Stefan Wieser and Verena Ruprecht performed and analyzed the experiments on dendritic cells presented in Fig. 7.2, under the joint supervision of Carl Philipp Heisenberg and Michael Sixt.
- the Institut Curie group in Paris. Paolo Maiuri, Franziska Lautenschlager, Mael Le Berre., Matthew Raab and Hawa Racine Thiam performed the cell migration experiments and the cell trajectory analysis presented in Figs. 7.1 and 7.4, under the supervision of Matthieu Piel and Anna Maria Lennon-Dumenil.
- Carolina Large-Crespo, from the San Raffaele Scientific Institute in Milan, performed the experiments on macrophages in live Medaka fish presented in Fig. 7.1,
- the theory group, including Olivier Bénichou, Nir Gov, Raphael Voituriez and me.

## Contents

---

<b>7.1</b>	<b>Introduction</b>	<b>144</b>
<b>7.2</b>	<b>Results</b>	<b>145</b>
7.2.1	Cell trajectory analysis reveals a universal coupling between cell speed and persistence	145
7.2.2	Faster actin retrograde flow lengthens cell persistence time	147
7.2.3	Faster actin retrograde flow enhances the asymmetry of polarity cues	149
7.2.4	Physical modeling predicts the USPC	151
7.2.4.1	Coupled equations between the retrograde flow and the concentration of cues	151
7.2.4.2	Decoupled equations due to fast diffusion of cues	153
7.2.5	Derivation of the USPC law	153
7.2.5.1	Polarisation time	155
7.2.5.2	Persistence time	155
7.2.6	Phase diagram of main cell migration patterns	155
7.2.7	Values of the fitting parameters	158
<b>7.3</b>	<b>Discussion and conclusion</b>	<b>158</b>
	Search Strategy	159
<b>7.4</b>	<b>Perspectives</b>	<b>161</b>

---

## 7.1 Introduction

Eukaryotic cell migration is essential for a large set of biological processes, including morphogenesis [148], wound healing [149], tumor spreading [150] or immune responses [43, 151, 152]. Assessing quantitatively the exploratory efficiency of cell trajectories is therefore crucial.

As mentioned in the general introduction of this thesis manuscript, cell movement in the absence of external cues can be described as a random motion (see 21). Models range from simple Brownian motion to persistent random walks [153, 154, 155], Lévy walks [156] or composite processes such as intermittent random walks [43, 157]. Such models essentially differ in the cell persistence, which quantifies the ability of a cell to maintain its direction of motion. The variety of behaviors, observed even along a single cell trajectory, stems from the fact that, as opposed to a passive tracer in a medium at thermal equilibrium, which generically performs a classical Brownian motion, a cell is self-propelled, and as such belongs to the class of *active* Brownian particles [158, 159]. This class of processes is extremely vast and needs to be restricted to have some explanatory or predicting power. Up to now universal behaviors have emerged in the context of the collective dynamics of self-propelled particles [160, 161, 162], but remain elusive at the level of single cells.

Recently, a vast amount of data of individual cell trajectories has been collected over many cell types in the context of the First World Cell Race [163] (see Fig. 7.1a,b). In spite of an apparent diversity at the level of the whole population analyzed, these data show there are correlations between the mean linear instantaneous cell speed and the persistence. The persistence time  $\tau_\phi$  is defined as the mean time during which a cell maintains its direction of motion, and can be interpreted as a MFPT quantity (see Sec. 7.2.5, p. 153). The fact that faster cells migrate more straight than slower cells suggests that robust mechanisms could constrain the possible characteristics of cell trajectories.

► The aim of the present project is to understand this correlation between cell speed and cell persistence from a universal mechanism based on the actin retrograde flow.

The experimental groups mentioned in p. 143 analyzed trajectories of:

- (i) cells of mammalian origin migrating in 1 or 2-dimensional geometries, with or without geometric confinement, or in 3-dimensional collagen gels,
- (ii) and macrophages moving in live tissues in Medaka fish [164].

This extensive data set reveals a universal coupling between cell speed and cell persistence (USPC). To explain what seems to be a universal law of cell migration, we developed a physical model relying on minimal hypothesis that shows that actin flows, which are the hallmark of motile cells [165, 166, 167, 168, 169, 170], generically reinforce cell polarity and consequently cell persistence.

► Our theoretical model has the following important merits:

- (i) the model is validated experimentally by a motility assay enabling a gradual modulation of actin flow speeds in dendritic cells (BMDCs),
- (ii) the model quantitatively predicts the observed exponential correlation between speed and persistence that characterizes the USPC,
- (iii) the model provides from minimal microscopic hypothesis an explicit construction of single cells dynamics as active Brownian particles,
- (iv) the model yields a generic phase diagram of cellular trajectories, which opens the way to the control of cell migration patterns.

I first present the experimental results and theoretical modelling, and discussion is summarized in Sec. 7.3, p. 158.

## 7.2 Results

### 7.2.1 Cell trajectory analysis reveals a universal coupling between cell speed and persistence

The First World Cell Race [163], which gathered recordings of individual cell trajectories on 1-dimensional adhesive tracks for 54 different adherent cell types made available an unprecedented amount of data. The Institut Curie performed a further analysis of this data and confirmed a clear positive correlation between:

- (i) the population averaged mean linear instantaneous cell speed ( $v$ ),
- (ii) the population averaged persistence time ( $\tau_\phi$ ) at the level of all cell types (Fig. 7.1 a), despite their variety.

To assess the robustness of this observation and check its validity at the level of single cell trajectories, the Institut Curie group performed new experiments on two representative examples of migrating cell with either a mesenchymal migration mode (hTERT-immortalized retinal pigment epithelial cell line, RPE1) or an amoeboid migration mode (immature bone marrow derived mice dendritic cells, BMDC), in various geometries: 1-dimensional adhesive tracks (Fig. 7.1c), 1-dimensional microchannels (Fig. 7.1d), 2-dimensional non confined adhesive substrates (Fig. 7.1e) and 2-dimensional confined substrates (Fig. 7.1f).

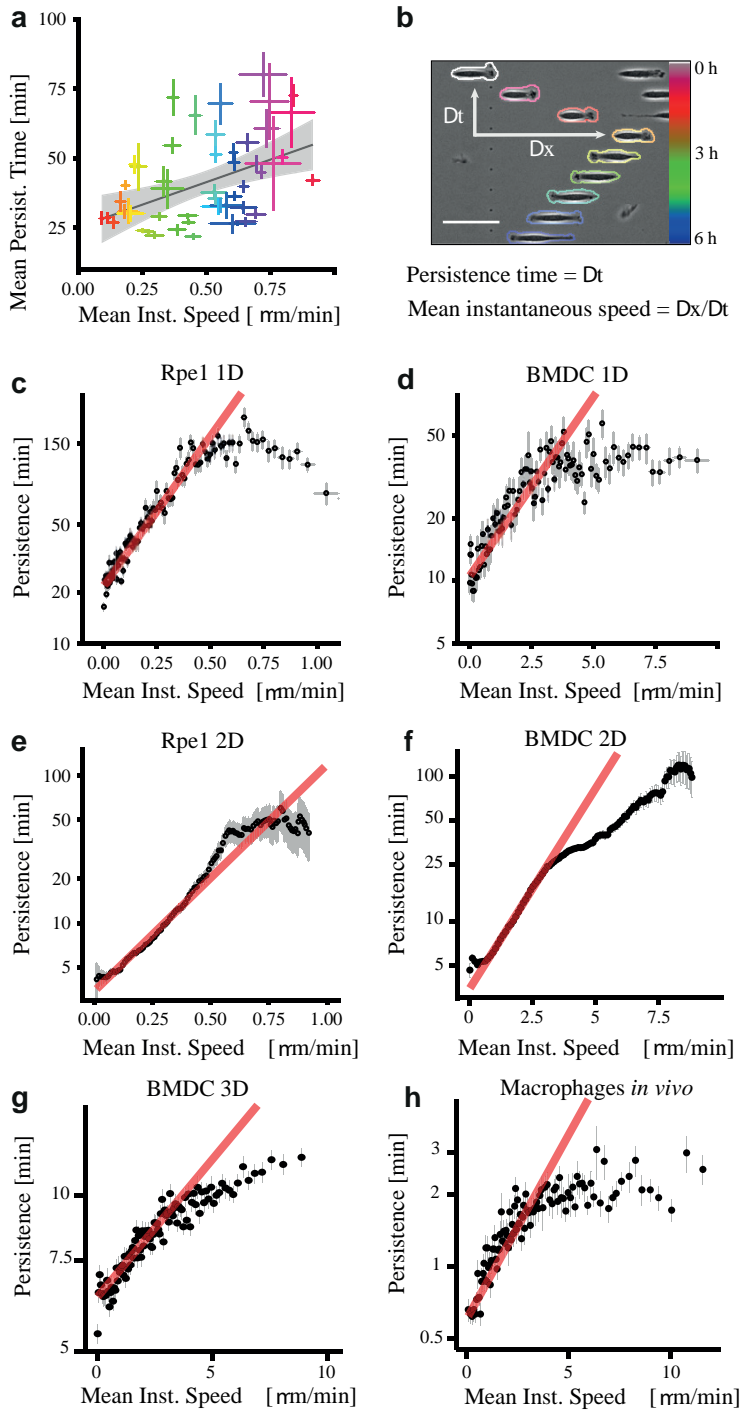


Figure 7.1: Correlation between cell persistence and cell speed. **a.** Population mean persistence time versus mean instantaneous speed. Data from the First World Cell Race, refers to the original paper [163] for the cell-type color code. **b.** Definition of mean persistence time and the mean instantaneous speed in 1D. Cell contour color shows the time progression. Scale bar  $50 \mu\text{m}$ . **c - f.** Persistence time, binned for the corresponding instantaneous speed, versus instantaneous speed. Red curve represents the exponential fit of the experimental data. **c.** Rpe1 cells on micropatterned lines of  $9 \mu\text{m}$  width coated with fibronectin. **d.** BMDCs in fibronectin treated channels with a  $5 \times 5 \mu\text{m}$  square section. **e - f.** The persistence time in 2D is defined here as the time needed for a cell to change its original direction of motion by  $90$  degrees. **e.** Data of Rpe1 cells on 2D surface uniformly treated with fibronectin. **f.** BMDCs confined between two parallel, fibronectin treated planes,  $5 \mu\text{m}$  apart from each other. **g.** BMDCs embedded in bovine collagen gel and confined between two planes  $5 \mu\text{m}$  apart from each other. **h.** Macrophages imaged in live Medaka fish.

Very long cell trajectories were recorded, allowing a clear assessment of individual cell persistence. Cell concentrations were low enough to treat cell trajectories as independent. In all cases, the Institut Curie group found a striking correlation within each population analyzed between persistence time  $\tau_\phi$  and mean instantaneous velocity  $v$  which is well fitted by a simple exponential curve:

$$\tau_\phi = Ae^{\lambda v}, \quad (7.1)$$

before eventually saturating at larger  $v$  (see Sec. Eq. (7.3)). The correlation is still valid when cells are migrating in more complex environments: the Institut Curie group recorded BMDCs migrating in 3D collagen gels (Fig. 7.1g) and Carolina Large-Crespo tracked macrophages migrating in live Medaka fish [164] (Fig. 7.1h). In both cases, persistence and speed were still

highly correlated.

## 7.2.2 Faster actin retrograde flow lengthens cell persistence time

► To elucidate the origin of the USPC, we reasoned that, as this law applies to all the tested cell types it had to rely on a very conserved aspect of cell locomotion. Even if many details might vary from one cell type to the other, the most conserved aspect of cell locomotion is the retrograde translocation of actin filaments in the frame of reference of the cell, from the front to the rear of its locomotory parts [165, 166, 167, 168, 169, 170, 171, 172]. Actin flows can either exist over large portions of the cell (in particular in cells known as amoeboids [173]), or in some cases be essentially limited to the protrusive parts (such as lamellipodia in cells known as mesenchymal cells [165, 166, 167, 168, 169, 170]). This retrograde movement is powered by the combined forces of actin polymerization at the leading edge and actomyosin contraction at the trailing edge and represents the driving force for locomotion. Upon coupling across the plasma membrane via adhesion receptors of the integrin family retrograde actin flow is turned into traction forces, which pull the cell forward while actin filaments and associated adhesion sites slide to the back of the cell [174, 175, 176, 177, 178].

To test if actin flows are involved in the coupling between cell persistence and cell speed, the IST group used mature bone marrow dendritic cells (mBMDCs), for which it was already demonstrated that actin retrograde flow can be varied without affecting cell speed when substrate adhesion strength is modulated [173]. Indeed, the cell speed  $v$  and the velocity of the actin flow  $V$  (note that it is defined hereafter in the frame of reference of the moving cell) are usually linearly coupled according to  $v = \alpha V$  [175], such linear approximation being valid at least in the lower range of velocities for each cell type. The coefficient  $\alpha$  models the effective friction between actin filaments and the substrate, usually mediated by specific cell adhesion proteins [179, 180, 181], and therefore depends on experimental conditions. In some cell types, varying the actin/substrate coupling parametrized by  $\alpha$  induces an adaptive response, which allows a cell to keep the speed of locomotion  $v$  relatively constant, despite different retrograde velocities  $V$  of the loosely coupled actin network. Such adaptation has been extensively characterized in mBMDCs. When placed in confined environments these cells can flexibly shift between integrin independent and integrin dependent force transduction as even in the absence of these adhesion receptors the cells are able to generate sufficient traction to migrate. However, depletion of integrins or their ligands and the associated drop in friction causes retrograde actin slippage, which is then compensated by up to twofold increase in actin polymerization [173]. To make analogy with a car bogged down in mud: the friction to the ground is low and though the wheels spin very fast the car does not move.

**Coupling to the actin flow, not to the velocity.** The IST group took advantage of this opportunity to independently study the influence of retrograde actin flow and actual cell speed on migratory persistence. They assayed 9 different experimental conditions. Surface adhesion was independently controlled by depletion of integrins and their ligands (coating the surfaces with an inert PEG layer), while cell speed was gradually varied by temperature changes and actomyosin contractility by pharmacological inhibition (blebbistatin). The retrograde flows can be varied between from 3 to 15  $\mu\text{m}/\text{min}$  independently of cell speed (Fig. 7.2a). Strikingly, we observed that the mean persistence time  $\tau_\phi$  measured for each experimental condition was strongly correlated with the mean speed  $V$  of the actin retrograde flow, and was well fitted by a simple exponential  $\tau_\phi = A'e^{\lambda V}$  (Fig. 7.2b). Note however that within each experimental condition ( $\alpha$  fixed) the linear scaling between  $v$  and  $V$  still held, so that the correlation between cell speed and cell persistence was preserved at the level of each experimental condition. Eventually these data strongly suggest that the observed USPC originates from a coupling between

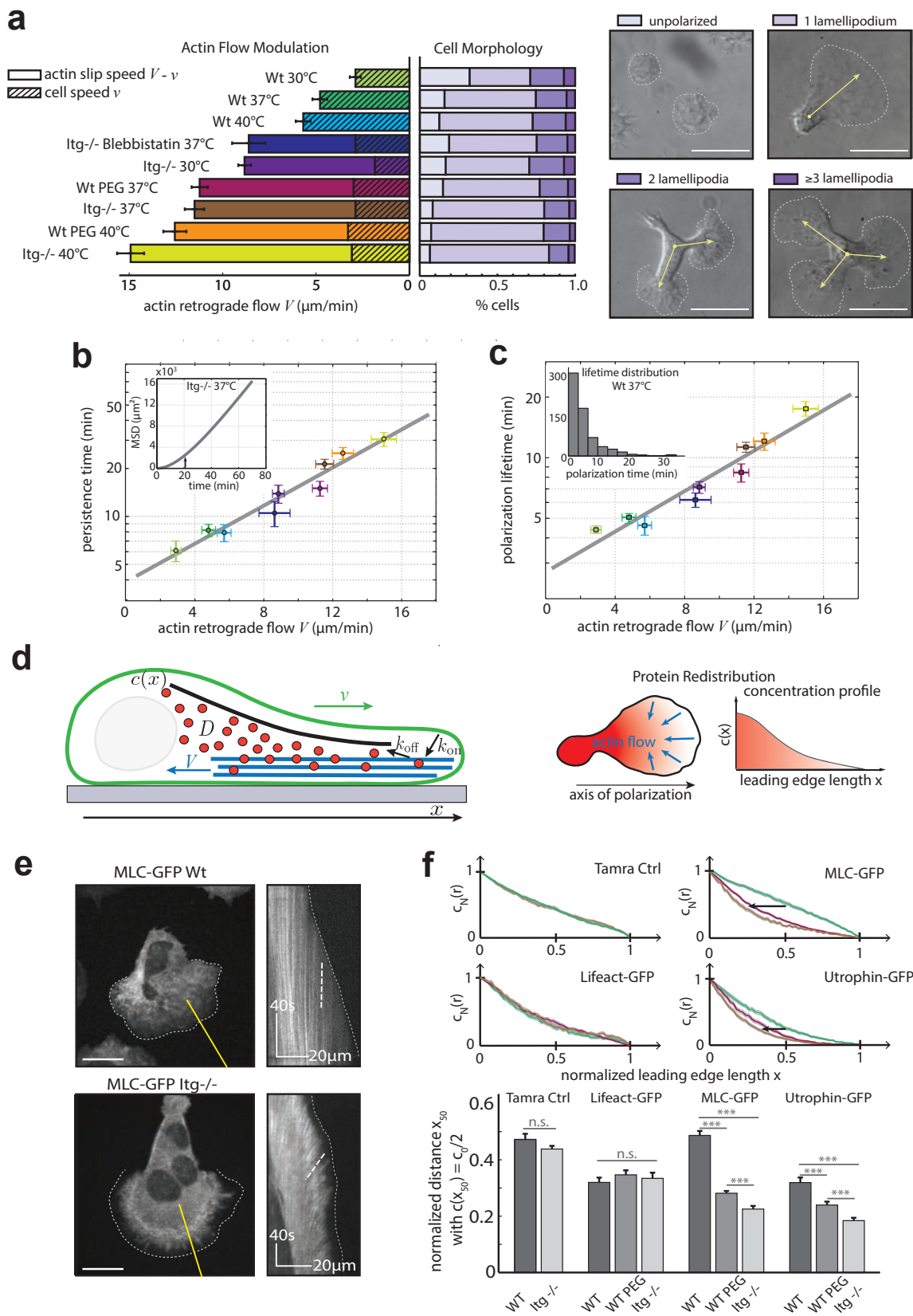


Figure 7.2: (Caption next page.)

cell persistence and the actin flow.

To further understand why a faster retrograde flow leads to a longer persistence time, the IST group quantified features known to strongly affect cell persistence. The number of

Figure 7.2: Modulation of actin retrograde flow speed induces protein re-localization in migrating cells and reveals a positive feedback loop on the stability of cell polarity and persistent cell migration. **a.** Modulation of actin retrograde flow speed  $V$  in 9 different conditions via a set of genetic, pharmacological and physical parameters (left). Differential Interference Contrast (DIC) images showing representative images of cells in the unpolarized states (no lamellipodium), polarized state (1 lamellipodium), and with 2 lamellipodia (di-polar) and 3 or more lamellipodia (multi-polar)). Arrows denote the axis of polarization (right). Scale bar  $20 \mu\text{m}$ . Histogram of observed cell morphologies (color code see DIC images) for 9 different conditions indicating that the number of polarized cells increases for higher actin retrograde flow speeds (middle). **b.** Cell persistence time and **c.** polarization lifetime during migration increases with higher retrograde flow speed. Gray lines indicate exponential fits to the data. Inset in **c.** shows the exponential distribution of polarization lifetimes for Wt dendritic cells at  $37^\circ\text{C}$ . Inset in **b.** depicts mean square displacement plot for Itg-/- cells at  $37^\circ\text{C}$ . Arrow highlights the crossover from persistent to random motility on longer time scales. **d.** Schematic diagram illustrating the model with a minimal set of kinetic parameters. A stronger redistribution of actin binding proteins towards the cell rear is observed for higher actin flow speeds via mechano-chemical coupling to the flowing actin network. **e.** (left) Fluorescence images of MLC-GFP localization in migrating wildtype (Wt) and integrin knockout (Itg-/-) dendritic cells under 2D confinement revealing different spatial myosin distribution patterns at the leading edge with myosin depletion from the front in Itg-/- vs. Wt cells. Dashed lines indicate cell borders. Scale bar  $\mu\text{m}$ . (right) Kymograph data along yellow lines showing myosin retrograde flow. White dashed lines indicate retrograde myosin flow speed. **f.** Normalized concentration profiles along the cell leading edge for a set of actin-binding molecules with increasing actin affinity from top to bottom. Concentration profiles are color coded for different cell-substrate adhesion strengths (green: Wt, magenta: Wt on Peg, brown: Itg-/-, all  $37^\circ\text{C}$ ). Arrows indicate a shift of the polarity cue concentration profile towards the cell rear with increasing actin binding affinity and decreasing adhesion strength. (right) Normalized distance  $x_{50}$  at which the concentration drops to  $c_{50} = c_0/2$ .

protrusions for each cell was measured, using the 9 experimental conditions previously defined which enables to vary the actin flow. The IST group found that in conditions in which cells had a faster actin flow, there was a larger proportion of cells with a single well polarized lamellipodium (see Fig. 7.2a). The life time of such unipolar configurations, called the polarization time and denoted  $\tau_p$ , was measured together with the actin retrograde flow speed in each protrusion.

► The IST group found that the polarization time is exponentially coupled to the velocity of the retrograde flow ( $V$ ), rather than to the real velocity of the cell ( $v$ , see Fig. 7.2c). This suggests that the origin of the coupling between the actin retrograde flow and cell persistence is that faster actin flows favor a unipolar configuration of the cell and lengthen protrusion lifetime.

### 7.2.3 Faster actin retrograde flow enhances the asymmetry of polarity cues

► A simple hypothesis to explain these effects of actin flows would be that, in polarized migrating cells, actin flows reinforce cell polarity by enhancing the asymmetry of polarity cues, as was proposed for the establishment of polarity in early C. Elegans embryo [182, 183, 184]. Examples of such cues, which are likely to vary with cell type, could be molecules responsible for the generation of contractile stress, such as myosin motors or their activators, or could alternatively be involved in the regulation of microtubule dynamics [185].

We introduce a first element of physical modeling to test this hypothesis. The cell is assumed to move on a 2D plane with a velocity  $\mathbf{v}$  which we assume is proportional to the retrograde flow velocity  $\mathbf{V}$  in the frame of reference of the moving cell (for the sake of simplicity we will



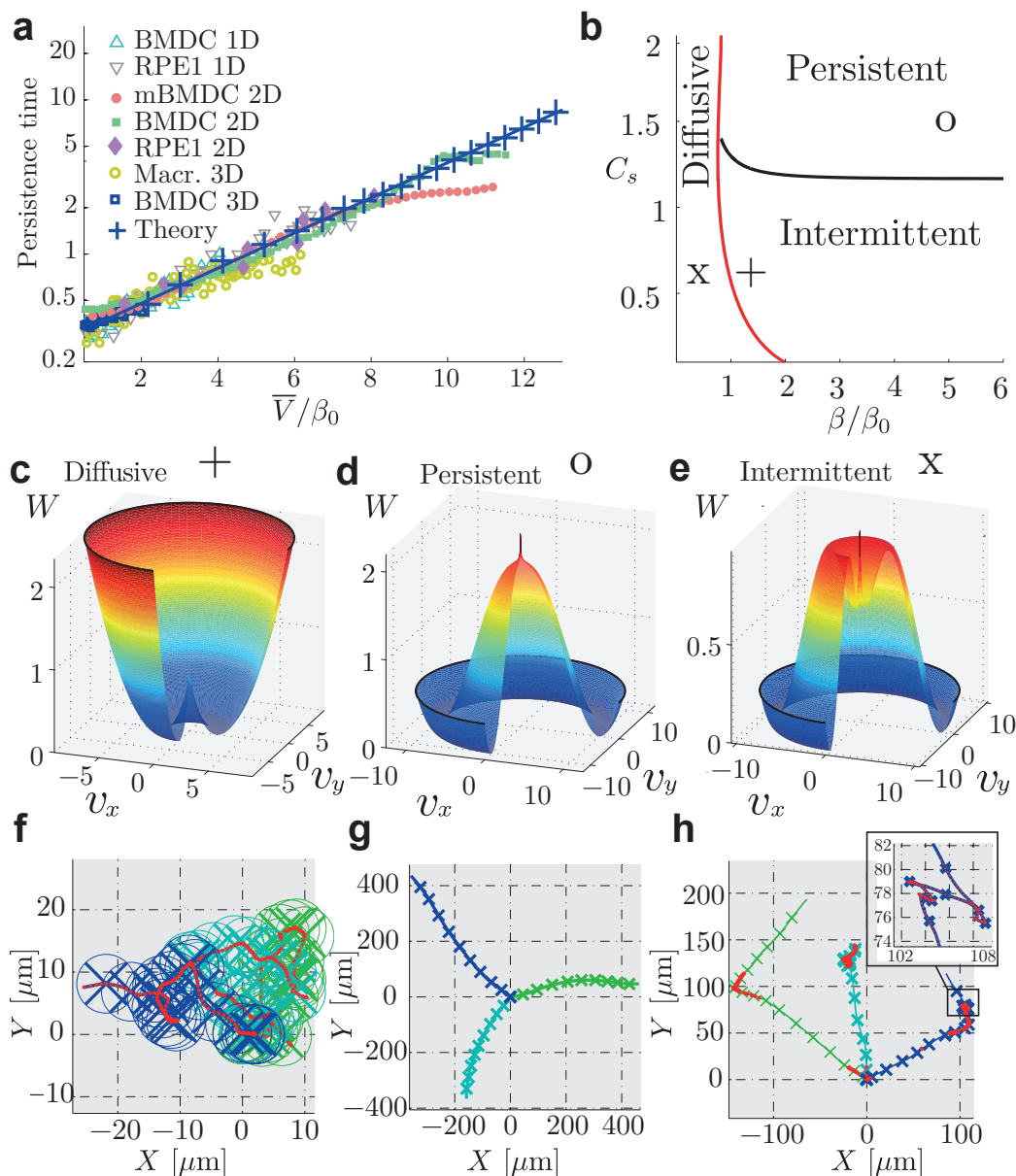


Figure 7.3: Model predictions: the USPC law and phase diagram of cell trajectories. The values of the parameters used in the figure (except for  $\beta, C_s$ ) and the fitting procedure are determined in Sec. 7.2.7, p. 158. **a.** Persistence time (in the units of  $1/\gamma$ ) as a function of the normalized mean velocity  $\bar{V}/\beta_0$ , where  $\beta_0 \equiv \tilde{D}/L$ . The prediction of the model (independent of space dimension in this regime of small angular diffusion) is compared to all available experimental data (rescaled). **b.** Phase diagram of cell trajectories in the  $\beta$  (maximal actin flow speed) and  $C_s$  (maximal concentration of activated cues) plane. Symbols correspond to the parameters used in **c,f** (+), **d,g** (\*), and **e,h** (x). **c, d, e.** Effective potential  $W$  as a function of the velocities  $V_x$  and  $V_y$  normalized by  $\beta_0$ . The singularity in  $W$  at the origin  $V = 0$  is due to the anisotropy of the diffusion process (as expected from [158]). **c.**  $W$  is locally quadratic for  $V$  small : diffusive phase (marked by + in **b**). **d.**  $W$  has a "sombbrero" shape : persistent phase (marked by \* in **b**). **e.**  $W$  has a mixed shape : intermittent phase (marked by x in **b**). **f, g, h.** Examples of simulated trajectories in the diffusive (**f**, parameters marked by + in **b**), persistent (**g**, parameters marked by \* in **b**) and intermittent phases (**h**, parameters marked by + in **b**). Colored crosses indicate the positions at regular time intervals. Circles in **f** indicate the cell size  $L$ .

write below  $\mathbf{v} = -\mathbf{V}$ ). The polarity axis  $\mathbf{e}_x$  of the cell is defined by the instantaneous direction of migration  $\mathbf{e}_x \equiv \mathbf{v}/|\mathbf{v}|$ , and we define by  $x$  the coordinate along  $\mathbf{e}_x$  in the frame of reference of the moving cell. The cell extension along  $\mathbf{e}_x$  is denoted by  $L$  (see Fig. 7.2d).

We are first interested in the dynamics of the concentration of a generic polarity cue  $c(x, t)$ , which we assume here depends only on  $x$ . This cue is assumed to specify the rear part of the cell, so that  $c(x = 0, t) > c(x = L)$  for a cell moving in the  $+$  direction. The polarity cue can either diffuse in the cytosol, with diffusion coefficient  $D$ , or, depending on its affinity for actin, be advected by the cytoskeletal flow, whose velocity along  $x$  is denoted by  $-V$  (with  $V > 0$ ) in the cell reference frame. We denote by  $k_{\text{on}}$  and  $k_{\text{off}}$  the corresponding binding and unbinding rates of the cue to the actin cytoskeleton. In the limit of fast exchange ( $k_{\text{on}}, k_{\text{off}} \gg L^2/D$ ), the dynamics of  $c(x, t)$  depends on advective transport and on diffusion as follows:

$$\partial_t c(x, t) - \partial_x [\tilde{V} c(x, t)] = \tilde{D} \partial_x^2 c(x, t) + \partial_x \zeta_c, \quad (7.2)$$

where  $\tilde{V} = V k_{\text{on}} / (k_{\text{on}} + k_{\text{off}})$  and  $\tilde{D} = D k_{\text{off}} / (k_{\text{on}} + k_{\text{off}})$ ; here  $\zeta_c$  is a Gaussian white noise that encompasses the fluctuations of the flux of cue molecules. No flux boundary conditions are imposed at  $x = 0, L$  so that the total amount of cues is conserved. At steady state, assuming  $V$  constant, the mean cue concentration profile is therefore given by:

$$\bar{c}_V(x) = \frac{L \tilde{V} e^{-\tilde{V}x/\tilde{D}}}{\tilde{D} \left(1 - \exp\left(-\frac{\tilde{V}L}{\tilde{D}}\right)\right)}, \quad (7.3)$$

where the dependence on the retrograde flow is denoted in subscript.

This simple argument predicts simple exponential concentration profiles whose steepness is directly controlled by the speed of the effective retrograde flow  $\tilde{V}$  (Fig. 7.2d). Note that non-uniform actin flow profiles (as observed for example in [170, 186]) would change the exponential shape of concentration profiles, but would leave such dependence of the gradient of concentration profiles on the actin flow speed qualitatively unchanged.

**Experimental validation** To check this very general prediction, we performed experiments on motile mBMDCs, for which concentration profiles along the polarity axis were measured for various molecules with different affinity for actin (see Fig. 7.2e): Tamra (which unspecifically labels cytoplasmic proteins), Lifeact-GFP (low affinity [187]), MLC-GFP (high affinity [188]), Utrophin-GFP (high affinity [189]). As expected from the model, we observed that increasing the actin retrograde flow could significantly increase the slope of the concentration profile of strong actin binders (MLC, Utrophin), while the profiles of molecules with low (Lifeact) or no (Tamra) affinity to actin remained unchanged (Fig. 7.2e,f).

## 7.2.4 Physical modeling predicts the USPC

We next reasoned that such mechanism in principle applies to any diffusing molecule that interacts with actin, and in particular to polarity cues.

► It is then expected that increasing actin flows should increase the asymmetry of the concentration profile of any polarity cue, thereby stabilizing cell polarization and consequently increasing cell persistence (a similar mechanism is proposed in Refs. [166, 184]).

### 7.2.4.1 Coupled equations between the retrograde flow and the concentration of cues

Following this idea, we developed a minimal theoretical model, which assumes that the actin flow  $V$  is also subject to fluctuations. These fluctuations are due to the stochasticity of polymerization/depolymerization processes or the heterogeneity of the environment, for example.

The model relies on the key assumption that the mean value  $V^*$  of the actin flow (for a fixed cue concentration profile) is governed by the asymmetry of the cue concentration profile. More precisely we assume that

$$V^* = \beta (c^*(0, t) - c^*(L, t)), \quad (7.4)$$

where

- (i)  $\beta$  is an effective parameter that controls the intensity of the coupling between the actin flow and the asymmetry of the cue concentration profile, and can be interpreted as the maximal possible velocity of the actin flow.
- (ii)  $c^*(x, t)$  denotes the fraction of activated cues, i.e. cues enabled to induce actin flow.

The phenomenological coupling (7.4) covers for example the cases where actin flows are generated by asymmetric distributions of either actin nucleators [190] or activators of contractility [177, 191, 178].

We do not aim here at describing the biochemical steps involved in the process. We assume a classical Hill response function of index  $n$  (results are qualitatively unchanged for other choices of response functions):

$$c^*(x, t) = \frac{c^n(x, t)}{C_s^n + c^n(x, t)}, \quad (7.5)$$

where  $C_s$  is the concentration of cues above which activation is saturated, and is therefore determined by the maximal concentration of activated cues. Considering a cell moving on a 2-dimensional substrate, the dynamics of the actin flow velocity  $\mathbf{V}$ , which is a vector of modulus  $V$  and polar angle  $\phi$ , is then given by the Langevin equations

$$\begin{aligned} \partial_t V &= -\gamma(V - V^*) + \frac{K}{2V} + \sqrt{K} \zeta_V, \\ \partial_t \phi &= \frac{\sqrt{K}}{V} \zeta_\phi, \end{aligned} \quad (7.6)$$

where

- (i)  $\zeta_V$  and  $\zeta_\phi$  are Gaussian white noises of variance unity,
- (ii)  $\gamma^{-1}$  is the typical time scale of the actin flow fluctuations,
- (iii)  $K$  controls the amplitude of the actin flow fluctuations.

The  $K/V$  term comes from the classical polar representation of an isotropic Brownian noise (Bessel process) in two dimensions [18]. Note in particular that

- the 1-dimensional case is deduced from the 2-dimensional case by taking a vanishing angular diffusion  $K = 0$ ,
- the 3-dimensional case is straightforwardly obtained by the substitution  $K/2V \rightarrow K/V$  in the first line of Eq. (7.6).

The non-linear stochastic Eqs. (7.2,7.4,7.5,7.6) then fully define the dynamics of the polarity cues and the actin flow.

### 7.2.4.2 Decoupled equations due to fast diffusion of cues

To go further, we make use of the fact that the typical diffusion time of cues over the cell length  $L^2/D$  (of the order of seconds) is significantly shorter than the characteristic time scale of fluctuations in the actin flow  $\gamma^{-1}$  (of the order of minutes). The concentration of cues is then taken at steady state, and Eq. (7.2) implies that it is a Poisson random variable, i.e.  $c(x, t) = \bar{c}_V(x) + \delta c$  with  $\overline{\delta c^2} = K_c \bar{c}_V(x)$ , where  $K_c$  is a constant that controls the intensity of the particle number fluctuations and  $\bar{c}_V(x)$  is the steady state profile defined in Eq. (7.3). The dynamics for  $\mathbf{V}$ , after linearization with respect to  $\delta c$ , can then be written as an autonomous system of stochastic differential equations (called Langevin equations) that reads:

$$\begin{aligned}\partial_t V &= \gamma \mathcal{F}(V) + \sigma(V) \zeta_V \\ \partial_t \phi &= \frac{\sqrt{K}}{V} \zeta_\phi,\end{aligned}\quad (7.7)$$

where the effective force reads

$$\mathcal{F}(V) = -V + \beta \left( \frac{\bar{c}_V^n(0)}{C_s^n + \bar{c}_V^n(0)} - \frac{\bar{c}_V^n(L)}{C_s^n + \bar{c}_V^n(L)} \right) + \frac{K}{2\gamma V}, \quad (7.8)$$

and the noise intensity is given by

$$\sigma^2(V) = K + K_c n^2 \beta^2 \gamma^2 C_s^{2n} \left( \frac{\bar{c}_V^{2n-1}(0)}{(C_s^n + \bar{c}_V^n(0))^4} + \frac{\bar{c}_V^{2n-1}(L)}{(C_s^n + \bar{c}_V^n(L))^4} \right). \quad (7.9)$$

The dynamics of  $V$  is therefore the dynamics of a Brownian particle in a force field  $\mathcal{F}(V)$  in the presence of a non trivial noise with additive and multiplicative parts. Assuming that, for any given experimental condition, the cell velocity is directly proportional to the actin flow velocity ( $\mathbf{v} = \alpha \mathbf{V}$ , where we set hereafter  $\alpha = -1$  for the sake of simplicity), Eqs (7.7) make it possible to fully characterize the resulting cell trajectories.

The steady state distribution  $P(V)$  of the velocity can be obtained. Following a classical procedure ([18]), the propagator  $P(V, t|V_0)$  (defined in Sec. 2.1.2) is shown to satisfy the following Fokker–Planck equation:

$$\partial_t p(V, t|V_0) = -\partial_V [\mathcal{F}(V)p(V, t|V_0)] + \frac{1}{2} \partial_V^2 [\sigma^2(V)P(V, t|V_0)]. \quad (7.10)$$

which is a particular case of forward equation on the propagator, see Eq. (2.4). The stationary distribution is then straightforwardly derived as:

$$P(V) = \frac{N}{\sigma^2(V)} \exp \left( 2\gamma \int_0^V du \frac{\mathcal{F}(u)}{\sigma^2(u)} \right) \equiv N e^{-\gamma W(V)}, \quad (7.11)$$

where  $W(V)$  is an effective potential and  $N$  a normalization constant.

In the next paragraph, we show that the polarization time  $\tau_p$  (defined as the mean lifetime of a cellular configuration, see Fig. 7.2c) can be defined as a MFPT to  $V = 0$  for a stochastic particle confined in the potential  $W(V)$ .

## 7.2.5 Derivation of the USPC law

We precise the distinction between the persistence and polarization time, which are respectively defined as two MFPT quantities, the first relatively to the the turning angle and the second relatively to the norm of the velocity vector:

- (1) the mean persistence time  $\tau_\phi$  is identified to the MFPT on the angular coordinate  $\phi$  for the modelled cell to first reach the threshold turning angle  $\phi = \pm\pi/2$  (denoted  $t(\phi_f|V_0, 0)$ , as the turning angle is initially set to zero).
- (2) the mean polarization time  $\tau_p$  is identified to the MFPT denoted  $t(V_f|V_0)$  for the modelled cell to first reach the threshold velocity  $V_f$ .

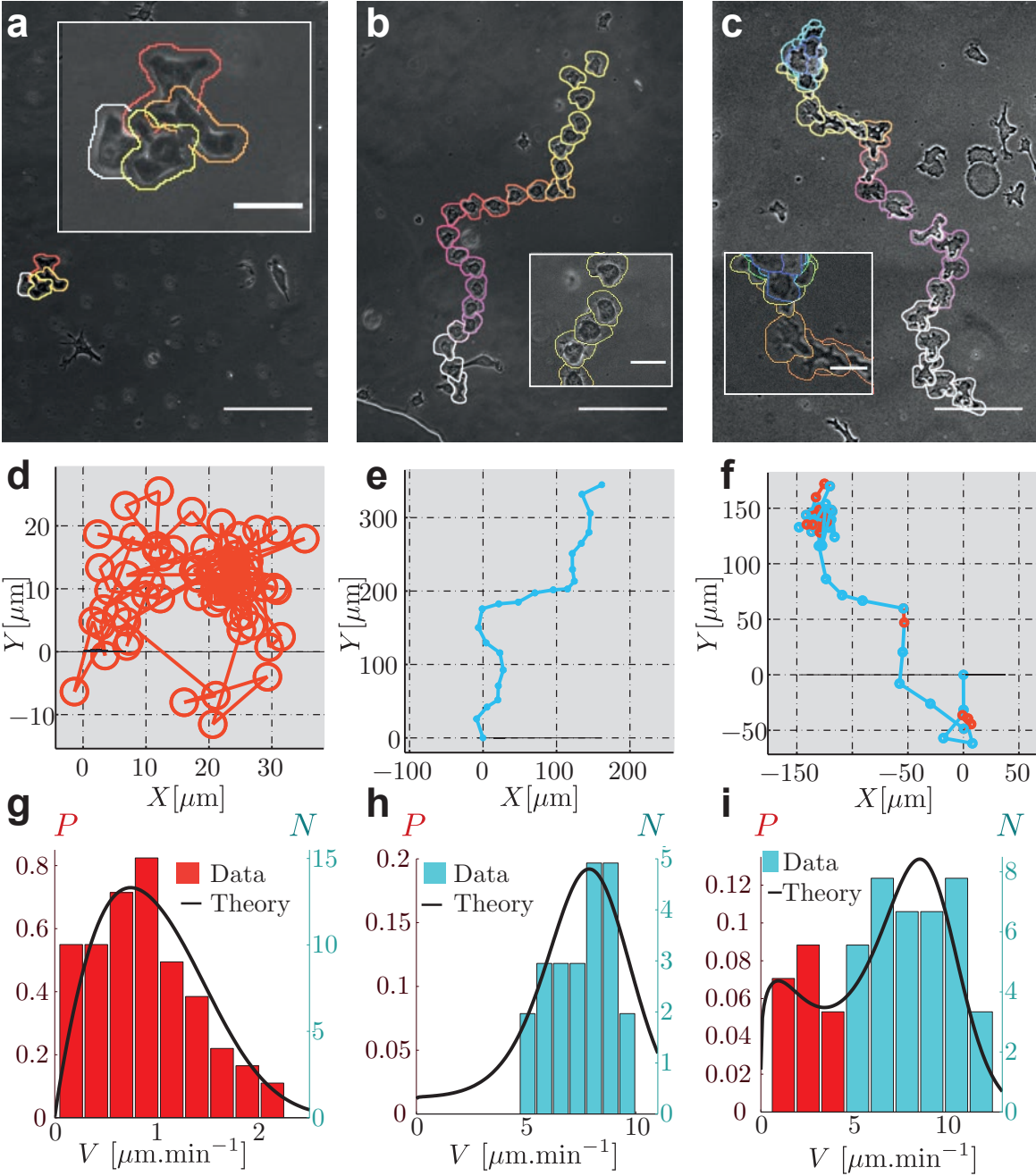


Figure 7.4: Experimental cell trajectories can be classified in the 3 classes predicted by the model: diffusive ( **a**, **d**, **g**), persistent ( **b**, **e**, **h**) and intermittent ( **c**, **f**, **i**). **a**, **b**, **c**. Examples of BMDCs migration patterns of each type. Color code indicates the time course (total duration: **a**, 276 min, **b**, 72 min, **c**, 141 min). Scale bar  $100 \mu\text{m}$  (in insets:  $25 \mu\text{m}$ ). **d**, **e**, **f**. Corresponding trajectories extracted from automated tracking of the nucleus. Circles indicate the confidence interval ( $3\mu\text{m}$ ). Blue stands for cell speed  $v > 4 \mu\text{m}\cdot\text{min}^{-1}$  and red for  $v < 4 \mu\text{m}\cdot\text{min}^{-1}$ . **g**, **h**, **i**. Histograms of velocities extracted from the corresponding experimental tracks are in agreement with the distribution of velocities  $P(v)$  (solid black line) from the model with the parameters of Sec. 7.2.7, p. 158 and  $\beta$ ,  $C_s$  are indicated in Fig. 7.3b: diffusive phase (+), persistent (\*), and intermittent (x).

### 7.2.5.1 Polarisation time

Concerning the point (1), we derive analytical results on the polarization time  $\tau_p$  identified to the MFPT  $t(0|V_0)$ . Note that in 2D and 3D, one needs to introduce a lower cut-off  $V_f$ , since the point  $V = 0$  cannot be reached by a diffusive process. In the following, we took  $V_f \approx 0.10 \beta_0$ .

As seen in the Mathematical Introduction Sec. 2.2.1, p. 36, we deduce from Eq. (7.10) that the MFPT satisfies the equation:

$$-1 = \mathcal{F}(V)\partial_V t(0|V) + \frac{1}{2}\sigma^2(V)\partial_V^2 t(0|V). \quad (7.12)$$

The general exact expression for  $t(0|V_0)$  is then [192]:

$$t(0|V_0) = 2 \int_0^{V_0} \frac{dy}{\psi(y)} \int_{-\infty}^y \frac{\psi(x)dx}{\sigma^2(x)} \quad \text{where} \quad \psi(y) = \exp\left(2 \int_0^y dV' \frac{\mathcal{F}(V')}{\sigma^2(V')}\right),$$

which gives an explicit expression of the polarization time  $\tau_p$ . In the following we set  $V_0$  to be equal to mean velocity at steady state, i.e. the average of  $V$  weighted by the distribution  $P(V)$ .

A standard approximation, which follows from the analogy with the classical Kramers escape problem [18] is to consider that

$$t(0|V_0) \approx 2 \int_0^{V_0} \frac{dy}{\psi(y)} \int_{-\infty}^0 \frac{\psi(x)dx}{\sigma^2(x)},$$

which leads to an expression of the form:

$$\ln(t(0|V_0)) \propto A(V_0) + W(V_0), \quad (7.13)$$

where  $A(V)$  is a slowly varying function with  $V$  (i.e. slower than  $\ln(V)$ ). As in the classical Kramers escape problem, the polarization time is therefore controlled by the height of the effective energy barrier  $W(V_0)$ . The obtained function  $\tau_p(V) \equiv t(0|V_0)$  can be showed to be very well approximated by a simple exponential  $\tau_p \simeq Ae^{\lambda V}$  for a wide range of biologically relevant parameters (see fitting procedure below). In particular the exponential fit holds for  $n \in [0.70, 1.5]$  (see Fig. 7.5), which shows that no strong non-linearity is needed.

### 7.2.5.2 Persistence time

Concerning the point (2), we emphasize that the persistence time represented Fig. 7.4 is the persistence  $\tau_\phi$  with a threshold angle  $\phi = \pi/2$ . We compare the theory to the experiments, we compute the theoretical persistence time  $\tau_\phi$  through Monte-Carlo simulations. It is also the criteria which is used to analyze the experimental trajectories (BMDC and RPE1). Note that it was checked that this definition yields, up to unimportant prefactors, the same results as the classical definition of the persistence time as the characteristic decay time of the velocity-velocity autocorrelation function. In the relevant regime of small enough angular diffusion (parametrized by the intensity of velocity fluctuations  $K$ ) the persistence time is quantitatively very close to the polarization time  $t(0|V_0)$  ( see Fig. 7.5). This allowed us to fit all the available data with a single universal exponential master curve  $\tau \simeq \tau_p \simeq Ae^{\lambda V}$ , and therefore reproduce quantitatively the USPC law (see Fig. 7.3).

## 7.2.6 Phase diagram of main cell migration patterns

In addition, Eqs (7.7) give an explicit construction of a cell trajectory as that of an active Brownian particle [158, 159]. While this concept has already proved to be useful to model phenomenologically cell trajectories [153, 154], so far no such bottom up approach was available.

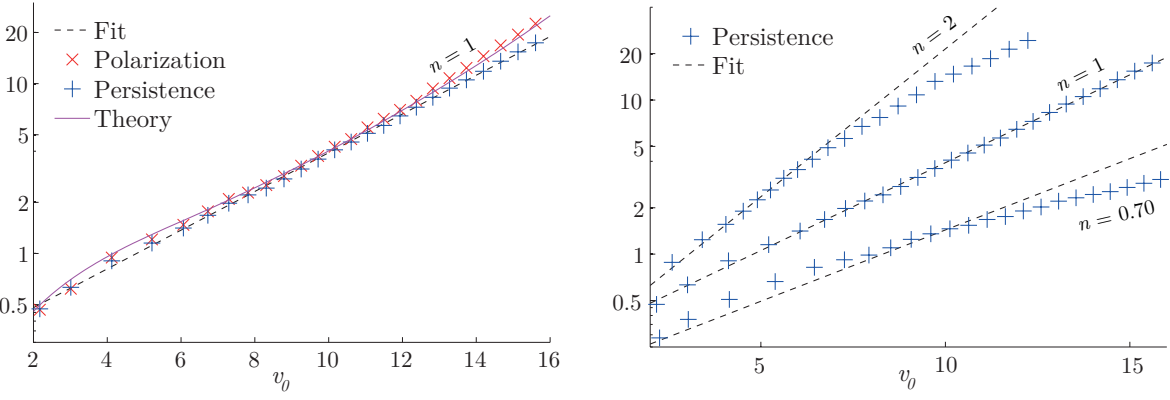


Figure 7.5: The theoretical expression for the polarization function  $t(V_f|V_0)$  (black solid line), i.e. the mean first passage time to reach  $V_f = 0.10 \beta_0$ , is plotted as a function of an initial velocity  $V_0 = \bar{V}$  equal to the mean velocity  $\bar{V}$ . Increasing the Hill exponent from 0.70 to 3 increases the persistence time. The other parameters  $C_s$ ,  $K$  and  $K_c$  are set in Sec. 7.2.7. The mean first passage time  $t(V_f|V_0)$  is compared to Monte-Carlo results: polarization (red x symbols) and persistence (blue + symbols). The dashed blue line represent the linear interpolation curved used in the main text.

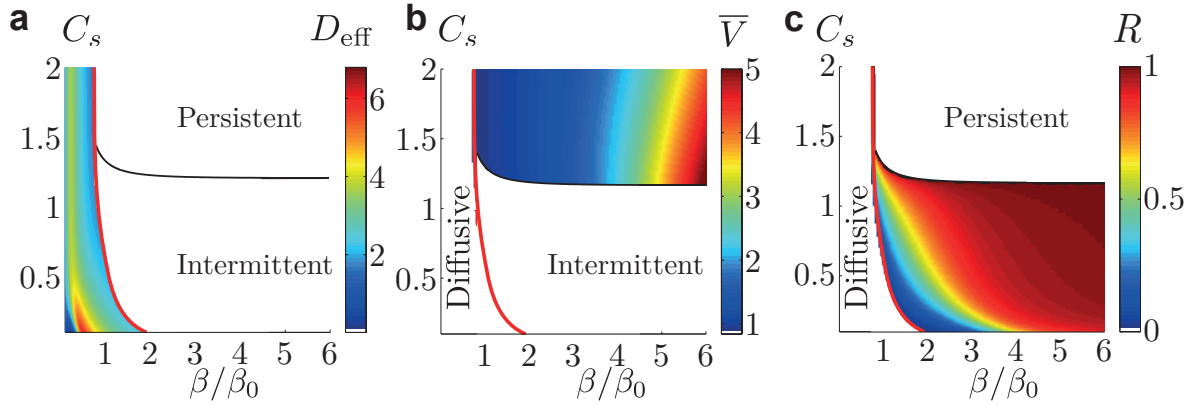


Figure 7.6: Phase diagrams in terms of the coupling strength  $\beta/\beta_0$  and of the saturation level  $C_s$ . **a.** Effective diffusion coefficient  $D_{\text{cell}}$  of the cell within the diffusive phase. **b.** Mean velocity  $\bar{V}$  within the persistent phase. **c.** Ratio  $R = u_1/(u_1 + u_2)$  of the time spent within the persistent phase  $u_1$  over the total time  $u_1 + u_2$ . The value of the parameter  $K_c$  is set in Sec. 7.2.7 and  $K = 0$ .

► The three phases are identified by analyzing the variations of the probability distribution  $P(V)$ . In the diffusive phase,  $P(V)$  has a single maximum at  $V = 0$  and  $P(V)$  is a monotonously decreasing function of  $V$ . In the persistent phase,  $P(V)$  has a single local maximum at  $V > 0$ . In the intermittent phase,  $P(V)$  has two local maxima: one at  $V = 0$  and another at  $V > 0$ . In the phase diagram in the main text and in Fig. 7.6, the solid red line  $\beta = \beta_c(C_s)$  separates the diffusive phase from the persistent and intermittent phases. The separation between the persistent and intermittent phases (solid black line) is analytically determined by a zero-curvature condition at  $V = 0$  for the probability distribution  $P(V)$ .

We recall that for generic active Brownian particles in 2D and 3D, the velocity distribution  $P(V)$  is singular at  $V = 0$  [158]; such singularity is irrelevant here and is expected to be smoothed by a lower velocity cut-off  $V_f$  (previous introduced p. 155). To construct the phase diagram of the main text and of Fig. 7.6 we consider for simplicity the 1D case, which is smooth

at  $V = 0$ . It was checked that in 2D and 3D the singularity has only local effects, so that the phase diagram is qualitatively unchanged.

Finally, the trajectories can be fully characterized inside each region of the phase diagram as follows:

- (i) *Brownian trajectories.* For  $\beta$  smaller than a critical value  $\beta_c(C_s)$ , the potential  $W(v)$  has a generic bowl shape centered at  $v = 0$  and the process can be well approximated by a classical Ornstein Uhlenbeck process [18] (see Fig. 5.2.2b,c,f). This regime of slow maximal actin flow is characterized by an autocorrelation of  $v$  that decays exponentially with a short characteristic time  $\tau \sim 1/\gamma$ , so that there is no stable polarized state since the actin flow remains slow and fluctuates around zero. At time scales larger than  $1/\gamma$  (which is the time scale of actin flow fluctuations, of the order of minutes) trajectories are then Brownian like. The effective diffusion coefficient can then be calculated from the analysis of Eq. (7.7) and is shown in Fig. 7.6.a.
- (ii) *Persistent trajectories.* For  $\beta > \beta_c(C_s)$  and  $C_s > C_s^c(\beta)$  (fast maximal actin flow and large maximal concentration of activated markers, see Fig. 7.6),  $W(V)$  has a sombrero shape which is the hallmark of systems with broken symmetry. The modulus of the velocity  $V$  fluctuates round a non-zero minimum and in that case trajectories correspond to a persistent random walk with long-lived polarization. Note that two time scales are involved in the persistence: (i) the polarization time (i.e. the time needed for  $V$  to reach 0) is exponentially larger than  $1/\gamma$  and (ii) the rotational diffusion time that scales as  $1/K$ . The mean velocity is derived from the steady state distribution given in Eq (7.11) and is shown in Fig. 7.6.b.
- (iii) *Intermittent trajectories.* For  $\beta > \beta_c(C_s)$  and  $C_s < C_s^c(\beta)$  (fast maximal actin flow and small maximal concentration of activated markers, see Fig. 7.6b),  $W(V)$  has both a local minimum around  $V = 0$  and a secondary non-zero minimum at  $V = V_m > 0$ . These two minima of the potential lead to intermittent trajectories (see [157]), characterized by an alternation of Brownian and persistent phases. The stabilization of the Brownian phase (around  $V = 0$ ) is due to the multiplicative noise term in Eq. (7.7) (see [193]): the small maximal concentration of activated markers induces large fluctuations, whose dependence on  $V$  leads to an effective restoring force towards the unpolarized state  $V = 0$ . The trajectories can then be characterized by the mean times spent in each mode (Brownian or persistent) as shown in Fig. 7.6.c. The polarization time and persistence time can also be obtained (Fig. 7.5).

These three classes of trajectories predicted by the model are well reported in the literature [153, 154, 162, 43], which provides a further validation of the model. To test this prediction more quantitatively, we analyzed 2-dimensional trajectories of BMDCs (Fig. 7.4a-f) obtained by automated tracking of cell nuclei. For each analyzed trajectory, the measured velocity distribution  $P(v)$  could be well fitted by the model by adjusting only  $\beta$  and  $C_s$ , while all other parameters values were kept as in Fig. 5.2.2 (see Fig. 7.4g-i). We found that indeed all trajectories could be classified according to the above three classes predicted by the model (Brownian, persistent, intermittent) depending on the value of the parameters  $\beta$  and  $C_s$  only, in agreement with the predicted phase diagram (see Fig. 5.2.2b).



### 7.2.7 Values of the fitting parameters

A natural time scale in the problem is  $1/\gamma$  and velocities can be conveniently expressed in units of  $\beta_0 = D/L$ . The analysis of both persistence data and BMDC trajectories in  $2D$  was performed with a single set of parameters :

- $\gamma^{-1} = 15$  min which is a typical relaxation time of large actin protrusions,
- $\beta_0 = 0.40 \mu\text{m}\cdot\text{min}^{-1}$  which is a typical actin flow velocity.

Note that the order of magnitude for  $L$  is  $L = 5 \mu\text{m}$  so that  $L^2/D = 2$  min. One therefore has  $L^2/D < \gamma^{-1}$  as expected. The best fit for both the persistence data and the probability distribution of BMDC trajectories was then obtained for  $K \approx 6.10^3 \mu\text{m}^2\cdot\text{min}^{-3}$  and  $K_c \approx 10^4 \mu\text{m}\cdot\text{min}^{-1}$ .

The scales  $\beta_0$  and  $\gamma^{-1}$  used for the fitting of the 7 experimental data sets are indicated in Table 7.1. Mind that Macr. stands for Macrophages.

	mBMDC 2D	BMDC 2D	BMDC 1D	RPE1 2D	RPE1 1D	Macr. 3D	BMDC 3D
$\beta_0$	$1.6 \pm 0.20$	$0.38 \pm 0.03$	$0.52 \pm 0.04$	$0.05 \pm 0.04$	$0.06 \pm 0.04$	$1.6 \pm 0.10$	$1.60 \pm 0.20$
$\gamma^{-1}$	$15 \pm 1.2$	$15 \pm 1.1$	$47 \pm 3.5$	$11 \pm 0.9$	$95 \pm 7$	$4.5 \pm 0.58$	$25 \pm 1.4$

Table 7.1: Scaling parameters in fit of experimental data to the master curve. The units are: ( $\mu\text{m}\cdot\text{min}^{-1}$ ) for  $\beta_0$  and (min) for  $\gamma^{-1}$ .

## 7.3 Discussion and conclusion

To conclude, we have reported a universal coupling between persistence and mean instantaneous migration speed in single cell trajectories. We have shown that this coupling relies on the effect of actin retrograde flow speed on protrusion lifetime and thus cell polarity. We then showed that faster actin flows would generate steeper gradients of molecules that bind to actin filaments. Based on these observations we constructed a theoretical model that explicitly takes into account the coupled dynamics of polarity cues and actin flows, and provides an explicit construction of the single cell dynamics as an active Brownian particle. The two main predictions of the model were validated experimentally:

- (i) we first showed that the model quantitatively predicts the observed exponential coupling between cell persistence and cell speed that defines the USPC law,
- (ii) we next showed that the model reproduces the main migratory behaviors reported so far – Brownian, persistent and intermittent –, and identifies the key parameters that control the properties of cell trajectories.

As seen in Fig. 7.1, the persistence time depends exponentially on the mean instantaneous velocity – which characterizes the USPC – in the lower range of speeds for each cell type, and a saturation to a plateau is observed at larger speeds. Such saturation could have several causes. In fact the model primarily predicts an exponential dependence of the polarization time  $\tau_p$  on the actin flow speed  $V$ , as observed experimentally in Fig. 7.2. Such dependence  $\tau_p(V)$  implies a similar exponential dependence  $\tau(v)$  between persistence time and cell speed under two conditions. First, it requires that polarization time  $\tau_p$  and persistence time  $\tau$  can be identified. While this is clear in 1-dimensional geometries, this does not always hold in dimensions 2 and 3, where two effects compete to destroy persistence : depolarization, characterized by the time scale  $\tau_p$ , and angular diffusion, characterized by the time scale  $\tau_\phi \sim \beta^2/K$ . One therefore

expects that  $\tau \sim \tau_p$  only for  $\tau_p \lesssim \tau_\phi$ , while  $\tau$  saturates for larger values of  $\tau_p$ . Second, it requires that cell speed and actin flow speed are linearly coupled ( $v = \alpha V$ ). As we argued, such linear dependence generally holds in the lower range of speeds for each cell type. Non-linear effects (which could be due for example to a motor-clutch mechanism [179]) are however expected at larger speeds, and could result in the observed saturation of the persistence time.

► An important observation we made is that this law also applies at the subcellular scale, to individual cell protrusions. This has two consequences: first it explains why cells with various modes of migration follow the USPC law, as it might apply to any locomotory subpart of the cell and the nature of the protrusions does not matter. Second, it suggests that such coupling between actin filaments flow rate (or even flows of other cytoskeletal elements) and lifetime of polarity might apply to other phenomena than cell migration, such as polarized secretion or growth, which also rely on actin polymerization.

The USPC law is validated on cells of mammalian origin migrating in 1 and 2-dimensional geometries, with or without confinement and in 3-dimensional collagen gels - the main in vitro migration assays. The USPC coupling was also observed for macrophages moving in live tissues in Medaka fish. The process we describe is generic and is likely to apply to cells from other organisms. Indeed a very similar correlation between speed and persistence was reported from migrating amoeba [194, 195]. A priori, the USPC law only applies to random migration but not to migration in the presence of cues (see Sec. Eq. (1.2.2)). It is however likely that the mechanism that we describe helps reinforce a weak external guidance and it might thus be also important for guided migration (see Perspective 7.4).

In this work we did not aim at investigating in more details the molecules that might be responsible for coupling the flow to the polarity for a given cell type. We believe that, even in a given cell type, there might be several molecules that could contribute to the coupling. For example, one of the most obvious player would be Myosin II [184], at least for amoeboid migration, as it fits the two requirements: it is transported by actin filaments and the steepest its gradient, the faster the flow. Such a mechanism inspired us in the choice of the feedback equation we used in the model (Eq.7.4). Nevertheless, inhibiting Myosin II in most cases induces a stronger Rac dependent protrusive activity and thus a stronger polymerization based actin flow (see [196]), which can also transport polarity cues. As a consequence, even if both speed and persistence might be affected, their exponential coupling is maintained when Myosin II is inhibited. It is even possible to envision that this coupling might be so deeply linked to actin based cell locomotion that it is impossible to break it without preventing locomotion itself. Last, we stress that our analysis does not exclude polarity cues involved in the regulation of other key actors of cell polarity such as microtubules, as long as they interact at least indirectly with actin.

**Search Strategy** Our model generates all the range of observed cell trajectories, with only two main parameters:

- (i) the maximal actin flow velocity  $\beta$ ,
- (ii) the maximal concentration of activated cues  $C_s$ .

While the parameter  $C_s$  might be difficult to vary experimentally, the parameter  $\beta$  is shown to be versatile (see Fig. 7.2a). Recent results identified optimal search patterns for both persistent (see [197] and Pub. 1) and intermittent trajectories ([157]). Therefore the search efficiency for a target is expected to be an optimizable function in terms of  $\beta$  and  $C_s$ .

The model provides a very generic ingredient of cell migration that could be used as a basis to model any process in which individual cell trajectories matter, such as search processes by

immune cells [156], neuronal cells migration or invasion by cancer cells.

### Summary of main results

Our model for the Universal cell Speed and Persistence Coupling (USPC)

- (i) quantitatively predicts the exponential correlation between speed and persistence,
- (ii) provides an explicit construction of single cells dynamics as active Brownian particles, from minimal microscopic hypothesis,
- (iii) yields a phase diagram of cellular trajectories (diffusive, intermittent, persistent).

## 7.4 Perspectives

In this thesis chapter, we developed the USPC model for non-interacting cells and in the absence of external cues. Ankush Sengupta is working on two possible extensions of the model that takes into account:

- (1) a chemotactic effect due to the presence of cues, which can be analytically treated by a directional bias in the potential  $W(v)$ .
- (2) hard-core interactions with velocity alignment between cells, which can be studied by numerical simulations

Concerning point (i), we point out that the USPC law has already been confirmed experimentally in Medaka chemotactic cells. The aim of the second point (ii) is to investigate the effect of the USPC law on collective phenomena, such as cell aggregation or tissue dynamic.

7. Universal speed-persistence  
coupling in cells

# General Conclusion

---

In Chap. 1, random search processes are shown to be ubiquitous in science, with numerous examples of applications ranging from nuclear reactions, enzymes searching for specific DNA sequences to animal foraging [113, 140, 198, 199].

In this manuscript, we focus on the time needed by individual searchers, which are moving at random, to find one or several fixed targets. One of my objectives is to design optimal search strategies. The term strategy refers to the choice of a set of parameters that minimizes the mean first passage time (MFPT) to the target. Hence we seek to obtain analytical expressions for first-passage observables and especially for the MFPT. I recall that in Chap. 2, p. 31, these observables were found to be solutions of linear integro-differential equations completed by boundary conditions.

► In this thesis, we determine new expressions for the MFPT for symmetric, biased and active random walks. These expressions lead to the identification of optimal search strategies. I summarize my main results in Table 8.1.

In Chap. 3, p. 49, we compute the distribution of exit times for symmetric Brownian particles in angular sectors, annuli and rectangles that contain an exit on their boundary. We extend these results to biased Brownian particles with a radial bias  $v(r) = \mu D/r$ .

In the annulus geometry, the exit time of symmetric Brownian particles can be optimized in terms of the geometrical factors that are the external and internal radii ( $R$  and  $R_c$ ). Given a specific value for  $R$ , the optimal radius  $R_c^{(c)}$  results from a trade-off between two competing geometrical effects:

- (i) increasing  $R_c \ll R$  reduces the accessibility to the exit for remote searchers which have to circumvent the reflecting boundary at  $r = R_c$ ,
- (ii) once a searcher is close to the exit, increasing  $R_c$  enhances the probability for the searcher to cross the exit.

In Chap. 4, p. 85, we consider exit processes with surface-mediated diffusion along the boundary. We show by analytical means that the MFPT can be optimized in terms of the exchange rates between the bulk and the surface, which are (i) the desorption rate  $\lambda$  and (ii) the adsorption parameter  $k$ . Bulk excursions reduce the time wasted due to the recurrence of surface Brownian motion by bringing particles through the bulk to unvisited regions of the sphere. We show that the optimality of the intermittent strategy is a robust result through a systematic study of the influence of

- (i) the space dimension ( $d = 2$  and  $d = 3$ ),
- (ii) the adsorption properties of both the target ( $k_t$ ) and the rest of the surface ( $k$ ),
- (iii) the drift strength ( $\mu$ ),
- (iv) the number ( $N_t$ ) of regularly spaced targets.

We explain why the coarse-grained approach of Ref. [130] eludes the optimization property (see Eq. (5.3.2), p. 116). Taking into account the spatial correlations between a desorption event and the next readsorption leads to technical challenges and is necessary to explain the optimizability of the MFPT. Nevertheless, I exhibit a simple mean-field expression for the MFPT that is an optimizable function of the desorption rate (see Sec. 5.4, p. 121).

In Chap. 6, p. 125, we consider a special active process called the exponential Pearson random walk (EPRW, defined p. 18). We develop a method to construct approximate expressions of the MFPT in  $d = 2$  and  $d = 3$ , for various boundary conditions. We show the existence of an optimal reorientation rate  $\tau_{\text{opt}}$  which minimizes the MFPT, under analytically determined criteria. The latter result holds even in the case of a diffusive boundary condition, which forbids trajectories of infinite length in a ballistic search ( $\tau = \infty$ ). The interpretation for the favourable effect of the optimal reorientation rate  $\tau_{\text{opt}}$  compared to the purely ballistic search is the following: at  $\tau_{\text{opt}}$ , the searcher has the opportunity to turn when it is close to the target, and after such reorientation it has a high probability to encounter the target in a very short time. The approximate resolution scheme can be applied to the chemotactic search processes (see Sec. 6.4.2, p. 141), with potential interest in the study of cell migration.

In Chap. 7, p. 143, we build a stochastic model which quantitatively predicts the observed exponential coupling between the persistence time, and the velocity of the retrograde flow within the cell. The persistence and the polarization time are fitted by a MFPT quantity, i.e. the MFPT of a particle confined in a potential field to reach a near zero threshold velocity. The model yields a phase diagram of the three experimentally observed cellular trajectories – diffusive, persistent and intermittent – in terms of two microscopic parameters:

- (i) the maximal actin flow velocity  $\beta$ ,
- (ii) the maximal concentration of activated cues  $C_s$ .

As optimal search patterns have been identified for both persistent processes (see Part. III) and intermittent processes (see Ref. [157]), the search efficiency for a target is expected to be an optimizable function of the two parameters  $\beta$  and  $C_s$ . The USPC model could be used as a basis to model any process in which individual cell trajectories matter, such as search processes of antigens by immune cells [156]

Our resolution schemes can find applications beyond the computation of first passage quantities. For example, the Helmholtz and the Poisson equations with mixed boundary conditions are encountered in the fields of microfluidics [106], heat propagation [114], quantum billiards [115], acoustics [116], mechanics and elasticity [99]. A representative example of this versatility is the problem considered in Sec. 3.2.4, p. 74: the resolution scheme is applied to a problem of flow optimization in a microchannel device.

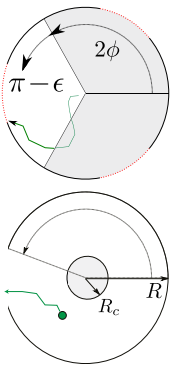
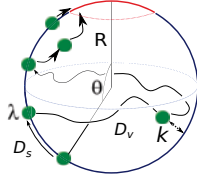
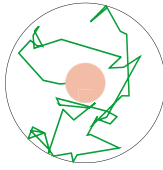
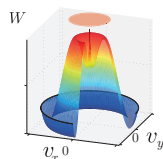
Part	Situation	MFPT
I	 <p>Symmetric or biased diffusion</p>	<p>Simplification of the MFPT Fourier coefficients, Eq. (3.13b). Density of FPT for symmetric and biased Brownian motion.</p> <p>(i) No optimization of biased Brownian motion, with radial bias <math>v(r) = (\mu D)/r</math> in the disk geometry in terms of the bias coefficient <math>\mu</math> (see Sec. 3.2.2, p. 73), (ii) Optimization of the symmetric Brownian motion in the annular geometry (see Sec. 3.2.1, p. 68) in terms of geometrical parameters (radii <math>R, R_c</math>, aperture size <math>\varepsilon</math>).</p>
II	 <p>Symmetric or biased diffusion in bulk</p>	<p>General expression for the MFPT in Eq. (4.49), p. 93.</p> <p>Optimization of the exit process of the surface-mediated search in terms of exchange rates <math>(\lambda, k)</math> (see Sec. 4.2.4, p. 92)</p>
III.6	 <p>Active process: Pearson walk</p>	<p>Optimization of the EPRW search in terms of turn rate <math>\tau</math> for <math>d &gt; 1</math>, for specular or diffuse boundary condition.</p>
III.7	 <p>Active process: Multiplicative noise, biased random velocity</p>	<p>Optimization of the active Brownian process in terms of microscopic parameters <math>(\beta, C_s)</math> (see Sec. 7.3, p. 159)</p>

Table 8.1: Summary of the geometries considered and the MFPT  $t(r)$  determined in this thesis manuscript. On the schemes of the geometry, the target region is indicated in red, the trajectory of the random particle in green. The MFPT is used to quantify the optimizability of the search process. In Chap. 7, p. 143, the MFPT provides an expression of the persistence time, which can be related to the turning rate  $\tau$  of the EPRW process studied in Chap. 6, p. 125.





# Publications

---

The results presented in this thesis manuscript led to the following publications in peer-reviewed journals:

1. J-F. Rupprecht, C. Touya, O. Bénichou, R. Voituriez, Search time optimization for continuous persistent random walks in confinement (final preparation).
2. P. Maiuri, J-F. Rupprecht, S. Wieser et al., Actin flows mediate a Universal Coupling between cell Speed and Persistence (reviewed in Cell).
3. J-F. Rupprecht, O. Bénichou, D. S. Grebenkov, R. Voituriez, Exit time distribution in spherically symmetric two-dimensional domains (submitted to J. Stat. Phys.).
4. J-F. Rupprecht, O. Bénichou, D. S. Grebenkov, R. Voituriez, Kinetics of Active Surface-Mediated Diffusion in Spherically Symmetric Domains, *Journal of Statistical Physics*, **5**, 891 (2012).
5. J-F. Rupprecht, O. Bénichou, D. S. Grebenkov, R. Voituriez, Exact mean exit time for surface-mediated diffusion, *Physical Review E*, **86**, 041135 (2012).



Part IV  
Appendix



# FPT in 2D spherically symmetric domains

## Contents

<b>A.1 Simplification of <math>\alpha_n</math> and <math>M_{nm}</math></b> . . . . .	<b>171</b>
A.1.1 Simplified expressions for $\alpha_0$ . . . . .	171
A.1.2 Simplified expressions for $\alpha_n, n \geq 1$ . . . . .	172
A.1.3 Simplified expression for $M_{nm}$ . . . . .	172
A.1.4 Perturbative expansion of $M_{nm}$ . . . . .	173
A.1.5 Summation identities . . . . .	174
A.1.5.1 Proof of the identity (3.65) . . . . .	174
A.1.5.2 An eigenvector of the matrix $M$ . . . . .	174
<b>A.2 Spatially averaged variances</b> . . . . .	<b>175</b>
<b>A.3 Convergence to an exponential distribution in the narrow-escape limit</b>	<b>175</b>
A.3.1 From the expression for the survival distribution . . . . .	175
A.3.2 From the expression for the moments . . . . .	176
<b>A.4 Computational aspects</b> . . . . .	<b>176</b>

## A.1 Simplification of $\alpha_n$ and $M_{nm}$

### A.1.1 Simplified expressions for $\alpha_0$

Herewith we prove the following identity for all  $0 \leq t < \pi$

$$\frac{\sqrt{2}}{\pi} \int_0^t dx \frac{x \sin(x/2)}{\sqrt{\cos x - \cos t}} = -2 \ln \left( \cos \left( \frac{t}{2} \right) \right). \quad (\text{A.1})$$

We proceed by a change of variable  $z = \cos x$  in the left-hand side term of Eq. (A.1) and we denote  $T = \cos(t)$ :

$$\int_0^t dx \frac{x \sin(x/2)}{\sqrt{\cos x - \cos t}} = \int_T^1 dz \left[ \frac{\arccos z}{\sqrt{2(1+z)}} \right] \frac{1}{\sqrt{z-T}}. \quad (\text{A.2})$$

We write the right-hand side of Eq. (A.1) in the form

$$-2 \log \left( \cos \left( \frac{t}{2} \right) \right) = \log \left( \frac{2}{1+T} \right). \quad (\text{A.3})$$

From Ref. [99], the Abel's equation

$$\int_T^1 \frac{y(z) dz}{\sqrt{z-T}} = \frac{\pi}{\sqrt{2}} \log \left( \frac{2}{1+T} \right) \quad (\text{A.4})$$

has an unique solution for all  $-1 < X < 1$

$$y(z) = \frac{1}{\pi} \frac{\pi}{\sqrt{2}} \int_1^z \frac{du}{\sqrt{u-z}(1+z)} = \frac{\arccos z}{\sqrt{2(1+z)}}. \quad (\text{A.5})$$

Identification of the kernels of Eqs. (A.2) and (A.5) proves the identity (A.1).

The expression for  $\alpha_0$  from Eq. (3.13a) is found by setting  $t = \pi - \varepsilon$  in Eq. (A.2). Note that the obtained expression for  $\alpha_0$  from Eq. (3.13a) could also be deduced from the expression of the MFPT from Ref. [100].

### A.1.2 Simplified expressions for $\alpha_n, n \geq 1$

The solution of Eqs. (3.10a), (3.10b) is given in [92] in the form:

$$\alpha_n = \frac{1}{\sqrt{2}\pi} \int_0^{\pi-\varepsilon} dt \left( \frac{\partial}{\partial t} \int_0^t dx \frac{x \sin(x/2)}{\sqrt{\cos x - \cos t}} \right) [P_n(\cos t) + P_{n-1}(\cos t)], \quad n \geq 1. \quad (\text{A.6})$$

Using the identity (A.1), we show that

$$\alpha_n = \frac{1}{2} \int_0^{\pi-\varepsilon} dt \tan\left(\frac{t}{2}\right) [P_n(\cos t) + P_{n-1}(\cos t)], \quad n \geq 1. \quad (\text{A.7})$$

After the change of variable  $u = \cos t$ , the latter identity leads to

$$\alpha_n = \frac{1}{2} \int_{-\cos \varepsilon}^1 \frac{du}{1+u} [P_n(u) + P_{n-1}(u)], \quad n \geq 1. \quad (\text{A.8})$$

We now use the identity

$$\frac{\partial}{\partial x} \left( \frac{P_m(x) - P_{m-1}(x)}{m} \right) \Big|_{x=X} = \frac{P_m(X) + P_{m-1}(X)}{1+X}, \quad m \geq 1, \quad (\text{A.9})$$

which is valid for all  $X \in [-1, 1]$ , to obtain the announced result:

$$\alpha_n = \frac{(-1)^{n-1}}{2n} [P_n(\cos \varepsilon) + P_{n-1}(\cos \varepsilon)], \quad n \geq 1. \quad (\text{A.10})$$

### A.1.3 Simplified expression for $M_{nm}$

The expression for  $M_{nm}$  from Eq. (3.32) can be simplified using Mehler's integral representation (3.21):

$$M_{nm} = \frac{1}{2} \int_0^{\pi-\varepsilon} dt \left\{ \frac{\partial}{\partial t} [P_m(\cos t) - P_{m-1}(\cos t)] \right\} [P_n(\cos t) + P_{n-1}(\cos t)], \quad n \geq 1, \quad m \geq 1. \quad (\text{A.11})$$

The identity Eq. (A.9) then leads to the announced expression (3.33). Notice that the following matrix

$$S_{nm} = \sqrt{\frac{n}{m}} M_{nm}, \quad n \geq 1, \quad m \geq 1, \quad (\text{A.12})$$

is symmetric. The eigenvalues of  $S_{nm}$  are real, and so are the eigenvalues of  $M$ . In Sec. A.1.5 we show that the coefficients  $\alpha_n$  are given by an eigenvector of the infinite-dimensional matrix  $M$ .

### A.1.4 Perturbative expansion of $M_{nm}$

We first derive an alternative identity to Eq. (A.9). Let us define

$$A_n(x) \equiv \frac{\partial}{\partial x}(P_n(x) - P_{n-1}(x)), \quad n \geq 1. \quad (\text{A.13})$$

Using the recurrence formulas for Legendre polynomials, we obtain

$$A_n(x) = (P'_n(x) - P'_{n-2}(x)) - (P'_{n-1}(x) - P'_{n-2}(x)) \quad (\text{A.14})$$

$$= (2n - 1)P_{n-1}(x) - A_{n-1}(x) \quad (\text{A.15})$$

$$= \sum_{k=1}^n (-1)^{n-k} (2k - 1) P_{k-1}(x), \quad (\text{A.16})$$

where we used  $P_0(x) = 1$ ,  $P_1(x) = x$ , and  $A_1(x) = 1 = (2 - 1)P_0(x)$ .

Combining Eq. (A.11) and the identity (A.16) we obtain the announced result:

$$\begin{aligned} M_{nm} &= \int_0^{\pi-\varepsilon} dt \frac{\sin t}{2} A_m(\cos t) [P_n(\cos t) + P_{n-1}(\cos t)], \\ &= \sum_{k=1}^m (-1)^{n-k} (2k - 1) (K_{k-1, n-1} + K_{k-1, n}), \end{aligned} \quad (\text{A.17})$$

where the coefficients  $K_{k,n}$  are defined by

$$K_{k,n} \equiv \int_0^{\pi-\varepsilon} dt P_k(\cos t) P_n(\cos t) \frac{\sin t}{2}. \quad (\text{A.18})$$

In the leading order in  $\varepsilon \ll 1$ , Eq. (A.17) reads

$$M_{nm} = \sum_{k=1}^m (-1)^{n-k} (2k - 1) \left( \frac{\delta_{k-1, n-1}}{2n-1} + \frac{\delta_{k-1, n}}{2n+1} \right) + \mathcal{O}(\varepsilon). \quad (\text{A.19})$$

If  $m < n$ , it is straightforward to show that  $M_{nm} = \mathcal{O}(\varepsilon)$ . If  $m > n$ ,  $M_{nm} = \mathcal{O}(\varepsilon)$  as successive terms with  $k = n$  and  $k = n + 1$  cancel each other. The matrix  $M_{nm}$  ( $n, m \geq 1$ ) is thus diagonal at the first order in  $\varepsilon$ :

$$M_{nm} = \delta_{nm} + \mathcal{O}(\varepsilon). \quad (\text{A.20})$$

In order to get the next term in the series expansion in  $\varepsilon \ll 1$ , we write

$$M_{nm} - \delta_{nm} = -\frac{m}{2} \int_{-1}^{-\cos \varepsilon} \frac{1}{1+x} [P_m(x) + P_{m-1}(x)] [P_n(x) + P_{n-1}(x)] dx, \quad n \geq 1, \quad m \geq 1. \quad (\text{A.21})$$

We now focus on the term in the right-hand side of Eq. (A.21). In the vicinity of  $x = -1$ , the integrand of Eq. (A.21) expands into

$$\frac{1}{1+x} [P_m(x) + P_{m-1}(x)] [P_n(x) + P_{n-1}(x)] = \frac{nm(-1)^{n+m}}{8} (1+x) + \mathcal{O}(1+x). \quad (\text{A.22})$$

Notice that

$$\int_{-1}^{-\cos \varepsilon} (1+x) dx = \frac{\varepsilon^4}{8} + \mathcal{O}(\varepsilon^5). \quad (\text{A.23})$$

Substituting Eqs. (A.22) and (A.23) into Eq. (A.21) leads to

$$M_{nm} = \delta_{mn} + \frac{nm^2(-1)^{n+m}}{8} \varepsilon^4 + \mathcal{O}(\varepsilon^5). \quad (\text{A.24})$$



### A.1.5 Summation identities

Using the identities for sums of Legendre polynomials from Ref. [200], we derive the following equation

$$S \equiv \sum_{m=1}^{\infty} (-1)^{m-1} [P_m(\cos x) + P_{m-1}(\cos x)] [P_m(\cos \varepsilon) + P_{m-1}(\cos \varepsilon)] = 2, \quad 0 < x < \pi - \varepsilon. \quad (\text{A.25})$$

To prove this identity, we first use the Mehler's representation (3.21) for Legendre polynomials  $P_m(\cos \varepsilon)$  and  $P_{m-1}(\cos \varepsilon)$  to obtain

$$S = \frac{2}{\pi} \int_0^{\pi-\varepsilon} \frac{\sum_{m=1}^{\infty} [P_m(\cos x) + P_{m-1}(\cos x)] [\cos((m + \frac{1}{2})t) - \cos((m - \frac{1}{2})t)]}{\sqrt{(\cos(t) + \cos \varepsilon)(\cos x - \cos(t))}} dt, \quad 0 < x < \pi. \quad (\text{A.26})$$

We then use trigonometric identities and the series identity (3.25) to obtain the following integral representation

$$S = -\frac{2}{\pi} \int_x^{\pi-\varepsilon} dt \frac{2 \sin(\frac{t}{2}) \cos(\frac{t}{2})}{\sqrt{(\cos(t) + \cos \varepsilon)(\cos x - \cos(t))}}, \quad 0 < x < \pi - \varepsilon. \quad (\text{A.27})$$

The consecutive change of variables  $z = \cos(t)$  and  $U = \sqrt{(z + \cos \varepsilon)(\cos x - z)}$  leads to

$$S = \frac{2}{\pi} \int_{-\cos x}^{\cos x} \frac{dz}{\sqrt{(z + \cos \varepsilon)(\cos x - z)}} = 2, \quad (\text{A.28})$$

which proves the identity (A.25). We will use this identity in the following form:

$$\sum_{m=1}^{\infty} [P_m(\cos x) + P_{m-1}(\cos x)] m \alpha_m = 1, \quad 0 < x < \pi - \varepsilon. \quad (\text{A.29})$$

where  $\alpha_m$  are given by Eq. (3.13b).

#### A.1.5.1 Proof of the identity (3.65)

We write  $\alpha_m$  from Eq. (3.11b) and exchange the sum and the integral to obtain:

$$\sum_{m=1}^{\infty} 2m\alpha_m^2 = \frac{\sqrt{2}}{\pi} \int_0^{\pi-\varepsilon} dt \left( \frac{\partial}{\partial t} \int_0^t dx \frac{x \sin(x/2)}{\sqrt{\cos x - \cos t}} \right) \left( \sum_{m=1}^{\infty} [P_m(\cos t) + P_{m-1}(\cos t)] m \alpha_m \right). \quad (\text{A.30})$$

Using the identity (A.25) in the right-hand side of Eq. (A.30) and the representation (3.11a) of  $\alpha_0$  leads to the result of Eq. (3.65).

#### A.1.5.2 An eigenvector of the matrix $M$

We show that the coefficients  $\alpha_n$  (with  $n \geq 1$ ) form an eigenvector of the matrix  $M$ :

$$\sum_{m=1}^{\infty} M_{nm} \alpha_m = \alpha_n. \quad (\text{A.31})$$

We express  $M_{nm}$  through Eq. (3.33) and exchange the sum and the integral:

$$\sum_{m=1}^{\infty} M_{nm} \alpha_m = \frac{1}{2} \int_{-\cos(\varepsilon)}^1 \frac{1}{1+x} (P_n(x) + P_{n-1}(x)) \left( \sum_{m=1}^{\infty} [P_m(\cos t) + P_{m-1}(\cos t)] m \alpha_m \right) dx, \quad (\text{A.32})$$

from which the identity (A.25) leads to the announced identity (A.31).

## A.2 Spatially averaged variances

We denote by  $\overline{\mathbb{E}[\tau^n]}$  the spatial average of the  $n$ -th moment of the exit time:

$$\overline{\mathbb{E}[\tau^n]} \equiv \frac{1}{\pi} \int_{\mathbf{r}_0 \in \Omega} d\mathbf{r}_0 \mathbb{E}[\tau_{\mathbf{r}_0}^n], \quad (\text{A.33})$$

where  $d\mathbf{r}_0$  is the uniform measure over  $\Omega$ . Let us now consider the random variable  $\tau_\Omega$ , defined in Sec. 3.1.4.1 as the exit time of a particle started at a random starting position  $X$ . The  $n$ -th moment  $\tau_\Omega$  reads

$$\mathbb{E}[\tau_\Omega^n] \equiv \int_{\mathbf{r}_0 \in \Omega} d\mu(X = \mathbf{r}_0) \mathbb{E}[\tau_X^n], \quad (\text{A.34})$$

where  $d\mu(X = \mathbf{r}_0)$  is the probability density for  $X$  to be started at the position  $\mathbf{r}_0$ . If  $d\mu(X = \mathbf{r}_0) = d\mathbf{r}_0$  is the uniform probability distribution, we can identify Eqs. (A.33) and (A.34),  $\mathbb{E}[\tau_\Omega^n] = \overline{\mathbb{E}[\tau^n]}$ , and the variance of the random variable  $\tau_\Omega$  is

$$\text{Var}[\tau_\Omega] \equiv \left( \int_{\mathbf{r}_0 \in \Omega} d\mu(X = \mathbf{r}_0) \mathbb{E}[\tau_X^2] \right) - \left( \int_{\mathbf{r}_0 \in \Omega} d\mu(X = \mathbf{r}_0) \mathbb{E}[\tau_X] \right)^2 = \overline{\mathbb{E}[\tau^2]} - \overline{\mathbb{E}[\tau]}^2. \quad (\text{A.35})$$

Note that  $\text{Var}[\tau_\Omega]$  differs from the spatial average of the variance:  $\text{Var}[\tau_\Omega] \neq \overline{\text{Var}[\tau]} = \overline{\mathbb{E}[\tau^2]} - \overline{\mathbb{E}[\tau]}^2$ , because  $\overline{\mathbb{E}[\tau]^2} \neq \overline{\mathbb{E}[\tau^2]}$ .

## A.3 Convergence to an exponential distribution in the narrow-escape limit

### A.3.1 From the expression for the survival distribution

We recall that the expressions for  $(\alpha_n)$ ,  $n \geq 0$ , in the limit  $\varepsilon \ll 1$  are provided in Eqs. (3.44a)–(3.44b). We denote by  $\tilde{S}_e(t)$  the normalized single exponential distribution whose mean is equal to the GMFPT defined in Eq. (2.19). The Laplace transform of the distribution  $\tilde{S}_e^{(t)}$  is

$$S_e^{(p)} = \frac{\overline{\mathbb{E}[\tau]}}{1 + p \overline{\mathbb{E}[\tau]}}. \quad (\text{A.36})$$

We show that in the narrow-escape limit ( $\varepsilon \ll 1$ ), the averaged exit time distribution  $\overline{S^{(p)}} \approx a_0^{(p)}/2$  converges to  $S_e^{(p)}$ , as expected from Ref. [96]. Due to the divergence of the coefficient  $\alpha_0$  from Eq. (3.44a), the asymptotic expansion of Eq. (3.37a) at the first order in  $\varepsilon \ll 1$  reads

$$\frac{a_0^{(p)}}{2} = \alpha_0 \left[ \partial_r f_0^{[1]} \right]_{|r=1} \left[ \sum_{k=0}^{\infty} \left( p \left[ \partial_r f_0^{[1]} \right]_{|r=1} \alpha_0 \right)^k \right] + \mathcal{O}(\varepsilon). \quad (\text{A.37})$$

where  $\left[ \partial_r f_0^{[1]} \right]_{|r=1}$  is the first-order expansion in  $p \ll 1$  of  $\left[ \partial_r f_0^{(p)} \right]_{|r=1}$ . At the leading order in  $\varepsilon$ , the averaged survival probability over  $\Omega$  is

$$\overline{S^{(p)}} = \frac{\alpha_0 \left[ \partial_r f_0^{[1]} \right]_{|r=1}}{1 + \alpha_0 \left[ \partial_r f_0^{[1]} \right]_{|r=1}} + \mathcal{O}(\varepsilon). \quad (\text{A.38})$$

Combining Eqs. (3.7) and (3.37a), the GMFPT at the leading order in  $\varepsilon \ll 1$  is

$$\overline{\mathbb{E}[\tau]} = \alpha_0 \left[ \partial_r f_0^{[1]} \right]_{|r=1} + \mathcal{O}(\varepsilon). \quad (\text{A.39})$$

Combining Eqs. (A.36) and (A.38) leads to

$$\overline{S^{(p)}} = \overline{S_e^{(p)}} + \mathcal{O}(\varepsilon). \quad (\text{A.40})$$

This shows the convergence in law of the FPT distribution to an exponential distribution whose mean is the GMFPT as expected for the narrow-space limit [96].

### A.3.2 From the expression for the moments

Let us consider the random variable  $\tau_\Omega$ , defined in Sec. 3.1.4.1 as the exit time of a particle started at a random starting position. We provide a positive answer to the following question: does the distribution of  $\tau_\Omega$  converge to an exponential distribution in the limit  $\varepsilon \ll 1$ , even though the starting positions within the boundary layer contribute to the statistics of  $\tau_\Omega$ ? Using the recurrence scheme of Sec. 3.1.4.1, we verify that at the leading order in  $\varepsilon \ll 1$  the moments of  $\tau_\Omega$  are

$$\mathbb{E}[\tau_\Omega^n] = n! \left( \frac{\alpha_0}{2} \right)^n + \mathcal{O}(\ln(\varepsilon)^{n-1}), \quad (\text{A.41})$$

which leads to  $\mathbb{E}[\tau_\Omega^n] = n! \mathbb{E}[\tau_\Omega]$  ( $n \geq 1$ ) at the leading order in  $\varepsilon$ . The latter identity indicates that the FPT distribution of  $\tau_\Omega$  converges to an exponential distribution whose mean is the GMFPT defined by Eq. (3.15), as expected from Sec. A.3.1. We emphasize that the relation  $\mathbb{E}[\tau_\Omega^n] = n! \mathbb{E}[\tau_\Omega]$  ( $n \geq 1$ ), implies that the GMFPT characterizes the whole distribution of the exit time, in contrast to the statement of Eq. (18) from Ref. [104].

## A.4 Computational aspects

We summarize the numerical methods used to compute the FPT distribution.

(i) The Monte Carlo simulations rely on a sample of  $2 \cdot 10^6$  of random walks. This sample is obtained through 2 hours of computation on 200 CPUs (3.20 GHz Intel Core™ i7). The home-built C++ program uses an adaptative time step method so that the time steps are given by a decreasing function with the distance to the exit.

(ii) A finite element method realized in COMSOL Multiphysics v4.2 [201] allowed to greatly reduce the computational time. For instance, the FPT probability density shown in Fig.3.2(a),(b) required 5 to 10 minutes on a single CPU (2,66 GHz Intel Core™ i5).

(iii) The exact and approximate analytical solutions were computed in MATLAB and using the numerical Laplace inversion package INVLAP [202]. The series were truncated at  $N = 100$  terms and the computational time is of the order of a few minutes on a single CPU (2,66 GHz Intel Core™ i5).

# Surface-mediated diffusion

## Contents

<b>B.1 Radiative boundary condition on the MFPT</b> . . . . .	<b>177</b>
B.1.1 With an ejection distance ( $a > 0$ ) . . . . .	177
B.1.2 Without an ejection distance ( $a = 0$ ) . . . . .	179
<b>B.2 Quantity <math>\eta_d/D_2</math> is a mean first return time</b> . . . . .	<b>181</b>
B.2.1 Measure of correlations . . . . .	181
B.2.2 Interpretation of $\eta_d/D_2$ as a mean first passage time . . . . .	182
<b>B.3 Detailed calculations</b> . . . . .	<b>183</b>
B.3.1 Matrix elements $I_\varepsilon(n, m)$ in 3D . . . . .	183
B.3.2 Case of a $1/r^2$ velocity field . . . . .	183
<b>B.4 Mixed boundary condition: generalizations</b> . . . . .	<b>184</b>
B.4.1 The disk case (2D) . . . . .	184
B.4.2 Generalization to semi-reflecting targets . . . . .	186

## B.1 Radiative boundary condition on the MFPT

### B.1.1 With an ejection distance ( $a > 0$ )

We now check that the MFPT condition of Eq. (4.5) is compatible with the following boundary condition on the conditional probability [113]

$$\left. \frac{\partial p((r, \theta), t | \mathbf{x}, t')}{\partial r} \right|_{r=R} = -k p((r, \theta) | \mathbf{x}, t')|_{r=R}, \quad (\text{B.1})$$

where  $p(\mathbf{x}, t | \mathbf{x}', t')$  is the probability for a molecule to be at  $\mathbf{x}$  at time  $t$  provided that the molecule was at  $\mathbf{x}'$  at an earlier time  $t' < t$ . We denote the spatial coordinate  $\mathbf{x} = (r, \theta)$  if the molecule is in the bulk and  $\mathbf{x} = \theta$  if it is adsorbed on the surface.

We follow the standard method presented in [18]. The stochastic process under study is Markovian hence the conditional probabilities satisfy the Chapman-Kolmogorov equation, with  $t > s > t'$ ,

$$p(\mathbf{x}, t | \mathbf{x}', t') = \int_S d\nu(\mathbf{y}) p(\mathbf{x}, t | \mathbf{y}, s) p(\mathbf{y}, s | \mathbf{x}', t') + \int_0^\pi R^{d-1} d\nu(\theta) p(\mathbf{x}, t | \theta, s) p(\theta, s | \mathbf{x}', t'),$$

where  $S = (R, R_c) \times [0, \pi]$  and the measure  $d\nu$  is

$$d\nu_2(r, \theta) = 2r dr d\theta, \quad d\nu_2(\theta) = 2d\theta, \quad d\nu_3(r, \theta) = 2\pi r \sin\theta dr d\theta, \quad d\nu_3(\theta) = 2\pi \sin\theta d\theta.$$

Taking the derivative with respect to the intermediate time  $s$  leads to the expression

$$0 = \frac{\partial}{\partial s} p(\mathbf{x}, t | \mathbf{x}', t') = \int_S d\nu(\mathbf{y}) \frac{\partial p(\mathbf{x}, t | \mathbf{y}, s)}{\partial s} p(\mathbf{y}, s | \mathbf{x}', t') + \int_S d\nu(\mathbf{y}) p(\mathbf{x}, t | \mathbf{y}, s) \frac{\partial p(\mathbf{y}, s | \mathbf{x}', t')}{\partial s} \\ + \int_0^\pi d\nu(\theta) \frac{\partial p(\mathbf{x}, t | \theta, s)}{\partial s} p(\theta, s | \mathbf{x}', t') + \int_0^\pi d\nu(\theta) p(\mathbf{x}, t | \theta, s) \frac{\partial p(\theta, s | \mathbf{x}', t')}{\partial s} \quad (\text{B.2})$$

The backward Chapman-Kolmogorov equations read

$$\frac{\partial p(\mathbf{x}, t|\theta, s)}{\partial s} = -\frac{D_1}{R^2} \Delta_\theta p(\mathbf{x}, t|\theta, s) + \lambda \left\{ p(\mathbf{x}, t|\theta, s) - p(\mathbf{x}, t|R-a, \theta, s) \right\}, \quad (\text{B.3})$$

$$\frac{\partial p(\mathbf{x}, t|(r, \theta), s)}{\partial s} = -D_2 \Delta_{(r, \theta)} p(\mathbf{x}, t|(r, \theta), s) - v(r) \nabla p(\mathbf{x}, t|(r, \theta), s). \quad (\text{B.4})$$

The forward Chapman-Kolmogorov equations are

$$\begin{aligned} \frac{\partial p(\theta, s|\mathbf{x}', t')}{\partial s} = & +\frac{D_1}{R^d} \Delta_\theta p(\theta, s|\mathbf{x}', t') - \lambda p(\theta, s|\mathbf{x}', t') - D_2 \frac{\partial p((r, \theta), s|\mathbf{x}', t')}{\partial r} \Big|_{r=R} \\ & + v(R) p((R, \theta), s|\mathbf{x}', t'), \end{aligned} \quad (\text{B.5})$$

$$\begin{aligned} \frac{\partial p(\mathbf{y}, s|\mathbf{x}', t')}{\partial s} = & D_2 \Delta_{\mathbf{y}} p(\mathbf{y}, s|\mathbf{x}', t') - \nabla (v(r)p(\mathbf{y}, s|\mathbf{x}', t')) \\ & + \lambda \left( \frac{R}{R-a} \right)^{d-1} \delta^d(\mathbf{r} - (R-a, \theta)) p(\theta, s|\mathbf{x}', t'). \end{aligned} \quad (\text{B.6})$$

The terms in Eqs. (B.5) and (B.6) are justified as follows: (i)  $-\lambda p(\theta, s|\mathbf{x}', t')$  corresponds to a constant rate of desorption from the surface to the bulk; (ii)  $-D_2 \partial_r p((r, \theta), s|\mathbf{x}', t')$  is the flux into the surface due to diffusion; (iii)  $v(R) p((R, \theta), s|\mathbf{x}', t')$  is the flux into the surface due to the drift (by convention,  $v(R) > 0$  for a velocity drift field oriented towards to the exterior); (iv)  $\lambda [R/(R-a)]^{d-1} \delta^d(\mathbf{r} - (R-a, \theta)) p(\theta, s|\mathbf{x}', t')$  corresponds to the flux into the bulk due to the desorption from the surface and the ejection at a distance  $a$  ( $\delta$  being the Dirac delta function).

For convenience, we will use the shorthand notations  $p(\mathbf{y}, s|\mathbf{x}', t') \equiv p(\mathbf{y})$ ,  $p(\mathbf{x}, t|\mathbf{y}, s) \equiv \bar{p}(\mathbf{y})$  and  $p(\theta, s|\mathbf{x}', t') \equiv p(\theta)$ . Substituting the Chapman-Kolmogorov Eqs. (B.3 – B.6) into Eq. (B.2) leads to the following equation

$$\begin{aligned} 0 = & \int_S d\nu(\mathbf{y}) [-D_2 \Delta_{\mathbf{y} \in S} \bar{p}(\mathbf{y})] p(\mathbf{y}) \\ & + \int_S d\nu(\mathbf{y}) \bar{p}(\mathbf{y}) \left[ D_2 \Delta_{\mathbf{y} \in S} p(\mathbf{y}) + \lambda \left( \frac{R}{R-a} \right)^{d-1} \delta^d(\mathbf{r} - (R-a, \theta)) p(\theta) \right] \\ & + \int_0^\pi R^{d-1} d\nu(\theta) \left[ -\frac{D_1}{R^d} \Delta_\theta \bar{p}(\theta) + \lambda \{ \bar{p}(\theta, s) - \bar{p}(R-a, \theta) \} \right] p(\theta, s) \\ & + \int_0^\pi R^{d-1} d\nu(\theta) \bar{p}(\theta) \left[ \frac{D_1}{R^d} \Delta_\theta p(\theta) - \lambda p(\theta) - D_2 \frac{\partial p(r, \theta)}{\partial r} \Big|_{r=R} \right]. \end{aligned}$$

One notices that

$$\int_S d\nu(\mathbf{y}) \left( \frac{R}{R-a} \right)^{d-1} \delta^d(\mathbf{r} - (R-a, \theta)) \bar{p}(r, \theta) p(\theta) + \int_0^\pi R^{d-1} d\nu(\theta) \bar{p}(R-a, \theta) p(\theta) = 0,$$

and that the four terms proportional to  $\lambda$  vanish. Two terms with angular Laplacians also cancel each other due to the hermiticity of the angular diffusion operator:

$$\int_0^\pi d\nu(\theta) \Delta_\theta \bar{p}(\theta) p(\mathbf{y}) - \int_0^\pi d\nu(\theta) \Delta_\theta p(\theta) \bar{p}(\mathbf{y}) = 0.$$

The divergence theorem yields the integral over the frontier  $\partial S$  of the annulus  $S$ :

$$0 = D_2 \int_{\partial S} d\nu(\theta) \left[ \frac{\partial p(r, \theta)}{\partial r} \Big|_{r=R} \bar{p}(r, \theta) - \frac{\partial \bar{p}(r, \theta)}{\partial r} \Big|_{r=R} p(r, \theta) - \frac{\partial p(r, \theta)}{\partial r} \Big|_{r=R} \bar{p}(\theta, s) \right].$$

This equality can be satisfied only if:

$$\frac{\partial \bar{p}((r, \theta), s)}{\partial r} \Big|_{r=R} p((R, \theta), s) = \frac{\partial p((r, \theta), s)}{\partial r} \Big|_{r=R} \left[ \bar{p}((r, \theta), s) - \bar{p}(\theta, s) \right]. \quad (\text{B.7})$$

Inserting the forward boundary condition (B.1) into Eq. (B.7) gives the boundary condition on the backward probability distribution

$$\frac{\partial p(\mathbf{x}, t|(r, \theta), s)}{\partial r} \Big|_{r=R} = k \left[ p(\mathbf{x}, t|\theta, s) - p(\mathbf{x}, t|(r, \theta), s) \right] \Big|_{r=R}.$$

Integrating over the space and time variables  $\mathbf{x}$  and  $t$ , we obtain the boundary condition for the MFPT:

$$\frac{\partial t_2}{\partial r} \Big|_{r=(R, \theta)} = k \{ t_1(\theta) - t_2(R, \theta) \} \quad (0 \leq \theta \leq \pi),$$

which identifies with Eq. (4.5).

### B.1.2 Without an ejection distance ( $a = 0$ )

Using a standard formalism of backward equations [18], we derive the diffusive equations (B.15, B.16) and the appropriate boundary conditions (5.6, 5.7) satisfied by the MFPT, which we proceed to solve in the next section.

We define  $p((r, \theta, \phi), s | (\mathbf{x}', \phi'), t')$  (resp.  $p((\theta, \phi), s | \mathbf{x}', t')$ ) as the probability for a particle located at time  $t'$  at  $\mathbf{x}'$  – with either  $\mathbf{x}' = r', \theta'$  into the bulk or  $\mathbf{x}' = \theta'$  on the sphere – to reach at time  $s > t'$  the point  $(r, \theta, \phi)$  in the bulk (resp. the point  $(\theta, \phi)$  on the surface). In what follows, we omit the azimuthal coordinates by referring to probabilities averaged over the initial and final azimuthal angles

$$p((r, \theta), s | \mathbf{x}', t') \equiv \int_0^{2\pi} d\phi \int_0^{2\pi} d\phi' p((r, \theta, \phi), s | (\mathbf{x}', \phi'), t').$$

For convenience, in this section we will use the shorthand notations

$$p((r, \theta), s | \mathbf{x}', t') \equiv p(r, \theta), \quad p(\theta, s | \mathbf{x}', t') \equiv p(\theta). \quad (\text{B.8})$$

Conversely, we define the conditional probabilities  $p(\bar{\mathbf{x}}, \bar{t} | (r, \theta), s) \equiv \bar{p}(r, \theta)$  and  $p(\bar{\mathbf{x}}, \bar{t} | \theta, s) \equiv \bar{p}(\theta)$ , with  $\bar{t} > s$  and  $\bar{\mathbf{x}} = (\bar{r}, \bar{\theta})$  in the bulk or  $\bar{\mathbf{x}} = \bar{\theta}$  on the sphere.

For the process under study the conditional probability  $p(r, \theta)$  satisfies the *forward* diffusion equations, for all  $s > t'$ , [130],

$$\frac{\partial p(r, \theta)}{\partial s} = D_2 \Delta_{(r, \theta)} p(r, \theta) \quad (\text{B.9})$$

$$\frac{\partial p(\theta)}{\partial s} = \frac{D_1}{R^2} \Delta_\theta p(\theta) - \lambda p(\theta) + k D_2 p(R, \theta). \quad (\text{B.10})$$

Each term in the right-hand side of Eq. (B.10) has a straightforward physical interpretation; these are (from left to right) (i) the diffusion within the surface state; (ii) desorption events with a constant rate  $\lambda$ ; (iii) adsorption events with a success rate quantified by  $k$  ([112]).

Equivalently to Eqs. (B.9) and (B.10), the conditional probabilities satisfy the backward equations, for all  $t > s'$ , [18]

$$\frac{\partial \bar{p}(r, \theta)}{\partial s} = -D_2 \Delta_{(r, \theta)} \bar{p}(r, \theta). \quad (\text{B.11})$$

$$\frac{\partial \bar{p}(\theta)}{\partial s} = -\frac{D_1}{R^2} \Delta_\theta \bar{p}(\theta) + \lambda \left\{ \bar{p}(\theta) - \bar{p}(R, \theta) \right\} \quad (\text{B.12})$$

These backward diffusion equations are commonly used to determine first passage time observables [113].

We define  $t_1(\theta)$  as the MFPT for particles started on the sphere at the angle  $\theta$ , and  $t_2(r, \theta)$  stands for the MFPT for particles started at the bulk point  $(r, \theta)$  (the second angular coordinate

$\phi$  is irrelevant due to the symmetry and thus ignored). The MFPTs are expressed in terms of the conditional probabilities through the relations [18]

$$t_1(\theta) \equiv \int_0^\infty dt \left( \int_0^\pi 2\pi R^2 \sin \tilde{\theta} d\tilde{\theta} p(\tilde{\theta}, t|\theta, 0) + \int_\Omega 2\pi r^2 dr \sin \tilde{\theta} d\tilde{\theta} p(r, \tilde{\theta}, t|\theta, 0) \right), \quad (\text{B.13})$$

$$t_2(r, \theta) \equiv \int_0^\infty dt \left( \int_0^\pi 2\pi R^2 \sin \tilde{\theta} d\tilde{\theta} p(\tilde{\theta}, t|r, \theta, 0) + \int_\Omega 2\pi r^2 dr \sin \tilde{\theta} d\tilde{\theta} p(r, \tilde{\theta}, t|r, \theta, 0) \right), \quad (\text{B.14})$$

where  $\Omega \equiv (0, R) \times (0, 2\pi)$ .

Substituting the latter relations (B.13) and (B.14) into Eqs. (B.11,B.12), one can show that the MFPTs satisfy the set of equations

$$\frac{D_1}{R^2} \Delta_\theta t_1(\theta) + \lambda (t_2(R, \theta) - t_1(\theta)) = -1 \quad (\varepsilon < \theta < \pi), \quad (\text{B.15})$$

$$D_2 \left( \Delta_r + \frac{\Delta_\theta}{r^2} \right) t_2(r, \theta) = -1 \quad ((r, \theta) \in \Omega). \quad (\text{B.16})$$

In the next section we specify the appropriate boundary conditions for the MFPT.

In order to justify the form of the radiative B.C. (5.7), we determine the backward B.C. on the probability distribution from a well-known forward B.C. For the process defined in Sec. 5.1, the forward B.C. equation on the probability distribution is [130]

$$D_2 \frac{\partial p(r, \theta)}{\partial r} \Big|_{r=R} = -k D_2 p(R, \theta) + \lambda p(\theta). \quad (\text{B.17})$$

Since the stochastic process under study is Markovian, one obtains the following Chapman-Kolmogorov equation on the conditional probabilities, for  $\bar{t} > s > t'$ ,

$$p(\bar{\mathbf{x}}, \bar{t}|\mathbf{x}', t') = \int_0^\pi \int_0^R 2\pi r^2 dr \sin \theta d\theta \bar{p}(r, \theta) p(r, \theta) + \int_0^\pi 2R^2 \pi \sin \theta d\theta \bar{p}(\theta) p(\theta). \quad (\text{B.18})$$

Taking the derivative with respect to the intermediate time  $s$  of the above relation leads to the identity

$$\begin{aligned} & \int_0^\pi \int_0^R 2\pi r^2 \sin \theta d\theta dr \left( \frac{\partial p(r, \theta)}{\partial s} \bar{p}(r, \theta) + p(r, \theta) \frac{\partial \bar{p}(r, \theta)}{\partial s} \right) \\ & + \int_0^\pi 2\pi R^2 \sin \theta d\theta \left( \frac{\partial p(\theta)}{\partial s} \bar{p}(\theta) + \frac{\partial \bar{p}(\theta)}{\partial s} p(\theta) \right) = 0. \end{aligned}$$

The next step is to substitute diffusion Eqs. (B.9 – B.11) into the last relation. The two terms with the angular Laplace operators cancel each other due to its hermiticity

$$\int_0^\pi \sin \theta d\theta (\Delta_\theta \bar{p}(\theta) p(\theta) - \Delta_\theta p(\theta) \bar{p}(\theta)) = 0.$$

The divergence theorem applied on the bulk Laplacian  $\Delta_{(r, \theta)}$  and the backward equations (B.11,B.12) yield the following relation over the sphere surface

$$\begin{aligned} 0 = \int_0^\pi 2R^2 \pi \sin \theta d\theta \left( D_2 \frac{\partial p(r, \theta)}{\partial r} \Big|_R \bar{p}(r, \theta) - D_2 \frac{\partial \bar{p}(r, \theta)}{\partial r} \Big|_R p(r, \theta) + \lambda \left\{ \bar{p}(\theta) - \bar{p}(R, \theta) \right\} p(\theta) \right. \\ \left. + \left\{ -\lambda p(\theta) + k D_2 p(R, \theta) \right\} \bar{p}(\theta) \right), \end{aligned}$$

which is satisfied only if

$$D_2 \frac{\partial \bar{p}(r, \theta)}{\partial r} \Big|_R p(R, \theta) = D_2 \frac{\partial p(r, \theta)}{\partial r} \Big|_R \bar{p}(R, \theta) - \lambda \bar{p}(R, \theta) p(\theta) + k D_2 p(R, \theta) \bar{p}(\theta). \quad (\text{B.19})$$

Insertion of the forward B.C. (B.17) into Eq. (B.19) gives the B.C. on the backward probability distribution

$$\frac{\partial p(\bar{\mathbf{x}}, \bar{t}|(r, \theta), s)}{\partial r} \Big|_{r=R} = k \{ p(\bar{\mathbf{x}}, \bar{t}|\theta, s) - p(\bar{\mathbf{x}}, \bar{t}|(r, \theta), s) \} \Big|_R. \quad (\text{B.20})$$

We then integrate Eq. (B.20) over the space and time variables  $\mathbf{x}$  and  $t$  according to Eqs. (B.13) and (B.14) to obtain the B.C. on the MFPT

$$\frac{\partial t_2}{\partial r} \Big|_{r=(R, \theta)} = k \{ t_1(\theta) - t_2(R, \theta) \} \quad (\varepsilon \leq \theta \leq \pi),$$

which identifies with Eq. (5.7).

The diffusion equation and the boundary condition for the occupation probability distribution in the bulk appear at first sight to be different in [130] and [112]. In this section, we show that these two sets of equations are in agreement and lead to the same radiative boundary condition (5.7) for the MFPT. In [112] we defined a different set of equations for the conditional probability distribution to include a radial ejection distance  $a$  after each desorption event, in the presence of a velocity field. With the shorthand notations of Sec. 5.2.1, the forward advection-diffusion equation of [112] reads

$$\frac{\partial p(r, \theta)}{\partial r} \Big|_R = -k p(R, \theta) + \frac{v(R)}{D_2} p(R, \theta), \quad (\text{B.21})$$

$$\frac{\partial p(r, \theta)}{\partial s} = D_2 \left( \Delta_{(r, \theta)} + \frac{v(r)}{D_2 r} \right) p(r, \theta) + \lambda \left( \frac{R}{R-a} \right)^2 \delta^3(\mathbf{r} - (R-a, \theta)) p(\theta), \quad (\text{B.22})$$

where  $v(r)$  is a radial velocity field positive for an outward drift. The other diffusion equations on the conditional probabilities are the same as in [112].

Notice that Eq. (B.21) does not involve the desorption rate  $\lambda$ . However there is no contradiction with Eq. (B.17), as Eq. (B.21) (without drift) leads the same backward boundary Eq. (B.20) as long the appropriate limit for  $a = 0$  in the Dirac function in Eq. (B.22) is

$$\int_0^R \left( \frac{R}{R-a} \right)^2 \delta(r - (R-a, \theta)) p(r, \theta) r^2 dr \xrightarrow{a \rightarrow 0} R^2 p(R, \theta),$$

It can be proved that this condition is required from normalization of the probability density.

## B.2 Quantity $\eta_d/D_2$ is a mean first return time

### B.2.1 Measure of correlations

In this section we quantify the spatial correlations between the starting and ending points of a bulk excursion. We then provide the range of values for  $k$  in which the spatial correlations are negligible. The probability density  $\Pi(\theta)$  for a particle initially started from the surface state at the angle  $\theta_0 = 0$ ,  $\phi_0 = 0$  to first return on the surface to any point  $(\theta, \phi)$  (with  $\phi \in [0, 2\pi]$ ) is [112]

$$\Pi(\theta) = \frac{\sin \theta}{2} \left( 1 + \sum_{n=1}^{\infty} \frac{2n+1}{1 + \frac{n}{kR}} P_n(\cos \theta) \right). \quad (\text{B.23})$$

The cumulative probability distribution for the relocation angle  $\theta \in [0, \pi]$  is the integral of the probability density

$$F(\theta) \equiv \frac{1}{2} \int_{-\pi}^{\theta} \Pi(\theta') \sin \theta' d\theta'. \quad (\text{B.24})$$

By analogy with the Kolmogorov-Smirnov test [203], we propose to measure the spatial correlations between the starting and ending points of a bulk excursion by the norm

$$N_K \equiv \max_{\theta \in [0, \pi]} |\delta F(\theta)|, \quad (\text{B.25})$$



with

$$\delta F(\theta) \equiv F(\theta) - F_u(\theta) = \frac{1}{2} \sum_{n=1}^{\infty} \frac{P_{n-1}(\cos \theta) - P_{n+1}(\cos \theta)}{1 + \frac{n}{kR}}, \quad (\text{B.26})$$

and  $F_u(\theta) = (1 - \cos \theta)/2$  is the cumulative distribution for uncorrelated random relocation on the sphere. This leads a correlation angle  $\Theta$  which is defined as the solution of the equation  $\delta F(\Theta) = N_K$ .

As shown on Fig. B.1, the spatial correlation is negligible ( $N_K \ll 1, \Theta \approx 1$ ) as long as  $kR < 1$ . In particular for the reference values  $kR = 6.4 \cdot 10^{-4}$ ,  $6.4 \cdot 10^{-3}$ ,  $6.4 \cdot 10^{-2}$  used in [130], the norm  $N_K$  is smaller than 0.05 and the correlation length is nearly constant at  $\Theta \approx 1.2$ .

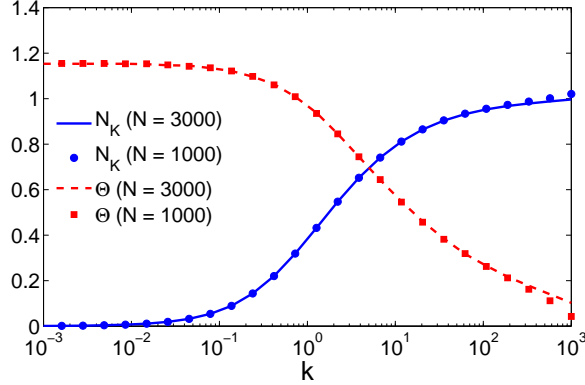


Figure B.1: (Color online). The norm  $N_K$  (blue solid line and circles) and the correlation angle  $\Theta$  in radians (red dashed line and squares) as functions of the adsorption coefficient  $k$ , for the truncation size  $N = 3000$  (lines) and  $N = 1000$  (symbols).

## B.2.2 Interpretation of $\eta_d/D_2$ as a mean first passage time

We consider the probability density  $\Pi(\tilde{\theta}|\theta)$  for a molecule initially at the bulk point  $(R - a, \theta)$  to first reach the surface  $r = R$  at the angle  $\tilde{\theta}$ . The mean duration of this Brownian path is denoted  $t_c(\tilde{\theta}|\theta)$ .

The MFPT  $t_2(R - a, \theta)$  to reach the target can be expressed as the averaged sum of the MFPT to reach a point  $(R, \tilde{\theta})$  on the surface with the MFPT to reach the target from this point of the surface, the probability density for the first hitting point  $(R, \tilde{\theta})$  being the harmonic measure  $\Pi(\tilde{\theta}|\theta)$  :

$$t_2(R - a, \theta) = \int_0^\pi \left( t_c(\tilde{\theta}|\theta) + t_1(\tilde{\theta}) \right) \Pi(\tilde{\theta}|\theta) d\mu_d(\tilde{\theta}). \quad (\text{B.27})$$

In 2D and in the general case considered in Sec. 4.2, the probability density  $\Pi(\tilde{\theta}|\theta)$  is

$$\Pi(\tilde{\theta}|\theta) = 1 + 2 \sum_{n=1}^{\infty} (X_n + 1) \cos(n(\tilde{\theta} - \theta)), \quad (\text{B.28})$$

where  $X_n$  is given by Eq. (4.27). Substitution of this expression in Eq. (B.27) leads to

$$t_2(R - a, \theta) = \langle t_1 \rangle + \frac{1}{\pi} \int_0^\pi t_c(\tilde{\theta}|\theta) \Pi(\tilde{\theta}|\theta) d\tilde{\theta} + \frac{2}{\pi} \sum_{n=1}^{\infty} (X_n + 1) \int_0^\pi \cos(n(\tilde{\theta} - \theta)) t_1(\tilde{\theta}) d\tilde{\theta}. \quad (\text{B.29})$$

Identification with Eq. (4.38) gives

$$\frac{\eta_d}{D_2} = \frac{1}{\pi} \int_0^\pi t_c(\tilde{\theta}|\theta) \Pi(\tilde{\theta}|\theta) d\tilde{\theta} = \frac{1}{\pi} \int_0^\pi t_c(\tilde{\theta}|0) \Pi(\tilde{\theta}|0) d\tilde{\theta}, \quad (\text{B.30})$$

► The latter Eq. (B.30) shows that  $\eta_d/D_2$  is the MFPT to the circle of radius  $R$ .

In particular, it can be shown that in the 2D case of Sec. 4.3.1.1

$$\Pi(\tilde{\theta}|\theta)t_c(\tilde{\theta}|\theta) = \frac{R^2}{4D_2} (1 - (r/R)^2) \left( 1 + \sum_{n=1}^{\infty} \frac{(r/R)^n}{2(1+n)} \cos(n(\theta - \tilde{\theta})) \right). \quad (\text{B.31})$$

One can verify that the substitution of this expression into Eq. (B.30) leads to the well known result of Eq. (4.50),  $\eta_2 = R^2(1 - x^2)/4$ .

The argument leading to Eq. (B.30) can be extended to the 3D case with the following expression for the probability density:

$$\Pi(\tilde{\theta}|\theta) = 1 + \sum_{n=1}^{\infty} (2n+1)(X_n+1)P_n(\cos \tilde{\theta})P_n(\cos \theta). \quad (\text{B.32})$$

## B.3 Detailed calculations

### B.3.1 Matrix elements $I_\varepsilon(n, m)$ in 3D

The matrix elements  $I_\varepsilon(n, m)$  in 3D were computed in [204]. An explicit formula for non-diagonal elements ( $m \neq n$ ) is given in Table 4.2. In turn, the diagonal elements  $I_\varepsilon(n, n)$  can be expressed as

$$I_\varepsilon(n, n) = -P_n(u) \frac{uP_n(u) - P_{n-1}(u)}{n+1} + \frac{F_n(u) + 1}{2n+1}, \quad u = \cos \varepsilon,$$

through the function  $F_n(u)$ , for which the explicit representation was derived in [204]

$$\begin{aligned} F_n(u) &= u[P_n^2(u) + 2P_{n-1}^2(u) + \dots + 2P_1^2(u) + P_0(u)] \\ &\quad - 2P_n(u)P_{n-1}(u) - 2P_{n-1}(u)P_{n-2}(u) - \dots - 2P_1(u)P_0(u) + u \\ &= \sum_{k=1}^n [2(u-1)P_k^2(u) + [P_k(u) - P_{k-1}(u)]^2] - (u-1)P_n^2(u) + (u-1)P_0^2(u) + u. \end{aligned} \quad (\text{B.33})$$

One can also check that this function satisfies the recurrence relations

$$F_n(u) = F_{n-1}(u) + u[P_n^2(u) + P_{n-1}^2(u)] - 2P_n(u)P_{n-1}(u), \quad F_0(u) = u. \quad (\text{B.34})$$

that simplifies its numerical computation. Note that  $F_n(\pm 1) = F_{n-1}(\pm 1) = \dots = \pm 1$ .

### B.3.2 Case of a $1/r^2$ velocity field

We now examine the 3D case of a radial  $1/r^2$  velocity field  $\vec{v}(r)$ , which is characterized by the dimensionless parameter  $\mu$ :

$$\vec{v}(r) = -\frac{\mu D_2 R}{r^3} \vec{r}. \quad (\text{B.35})$$

The function  $\hat{f}$  is expressed as

$$\hat{f}(r) = -\frac{r^2}{6} - \frac{rR\mu}{6} + \frac{R^2\mu^2}{6} e^{-\mu R/r} \text{Ei}(\mu R/r), \quad (\text{B.36})$$

where  $\text{Ei}(z)$  is the exponential integral:

$$\text{Ei}(z) = \int_{-\infty}^z \frac{e^x}{x} dx.$$

The function  $f_0$  is

$$f_0(r) = \frac{1 - e^{-\mu R/r}}{\mu} \quad (\text{B.37})$$

(this particular choice of the additive and multiplicative constants ensures that  $R/r$  is retrieved in the limit  $\mu \rightarrow 0$ ). Radial functions  $f_n(r)$  are found as products of powers and confluent hypergeometric functions  ${}_1F_1$  of  $r$ :

$$f_n(r) = r^n {}_1F_1(-n, -2n, -\mu R/r) \quad (n > 0), \quad (\text{B.38})$$

$$f_{-n}(r) = r^{-n-1} {}_1F_1(n+1, 2n+2, -\mu R/r) \quad (n > 0). \quad (\text{B.39})$$

For  $n = 0$ , this expression is reduced to  $e^{-\mu R/r}$ . In the limit  $\mu \rightarrow 0$ , the above functions reduce to  $r^n$  and  $r^{-n-1}$  from the earlier case  $\mu = 0$ . On the one hand we have

$$\begin{aligned} \partial_r f_n(r) &= nr^{n-1} {}_1F_1(-n+1, -2n, -\mu R/r) \quad (n > 0), \\ \partial_r f_{-n}(r) &= -(n+1)r^{-n-2} {}_1F_1(n+2, 2n+2, -\mu R/r) \quad (n > 0), \end{aligned}$$

from which

$$\frac{\partial_r f_n(r)}{\partial_r f_{-n}(r)} = -\frac{n}{n+1} r^{2n+1} \frac{{}_1F_1(-n+1, -2n, -\mu R/r)}{{}_1F_1(n+2, 2n+2, -\mu R/r)}. \quad (\text{B.40})$$

On the other hand we have

$$\begin{aligned} \partial_r \hat{f}(r) &= \frac{1}{6} \left[ \frac{(\mu R)^3}{r^2} e^{-\mu R/r} \text{Ei}(\mu R/r) - \frac{(\mu R)^2}{r} - (\mu R) - 2r \right], \\ \partial_r f_0(r) &= -\frac{R}{r^2} e^{-\mu R/r}, \end{aligned}$$

from which

$$\frac{\partial_r \hat{f}(r)}{\partial_r f_0(r)} = -\frac{\mu}{6} \left[ (\mu R)^2 \text{Ei}(\mu R/r) - e^{\mu R/r} [\mu R r + r^2 - 2r^3/(\mu R)] \right]. \quad (\text{B.41})$$

This last expression is needed to compute the quantities  $\eta_d$  and  $X_n$ .

## B.4 Mixed boundary condition: generalizations

### B.4.1 The disk case (2D)

In 2D, the diffusion equations on the MFPT are identical to Eqs. (B.15, B.16) provided that Laplace operators is now defined for  $d = 2$  in Eq. (2.32). The eigenfunctions  $V_n(\theta)$  and eigenvalues  $\rho_n$  of the angular Laplace operator  $\Delta_\theta$  become

$$V_n(\theta) = \sqrt{2} \cos n\theta, \quad \rho_n = n^2 \quad (n \geq 0). \quad (\text{B.42})$$

The inner scalar product (4.17) is replaced by

$$(f, g) \rightarrow \langle f|g \rangle_\varepsilon \equiv \frac{1}{\pi} \int_\varepsilon^\pi f(\theta)g(\theta)d\theta. \quad (\text{B.43})$$

In Table B.1, we summarize the expressions for the surface MFPT  $g_\varepsilon(\theta)$  and for the matrix elements  $K_{mn}^{(\varepsilon)}$  and  $I_{mn}^{(\varepsilon)}$  which replace those from Table 5.1.

The method of derivation and the remaining quantities are not modified. In particular, Eq. (5.34) for the MFPT  $t_1(\theta)$ , Eq. (5.35) for the surface GMFPT  $\langle t_1 \rangle$  and Eq. (5.41) for the lower

$V_n(\theta)$	$\sqrt{2} \cos(n\theta)$
$g_\varepsilon(\theta)$	$\frac{1}{2}(\theta - \varepsilon)(2\pi - \varepsilon - \theta)$
$\langle g_\varepsilon   1 \rangle_\varepsilon \equiv \langle g_\varepsilon \rangle_\varepsilon$	$\frac{1}{3\pi}(\pi - \varepsilon)^3$
$\xi_n \ (n \geq 1)$	$-\frac{\sqrt{2}}{\pi} \{(\pi - \varepsilon) \cos(n\varepsilon) + \sin(n\varepsilon)/n\}$
$K_{00}^{(\varepsilon)}$	$(\pi - \varepsilon)/\pi$
$K_{n0}^{(\varepsilon)} \ (n \geq 1)$	$-\frac{\sqrt{2}}{n\pi} \sin(n\varepsilon)$
$K_{nn}^{(\varepsilon)} \ (n \geq 1)$	$\frac{1}{\pi} \left( \pi - \varepsilon - \frac{\sin(2n\varepsilon)}{2n} \right)$
$K_{nm}^{(\varepsilon)} \ n, m \geq 1, m \neq n$	$\frac{1}{\pi} \left( \frac{\sin((m-n)\varepsilon)}{m-n} + \frac{\sin((m+n)\varepsilon)}{m+n} \right)$
$I_{nn}^{(\varepsilon)} \ (n \geq 1)$	$\frac{1}{\pi} \left( \pi - \varepsilon + \frac{\sin 2n\varepsilon}{2n} \right)$
$I_{nm}^{(\varepsilon)} \ m, n \geq 1, m \neq n$	$\frac{2}{\pi} \frac{\cos(n\varepsilon) \frac{\sin(m\varepsilon)}{m} - \cos(m\varepsilon) \frac{\sin(n\varepsilon)}{n}}{n^2 - m^2} m^2$

Table B.1: Summary for the 2D case of the quantities involved in the computation of the vector  $\xi$  and the matrices  $Q$  and  $M$  in Eqs. (5.29, 5.31) that determine the Fourier coefficients  $d_n$  of  $t_1(\theta)$  according to Eq. (5.33).

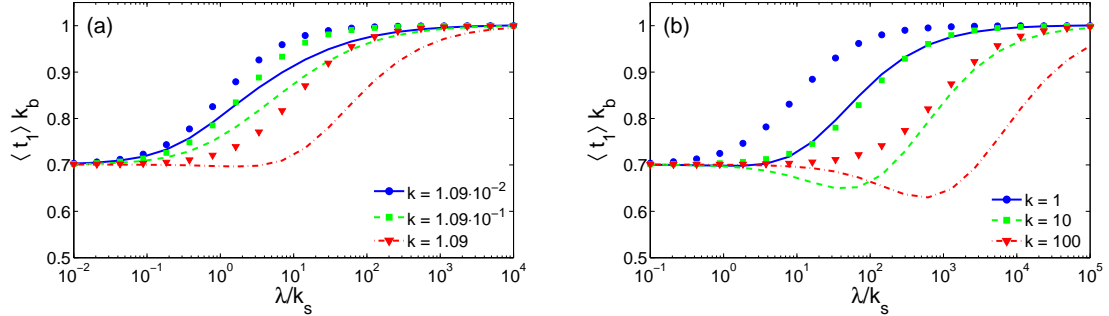


Figure B.2: The surface GMFPT  $\langle t_1 \rangle$ , defined as the mean first passage time averaged along the circle, as a function of the desorption rate  $\lambda$ , for  $\varepsilon = 0.02$ ,  $D_2/D_1 = 1$ , and (a)  $kR = 1.09 \cdot 10^{-2}$ ,  $1.09 \cdot 10^{-1}$ ,  $1.09$  (corresponding to  $\alpha = 0.1k_b, k_b, 10k_b$ ) and (b)  $kR = 1, 10, 100$ . Series are truncated at  $N = 3 \cdot 10^4$ .

bound on the diffusion coefficient ratio  $(D_2/D_1)_{\text{low}}$  are applicable for the disk. In turn, the asymptotic relations on the exit time (5.2, 5.3) are modified

$$t_s = \langle t_1 \rangle_{\lambda=0} = \frac{R^2}{D_1} \frac{(\pi - \varepsilon)^3}{3\pi}, \quad (\text{B.44})$$

$$t_b = \langle t_1 \rangle_{\lambda \rightarrow \infty} \simeq \frac{R^2}{D_2} \left[ \ln(2/\varepsilon) + O(1) \right] \quad (\text{B.45})$$

that leads to the following expression for the upper bound on the diffusion coefficients

$$\left( \frac{D_2}{D_1} \right)_{\text{up}} = \frac{3\pi \ln(2/\varepsilon)}{(\pi - \varepsilon)^3} + O(1). \quad (\text{B.46})$$

Figure B.2 illustrates the fact that the surface GMFPT is an optimizable function of the desorption rate  $\lambda$  in the range of parameters represented on Fig. B.3.

Figure B.3: The regions of optimality for the surface GMFPT  $\langle t_1 \rangle$ , defined as the mean first passage time averaged along the circle, for a disk of radius  $R = 1$  with an aperture of half-width  $\varepsilon = 0.02$ . Below the lower bound (solid red line) surface diffusion is preferred. Above the upper bound (dashed green line), the surface GMFPT is higher in the adsorbed state than in the desorbed state. In between, the surface GMFPT is an optimizable function of  $\lambda$ . Series are truncated at  $N = 10^4$ .

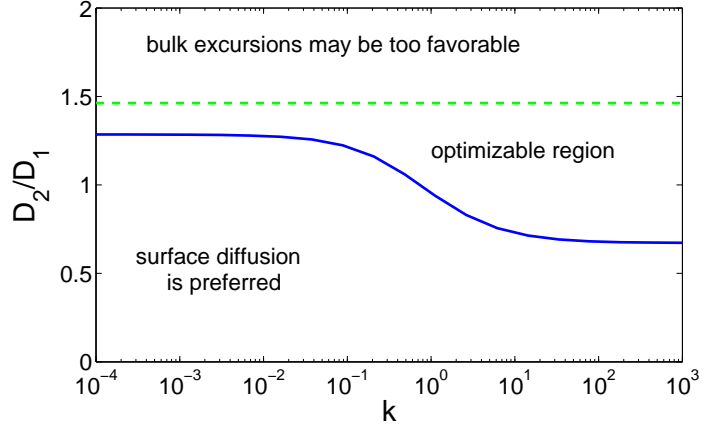
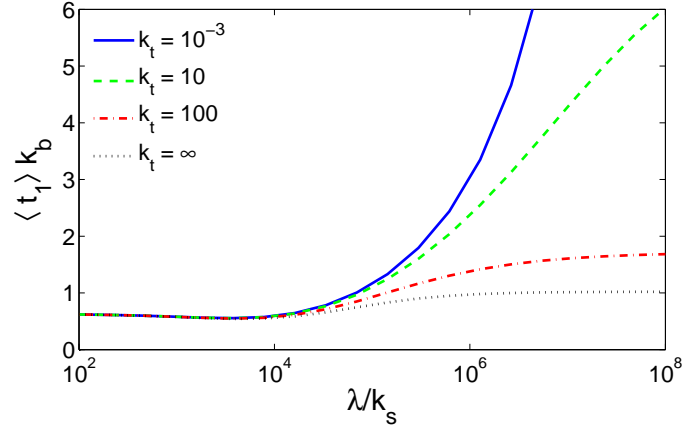


Figure B.4: The surface GMFPT  $\langle t_1 \rangle$  as a function of the desorption rate  $\lambda$ , for several values of the target adsorption parameter  $k_t$  (for particles hitting the target from the bulk), with  $\varepsilon = 0.02$  and  $D_2 = D_1 = 1$  in units in which  $R = 1$ . The non-reactive part of the surface is semi-reflecting with an adsorption parameter  $k = 100$ . Note that the target is perfectly reactive for particles adsorbed on the surface. Series are truncated at  $N = 3 \cdot 10^4$ .



#### B.4.2 Generalization to semi-reflecting targets

In this section, we briefly generalize our method to the case of a semi-reflecting target, for which the B.C. reads as

$$t_2(R, \theta) = \begin{cases} -\frac{1}{k_t} \frac{\partial t_2}{\partial r} \Big|_{\mathbf{r}=(R, \theta)} & (0 \leq \theta \leq \varepsilon), \\ t_1(\theta) - \frac{1}{k} \frac{\partial t_2}{\partial r} \Big|_{\mathbf{r}=(R, \theta)} & (\varepsilon < \theta \leq \pi). \end{cases} \quad (\text{B.47})$$

This general description includes the following cases:

- (i)  $k_t = \infty$  is the case of a fully adsorbing target (Eq. (5.7)), considered in the Sec. 5.2 of the present chapter;
- (ii)  $k_t = k$  has been considered in Chap. of this thesis 4 and in Ref. [112];
- (iii)  $k_t = 0$  corresponds to a target which is fully reflecting for particles hitting the target from the bulk.

Using the mixed boundary condition (B.47), the projection of a series representation (5.10) for  $t_2(R, \theta)$  onto the basis  $\{V_n(\theta)\}_{n \geq 0}$  becomes

$$\int_0^\pi \left\{ t_2(R, \theta) + \frac{1}{k_t} \frac{\partial t_2}{\partial r} \Big|_R \right\} V_n(\theta) d\mu(\theta) = \int_\varepsilon^\pi \left\{ t_1(\theta) + \left( \frac{1}{k} - \frac{1}{k_t} \right) \frac{\partial t_2}{\partial r} \Big|_R \right\} V_n(\theta) d\mu(\theta), \quad (\text{B.48})$$

which replaces Eq. (5.11), with  $d\mu(\theta) = \frac{1}{2} \sin \theta d\theta$ . This leads to the following equations on coefficients  $\alpha_n$  and  $a_n, n \geq 1$

$$a_0 = \langle t_1 | 1 \rangle - \frac{R^2}{2dD_2} \left\{ 1 + 2 \left( \frac{1}{kR} - \frac{1}{k_t R} \right) K_{00}^{(\varepsilon)} \right\} - \sum_{m=1}^{\infty} m \left( \frac{1}{kR} - \frac{1}{k_t R} \right) K_{0m}^{(\varepsilon)} \alpha_m, \quad (\text{B.49})$$

$$a_n \left( 1 + \frac{n}{k_t R} \right) = \langle t_1 | V_n \rangle + \frac{R^2}{dD_2} \left( \frac{1}{kR} - \frac{1}{k_t R} \right) K_{n0}^{(\varepsilon)} - \sum_{m=1}^{\infty} m \left( \frac{1}{kR} - \frac{1}{k_t R} \right) K_{nm}^{(\varepsilon)} \alpha_m. \quad (\text{B.50})$$

From these equations, we extend the definition of  $M_{nm}$  and  $\hat{U}_m$  from Eq. (5.15) to

$$M_{nm} \equiv \delta_{mn} \frac{n}{k_t R} + m \left( \frac{1}{kR} - \frac{1}{k_t R} \right) K_{nm}^{(\varepsilon)}, \quad (\text{B.51})$$

$$\hat{U}_n \equiv \langle t_1 | V_n \rangle + \frac{R^2}{dD_2} \left( \frac{1}{kR} - \frac{1}{k_t R} \right) K_{n0}^{(\varepsilon)}. \quad (\text{B.52})$$

Following the same steps as in Sec. 5.2.2, one gets an integral equation on the dimensionless MFPT  $\psi(\theta)$

$$\psi(\theta) = g_\varepsilon(\theta) + \sum_{n,m=1}^{\infty} \frac{V_n(\theta) - V_n(\varepsilon)}{\rho_n} X_{nm} \left\{ \frac{R^2}{dD_2 T} \left( \frac{1}{kR} - \frac{1}{k_t R} \right) K_{0m}^{(\varepsilon)} + \omega^2 \langle \psi | V_m \rangle \right\}, \quad (\text{B.53})$$

which generalizes Eq. (5.25). Expanding this function onto the basis  $\{V_n(\theta) - V_n(\varepsilon)\}$  yields Eq. (5.33), with

$$U_n \equiv \frac{1}{\rho_n} \sum_{m=1}^{\infty} X_{nm} \left\{ \frac{\xi_m}{\rho_m} + \frac{R^2}{dD_2} \left( \frac{1}{kR} - \frac{1}{k_t R} \right) \frac{K_{m0}^{(\varepsilon)}}{\omega^2 T} \right\}, \quad (\text{B.54})$$

which generalizes Eq. (5.29). This relation can also be written as

$$U_n = Z_n + \frac{D_1}{dD_2(1 + \lambda/\alpha)} \left( \frac{1}{kR} - \frac{1}{k_t R} \right) W_n, \quad (\text{B.55})$$

where  $Z_n$  and  $W_n$  are still defined through Eqs. (5.39). Other quantities and representations remain unchanged. Repeating the computation of the derivative of  $\langle t_1 \rangle$  at  $\lambda = 0$ , one gets the lower bound as

$$\left( \frac{D_2}{D_1} \right)_{\text{low}} = -\frac{1}{dkR} \frac{\langle g_\varepsilon \rangle + (\boldsymbol{\xi} \cdot \mathbf{W})(1 - k/k_t)}{(\boldsymbol{\xi} \cdot \mathbf{Z})}. \quad (\text{B.56})$$

One can see that the change in the boundary condition, i.e., extension from Eq. (5.7) to Eq. (B.47), does not affect the method and the structure of the solution. As a consequence, the conclusions on the optimality of the surface GMFPT remain qualitatively unchanged, although values of the lower bound may be different. Note that the determination of the upper bound requires the expression of the surface GMFPT for a semi-reflecting target in an otherwise reflecting sphere, which is still unknown.

► As shown on Fig. B.4, optimization in  $\lambda$  remains possible even in the case of a target which is fully reflecting ( $k_t = 0$ ) for particles hitting the target from the bulk.



# Search strategy for the Pearson random walks

## Contents

<b>C.1 Monte–Carlo simulations</b> . . . . .	<b>189</b>
C.1.1 Description of trajectories . . . . .	189
C.1.2 Supplementary figures . . . . .	190
<b>C.2 Exact relations at the boundary conditions</b> . . . . .	<b>191</b>
C.2.1 Condition at $r = a$ . . . . .	191
C.2.2 Condition at $r = b$ . . . . .	192
C.2.3 Solution . . . . .	192
C.2.4 Comparison with simulations . . . . .	194

## C.1 Monte–Carlo simulations

### C.1.1 Description of trajectories

We describe the kinetic equations for the searcher that we use to generate the random trajectories. Consider that the searcher is purely ballistic (e.g.  $\tau \rightarrow \infty$ ). Starting at the  $r = a$  with a velocity vector in the direction  $\theta$ , the ballistic searcher hits the boundary  $r = b$  at the time  $t = t_a$  defined as

$$t_a = -a/v \cos \theta + \sqrt{b^2 - a^2 \sin^2 \theta}/v. \quad (\text{C.1})$$

For all  $t \in [0, t_a]$ , the value of  $r$  at the time  $t$  is

$$r_a(t) = \sqrt{v^2 t^2 + a^2 + 2avt \cos \theta}. \quad (\text{C.2})$$

Mind that these expressions Eqs. (C.1) and (C.2) are valid in both  $d = 2$  and  $d = 3$ .

We define the angle  $\tilde{\theta} = \arcsin(a/b)$ , the angular width of the target seen from  $r = b$  (see Fig. 6.1). The kinetic equations for a ballistic searcher initially at  $r = b$  and depend on the direction  $\theta$  of its velocity vector picked after a reorientation event.

- For  $\theta \in [\pi - \tilde{\theta}, \pi]$ , a ballistic searcher crosses the target  $r = a$  at the time

$$t_{b1} = -b/v \cos \theta - \sqrt{a^2 - b^2 \sin^2 \theta}/v.$$

- For  $\theta \in [\pi/2, \pi - \tilde{\theta}]$ , the searcher hits the boundary  $r = b$  at the time

$$t_{b2} = -2b/v \cos \theta.$$



- For  $\theta \in [\pi/2, \pi - \tilde{\theta}]$  and in the case of a specular reflection at  $r = b$ , a ballistic searcher perpetually hits the reflecting boundary at the times  $t_{bn} = nt_{b2}$ , where  $n \geq 1$  is the number of reflections, and we define  $t_{b0} = 0$ . At the time  $t$  within  $nt_{b2} \leq t < (n+1)t_{b2}$ ,  $n \geq 0$ , the position of the searcher is

$$r_{bn}(t) = \sqrt{v^2(t - nt_{b2})^2 + b^2 + 2vb(t - nt_{b2}) \cos \theta(t)}. \quad (\text{C.3})$$

where the angle  $\theta(t)$  at all times  $t$  within  $nt_{b2} \leq t < (n+1)t_{b2}$  reads

$$\theta(t) = \pi - \arccos \left( \frac{b^2 + (vt_{b0})^2 + r_{bn}(t_{bn})^2}{2bvt_{bn}} \right) \quad (\text{C.4})$$

Notice that  $r_{bn}(t + nt_{b2}) = r_{b0}(t)$ ,  $n \geq 0$ . Due to these trajectories of diverging length, the GMFPT  $\bar{t}$  is expected to diverge in the limit  $\tau \gg b/v$ .

### C.1.2 Supplementary figures

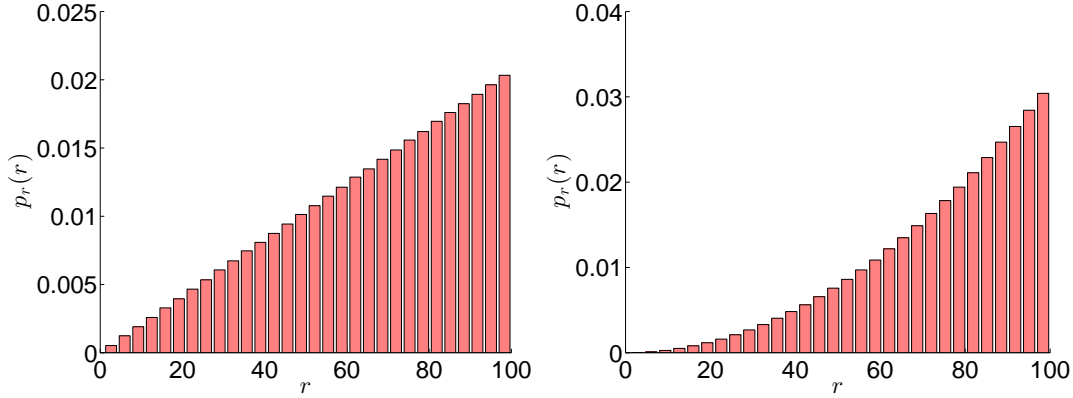


Figure C.1: The probability distribution  $dp_r(r)$  of the radial position of a particle at a reorientation event, defined p. 131, fits to the uniform measure on the volume of the  $(d-1)$ -sphere, with  $a = 1$  and specular confinement at  $b = 100$  with  $\tau = 10$  in the (left)  $d = 2$  geometry and (right)  $d = 3$  geometry.

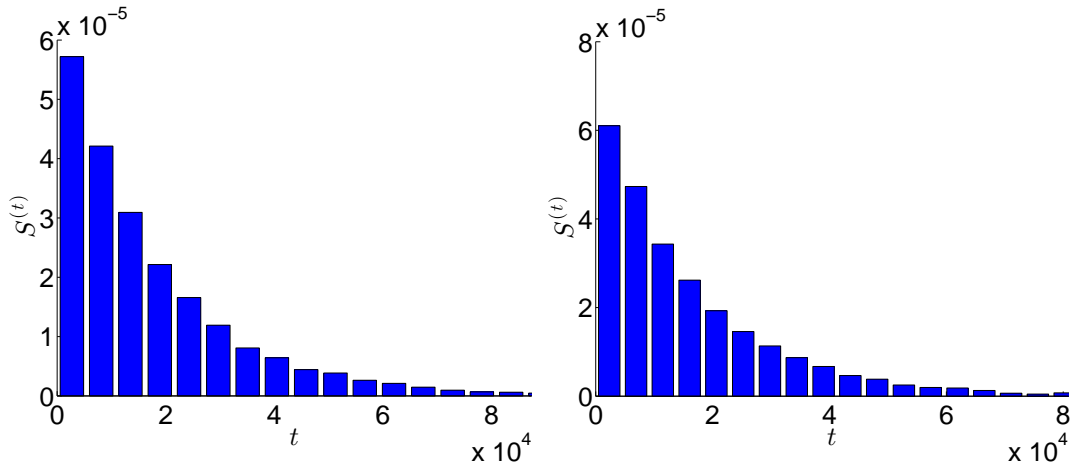


Figure C.2: The global distribution of first passage times  $\overline{S^{(t)}}$  with  $a = 1$ , with (left) diffusive or (right) specular confinement at  $b = 100$  with  $\tau = 10$ .

## C.2 Exact relations at the boundary conditions

► In this section, we use the shorthand notation:  $\langle t(r) \rangle = S(r)$ .

We determine exact relations at  $S(b)$  and  $S(a)$  through a general approach which encompasses the  $d = 2$  and  $d = 3$  spherical geometries. We provide a detailed calculation in the case of a specular reflection at the confining boundary  $r = b$  (defined by Eq. (6.2)). The method can be applied to the diffusive and stubborn boundaries.

The method relies on the quantity  $F(r, \mathbf{v}, t)$ , the mean first passage time conditioned to the facts that

- (i) that the searcher starts at the position  $r$  with velocity  $\mathbf{v}$ ,
- (ii) that the result of the distribution  $\pi$  is the time  $t$ .

The MFPT  $t(r, \mathbf{v})$  is the average of  $F(r, \mathbf{v}, t)$  over the reorientation times  $t$ :

$$t(r, \mathbf{v}) = \int_0^\infty dt F(r, \mathbf{v}, t) \pi(t). \quad (\text{C.5})$$

### C.2.1 Condition at $r = a$

In the case of specular boundary condition at  $r = b$ , the boundary conditions at  $r = a$  for  $F(r, \theta, t)$  can then be summarized as follows,

$$F(a, \theta, t) = 0 \quad \forall t \geq 0 \quad \text{and} \quad \theta \in \left[ \frac{\pi}{2}, \pi \right], \quad (\text{C.6})$$

$$F(a, \theta, t) = t + S(r_a(t)) \quad \text{for} \quad t \leq t_a \quad \text{and} \quad \theta \in \left[ 0, \frac{\pi}{2} \right], \quad (\text{C.7})$$

$$F(a, \theta, t) = t + S(r_a(2t_a - t)) \quad \text{for} \quad t_a < t \leq 2t_a \quad \text{and} \quad \theta \in \left[ 0, \frac{\pi}{2} \right], \quad (\text{C.8})$$

$$F(a, \theta, t) = 2t_a \quad \text{for} \quad t > 2t_a \quad \text{and} \quad \theta \in \left[ 0, \frac{\pi}{2} \right], \quad (\text{C.9})$$

where  $r_a(t)$  is the value of  $r$  at the time  $t$  of the first reorientation (see Eq. (C.2)) and  $t_a$  is the time required to reach the reflecting boundary  $r = b$  (see Eq. (C.1)). The relation  $r_a(t) = r_a(2t_a - t)$  for all  $t_a < t < 2t_a$  is due to reflection at  $r = b$ .

The integrations over  $t$  and  $\theta$  defined in Eq. (C.5) yields the following equation on  $S(a)$ :

$$S(a) = \left\langle \tau \left( 1 - e^{-\frac{2t_a}{\tau}} \right) \right\rangle_{\left[ 0, \frac{\pi}{2} \right]} + \left\langle \int_0^{t_a} \frac{S(r_a(t))}{\tau} \left( e^{-\frac{t}{\tau}} + e^{-\frac{t-2t_a}{\tau}} \right) dt \right\rangle_{\left[ 0, \frac{\pi}{2} \right]}. \quad (\text{C.10})$$

and we recall that the notation  $\langle \cdot \rangle$  is defined in Eq. (6.3). We have used the identity

$$\int_0^u dt t \pi(t) + \int_u^\infty dt u \pi(t) = \tau \left[ 1 - e^{-\frac{u}{\tau}} \right], \quad (\text{C.11})$$

with  $u = 2t_a$ , as well as the relation  $r_a(t) = r_a(2t_a - t)$  for all  $t_a < t < 2t_a$  due to the specular nature of the reflection at  $r = b$ . This leads to the system of equation on  $b_0$  and  $a_0$

$$\begin{aligned} a_0 = & \left\langle \tau \left( 1 - e^{-\frac{2t_a}{\tau}} \right) \right\rangle_{\left[ 0, \frac{\pi}{2} \right]} + \left\langle \int_0^{t_a} \{h[r(t)] + b_0 g[r(t)]\} \frac{e^{-\frac{t}{\tau}} + e^{-\frac{t-2t_a}{\tau}}}{\tau} dt \right\rangle_{\left[ 0, \frac{\pi}{2} \right]} \\ & + a_0 \left\langle \int_0^{t_a} \frac{e^{-\frac{t}{\tau}} + e^{-\frac{t-2t_a}{\tau}}}{\tau} dt \right\rangle_{\left[ 0, \frac{\pi}{2} \right]}. \end{aligned} \quad (\text{C.12})$$

where

$$M_{a0} = \left\langle \tau \left( 1 - e^{-\frac{2t_a}{\tau}} \right) \right\rangle_{[0, \frac{\pi}{2}]} + \left\langle \int_0^{t_a} h[r(t)] \frac{e^{-\frac{t}{\tau}} + e^{-\frac{t-2t_a}{\tau}}}{\tau} dt \right\rangle_{[0, \frac{\pi}{2}]} \quad (\text{C.13})$$

$$M_{a1} = - \left\langle \int_0^{t_a} g[r(t)] \frac{e^{-\frac{t}{\tau}} + e^{-\frac{t-2t_a}{\tau}}}{\tau} dt \right\rangle_{[0, \frac{\pi}{2}]} \quad (\text{C.14})$$

$$M_{a2} = 1 - \left\langle \int_0^{t_a} \frac{e^{-\frac{t}{\tau}} + e^{-\frac{t-2t_a}{\tau}}}{\tau} dt \right\rangle_{[0, \frac{\pi}{2}]} , \quad (\text{C.15})$$

and

$$a_0 M_{a2} + b_0 M_{a1} = M_{a0} \quad (\text{C.16})$$

### C.2.2 Condition at $r = b$

We now determine the conditions on  $F(b, \theta, t)$ . I recall that the boundary at  $r = b$  is taken as specular. For  $\theta \in [0, \pi/2]$ , the searcher is immediately reflected and the conditional MFPT  $F(b, \theta, t)$  satisfies the relation

$$F(b, \theta, t) = F(b, \pi - \theta, t) \quad \forall t \geq 0 \quad \text{and} \quad \theta \in \left[ -\frac{\pi}{2}, \frac{\pi}{2} \right], \quad (\text{C.17})$$

Due to the symmetry relation from Eq. (C.17) we can fold  $\theta$  into the last quadrant:  $\theta \in [\pi/2, \pi]$ . We express the relation on  $F(b, \theta, t)$  for all  $\theta \in [\pi/2, \pi]$  to obtain :

$$F(b, \theta, t) = t + S(r_{b0}(t)) \quad \forall t \leq t_{b1} \quad \text{and} \quad \theta \in [\pi - \tilde{\theta}, \pi], \quad (\text{C.18})$$

$$F(b, \theta, t) = t_{b1} \quad \forall t > t_{b1} \quad \text{and} \quad \theta \in [\pi - \tilde{\theta}, \pi], \quad (\text{C.19})$$

$$F(b, \theta, t) = t + S(r_{bn}(t)) \quad \forall n \geq 0, \forall n t_{b2} \leq t < (n+1)t_{b2} \quad \text{and} \quad \theta \in \left[ \frac{\pi}{2}, \pi - \tilde{\theta} \right]. \quad (\text{C.20})$$

From Eq. (C.5) we obtain the following expression of  $S(b)$  after integration of  $F(b, \theta, t)$

$$S(b) = 2 \left\langle \tau + \frac{e^{-\frac{t_{b2}}{\tau}}}{e^{-\frac{t_{b2}}{\tau}} - 1} \int_0^{t_{b2}} \frac{S(r_{b0}(t))}{\tau} e^{-\frac{t}{\tau}} dt \right\rangle_{[\frac{\pi}{2}, \pi - \tilde{\theta}]} + 2 \left\langle \tau \left( 1 - e^{-\frac{t_{b1}}{\tau}} \right) + \int_0^{t_{b1}} \frac{S(r_{b0}(t))}{\tau} e^{-\frac{t}{\tau}} dt \right\rangle_{[\pi - \tilde{\theta}, \pi]}. \quad (\text{C.21})$$

To obtain each term in the latter Eq. (C.21), we have used (from left to right): (i) the identity of Eq. (C.11) with  $u = \infty$ , (ii) the identity  $S(r_{b0}(t)) = S(r_{bn}(t + nt_{b2}))$ ,  $n \geq 0$ , which leads to the following relation (for an exponential reorientation rate  $\pi(t)$ ):

$$\int_0^{\infty} dt S(r_{bn}(t)) \pi(t) = \sum_{n=0}^{\infty} \int_{nt_{b2}}^{(n+1)t_{b2}} dt S(r_{bn}(t)) \pi(t) = \frac{e^{-\frac{t_{b2}}{\tau}}}{e^{-\frac{t_{b2}}{\tau}} - 1} \int_0^{t_{b2}} \frac{S(r_{b0}(t))}{\tau} e^{-\frac{t}{\tau}} dt, \quad (\text{C.22})$$

and (iii) the identity of Eq. (C.11) with  $u = t_{b1}$ .

### C.2.3 Solution

Equation (C.21) leads to the system of equation on  $b_0$  and  $a_0$

$$-\frac{b^2 - a^2}{2v\tau} + b_0 g[b] + a_0 = 2 \left\langle \tau + \frac{e^{-\frac{t_{b2}}{\tau}}}{e^{-\frac{t_{b2}}{\tau}} - 1} \int_0^{t_{b2}} S(r_{b0}(t)) \frac{e^{-\frac{t}{\tau}}}{\tau} dt \right\rangle_{[\frac{\pi}{2}, \pi - \tilde{\theta}]} \quad (\text{C.23})$$

$$+ 2 \left\langle \tau \left( 1 - e^{-\frac{t_{b1}}{\tau}} \right) + \int_0^{t_{b1}} S(r_{b0}(t)) \frac{e^{-\frac{t}{\tau}}}{\tau} dt \right\rangle_{[\pi - \tilde{\theta}, \pi]}. \quad (\text{C.24})$$

where

$$M_{b0} = \frac{b^2 - a^2}{2v\tau} + 2 \left\langle \tau + \frac{e^{\frac{tb_2}{\tau}}}{e^{\frac{tb_2}{\tau}} - 1} \int_0^{tb_2} h[r_{b0}(t)] \frac{e^{-\frac{t}{\tau}}}{\tau} dt \right\rangle_{[\frac{\pi}{2}, \pi - \bar{\theta}]} + 2 \left\langle \tau \left(1 - e^{-\frac{tb_1}{\tau}}\right) + \int_0^{tb_1} h[r_{b0}(t)] \frac{e^{-\frac{t}{\tau}}}{\tau} dt \right\rangle_{[\pi - \bar{\theta}, \pi]} \quad (\text{C.25})$$

$$M_{b1} = g[b] - 2 \left\langle \frac{e^{\frac{tb_2}{\tau}}}{e^{\frac{tb_2}{\tau}} - 1} \int_0^{tb_2} g[r_{b0}(t)] \frac{e^{-\frac{t}{\tau}}}{\tau} dt \right\rangle_{[\frac{\pi}{2}, \pi - \bar{\theta}]} - 2 \left\langle \int_0^{tb_1} g[r_{b0}(t)] \frac{e^{-\frac{t}{\tau}}}{\tau} dt \right\rangle_{[\pi - \bar{\theta}, \pi]} \quad (\text{C.26})$$

$$M_{b2} = 1 - 2 \left\langle \frac{e^{\frac{tb_2}{\tau}}}{e^{\frac{tb_2}{\tau}} - 1} \int_0^{tb_2} \frac{e^{-\frac{t}{\tau}}}{\tau} dt \right\rangle_{[\frac{\pi}{2}, \pi - \bar{\theta}]} - 2 \left\langle \int_0^{tb_1} \frac{e^{-\frac{t}{\tau}}}{\tau} dt \right\rangle_{[\pi - \bar{\theta}, \pi]}, \quad (\text{C.27})$$

and

$$a_0 M_{b2} + b_0 M_{b1} = M_{b0} \quad (\text{C.28})$$

The solution is

$$b_0 = \frac{M_{a0} M_{b2} - M_{a2} M_{b0}}{M_{a1} M_{b2} - M_{a2} M_{b1}}, \quad a_0 = \frac{M_{a1} M_{b0} - M_{a0} M_{b1}}{M_{a1} M_{b2} - M_{a2} M_{b1}} \quad (\text{C.29})$$

The conditions of Eqs. (C.10) and (C.21) yield two equations on the unknown constants  $b_0$  and  $a_0$  (defined in Eq. (2.34)). The unique solution of this system of equations reads

$$a_0 = \frac{\left\langle 2t_a e^{-\frac{t_a}{\tau}} \right\rangle_{[-\frac{\pi}{2}, \frac{\pi}{2}]} - \frac{a}{v} \left\langle \left(1 - e^{-\frac{t_a}{\tau}}\right)^2 \cos \theta \right\rangle_{[-\frac{\pi}{2}, \frac{\pi}{2}]} + A_1 I_a}{1 - \left\langle 1 - e^{-2\frac{t_a}{\tau}} \right\rangle_{[-\frac{\pi}{2}, \frac{\pi}{2}]}} \quad (\text{C.30})$$

and

$$b_0 = \frac{b}{v} \left( \frac{1}{2\pi} + \left\langle \cos \theta e^{-\frac{tb_1}{\tau}} \right\rangle_{[\pi - \bar{\theta}, \pi]} \right) + \left( \left\langle \frac{t_{b2}^2 + 2t_{b2}\tau + \frac{2bt_{b2}}{v} \cos \theta}{2\tau \left(e^{\frac{tb_2}{\tau}} - 1\right)} \right\rangle_{[\frac{\pi}{2}, \pi - \bar{\theta}]} + \left\langle \frac{e^{-\frac{tb_1}{\tau}}}{2\tau} \left( t_{b1}^2 + 2t_{b1}\tau + \frac{2bt_{b1}}{v} \cos \theta \right) \right\rangle_{[\pi - \bar{\theta}, \pi]} + \left\langle e^{-\frac{tb_1}{\tau}} \right\rangle_{[\pi - \bar{\theta}, \pi]} \left[ \frac{b^2 - a^2}{2v^2\tau} + \frac{\frac{a}{v} \left\langle \left(1 - e^{-\frac{t_a}{\tau}}\right)^2 \cos \theta \right\rangle_{[-\frac{\pi}{2}, \frac{\pi}{2}]} - \left\langle 2t_a e^{-\frac{t_a}{\tau}} \right\rangle_{[-\frac{\pi}{2}, \frac{\pi}{2}]}}{1 - \left\langle 1 - e^{-2\frac{t_a}{\tau}} \right\rangle_{[-\frac{\pi}{2}, \frac{\pi}{2}]}} \right] \right) W. \quad (\text{C.31})$$

with

$$I_a = \frac{1}{2} \left\langle e^{-\frac{ae^{i\theta} + 2t_a v}{\tau v}} \left( E_i \left[ \frac{ae^{i\theta}}{\tau v} \right] - E_i \left[ \frac{ae^{i\theta} + t_a v}{\tau v} \right] \right) + e^{\frac{ae^{i\theta}}{\tau v}} \left( E_i \left[ -\frac{ae^{i\theta} + t_a v}{\tau v} \right] - E_i \left[ -\frac{ae^{i\theta}}{\tau v} \right] \right) \right\rangle_{[-\frac{\pi}{2}, \frac{\pi}{2}]}, \quad (\text{C.32})$$

$$I_b = \frac{1}{2} \left( \left\langle \frac{e^{\frac{be^{-i\theta} + t_{b2} v}{\tau v}}}{e^{\frac{t_{b2}}{\tau} - 1}} \left( E_i \left[ -\frac{be^{-i\theta} + t_{b2} v}{\tau v} \right] - E_i \left[ -\frac{be^{-i\theta}}{\tau v} \right] \right) + \frac{e^{\frac{be^{i\theta} + t_{b2} v}{\tau v}}}{e^{\frac{t_{b2}}{\tau} - 1}} \left( E_i \left[ -\frac{be^{i\theta} + t_{b2} v}{\tau v} \right] - E_i \left[ -\frac{be^{i\theta}}{\tau v} \right] \right) \right. \right. \\ \left. \left. - \frac{\ln \left( 1 + \frac{t_{b2}^2 v^2}{b^2} + \frac{2t_{b2} v}{b} \cos \theta \right)}{e^{\frac{t_{b2}}{\tau} - 1}} \right\rangle_{[\frac{\pi}{2}, \pi - \tilde{\theta}]} \right. \\ \left. + \left\langle e^{\frac{be^{-i\theta}}{\tau v}} \left( E_i \left[ -\frac{be^{-i\theta} + t_{b1} v}{\tau v} \right] - E_i \left[ -\frac{be^{-i\theta}}{\tau v} \right] \right) + e^{\frac{be^{i\theta}}{\tau v}} \left( E_i \left[ -\frac{be^{i\theta} + t_{b1} v}{\tau v} \right] - E_i \left[ -\frac{be^{i\theta}}{\tau v} \right] \right) - e^{-\frac{t_{b1}}{\tau}} \ln \left( 1 + \frac{t_{b1}^2 v^2}{b^2} + \frac{2t_{b1} v}{b} \cos \theta \right) \right\rangle_{[\pi - \tilde{\theta}, \pi]} \right). \quad (\text{C.33})$$

and

$$W = \left( \left\langle e^{-\frac{t_{b1}}{\tau}} \right\rangle_{[\pi - \tilde{\theta}, \pi]} \left( \ln \frac{b}{a} + \frac{I_a}{1 - \left\langle 1 - e^{-2\frac{t_a}{\tau}} \right\rangle_{[-\frac{\pi}{2}, \frac{\pi}{2}]}} \right) - I_b \right)^{-1} \quad (\text{C.34})$$

Here  $E_i(x)$  denotes the exponential integral defined by  $E_i(x) = \int_{-\infty}^x e^t/t dt$ .

We have used the fact that for  $\alpha = \{-1, +1\}$

$$\int_0^{t_a} \alpha \frac{e^{-\alpha \frac{t'}{\tau}}}{\tau} \ln \left( \left[ 1 + \frac{at'}{v} e^{i\theta} \right] \left[ 1 + \frac{at'}{v} e^{-i\theta} \right] \right) dt' = -\frac{e^{-\frac{\alpha t_a}{\tau}}}{\tau} \ln \left( 1 + \frac{t_a^2 v^2}{a^2} + 2\frac{t_a v}{a} \cos \theta \right) \\ + e^{\frac{ae^{i\theta}}{\tau v}} \left( E_i \left[ -\alpha \frac{ae^{i\theta} + t_a v}{\tau v} \right] - E_i \left[ -\alpha \frac{ae^{i\theta}}{\tau v} \right] \right) \\ + e^{\frac{ae^{-i\theta}}{\tau v}} \left( E_i \left[ -\alpha \frac{ae^{-i\theta} + t_a v}{\tau v} \right] - E_i \left[ -\alpha \frac{ae^{-i\theta}}{\tau v} \right] \right). \quad (\text{C.35})$$

We substitute the expressions for  $b_0$  and  $a_0$  within Eq. (6.10) to obtain an explicit approximate expression for the averaged MFPT  $\langle t \rangle$ . Figure C.3 shows that the approximate expression for  $\langle t \rangle$  is in good agreement with the numerical results for  $\tau \ll a/v$ .

## C.2.4 Comparison with simulations

As visible in Fig. C.3, the obtained expression for the MFPT diverges in the limit  $\tau \gg b/v$ . The latter divergence is all the more remarkable since the computation is expected to be valid within the range of validity of the decoupling approximation ( $\tau \ll b/v$ ). However, the model developed in this section does not predict the appropriate scaling for the optimal reorientation rate  $\tau_{\text{opt}}$  and the discrepancy with simulations at the optimal search time is large.

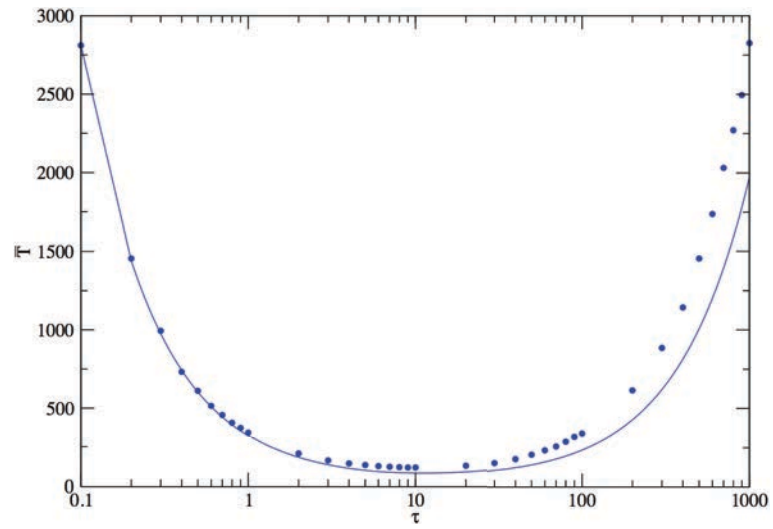


Figure C.3: GMFPT in the specular case,  $b = 100$ ,  $a = 1$ : (dots line), Monte–Carlo simulations, (solid line), theoretical curve from in Sec. C.2, p. 191.



# Bibliography

- [1] Strutt Rayleigh. The Theory of Sound. 1896. (Cited p. 16 et 18.)
- [2] Louis Bachelier. *Théorie de la spéculation*. PhD thesis, 1900. (Cited p. 16.)
- [3] Karl Pearson. The problem of the Random Walk. *Nature*, 72:294, 1905. (Cited p. 16 et 17.)
- [4] Albert Einstein. *Investigations on the Theory of the Brownian Movement*. 1956. (Cited p. 16 et 19.)
- [5] G M Viswanathan, Sergey V Buldyrev, Shlomo Havlin, M G E da Luz, E P Raposo, and H Eugene Stanley. Optimizing the success of random searches. *Nature*, 401(6756):911–914, 1999. (Cited p. 16 et 23.)
- [6] Andrew M Edwards, Richard A Phillips, Nicholas W Watkins, Mervyn P Freeman, Eugene J Murphy, Vsevolod Afanasyev, Sergey V Buldyrev, M G E da Luz, E P Raposo, H Eugene Stanley, and Gandhimohan M Viswanathan. Revisiting Levy flight search patterns of wandering albatrosses, bumblebees and deer. *Nature*, 449(7165):1044–1048, 2007. (Cited p. 16, 17 et 23.)
- [7] M C Santos, E P Raposo, G M Viswanathan, and M G E da Luz. Optimal random searches of revisitable targets: Crossover from superdiffusive to ballistic random walks. *EPL (Europhysics Letters)*, 67(5):734–740, 2004. (Cited p. 16 et 23.)
- [8] Edward A Codling, Michael J Plank, and Simon Benhamou. Random walk models in biology. *Journal of the Royal Society, Interface / the Royal Society*, 5(25):813–34, August 2008. (Cited p. 17.)
- [9] Wolfgang Alt. Biased random walk models for chemotaxis and related diffusion approximations. *Journal of Mathematical Biology*, 9(2):147–177, April 1980. (Cited p. 17.)
- [10] James M. Dobbie. A Survey of Search Theory. *Operations Research*, 16(3):525–537, June 1968. (Cited p. 17.)
- [11] L. Champagne, E.G. Carl, and R. Hill. Search theory, agent-based simulation, and u-boats in the Bay of Biscay. In *Proceedings of the 2003 International Conference on Machine Learning and Cybernetics (IEEE Cat. No.03EX693)*, volume 1, pages 991–998. IEEE. (Cited p. 17.)
- [12] Jonathan M Borwein, Armin Straub, James Wan, and Wadim Zudilin. Densities of Short Uniform Random Walks. *Canadian Journal of Mathematics*, 64(5):961–990, November 2011. (Cited p. 18.)
- [13] G H Weiss. *Aspects and Applications of the Random Walk*. Amsterdam, Netherlands: North-Holland, 1994. (Cited p. 18.)
- [14] O Bénichou, C Loverdo, M Moreau, and R Voituriez. Intermittent search strategies. *Review of Modern Physics*. (Cited p. 18, 22, 23, 24 et 126.)
- [15] Eric Monson and Raoul Kopelman. Observation of Laser Speckle Effects and Nonclassical Kinetics in an Elementary Chemical Reaction. *Physical Review Letters*, 85(3), 2000. (Cited p. 18.)



- [16] Sushil Mujumdar, Marilena Ricci, Renato Torre, and Diederik Wiersma. Amplified Extended Modes in Random Lasers. *Physical Review Letters*, 93(5):053903, July 2004. (Cited p. 18.)
- [17] Thierry Bodineau, Isabelle Gallagher, and Laure Saint-Raymond. The Brownian motion as the limit of a deterministic system of hard-spheres. pages 1–40, May 2013. (Cited p. 20.)
- [18] C W Gardiner. *Handbook of Stochastic Methods for Physics, Chemistry and Natural Sciences*. Springer, 2004. (Cited p. 20, 32, 33, 34, 73, 152, 153, 155, 157, 177, 179 et 180.)
- [19] Laurent Golé, Charlotte Rivière, Yoshinori Hayakawa, and Jean-Paul Rieu. A quorum-sensing factor in vegetative Dictyostelium discoideum cells revealed by quantitative migration analysis. *PLoS one*, 6(11):e26901, January 2011. (Cited p. 20.)
- [20] Jonathan Howse, Richard Jones, Anthony Ryan, Tim Gough, Reza Vafabakhsh, and Ramin Golestanian. Self-Motile Colloidal Particles: From Directed Propulsion to Random Walk. *Physical Review Letters*, 99(4):048102, July 2007. (Cited p. 20.)
- [21] O G Berg and C Blomberg. No Title. *Biophysical Chemistry*, 4:367, 1976. (Cited p. 21.)
- [22] B Alberts, A Johnson, J Lewis, M Raff, K Roberts, and P Walter. *Molecular Biology of the Cell*. Garland New York, 2002. (Cited p. 21.)
- [23] Jurgen Reingruber and David Holcman. Diffusion in narrow domains and application to phototransduction. *Physical Review E (Statistical, Nonlinear, and Soft Matter Physics)*, 79(3):30904, 2009. (Cited p. 21 et 52.)
- [24] B Meyer, O Bénichou, Y Kafri, and R Voituriez. Geometry-Induced Bursting Dynamics in Gene Expression. *Biophysical journal*, 102(9):2186–2191, 2012. (Cited p. 21.)
- [25] Paul C. Bressloff and Jay M. Newby. Stochastic models of intracellular transport. *Reviews of Modern Physics*, 85(1):135–196, January 2013. (Cited p. 21.)
- [26] T Lagache and D Holcman. Effective Motion of a Virus Trafficking Inside a Biological Cell. *SIAM J. Appl. Math.*, 68(4), 2008. (Cited p. 21, 53, 84 et 104.)
- [27] Sebastien Huet, Erdem Karatekin, Viet Samuel Tran, Isabelle Fanget, Sophie Cribier, and Jean-Pierre Henry. Analysis of Transient Behavior in Complex Trajectories: Application to Secretory Vesicle Dynamics. *Biophys. J.*, 91(9):3542–3559, 2006. (Cited p. 21.)
- [28] C Loverdo, O Bénichou, M Moreau, and R Voituriez. Enhanced reaction kinetics in biological cells. *Nat Phys*, 4(2):134–137, 2008. (Cited p. 21.)
- [29] Delphine Arcizet, Born Meier, Erich Sackmann, Joachim O Radler, and Doris Heinrich. Temporal Analysis of Active and Passive Transport in Living Cells. *Physical Review Letters*, 101(24):248103–248104, 2008. (Cited p. 21.)
- [30] Martin Bier and R. Dean Astumian. Biased Brownian motion as the operating principle for microscopic engines. *Bioelectrochemistry and Bioenergetics*, 39(1):67–75, February 1996. (Cited p. 21.)
- [31] F Nedelec, T Surrey, and A C Maggs. Dynamic concentration of motors in microtubule arrays. *Physical Review Letters*, 86(14):3192–3195, April 2001. (Cited p. 21 et 84.)

- [32] Jae-Hyung Jeon, Vincent Tejedor, Stas Burov, Eli Barkai, Christine Selhuber-Unkel, Kirstine Berg-Sørensen, Lene Oddershede, and Ralf Metzler. In Vivo Anomalous Diffusion and Weak Ergodicity Breaking of Lipid Granules. *Physical Review Letters*, 106(4):048103, January 2011. (Cited p. 21.)
- [33] Joseph Klafter, S C Lim, and Ralf Metzler. *Fractional Dynamics*. World Scientific Publishing Company, October 2011. (Cited p. 21.)
- [34] Z Schuss, A Singer, and D Holcman. The narrow escape problem for diffusion in cellular microdomains. *Proc Natl Acad Sci U S A*, 104(41):16098–16103, October 2007. (Cited p. 21 et 78.)
- [35] A Zoia, E Dumonteil, and A Mazzolo. Collision densities and mean residence times for d-dimensional exponential flights. *Physical Review E*, 83(4), 2011. (Cited p. 21.)
- [36] Alain Mazzolo. On the mean number of collisions suffered by neutrons in bounded domains. *Annals of Nuclear Energy*, 32(6):549–557, 2005. (Cited p. 21.)
- [37] P F Zweifel. *Reactor Physics*. MCGraw-Hill, New York, 1973. (Cited p. 21 et 85.)
- [38] George H Weiss. Some applications of persistent random walks and the telegrapher's equation. 311(2002):381–410, 2007. (Cited p. 21.)
- [39] P G de Gennes. *Scaling Concepts in Polymer Physics*. Ithaca, 1979. (Cited p. 22.)
- [40] T Guérin, O Bénichou, and R Voituriez. Reactive conformations and non-Markovian cyclization kinetics of a Rouse polymer. *The Journal of chemical physics*, 138(9):094908, March 2013. (Cited p. 22.)
- [41] HOWARD C. BERG and DOUGLAS A. BROWN. Chemotaxis in *Escherichia coli* analysed by Three-dimensional Tracking. *Nature*, 239(5374):500–504, October 1972. (Cited p. 22.)
- [42] Paolo Maiuri, Emmanuel Terriac, Perrine Paul-Gilloteaux, Timothee Vignaud, Krista McNally, James Onuffer, Kurt Thorn, Phuong a Nguyen, Nefeli Georgoulia, Daniel Soong, Asier Jayo, Nina Beil, Jürgen Beneke, Joleen Chooi Hong Lim, Chloe Pei-Ying Sim, Yeh-Shiu Chu, Andrea Jimenez-Dalmaroni, Jean-François Joanny, Jean-Paul Thiery, Holger Erfle, Maddy Parsons, Timothy J Mitchison, Wendell a Lim, Ana-Maria Lennon-Dumenil, Matthieu Piel, and Manuel Thery. The first World Cell Race. *Current biology : CB*, 22(17):R673–5, September 2012. (Cited p. 22.)
- [43] Gabrielle Faure-Andre, Pablo Vargas, Maria-Isabel Yuseff, Melina Heuze, Jheimmy Diaz, Danielle Lankar, Veronica Steri, Jeremy Manry, Stephanie Hugues, Fulvia Vascotto, Jerome Boulanger, Graca Raposo, Maria-Rosa Bono, Mario Roseblatt, Matthieu Piel, and Ana-Maria Lennon-Dumenil. Regulation of Dendritic Cell Migration by CD74, the MHC Class II-Associated Invariant Chain. *Science*, 322(5908):1705–1710, 2008. (Cited p. 22, 144 et 157.)
- [44] K Rayner. Eye movements in reading and information processing: 20 years of research. *Psychological bulletin*, 124(3):372–422, November 1998. (Cited p. 23.)
- [45] Gary Feng. Eye movements as time-series random variables: A stochastic model of eye movement control in reading. *Cognitive Systems Research*, 7(1):70–95, March 2006. (Cited p. 23.)

- [46] Carita M Bergman and James A Schaefer. Caribou movement as a correlated random walk. (July 1999):364–374, 2000. (Cited p. 23.)
- [47] Nicolas E Humphries, Nuno Queiroz, Jennifer R M Dyer, Nicolas G Pade, Michael K Musyl, Kurt M Schaefer, Daniel W Fuller, Juerg M Brunnschweiler, Thomas K Doyle, Jonathan D R Houghton, Graeme C Hays, Catherine S Jones, Leslie R Noble, Victoria J Wearmouth, Emily J Southall, and David W Sims. Environmental context explains Lévy and Brownian movement patterns of marine predators. *Nature*, 465(7301):1066–9, June 2010. (Cited p. 23.)
- [48] O Bénichou, C Loverdo, M Moreau, and R Voituriez. Intermittent search strategies. *Reviews of Modern Physics*, 83(1), 2011. (Cited p. 23 et 130.)
- [49] P. Levitz, P. a. Bonnaud, P.-a. Cazade, R. J.-M. Pellenq, and B. Coasne. Molecular intermittent dynamics of interfacial water: probing adsorption and bulk confinement. *Soft Matter*, 9(36):8654, 2013. (Cited p. 25.)
- [50] Indira Sriram, Robert Walder, and Daniel K Schwartz. Stokes-Einstein and desorption-mediated diffusion of protein molecules at the oil-water interface. *Soft Matter*, 2012. (Cited p. 25.)
- [51] Mark Kastantin, Robert Walder, and Daniel K Schwartz. Identifying mechanisms of interfacial dynamics using single-molecule tracking. *Langmuir : the ACS journal of surfaces and colloids*, 28(34):12443–56, August 2012. (Cited p. 25.)
- [52] JH Strange, M Rahman, and EG Smith. Characterization of porous solids by NMR. *Physical review letters*, 71(21):3589–3591, November 1993. (Cited p. 25.)
- [53] S. G. Allen, P. C. L. Stephenson, and J. H. Strange. Morphology of porous media studied by nuclear magnetic resonance. *The Journal of Chemical Physics*, 106(18):7802, May 1997. (Cited p. 25.)
- [54] Denis S Grebenkov. NMR survey of reflected Brownian motion. *Reviews of Modern Physics*, 79(3):1061–1077, 2007. (Cited p. 25.)
- [55] Robert Walder, Nathaniel Nelson, and Daniel K Schwartz. Super-resolution surface mapping using the trajectories of molecular probes. *Nature communications*, 2(May):515, January 2011. (Cited p. 25.)
- [56] Christian Sendner, Dominik Horinek, Lyderic Bocquet, and Roland R Netz. Interfacial water at hydrophobic and hydrophilic surfaces: slip, viscosity, and diffusion. *Langmuir : the ACS journal of surfaces and colloids*, 25(18):10768–81, September 2009. (Cited p. 25.)
- [57] John Meurig Thomas and W. John Thomas. *Principles and Practice of Heterogeneous Catalysis*. Wiley-VCH, 1997. (Cited p. 25.)
- [58] BM Weckhuysen. Heterogeneous catalysis: Catch me if you can! *Nature chemistry*, 1(December):690–692, 2009. (Cited p. 25.)
- [59] G C Bond. *Heterogeneous Catalysis: Principles and Applications*. Clarendon, Oxford, 1987. (Cited p. 25.)
- [60] John D. Taylor and Stephen E. Halford. Discrimination between DNA sequences by the EcoRV restriction endonuclease. *Biochemistry*, 28(15):6198–6207, July 1989. (Cited p. 25.)

- [61] Arthur D. Riggs, Suzanne Bourgeois, and Melvin Cohn. The lac repressor-operator interaction. *Journal of Molecular Biology*, 53(3):401–417, November 1970. (Cited p. 25.)
- [62] O G Berg, R B Winter, and P H von Hippel. Diffusion-driven mechanisms of protein translocation on nucleic acids. 1. Models and theory. *Biochemistry*, 20:6929, 1981. (Cited p. 25.)
- [63] Robert B. Winter and Peter H. Von Hippel. Diffusion-driven mechanisms of protein translocation on nucleic acids. 2. The Escherichia coli lac repressor-operator interaction: equilibrium measurements. *Biochemistry*, 20(24):6948–6960, November 1981. (Cited p. 25.)
- [64] Isabelle Bonnet, Andreas Biebricher, Pierre-Louis Porte, Claude Loverdo, Olivier Bénichou, Raphael Voituriez, Christophe Escude, Wolfgang Wende, Alfred Pingoud, and Pierre Desbiolles. Sliding and jumping of single EcoRV restriction enzymes on non-cognate DNA. *Nucleic Acids Research*, pages gkn376—, 2008. (Cited p. 25.)
- [65] D M Gowers, G G Wilson, and S E Halford. No Title. *PNAS*, 102:15883, 2005. (Cited p. 25.)
- [66] B van den Broek, M A Lomholt, S M. J Kalisch, R Metzler, and G J L Wuite. How DNA coiling enhances target localization by proteins. *Proceedings of the National Academy of Sciences*, pages —, 2008. (Cited p. 25.)
- [67] Johan Elf, Gene-Wei Li, and X Sunney Xie. Probing transcription factor dynamics at the single-molecule level in a living cell. *Science (New York, N.Y.)*, 316(5828):1191–4, May 2007. (Cited p. 25.)
- [68] G Adam and M Delbrück. *Reduction of dimensionality in biological diffusion processes*. W.H. Freeman Co, Publishers, San Francisco, 1968. (Cited p. 25.)
- [69] O Bénichou, C Loverdo, M Moreau, and R Voituriez. Optimizing intermittent reaction paths. *Physical chemistry chemical physics : PCCP*, 10(47):7059–72, December 2008. (Cited p. 25.)
- [70] G Seisenberger, M U Ried, T Endress, H Büning, M Hallek, and C Bräuchle. Real-time single-molecule imaging of the infection pathway of an adeno-associated virus. *Science (New York, N.Y.)*, 294(5548):1929–32, November 2001. (Cited p. 25.)
- [71] O. Gapenne, P. Simon, and J. Lannou. A simple method for recording the path of a rat in an open field. *Behavior Research Methods, Instruments, & Computers*, 22(5):443–448, September 1990. (Cited p. 26.)
- [72] Raphaël Jeanson, Stéphane Blanco, Richard Fournier, Jean-Louis Deneubourg, Vincent Fourcassié, and Guy Theraulaz. A model of animal movements in a bounded space. *Journal of Theoretical Biology*, 225(4):443–451, December 2003. (Cited p. 26.)
- [73] Howard C. Berg, editor. *E. coli in Motion*, volume 7 of *Biological and Medical Physics, Biomedical Engineering*. Springer New York, New York, NY, January 2004. (Cited p. 26.)
- [74] Clemens Grabher, Adam Cliffe, Kota Miura, Joel Hayflick, Rainer Pepperkok, Pernille Rørth, and Joachim Wittbrodt. Birth and life of tissue macrophages and their migration in embryogenesis and inflammation in medaka. *J Leukoc Biol*, 81(1):263–271, January 2007. (Cited p. 26.)

- [75] Hanna Salman and Albert Libchaber. A concentration-dependent switch in the bacterial response to temperature. *Nature cell biology*, 9(9):1098–100, September 2007. (Cited p. 26.)
- [76] Gáspár Jékely, Julien Colombelli, Harald Hausen, Keren Guy, Ernst Stelzer, François Nédélec, and Detlev Arendt. Mechanism of phototaxis in marine zooplankton. *Nature*, 456(7220):395–9, November 2008. (Cited p. 26.)
- [77] Jens Baumgartner, Guillaume Morin, Nicolas Menguy, Teresa Perez Gonzalez, Marc Widdrat, Julie Cosmidis, and Damien Faivre. Magnetotactic bacteria form magnetite from a phosphate-rich ferric hydroxide via nanometric ferric (oxyhydr)oxide intermediates. *Proceedings of the National Academy of Sciences of the United States of America*, 110(37):14883–8, September 2013. (Cited p. 26.)
- [78] Massimo Vergassola, Emmanuel Villermaux, and Boris I Shraiman. /‘Infotaxis/’ as a strategy for searching without gradients. *Nature*, 445(7126):406–409, 2007. (Cited p. 26.)
- [79] Eugene Balkovsky and Boris I Shraiman. Olfactory search at high Reynolds number. *Proceedings of the National Academy of Sciences of the United States of America*, 99(20):12589–93, October 2002. (Cited p. 26.)
- [80] J-B Masson, M Bailly Bechet, and M Vergassola. Chasing information to search in random environments. *Journal of Physics A: Mathematical and Theoretical*, 42(43):434009, October 2009. (Cited p. 26.)
- [81] Jean-Claude Latombe. *Robot Motion Planning*. Springer, 1991. (Cited p. 27.)
- [82] L.E. Kavraki, P. Svestka, J.-C. Latombe, and M.H. Overmars. Probabilistic roadmaps for path planning in high-dimensional configuration spaces. *IEEE Transactions on Robotics and Automation*, 12(4):566–580, 1996. (Cited p. 27.)
- [83] S.M. LaValle and Jr. Kuffner, J.J. Randomized kinodynamic planning. *Proceedings 1999 IEEE International Conference on Robotics and Automation (Cat. No.99CH36288C)*, 1, 1999. (Cited p. 27.)
- [84] D. Hsu, R. Kindel, J.-C. Latombe, and S. Rock. Randomized Kinodynamic Motion Planning with Moving Obstacles, 2002. (Cited p. 27.)
- [85] O Bénichou, D Grebenkov, P Levitz, C Loverdo, and R Voituriez. Optimal Reaction Time for Surface-Mediated Diffusion. *Physical Review Letters*, 105:150606, 2010. (Cited p. 28 et 59.)
- [86] S. Chandrasekhar. Stochastic Problems in Physics and Astronomy. *Reviews of Modern Physics*, 15(1):1–89, January 1943. (Cited p. 33.)
- [87] Grégoire Allaire. *Analyse numérique et optimisation*. Ecole Polytechnique, 2005. (Cited p. 34 et 43.)
- [88] D. Grebenkov. Residence times and other functionals of reflected Brownian motion. *Physical Review E*, 76(4):041139, October 2007. (Cited p. 35.)
- [89] Denis S Grebenkov. Searching for partially reactive sites: Analytical results for spherical targets. *The Journal of chemical physics*, 132(3):034104, January 2010. (Cited p. 35, 78 et 85.)

- [90] A. Singer, Z. Schuss, A. Osipov, and D. Holcman. Partially Reflected Diffusion. *SIAM Journal on Applied Mathematics*, 68(3):844–868, January 2008. (Cited p. 35 et 85.)
- [91] Sidney Redner. *A Guide to First-Passage Processes*. Cambridge University Press, 2001. (Cited p. 37.)
- [92] A Singer, Z Schuss, and D Holcman. Narrow Escape, Part II: The Circular Disk. *Journal of Statistical Physics*, 122(3):465–489, 2006. (Cited p. 50, 52, 53, 55, 62, 67, 71, 108, 116 et 172.)
- [93] S Pillay, M J Ward, A Peirce, and T Kolokolnikov. An Asymptotic Analysis of the Mean First Passage Time for Narrow Escape Problems: Part I: Two-Dimensional Domains. 2009. (Cited p. 50 et 62.)
- [94] C Chevalier, O Bénichou, B Meyer, and R Voituriez. First-passage quantities of Brownian motion in a bounded domain with multiple targets: a unified approach. *Journal of Physics A: Mathematical and Theoretical*, 44:25002, 2011. (Cited p. 50.)
- [95] Samuel A. Isaacson and Jay Newby. Uniform asymptotic approximation of diffusion to a small target. *Physical Review E*, 88(1):012820, July 2013. (Cited p. 50.)
- [96] O Bénichou, C Chevalier, J Klafter, B Meyer, and R Voituriez. Geometry-controlled kinetics. *Nat Chem*, 2(6):472–477, June 2010. (Cited p. 50, 175 et 176.)
- [97] B Meyer, C Chevalier, R Voituriez, and O Bénichou. Universality classes of first-passage-time distribution in confined media. *Physical Review E*, 83(5):51116, 2011. (Cited p. 50.)
- [98] Binh T. Nguyen and Denis S. Grebenkov. A Spectral Approach to Survival Probabilities in Porous Media. *Journal of Statistical Physics*, 141(3):532–554, September 2010. (Cited p. 50 et 56.)
- [99] Ian Naismith Sneddon. *Mixed boundary value problems in potential theory*. 1966. (Cited p. 50, 56, 57, 164 et 171.)
- [100] Carey Caginalp and Xinfu Chen. for an Escape Problem. 203:329–342, 2012. (Cited p. 52, 66 et 172.)
- [101] O Bénichou, C Chevalier, J Klafter, B Meyer, and R Voituriez. Geometry-controlled kinetics. *Nature chemistry*, 2(6):472–7, June 2010. (Cited p. 52, 53, 62, 63, 65, 67, 83, 104, 118 et 119.)
- [102] A Singer, Z Schuss, and D Holcman. Narrow escape, part II: The circular disk. *Journal of Statistical Physics*, 122(3):465–489, February 2006. (Cited p. 52.)
- [103] O Benichou and R Voituriez. Narrow-Escape Time Problem: Time Needed for a Particle to Exit a Confining Domain through a Small Window. *Physical Review Letters*, 100(16):168104–168105, 2008. (Cited p. 52.)
- [104] Thiago G. Mattos, Carlos Mejía-Monasterio, Ralf Metzler, and Gleb Oshanin. First passages in bounded domains: When is the mean first passage time meaningful? *Physical Review E*, 86(3):031143, September 2012. (Cited p. 53 et 176.)
- [105] A Singer, Z Schuss, and D Holcman. Narrow Escape, Part III: Non-Smooth Domains and Riemann Surfaces. *Journal of Statistical Physics*, 122(3):491–509. (Cited p. 53, 71 et 74.)

- [106] M. Sbragaglia and A. Prosperetti. A note on the effective slip properties for microchannel flows with ultrahydrophobic surfaces. *Physics of Fluids*, 19(4):043603, 2007. (Cited p. 53, 74, 75, 76, 77 et 164.)
- [107] P. Joseph, C. Cottin-Bizonne, J.-M. Benoît, C. Ybert, C. Journet, P. Tabeling, and L. Bocquet. Slippage of Water Past Superhydrophobic Carbon Nanotube Forests in Microchannels. *Physical Review Letters*, 97(15):156104, October 2006. (Cited p. 53 et 74.)
- [108] C Cottin-Bizonne, C Barentin, E Charlaix, L Bocquet, and J-L Barrat. Dynamics of simple liquids at heterogeneous surfaces: molecular-dynamics simulations and hydrodynamic description. *The European physical journal. E, Soft matter*, 15(4):427–38, December 2004. (Cited p. 53 et 74.)
- [109] Denis Grebenkov. Efficient Monte Carlo methods for simulating diffusion-reaction processes in complex systems. April 2013. (Cited p. 54 et 61.)
- [110] A M Berezhkovskii and A V Barzykin. Extended narrow escape problem: Boundary homogenization-based analysis. *Physical Review E*, 82(1), 2010. (Cited p. 56.)
- [111] O Bénichou, D Grebenkov, P Levitz, C Loverdo, and R Voituriez. Mean First-Passage Time of Surface-Mediated Diffusion in Spherical Domains. *Journal of Statistical Physics*, 142(4):657–685, 2011. (Cited p. 59, 83, 84, 85, 95, 104, 107, 118 et 119.)
- [112] J F. Rupprecht, O Bénichou, D Grebenkov, and R Voituriez. Kinetics of Active Surface-Mediated Diffusion in Spherically Symmetric Domains. *Journal of Statistical Physics*, 147(5):891–918, 2012. (Cited p. 59, 86, 107, 119, 179, 181 et 186.)
- [113] S Redner. *A guide to First-Passage Processes*. Cambridge University Press, Cambridge, England, 2001. (Cited p. 61, 73, 132, 139, 163, 177 et 179.)
- [114] H Carslaw. *Conduction of heat in solids*. Clarendon Press, Oxford, 1959. (Cited p. 77 et 164.)
- [115] L. P. Castro, F. O. Speck, and F. S. Teixeira. Mixed Boundary Value Problems for the Helmholtz Equation in a Quadrant. *Integral Equations and Operator Theory*, 56(1):1–44, December 2005. (Cited p. 77 et 164.)
- [116] Samuel Temkin. *Suspension Acoustics*. Cambridge University Press, Cambridge, 2005. (Cited p. 77 et 164.)
- [117] D Holcman and Z Schuss. Escape Through a Small Opening: Receptor Trafficking in a Synaptic Membrane. *Journal of Statistical Physics*, 117(5):975–1014, 2004. (Cited p. 78.)
- [118] A. M. Berezhkovskii and A. V. Barzykin. Escape and reentry of a Brownian particle through a hole in a cavity. *The Journal of Chemical Physics*, 118(14):6700, 2003. (Cited p. 78.)
- [119] Alexander M Berezhkovskii, Yurii A Makhnovskii, Michael I Monine, Vladimir Yu. Zitserman, and Stanislav Y Shvartsman. Boundary homogenization for trapping by patchy surfaces. *The Journal of Chemical Physics*, 121(22):11390–11394, 2004. (Cited p. 78.)
- [120] Jurgen Reingruber, Enrique Abad, and David Holcman. Narrow escape time to a structured target located on the boundary of a microdomain. *The Journal of Chemical Physics*, 130(9):94907–94909, 2009. (Cited p. 78.)

- [121] Jürgen Reingruber and David Holcman. Narrow escape for a stochastically gated Brownian ligand. *Journal of physics Condensed matter an Institute of Physics journal*, 22(6):065103, 2010. (Cited p. 78.)
- [122] J. Andrew McCammon and Stephen C. Harvey. *Dynamics of Proteins and Nucleic Acids*. 1988. (Cited p. 78.)
- [123] P Levitz, M Zinsmeister, P Davidson, D Constantin, and O Poncelet. Intermittent Brownian dynamics over a rigid strand: Heavily tailed relocation statistics in a simple geometry. *Physical Review E (Statistical, Nonlinear, and Soft Matter Physics)*, 78(3):30102–30104, 2008. (Cited p. 83.)
- [124] Aleksei V Chechkin, Irwin M Zaid, Michael A Lomholt, Igor M Sokolov, and Ralf Metzler. Bulk-mediated surface diffusion along a cylinder: Propagators and crossovers. *Physical Review E*, 79(4), 2009. (Cited p. 83.)
- [125] O. Bénichou, M. Coppey, M. Moreau, P-H. Suet, and R. Voituriez. Optimal Search Strategies for Hidden Targets. *Physical Review Letters*, 94(19):198101, May 2005. (Cited p. 83.)
- [126] O Bénichou, M Coppey, M Moreau, P H Suet, and R Voituriez. Averaged residence times of stochastic motions in bounded domains. *EPL (Europhysics Letters)*, 70(1):42–48, 2005. (Cited p. 83.)
- [127] S N Majumdar. No Title. *Curr Sci*, 77:370, 1999. (Cited p. 83.)
- [128] P Levitz, D S Grebenkov, M Zinsmeister, K M Kolwankar, and B Sapoval. No Title. *Phys. Rev. Lett.*, 96:180601, 2006. (Cited p. 83.)
- [129] G Oshanin, M Tamm, and O Vasilyev. Narrow-escape times for diffusion in microdomains with a particle-surface affinity: Mean-field results. *The Journal of Chemical Physics*, 132(23):235101–235106, 2010. (Cited p. 83 et 107.)
- [130] Alexander M Berezhkovskii and Alexander V Barzykin. Search for a small hole in a cavity wall by intermittent bulk and surface diffusion. *The Journal of Chemical Physics*, 136(5):54115, 2012. (Cited p. 83, 84, 105, 107, 108, 114, 115, 116, 117, 118, 119, 164, 179, 180, 181 et 182.)
- [131] Félix Rojo and Carlos E Budde. Enhanced diffusion through surface excursion: A master-equation approach to the narrow-escape-time problem. *Physical Review E*, 84(2):21117, 2011. (Cited p. 83.)
- [132] F. Rojo, H. S. Wio, and C. E. Budde. Narrow-escape-time problem: the imperfect trapping case. page 9, June 2012. (Cited p. 83.)
- [133] B. Sapoval. General Formulation of Laplacian Transfer Across Irregular Surfaces. *Physical Review Letters*, 73(24):3314–3316, December 1994. (Cited p. 85.)
- [134] R J Hawkins, O Benichou, M Piel, and R Voituriez. Rebuilding cytoskeleton roads: Active-transport-induced polarization of cells. *Physical Review E (Statistical, Nonlinear, and Soft Matter Physics)*, 80(4):40903–40904, 2009. (Cited p. 87.)
- [135] Olivier Bénichou and Jean Desbois. Exit and occupation times for Brownian motion on graphs with general drift and diffusion constant. *Journal of Physics A: Mathematical and Theoretical*, 42(1):15004, 2009. (Cited p. 87.)



- [136] O Bénichou, C Loverdo, M Moreau, and R Voituriez. Optimizing intermittent reaction paths. *Physical Chemistry Chemical Physics*, 10(47):7059–7072, 2008. (Cited p. 121.)
- [137] Otto G. Berg and Clas Blomberg. Association kinetics with coupled diffusional flows. *Biophysical Chemistry*, 4(4):367–381, July 1976. (Cited p. 126 et 143.)
- [138] Nicholas Watkins. The Physics of Foraging: An Introduction to Random Searches and Biological Encounters. *Physics Today*, 65(1):44, January 2012. (Cited p. 126.)
- [139] P. Romanczuk, M. Bär, W. Ebeling, B. Lindner, and L. Schimansky-Geier. Active Brownian particles. *The European Physical Journal Special Topics*, 202(1):1–162, March 2012. (Cited p. 126.)
- [140] S Condamin, O Bénichou, V Tejedor, R Voituriez, and J Klafter. First-passage times in complex scale-invariant media. *Nature*, 450(7166):77–80, 2007. (Cited p. 126 et 163.)
- [141] Thomas Gilbert, Huu Chuong Nguyen, and David P Sanders. Diffusive properties of persistent walks on cubic lattices with application to periodic Lorentz gases. *Journal of Physics A: Mathematical and Theoretical*, 44(6), 2011. (Cited p. 126.)
- [142] Stephane Blanco and Richard Fournier. Short-Path Statistics and the Diffusion Approximation. *Physical Review Letters*, 97(23):230604, 2006. (Cited p. 126.)
- [143] A Zoia, E Dumonteil, and A Mazzolo. Collision-Number Statistics for Transport Processes. *Physical Review Letters*, 106(22), 2011. (Cited p. 126.)
- [144] Vincent Tejedor, Raphael Voituriez, and Olivier Bénichou. Optimizing Persistent Random Searches. *Physical Review Letters*, 108(8):088103—, 2012. (Cited p. 126, 134 et 135.)
- [145] J. Tailleur and M. Cates. Statistical Mechanics of Interacting Run-and-Tumble Bacteria. *Physical Review Letters*, 100(21):218103, May 2008. (Cited p. 128.)
- [146] O. Bénichou, C. Loverdo, M. Moreau, and R. Voituriez. Two-dimensional intermittent search processes: An alternative to Lévy flight strategies. *Physical Review E*, 74(2):020102, August 2006. (Cited p. 135.)
- [147] Rafał Weron. On the Chambers-Mallows-Stuck method for simulating skewed stable random variables. *Statistics & Probability Letters*, 28(2):165–171, June 1996. (Cited p. 140.)
- [148] Anne J Ridley, Martin A Schwartz, Keith Burridge, Richard A Firtel, Mark H Ginsberg, Gary Borisy, J Thomas Parsons, and Alan Rick Horwitz. Cell Migration: Integrating Signals from Front to Back. *Science*, 302(5651):1704–1709, 2003. (Cited p. 144.)
- [149] M Poujade, E Grasland-Mongrain, A Hertzog, J Jouanneau, P Chavrier, B Ladoux, A Buguin, and P Silberzan. Collective migration of an epithelial monolayer in response to a model wound. *Proceedings of the National Academy of Sciences*, 104(41):15988–15993, 2007. (Cited p. 144.)
- [150] Margit A Huber, Norbert Kraut, and Hartmut Beug. Molecular requirements for epithelial–mesenchymal transition during tumor progression. *Current Opinion in Cell Biology*, 17(5):548–558, 2005. (Cited p. 144.)
- [151] R J Hawkins, M Piel, G Faure-Andre, A M Lennon-Dumenil, J F Joanny, J Prost, and R Voituriez. Pushing off the walls: a mechanism of cell motility in confinement. *Phys Rev Lett*, 102(5):58103, February 2009. (Cited p. 144.)

- [152] Kathrin Schumann, Tim Lämmermann, Markus Bruckner, Daniel F Legler, Julien Polleux, Joachim P Spatz, Gerold Schuler, Reinhold Förster, Manfred B Lutz, Lydia Sorokin, and Michael Sixt. Immobilized Chemokine Fields and Soluble Chemokine Gradients Cooperatively Shape Migration Patterns of Dendritic Cells. *Immunity*, 32(5):703–713, 2010. (Cited p. 144.)
- [153] David Selmecki, Stephan Mosler, Peter H Hagedorn, Niels B Larsen, and Henrik Flyvbjerg. Cell motility as persistent random motion: theories from experiments. *Biophys J*, 89(2):912–931, August 2005. (Cited p. 144, 155 et 157.)
- [154] D Selmecki, L Li, L I I Pedersen, S F Nrrelykke, P H Hagedorn, S Mosler, N B Larsen, E C Cox, and H Flyvbjerg. Cell motility as random motion: A review. *EPJE-ST*, 157:1–15, April 2008. (Cited p. 144, 155 et 157.)
- [155] Liang Li, Edward C Cox, and Henrik Flyvbjerg. 'Dicty dynamics': Dictyostelium motility as persistent random motion. *Physical Biology*, 8(4):46006, 2011. (Cited p. 144.)
- [156] Tajie H Harris, Edward J Banigan, David A Christian, Christoph Konradt, Elia D Tait Wojno, Kazumi Norose, Emma H Wilson, Beena John, Wolfgang Weninger, Andrew D Luster, Andrea J Liu, and Christopher A Hunter. Generalized Levy walks and the role of chemokines in migration of effector CD8+ T cells. *Nature*, 486(7404):545–548, 2012. (Cited p. 144, 160 et 164.)
- [157] O Bénichou, C Loverdo, M Moreau, and R Voituriez. Intermittent search strategies. *Reviews of Modern Physics*, 83(1):81–129, 2011. (Cited p. 144, 157, 159 et 164.)
- [158] Pawel Romanczuk and Lutz Schimansky-Geier. Brownian Motion with Active Fluctuations. *Physical Review Letters*, 106(23), 2011. (Cited p. 144, 150, 155 et 156.)
- [159] P Romanczuk, M Bar, W Ebeling, B Lindner, and L Schimansky-Geier. Active Brownian particles From Individual to Collective Stochastic Dynamics. *EPJE-ST*, 202(1):1–162, March 2012. (Cited p. 144 et 155.)
- [160] András Czirók, Katalin Schlett, Emília Madarász, and Tamás Vicsek. Exponential Distribution of Locomotion Activity in Cell Cultures. *Physical Review Letters*, 81(14):3038–3041, 1998. (Cited p. 144.)
- [161] John Toner, Yuhai Tu, and Sriram Ramaswamy. Hydrodynamics and phases of flocks. *Annals of Physics*, 318(1):170–244, 2005. (Cited p. 144.)
- [162] S. Vedel, S. Tay, D. M Johnston, H. Bruus, and S. R Quake. Migration of cells in a social context. *Proc Natl Acad Sci U S A*, 110(1):129–134, January 2013. (Cited p. 144 et 157.)
- [163] Paolo Maiuri, Emmanuel Terriac, Perrine Paul-Gilloteaux, TimothÉe Vignaud, Krista McNally, James Onuffer, Kurt Thorn, Phuong A Nguyen, Nefeli Georgoulia, Daniel Soong, Asier Jayo, Nina Beil, JÁrgen Beneke, Joleen Chooi Hong Lim, Chloe Pei-Ying Sim, Yeh-Shiu Chu, Andrea JimÉnez-Dalmaroni, Jean-FranÁois Joanny, Jean-Paul Thiery, Holger Erfle, Maddy Parsons, Timothy J Mitchison, Wendell A Lim, Ana-Maria Lennon-DumÉnil, Matthieu Piel, and Manuel ThÉry. The first World Cell Race. *Current biology : CB*, 22(17):R673—R675, 2012. (Cited p. 144, 145 et 146.)
- [164] Clemens Grabher, Adam Cliffe, Kota Miura, Joel Hayflick, Rainer Pepperkok, Pernille Rø rth, and Joachim Wittbrodt. Birth and life of tissue macrophages and their migration in embryogenesis and inflammation in medaka. *Journal of Leukocyte Biology*, 81(1):263–271, 2007. (Cited p. 145 et 146.)

- [165] J A Theriot and T J Mitchison. Actin microfilament dynamics in locomoting cells. *Nature*, 352(6331):126–131, July 1991. (Cited p. 145 et 147.)
- [166] T M Svitkina, A B Verkhovsky, K M McQuade, and G G Borisy. Analysis of the actin-myosin II system in fish epidermal keratocytes: mechanism of cell body translocation. *J Cell Biol*, 139(2):397–415, October 1997. (Cited p. 145, 147 et 151.)
- [167] A B Verkhovsky, T M Svitkina, and G G Borisy. Self-polarization and directional motility of cytoplasm. *Curr Biol*, 9(1):11–20, January 1999. (Cited p. 145 et 147.)
- [168] Thomas D Pollard and Gary G Borisy. Cellular motility driven by assembly and disassembly of actin filaments. *Cell*, 112(4):453–465, February 2003. (Cited p. 145 et 147.)
- [169] Kinneret Keren, Zachary Pincus, Greg M Allen, Erin L Barnhart, Gerard Marriott, Alex Mogilner, and Julie A Theriot. Mechanism of shape determination in motile cells. *Nature*, 453(7194):475–480, May 2008. (Cited p. 145 et 147.)
- [170] Cyrus A Wilson, Mark A Tsuchida, Greg M Allen, Erin L Barnhart, Kathryn T Applegate, Patricia T Yam, Lin Ji, Kinneret Keren, Gaudenz Danuser, and Julie A Theriot. Myosin II contributes to cell-scale actin network treadmilling through network disassembly. *Nature*, 465(7296):373–377, May 2010. (Cited p. 145, 147 et 151.)
- [171] J Victor Small and Guenter P Resch. The comings and goings of actin: coupling protrusion and retraction in cell motility. *Curr Opin Cell Biol*, 17(5):517–523, October 2005. (Cited p. 147.)
- [172] Gaudenz Danuser, Jun Allard, and Alex Mogilner. Mathematical Modeling of Eukaryotic Cell Migration: Insights Beyond Experiments. *Annu Rev Cell Dev Biol*, July 2013. (Cited p. 147.)
- [173] Jörg Renkawitz, Kathrin Schumann, Michele Weber, Tim Lämmermann, Holger Pflücke, Matthieu Piel, Julien Polleux, Joachim P Spatz, and Michael Sixt. Adaptive force transmission in amoeboid cell migration. *Nat Cell Biol*, 11(12):1438–1443, December 2009. (Cited p. 147.)
- [174] A Mogilner and G Oster. Cell motility driven by actin polymerization. *Biophys J*, 71(6):3030–3045, December 1996. (Cited p. 147.)
- [175] Carlos Jurado, John R Haserick, and Juliet Lee. Slipping or Gripping? Fluorescent Speckle Microscopy in Fish Keratocytes Reveals Two Different Mechanisms for Generating a Retrograde Flow of Actin. *Molecular Biology of the Cell*, 16(2):507–518, 2005. (Cited p. 147.)
- [176] K Kruse, J F Joanny, F Jülicher, and J Prost. Contractility and retrograde flow in lamellipodium motion. *Phys Biol*, 3(2):130–137, June 2006. (Cited p. 147.)
- [177] Rhoda J Hawkins, Renaud Poincloux, Olivier Bénichou, Matthieu Piel, Philippe Chavrier, and Raphaël Voituriez. Spontaneous Contractility-Mediated Cortical Flow Generates Cell Migration in Three-Dimensional Environments. *Biophysical Journal*, 101(5):1041–1045, 2011. (Cited p. 147 et 152.)
- [178] A C Callan-Jones and R Voituriez. Active gel model of amoeboid cell motility. *New Journal of Physics*, 15(2):25022, 2013. (Cited p. 147 et 152.)
- [179] Tim Mitchison and Marc Kirschner. Cytoskeletal dynamics and nerve growth. *Neuron*, 1(9):761–772, 1988. (Cited p. 147 et 159.)

- [180] Ke Hu, Lin Ji, Kathryn T Applegate, Gaudenz Danuser, and Clare M Waterman-Storer. Differential Transmission of Actin Motion Within Focal Adhesions. *Science*, 315(5808):111–115, 2007. (Cited p. 147.)
- [181] Margaret L Gardel, Ian C Schneider, Yvonne Aratyn-Schaus, and Clare M Waterman. Mechanical Integration of Actin and Adhesion Dynamics in Cell Migration. *Annual Review of Cell and Developmental Biology*, 26(1):315–333, 2010. (Cited p. 147.)
- [182] Edwin Munro, Jeremy Nance, and James R Priess. Cortical flows powered by asymmetrical contraction transport PAR proteins to establish and maintain anterior-posterior polarity in the early *C. elegans* embryo. *Dev Cell*, 7(3):413–424, September 2004. (Cited p. 149.)
- [183] Nathan W Goehring, Philipp Khuc Trong, Justin S Bois, Debanjan Chowdhury, Ernesto M Nicola, Anthony A Hyman, and Stephan W Grill. Polarization of PAR proteins by advective triggering of a pattern-forming system. *Science*, 334(6059):1137–1141, November 2011. (Cited p. 149.)
- [184] Alexander B Verkhovsky. Cell polarization: mechanical switch for a chemical reaction. *Curr Biol*, 22(2):R58–61, January 2012. (Cited p. 149, 151 et 159.)
- [185] Guillaume Montagnac, Vannary Meas-Yedid, Marie Irondelle, Antonio Castro-Castro, Michel Franco, Toshinobu Shida, Maxence V Nachury, Alexandre Benmerah, Jean-Christophe Olivo-Marin, and Philippe Chavrier.  $\text{G}^{\text{I}}\text{TAT1}$  catalyses microtubule acetylation at clathrin-coated pits. *Nature*, 502(7472):567–570, 2013. (Cited p. 149.)
- [186] Noa Ofer, Alexander Mogilner, and Kinneret Keren. Actin disassembly clock determines shape and speed of lamellipodial fragments. *Proc Natl Acad Sci U S A*, 108(51):20394–20399, December 2011. (Cited p. 151.)
- [187] Julia Riedl, Alvaro H Crevenna, Kai Kessenbrock, Jerry Haochen Yu, Dorothee Neukirchen, Michal Bista, Frank Bradke, Dieter Jenne, Tad A Holak, Zena Werb, Michael Sixt, and Roland Wedlich-Soldner. Lifeact: a versatile marker to visualize F-actin. *Nat Meth*, 5(7):605–607, 2008. (Cited p. 151.)
- [188] Tomo Kondo, Kozue Hamao, Keiju Kamijo, Hiroshi Kimura, Makiko Morita, Masayuki Takahashi, and Hiroshi Hosoya. Enhancement of myosin II/actin turnover at the contractile ring induces slower furrowing in dividing HeLa cells. *Biochemical Journal*, 435(3):569–576, 2011. (Cited p. 151.)
- [189] Brian M Burkel, George von Dassow, and William M Bement. Versatile fluorescent probes for actin filaments based on the actin-binding domain of utrophin. *Cell Motility and the Cytoskeleton*, 64(11):822–832, 2007. (Cited p. 151.)
- [190] F Julicher, K Kruse, J Prost, and J F. Joanny. Active behavior of the Cytoskeleton. *Physics Reports*, 449(1-3):3–28, 2007. (Cited p. 152.)
- [191] Justin S Bois, Frank Jülicher, and Stephan W Grill. Pattern formation in active fluids. *Phys Rev Lett*, 106(2):28103, January 2011. (Cited p. 152.)
- [192] H.Risken. *The Fokker-Planck Equation: Method of Solution and Applications*. Springer-Verlag, 1996. (Cited p. 155.)
- [193] K Mallick and P Marcq. Noise-induced reentrant transition of the stochastic Duffing oscillator. *EPJB*, 38(1):99–102, 2004. (Cited p. 157.)

- [194] Hiromi Miyoshi, Noritaka Masaki, and Yoshimi Tsuchiya. Characteristics of trajectory in the migration of Amoeba proteus. *Protoplasma*, 222(3-4):175–181, 2003. (Cited p. 159.)
- [195] Laurent Golé, Charlotte Rivière, Yoshinori Hayakawa, and Jean-Paul Rieu. A quorum-sensing factor in vegetative Dictyostelium discoideum cells revealed by quantitative migration analysis. *PLoS One*, 6(11):e26901, 2011. (Cited p. 159.)
- [196] Victoria Sanz-Moreno, Gilles Gadea, Jessica Ahn, Hugh Paterson, Pierfrancesco Marra, Sophie Pinner, Erik Sahai, and Christopher J Marshall. Rac activation and inactivation control plasticity of tumor cell movement. *Cell*, 135(3):510–523, October 2008. (Cited p. 159.)
- [197] Vincent Tejedor, Raphael Voituriez, and Olivier Bénichou. Optimizing Persistent Random Searches. *Physical Review Letters*, 108(8):088103—, 2012. (Cited p. 159.)
- [198] O Bénichou, C Chevalier, B Meyer, and R Voituriez. Facilitated Diffusion of Proteins on Chromatin. *Physical Review Letters*, 106:38102, 2011. (Cited p. 163.)
- [199] M Sheinman, O Bénichou, Y Kafri, and R Voituriez. Classes of fast and specific search mechanisms for proteins on DNA. *Reports on Progress in Physics*, 75(2):26601, 2012. (Cited p. 163.)
- [200] Dean G. Duffy. *Mixed Boundary Value Problems*. CRC Press, 2008. (Cited p. 174.)
- [201] COMSOL. Multiphysics v. 4.2, 2013. (Cited p. 176.)
- [202] Valsa. Invlap package, 2011. (Cited p. 176.)
- [203] Frank J. Massey. The Kolmogorov-Smirnov Test for Goodness of Fit. *Journal of the American Statistical Association*, 46(253):68–78, March 1951. (Cited p. 181.)
- [204] O. Bénichou, D. S. Grebenkov, P. E. Levitz, C. Loverdo, and R. Voituriez. Mean First-Passage Time of Surface-Mediated Diffusion in Spherical Domains. *Journal of Statistical Physics*, 142(4):657–685, February 2011. (Cited p. 183.)

# Remerciements

Je remercie tout d'abord Pascal Viot, directeur du Laboratoire de Physique Théorique de la Matière Condensée pour m'avoir accueilli et prodigué de nombreux conseils.

Je remercie Athanasios Batakis et David Dean pour avoir accepté la charge de rapporteur de cette thèse, et Andrea Parmeggiani et Lydéric Bocquet celle d'examineur.

Je suis reconnaissant à Raphaël Voituriez et à Olivier Bénichou pour m'avoir aiguillé sur des projets intéressants tout en me garantissant une grande liberté. Merci aussi à Denis Grebenkov pour son aide et ses encouragements enthousiastes.

Je remercie également

- les secrétaires du LPTMC, Diane Domand, Sylvie Dalla Foglia et Liliane Cruzel pour leur aide administrative,
- les co-thésards qui m'ont rendu le quotidien plus agréable: tout d'abord Thibaut Calandre, qui, bien qu'écranté par un Mac, m'a poussé à faire du sport (escrime et Lindy), Pierre Illien, pour son grand sens de l'humour, Marie Chupeau, pour ses conseils pour MT180s, et le gourmet Nicolas Levernier.
- les anciens, Vincent Tejedor, Bob Meyer et Claude Loverdo, pour m'avoir transmis leurs codes (et parfois leur carte à puce de restauration),
- Thomas Guérin et Simon Mouliera pour leurs conseils expérimentés.
- les expérimentateurs de l'équipe de Curie, Matthieu Piel et les post-docs Franziska Lautenschlaeger, Paolo Maiuri et Maël Le Berre, pour avoir pris le temps de discuter et de me présenter leurs manips, ainsi que Nir Gov et Ankush Sengupta.
- Michel Zinsmeister pour m'avoir présenté une démonstration plus rigoureuse des identités sur  $a_0$ , Eq. (A.5), ainsi que pour des discussions sur les problèmes intermittents.
- Gleb Oshanin et les organisateurs de l'école d'été de Cargèse *Search & Exploration*.
- l'imperturbable Bertrand Delamotte, pour nous avoir fait découvrir le domaine de la renormalisation non-perturbative dans un cours de l'ED.
- Karim Essafi et Axel Cournac, mes premiers co-bureaux, ainsi que Thiago, Lucas, Jules, Tom, Axelle, Oscar, Thibaut, Andreas, Elena, Charlotte, Clément, Nicolas, Boris, Julien & Julien-Piera et toutes les personnes qui ont également contribué à l'ambiance chaleureuse du laboratoire.
- les autres amis qui n'ont pas eu la chance d'être au LPTMC, avec une mention spéciale pour les thésards-skieurs d'Alembertiens ainsi que pour les matheux du C6 de Montrouge, et en particulier Bastien Mallein qui a pris le temps de réfléchir à une méthode plus optimale de simulation Monte-Carlo pour les processus de sorties.
- Hélène Delanoë-Ayari et sa doctorante Sham Tlili pour m'avoir fait découvrir le logiciel d'éléments finis Comsol. Que de journées gagnées et de projets débloqués grâce à ce logiciel!
- à Sham et à mes parents pour leur soutien.







# Optimisation de processus de recherche par des marcheurs aléatoires symétriques, avec biais ou actifs

**Résumé :** Les marches aléatoires avec recherche de cible peuvent modéliser des réactions nucléaires ou la quête de nourriture par des animaux. Dans cette thèse, nous identifions des stratégies qui minimisent le temps moyen de première rencontre d'une cible (MFPT) pour plusieurs types de marches aléatoires.

Premièrement, pour des marches symétriques ou avec biais, nous déterminons la distribution des temps de première sortie par une ouverture dans une paroi en forme de secteur angulaire, d'anneau ou de rectangle. Nous concluons sur la minimisation du MFPT en termes de la géométrie du confinement.

Deuxièmement, pour des marches alternant entre diffusions volumique et surfacique, nous déterminons le temps moyen de première sortie par une ouverture dans la surface de confinement. Nous montrons qu'il existe un taux de désorption optimal qui minimise le MFPT. Nous justifions la généralité de l'optimalité par l'étude des rôles de la géométrie, de l'adsorption sur la surface et d'un biais en phase volumique.

Troisièmement, pour des marches actives composées de phases balistiques entrecoupées par des réorientations aléatoires, nous obtenons l'expression du taux de réorientation qui minimise le MFPT en géométries sphériques de dimension deux ou trois.

Dans un dernier chapitre, nous modélisons le mouvement de cellules eucaryotes par des marches browniennes actives. Nous expliquons pourquoi le temps de persistance évolue exponentiellement avec la vitesse de la cellule. Nous obtenons un diagramme des phases des types de trajectoires. Ce modèle minimal permet de quantifier l'efficacité des processus de recherche d'antigènes par des cellules immunitaires.

**Mots clés :** Temps de premier passage, mouvement Brownien, processus à saut, particules actives, Physique Statistique, Biophysique.

---

## Search optimization by symmetric, biased and active random walks

**Abstract:** Random search processes can model nuclear reactions or animal foraging. In this thesis, we identify optimal search strategies which minimize the mean first passage time (MFPT) to a target for various processes.

First, for symmetric and biased Brownian particles, we compute the distribution of exit times through an opening within the boundary of angular sectors, annuli and rectangles. We conclude on the optimizability of the MFPT in terms of geometric parameters.

Second, for walks that switch between volume and surface diffusions, we determine the mean exit time through an opening inside the bounding surface. Under analytical criteria, an optimal desorption rate minimizes the MFPT. We justify that this optimality is a general property through a study of the roles of the geometry, of the adsorption properties and of a bias in the bulk random walk.

Third, for active walks composed of straight runs interrupted by reorientations in a random direction, we obtain the expression of the optimal reorientation rate which minimizes the MFPT to a centered spherical target within a spherical confinement, in two and three dimensions.

In a last chapter, we model the motion of eukaryotic cells by active Brownian walks. We explain an experimental observation: the persistence time is exponentially coupled with the speed of the cell. We also obtain a phase diagram for each type of trajectories. This model is a first step to quantify the search efficiency of immune cells in terms of a minimal number of biological parameters.

**Keywords:** First passage time, Brownian motion, jump processes, active particles, Statistical Physics, Biophysics.

